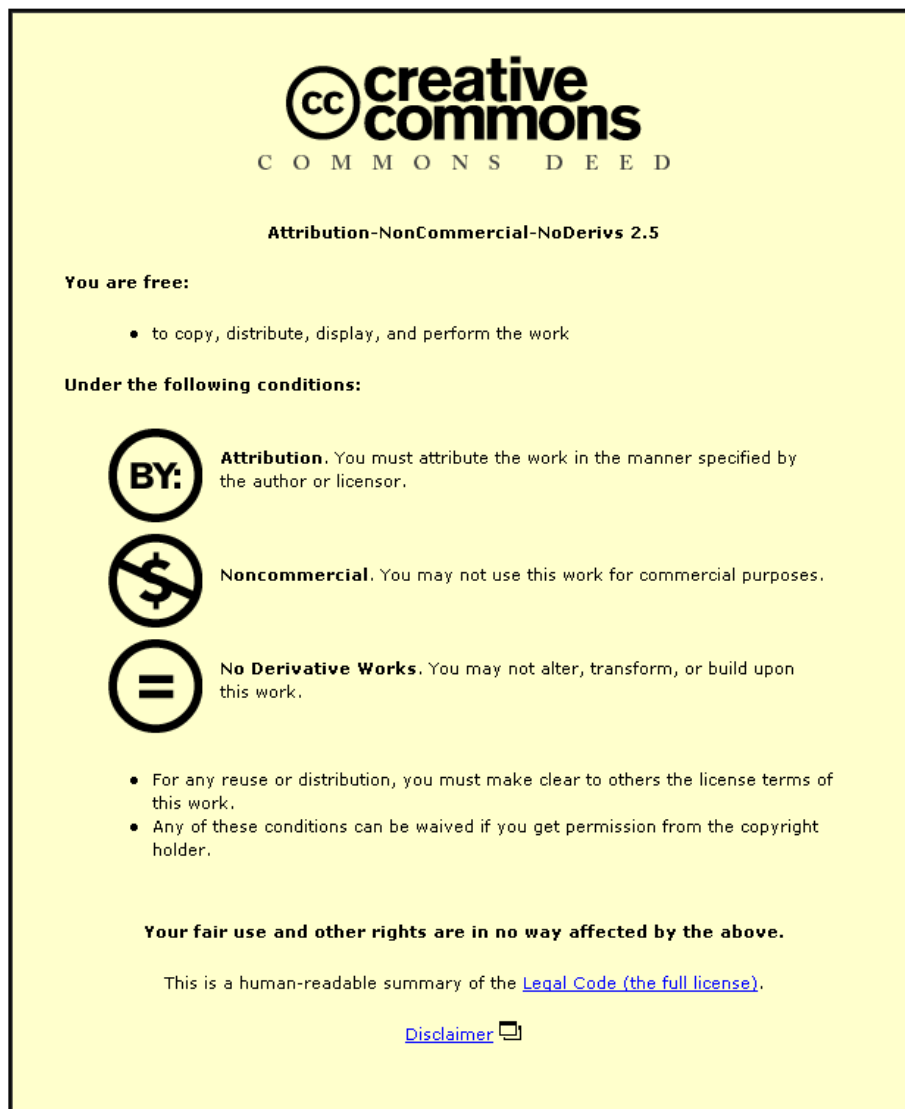


This item was submitted to Loughborough University as a PhD thesis by the author and is made available in the Institutional Repository (<https://dspace.lboro.ac.uk/>) under the following Creative Commons Licence conditions.



For the full text of this licence, please go to:
<http://creativecommons.org/licenses/by-nc-nd/2.5/>

Microwave-assisted Processing of Solid
Materials for Sustainable Energy
Related Electronic and Optoelectronic
Applications

By

T. A. Nirmal Peiris

**A Doctoral Thesis Submitted in Partial Fulfilment of
the Requirements for the Award of Doctor of
Philosophy of Loughborough University**

April 2014



Acknowledgements:

GOD...without your help and support, I could not achieve anything in my life.

First, I sincerely thank my supervisors Dr Upul Wijayantha and Dr Rob Potter for their support, advice, encouragement and guidance given to me throughout this study. It was truly a privilege for me to work with them for the past three years of time. I must also thank our past postdoctoral research associates, Dr Senthil Senthilarasu, Dr Asif A. Tahir and Dr Ijaz Ahmad Bhatti for their unlimited help and advice given during my studies. I would like to thank past and present enthusiastic researchers of energy research laboratory (ERL) in the chemistry department, Dr. S. Saremi Yarahmadi, Dr Mohd Asri Mat Teridi, Dr Anish Patel, Dr Tom Smith, Jagdeep Sagu, Hussain Alessa, Vanessa Silvestre, Andrew McInnes, Paul Brack, Joey Walker, Bader Altayeb, Subhashi Jayathilake for their help and support along the way. This work would not have possible without funding from the Johnson Matthey Plc and UK EPSRC, thank you for funding me on this project. I thank the staff of chemistry and materials departments for providing me with an excellent environment to perform my research.

Very special thanks go to my parents, Hector and Dayani Peiris and father and mother-in-laws, Kalum and Yamuna Jayathilake for their love, guidance and encouragement during my postgraduate studies in UK. Also I really appreciate the advice and support given from my two sisters Samindika and Duthika Peiris and brother-in-law, Nalaka Nanayakkara throughout my studies. I have not forgotten to thank Sr. Mary Cyrilline, for her prayers and encouragement given to me on my studies. Last but not least, a very special thanks to my loving wife, Subhashi Jayathilake for all that she has done for me thorough out my studies. She always found a way to support and help me during the hard times.

Table of Contents

List of Figures	vii
List of Tables	xiv
List of Abbreviations	xv
Abstract.....	xviii
Chapter 1	19
Introduction	
Chapter 2.....	24
Literature review	
2.1 Theory and Background.....	24
2.1.1 Microwave fundamentals and microwave heating	24
2.1.2 Polarization mechanisms of materials	27
2.1.3 Microwave heat generation.....	30
2.1.4 Microwave-material interactions	32
2.1.5 Semiconductor photonic materials.....	36
2.1.6 Energetics at semiconductor-electrolyte interface	42
2.1.7 Ideal behaviour of an n-type semiconductor under dark and light	49
2.2 Microwave synthesis and processing of materials.....	50
2.2.1 Semiconductor metal oxides	52
2.2.2 Non-oxide semiconductors	57
2.2.3 Metal oxide thin films.....	59
2.3 Industrial use of microwaves for material processing	60

2.4 Unique performance characteristics to microwaves	61
2.5. Microwave generators.....	63
Chapter 3.....	65
Experimental Methods and Materials Characterization	
3.1 Experimental Methods	65
3.1.1 Aerosol-assisted chemical vapour deposition.....	65
3.1.2 Chemical bath deposition.....	66
3.1.3 Annealing procedures	67
3.2 Materials Characterization	71
3.2.1 X-ray diffraction	71
3.2.2 Raman spectroscopy	73
3.2.3 Field emission gun scanning electron microscopy	74
3.2.4 UV-Vis optical absorbance	77
3.2.5 Incident photon to electron conversion efficiency.....	78
3.2.6 Surface area measurements – dye adsorption-desorption studies.....	79
Chapter 4.....	81
Enhancement of Photoelectrochemical Performance of AACVD-produced TiO ₂ Electrodes by Microwave Irradiation while Preserving the Nanostructure	
4.1 Overview.....	81
4.2 Introduction.....	82
4.3 Experimental.....	84
4.4 Results and Discussion	84

4.4.1 XRD characteristics	85
4.4.2 Morphological properties.....	87
4.4.3 Photoelectrochemical properties of electrodes	92
4.5 Conclusions.....	99
Chapter 5.....	100
Hierarchical ZnO nanorod electrodes: Effect of post annealing on structural and photoelectrochemical performance	
5.1 Overview.....	100
5.2 Introduction.....	101
5.3 Experimental.....	102
5.4 Results and Discussion	103
5.4.1 XRD characterization.....	103
5.4.2 Optical characterization	107
5.4.3 Morphological properties.....	108
5.4.4 Internal surface area determination.....	112
5.4.5 Photoelectrochemical characterization	113
5.5 Conclusions.....	116
Chapter 6.....	118
Microwave-assisted low temperature fabrication of nanostructured ZnO thin film electrodes for solar energy conversion	
6.1 Overview.....	118
6.2 Introduction.....	120

6.3 Experimental	122
6.4 Results and Discussion	124
6.4.1 Electrodeposition of Zn.....	124
6.4.2 XRD characterisation.....	124
6.4.3 Morphological properties and particle size.....	126
6.4.4 Photoelectrochemical properties of electrodes	130
6.4.5 Temperature-time profile	135
6.5 Conclusions.....	136
Chapter 7.....	137
Microwave-assisted synthesis and processing of inorganic materials for electronic and optoelectronic applications	
7.1 Microwave assisted in-situ activation of lattice oxygen of TiO ₂ by Pd ²⁺ ion; Microwave-assisted synthesis of Ti _{0.97} Pd _{0.03} O _{1.97} powders	137
7.1.1 Overview.....	137
7.1.2 Introduction.....	138
7.1.3 Experimental.....	139
7.1.3.1 Synthesis of Ti _{0.97} Pd _{0.03} O _{1.97} by traditional method.....	139
7.1.3.2 Synthesis of Ti _{0.97} Pd _{0.03} O _{1.97} by microwave assisted method.....	139
7.1.3.3 Characterization	141
7.1.4 Results and Discussion	142
7.1.4.1 Structural characterization	142
7.1.4.2 Surface morphology.....	144

7.1.5 Conclusions.....	147
7.2 The effect of post annealing on the electrical conductivity of lithium aluminium titanium phosphate pellets.....	148
7.2.1 Overview.....	148
7.2.2 Introduction.....	149
7.2.3 Experimental.....	150
7.2.4 Results and Discussion	151
7.2.4.1 X-ray diffraction analysis	151
7.2.4.2 Raman analysis	153
7.2.4.3 Impedance analysis	155
7.2.5 Conclusions.....	158
Chapter 8.....	159
8.1 Conclusions.....	159
8.2 Further Work.....	163
Chapter 9.....	164
References	
Chapter 10.....	198
Appendix	
10.1 Awards	198
10.2 Peer-reviewed and submitted articles in scientific journals.....	199
10.3 Conference participations and presentations	203

List of Figures

Figure 1-1. The temperature profiles of microwave and conventional annealing methods of the reaction mixture in the vessel.[10]	20
Figure 2-1. Electric and magnetic field components of electromagnetic radiation.[19]	24
Figure 2-2. The electromagnetic spectrum.[21].....	25
Figure 2-3. Transmission, Absorption, and Reflection of microwave radiation.	26
Figure 2-4. The electronic polarization in dielectric materials.	28
Figure 2-5. The ionic polarization in dielectric materials.....	29
Figure 2-6. The molecular (dipolar) polarization in dielectric materials.....	29
Figure 2-7. The interfacial (Space-charge) polarization in dielectric materials.	30
Figure 2-8. Two main heating mechanisms under microwave irradiation: (a) dipolar polarization; (b) ionic polarization.[34]	31
Figure 2-9. Frequency response of the complex permittivity for a typical dielectric material due to different polarization mechanisms.[39]	34
Figure 2-10. The electronic energies of metals, semiconductors and insulators.	37
Figure 2-11. Schematic energy diagram of an n-type semiconductor.	38
Figure 2-12. Schematic energy diagram of a p-type semiconductor.	39
Figure 2-13. Schematic energy diagram of an intrinsic semiconductor.	39
Figure 2-14. Band bending of an n-type semiconductor.....	42
Figure 2-15. Band bending of a p-type semiconductor.....	43
Figure 2-16. The energy band diagrams of an n-type semiconductor at flat band conditions. 44	
Figure 2-17. The energy band diagrams of a p-type semiconductor at flat band conditions... 44	

Figure 2-18. The energy band diagrams of an n-type semiconductor when applied potential is higher than the E_{fb}	45
Figure 2-19. The energy band diagrams of a p-type semiconductor when applied potential is lower than the E_{fb}	45
Figure 2-20. The energy band diagrams of an n-type semiconductor when applied potential is lower than the E_{fb}	46
Figure 2-21. The energy band diagrams of a p-type semiconductor when applied potential is higher than the E_{fb}	46
Figure 2-22. A simplified picture of the charge separation at the semiconductor/electrolyte interface for an n- type semiconductor under illumination conditions.....	48
Figure 2-23. A simplified picture of the charge separation at the semiconductor/electrolyte interface for a p- type semiconductor under illumination conditions.....	48
Figure 2-24. Ideal behaviour for an n-type semiconductor in (a) dark and (b) under light in an electrolyte.....	49
Figure 2-25. The variation in the penetration depth of microwaves with the density and the dispersion medium of SiC.....	51
Figure 2-26. Magnetron of 2kW power.[167]	63
Figure 2-27. A cross-section of a typical magnetron.[168]	64
Figure 3-1. Schematic of the aerosol-assisted chemical vapor deposition apparatus.[171]	65
Figure 3-2. Chemical Bath deposition set-up.[175].....	67
Figure 3-3. Conventional thermal MTF-10-25-130 tube furnace.....	68
Figure 3-4. The images of (a) industrial MRF 16/22 microwave furnace with Micro-Epsilon/TIM 400 thermal imaging camera. (b) Microwave furnace chamber and the insulator blocks.	69

Figure 3-5. The images of (a) custom processing BP-211/50 microwave furnace with M67S IR temperature transmitter. (b) Microwave furnace chamber and the insulation.	69
Figure 3-6. A screen shot of a thermal image of the itools software analysing the reading taken from the thermal imaging camera.	70
Figure 3-7. Biotage Initiator EXP 8 reactor.....	71
Figure 3-8. An X-ray diffraction beam schematic [177], showing the incident and scattered X-rays, from a pair of atoms in different lattice planes.	72
Figure 3-9. Photograph of the Bruker D8 X-ray diffractometer used in this study, the X-ray source is on the left, the sample is in the middle and the detector is on the right.....	73
Figure 3-10. HORIBA Jobin Yvon LabRAM HR (with 632.8 nm He-Ne laser) Raman.....	74
Figure 3-11. A schematic diagram of scanning electron microscope.[178]	75
Figure 3-12. The elastically and inelastically scattering of incident electron beam.....	75
Figure 3-13. Leo 1530 VP FEG-SEM set-up.....	76
Figure 3-14. Lambda 35 Perkin-Elmer UV-Vis spectrophotometer.....	78
Figure 3-15. Xenon lamp, monochromator and lock-in amplifier of the IPCE set-up.	79
Figure 4-1. XRD diffractograms of TiO ₂ electrodes deposited by AACVD at 350 °C and treated with different % of microwave radiation.	85
Figure 4-2. XRD diffractograms of TiO ₂ electrodes deposited by AACVD at 400 °C and treated with different % of microwave radiation.	86
Figure 4-3. SEM image of AACVD-produced TiO ₂ electrodes deposited at 350 °C and treated under 0 % microwave radiation.	88
Figure 4-4. SEM image of AACVD-produced TiO ₂ electrodes deposited at 350 °C and treated under 25 % microwave radiation.	88

Figure 4-5. SEM image of AACVD-produced TiO ₂ electrodes deposited at 350 °C and treated under 50 % microwave radiation.	89
Figure 4-6. SEM image of AACVD-produced TiO ₂ electrodes deposited at 350 °C and treated under 100 % microwave radiation.	89
Figure 4-7. SEM image of AACVD-produced TiO ₂ electrodes deposited at 400 °C and treated under 0 % microwave radiation.	90
Figure 4-8. SEM image of AACVD-produced TiO ₂ electrodes deposited at 400 °C and treated under 25 % microwave radiation.	90
Figure 4-9. SEM image of AACVD-produced TiO ₂ electrodes deposited at 400 °C and treated under 50 % microwave radiation.	91
Figure 4-10. SEM image of AACVD-produced TiO ₂ electrodes deposited at 400 °C and treated under 100 % microwave radiation.	91
Figure 4-11. Cross-sectional image of AACVD-produced TiO ₂ electrodes deposited at 400 °C and treated under 100 % microwave radiation.	92
Figure 4-12. J-V Characteristics of TiO ₂ photoelectrodes fabricated at 350 °C and irradiated under various % microwaves.	94
Figure 4-13. J-V Characteristics of TiO ₂ photoelectrodes fabricated at 400 °C and irradiated under various % microwaves.	94
Figure 4-14. J-V characteristics of TiO ₂ photoelectrodes fabricated at 350 °C under various percentages of microwave irradiation (2.45 GHz) [The data has been taken from figure 4.11].	95
Figure 4-15. J-V characteristics of TiO ₂ photoelectrodes fabricated at 400 °C under various percentages of microwave irradiation (2.45 GHz) [The data has been taken from figure 4.12].	96
Figure 4-16. IPCE plots for as deposited film at 400 °C and after 100 % microwave treatment.	96

Figure 4-17. The variation of the photocurrent density of AACVD deposited TiO ₂ electrodes at 350 °C and 400 °C against microwave power level.	97
Figure 4-18. Variation of the photocurrent density against microwave and conventional annealing.	98
Figure 4-19. Temperature- time profile of microwave and conventionally deposited samples at 400 °C at the same power conditions	98
Figure 5-1. XRD diffractogram of as-deposited ZnO electrode.	104
Figure 5-2. XRD diffractogram of microwave treated ZnO electrode.	104
Figure 5-3. XRD diffractogram of conventionally annealed ZnO electrode.	105
Figure 5-4. XRD diffractograms of (a) as-deposited, (b) microwave irradiated and (c) conventional thermal annealed ZnO electrodes. [The data has been taken from figures 5-1, 5-2 and 5.3]	106
Figure 5-5. UV-Vis spectrum of ZnO nanorods on the FTO glass substrate.	107
Figure 5-6. The plot for direct band gap determination of ZnO films.	108
Figure 5-7. The FEG-SEM images of as deposited ZnO nanorods (a) low magnification (b) higher magnification.	109
Figure 5-8. Cross-sectional image of ZnO nanorods grown on ZnO seed layer.	110
Figure 5-9. The FEG-SEM images of microwave treated ZnO nanorods (a) low magnification (b) higher magnification.	111
Figure 5-10. The FEG-SEM images of conventional thermal annealed ZnO nanorods (a) low magnification (b) higher magnification.	112
Figure 5-11. Current density versus voltage (<i>J-V</i>) characteristics of (a) as-deposited, (b) microwave irradiated and (c) conventional thermal annealed ZnO electrodes. The current density of each electrode is uncorrected for the internal surface area.	114

Figure 5-12. The comparison of estimated internal surface area versus corrected photocurrent density for internal surface area of as-deposited and treated ZnO electrodes.	115
Figure 5-13. The normalised J-V plots of as-deposited, microwave irradiated and conventionally annealed ZnO electrodes.	116
Figure 6-1. XRD diffractograms of (a) as electrodeposited Zn, (b) conventionally annealed at 425 °C for 15 min and (c) microwave annealed at 250 °C for 3 min. The (101) peak of Zn is shown with an arrow. The standard XRD reflections of SnO ₂ , Zn and ZnO are also shown.	126
Figure 6-2. Surface topographical images of (a) as electrodeposited Zn, conventionally annealed Zn electrodes at (b) 400 °C (c) 425 °C and (d) 600 °C.	127
Figure 6-3. The magnified SEM images of (a) as electrodeposited Zn, conventionally annealed Zn electrodes at (b) 400 °C (c) 425 °C and (d) 600 °C [Respective magnified images of figure 6-2].	128
Figure 6-4. Surface topographical images of (a) as electrodeposited Zn, Microwave annealed Zn electrodes at (b) 180 °C (c) 250 °C and (d) 300 °C.	129
Figure 6-5. The magnified SEM images of (a) as electrodeposited Zn, microwave annealed Zn electrodes at (b) 180 °C (c) 250 °C and (d) 300 °C. [Respective magnified images of figure 6-4].	130
Figure 6-6. The chopped photocurrent density-applied potential plot of conventionally annealed electrodeposited Zn electrodes at various temperatures. Inset shows photocurrent densities obtained for the electrodes at 1.23 V vs. NHE annealed at corresponding temperatures using conventional heating.	132
Figure 6-7. The chopped photocurrent density-applied potential plot of microwave annealed electrodeposited Zn electrodes at various temperatures. Inset shows photocurrent densities	

obtained for the electrodes at 1.23 V vs. NHE annealed at corresponding temperatures using microwave heating.	132
Figure 6-8. The plot of photocurrent density vs. applied potential for the electrodeposited Zn electrodes annealed at 425 °C for 15 min and 250 °C for 3 min using conventional and microwave heating respectively. Inset shows the photocurrent density obtained at 1.23 V vs NHE as a function of annealing temperature for the samples.	133
Figure 6-9. IPCE spectra as a function of wavelength at 1.23 V vs. NHE for electrodeposited Zn electrodes annealed under conventional and microwave radiation at 425 °C for 15 min and 250 °C for 3 min respectively.	134
Figure 6-10. Temperature-time profile of the samples annealed at 425 and 250 °C for 15 and 3 min using conventional and microwave-assisted annealing respectively. The maximum power used at the soaking temperature corresponding to each annealing technique is also mentioned.....	135
Figure 7.1-1. The images of reaction mixtures and the product at various preparation stages.	140
Figure 7.1-2. The microwave reactor conditions during the microwave treatment (a) power curve (b) Pressure curve (c) temperature curve.	141
Figure 7.1-3. The rietveld refined XRD profile of $Ti_{0.97}Pd_{0.03}O_{1.97}$. [264].....	142
Figure 7.1-4. XRD reflections obtained for $Ti_{0.97}Pd_{0.03}O_{1.97}$ powder samples made using conventional and microwave assisted methods.	143
Figure 7.1-5. The Raman spectra obtained for $Ti_{0.97}Pd_{0.03}O_{1.97}$ under conventional and microwave assisted methods.....	144
Figure 7.1-6. The SEM images of $Ti_{0.97}Pd_{0.03}O_{1.97}$ powder synthesised using microwave radiation.	145

Figure 7.1-7. The SEM images of $\text{Ti}_{0.97}\text{Pd}_{0.03}\text{O}_{1.97}$ powder synthesised by conventional method.....	146
Figure 7.2-1. X-ray diffraction pattern of LATP powder pellet obtained from JM.....	151
Figure 7.2-2. The XRD reflections of (a) as-prepared, (b) conventionally annealed at 600 °C (c) conventionally annealed at 800 °C and (d) microwave treated LATP pellets.....	152
Figure 7.2-3. Raman spectra of as-prepared, conventionally annealed at 600 °C and 800 °C and microwave treated LATP pellets.....	153
Figure 7.2-4. The SEM images of LATP pellets; (a-c) as-prepared, (d-f) microwave irradiated and (g-i) conventionally annealed at 800 °C.....	155
Figure 7.2-5. Nyquist plots of (a) as-prepared and post treated LATP pellets (b) the respective equivalent circuit model.....	156

List of Tables

Table 1. Brownian motion and bond energies.[31].....	27
Table 2. The list of microwave-assisted synthesised metal oxides.[58].....	52
Table 3. A summary of some metal chalcogenides synthesised by microwave irradiation.	58
Table 4. The summary of the total conductivities of as-prepared and post treated LATP pellets.....	157

List of Abbreviations

E_i - Electromagnetic radiation energy

ν - Frequency

λ - Wavelength

ω - Angular frequency

h - Planck's constant

c - Speed of light in vacuum

P - Net polarization

P_e - Electronic polarization

P_i - Ionic polarization

P_m - Molecular (dipole) polarization

P_s - Interfacial (space-charge) polarization

E - Electric field

ϵ' - Dielectric constant

ϵ - Permittivity

μ - Permeability

ϵ^* - Complex permittivity

μ^* - Complex permeability

ϵ'' - Dielectric loss

ϵ_0 - Permittivity of free space

ϵ'_r - Relative permittivity

ϵ''_{eff} - Effective relative loss factor

μ' - Permeability

μ'' - Magnetic loss factor

μ_0 - Permeability of free space

μ'_r - Relative permeability

μ''_{eff} - Effective relative magnetic loss factor

$\tan\delta$ - Loss tangent

P - Microwave power absorbed

σ - Total effective conductivity

f - Frequency of microwaves

D - Penetration depth

λ_0 - Free space wavelength of microwaves

E_{vb} - Valence band energy level

E_{cb} - Conduction band energy level

E_g - Band gap

E_D - Lower edge of the conduction band energy level

E_A - Upper edge of the valence band energy level

E_F - Fermi energy level

C_{id} - Interfacial double layer capacitance

C_{sc} - Space charge double layer capacitance

E_{fb} - Flatband potential

V_{oc} - Open circuit potential

J - Photocurrent density

C_p - Specific heat capacity

ΔT - Rise in temperature

t – Time

P_w - Power density

m - Mass

n - An integer

d - Lattice spacing of a (h,k,l) plane

θ - The angle between the incident ray and the scattering planes

η_c - Electron collecting efficiency

ϕ_{inj} - Electron injection efficiency

R - Resistance

d - Thickness

Microwave-assisted processing of solid materials for sustainable energy related electronic and optoelectronic applications

Abstract

Materials processing using microwave radiation is emerging as a novel and innovative technology that has proven useful in a number of applications. It has various advantages over conventional processing, such as; time and energy saving, very rapid heating rates, considerably reduced processing time and temperature, fine microstructures and improved mechanical properties, better product performance, etc. Microwave irradiation has shown great potential for the processing of different semiconductor materials and inorganic solids for various advanced electronic and optoelectronic devices such as solar cells, batteries, supercapacitors, fuel cells etc. This work intends to investigate the effect of microwave radiation on various semiconductor materials and inorganic solids, in particular the changes in their chemical, physical and photoelectrochemical properties after microwave treatment. Microwaves have been used as an alternative method to conventional thermal annealing for post annealing of widely used semiconductors (TiO_2 , ZnO nanorods), battery materials (lithium aluminium titanium phosphates), and synthesis of materials (ZnO , $\text{Ti}_{0.97}\text{Pd}_{0.03}\text{O}_{1.97}$). It is found that, in contrast to conventional thermal annealing, microwave treatment of such materials improves the crystallinity without any structural changes by preserving their nanostructure due to the difference in the heating mechanism (volumetric heating). The results demonstrate that microwave processing is a promising alternative method to the traditional conventional sintering for materials processing for advanced electronic and optoelectronic devices. Also the microwave annealing method offers energy savings of up to ~75%, which would make it highly desirable for industrial scale up.

Chapter 1

Introduction

Before and during World War II, microwave radiation was widely used for telecommunication purposes such as radar, navigation, and sensing.[1] The heating ability of microwaves was accidentally discovered in 1947 by Dr. Percy Spencer, an engineer at the Raytheon Company, as he found a candy bar in his pocket had melted during his experiments on a microwave generation tube.[2] Since then, microwave heating has been applied to various fields.[3,4] Microwave ovens for the home were introduced in the early 1950s and by the mid-1970s they became more popular in domestic kitchens for cooking.[4,5] However, the oil shock or natural gas crisis in the 1970s promoted research on microwaves in western countries, due to political pressures to make use of electrical heating methods such as microwaves rather than oil or gas.[5] Since then many researchers have used microwave radiation as an alternative energy source in the synthesis and processing of polymers, ceramics, glass and other organic and inorganic materials. However, the lack of awareness of the fundamental properties of the microwave heating mechanism and its interaction with materials limited the potential use of microwave radiation for these purposes at that time.[3]

Microwave heat generation is fundamentally different from conventional heating methods as the microwave energy absorbed by the material is converted into heat instead of originating from the external heating elements.[6] Conventionally heated ovens and furnaces use resistance heating elements which generate heat by resisting the flow of electricity through them. The heat generated by the elements is then transmitted onto the material being heated through convection, conduction, and radiation, thus heating the materials from outside. Since all materials have a characteristic thermal conductivity, there will always be a thermal

gradient from the surface to the core of the sample. The temperature of the sample may also be lower than that of the furnace due to thermal inertia, with larger samples tending to lag more than smaller ones. In contrast, microwave energy is provided directly to the material through molecular interaction with the electromagnetic field.[7] Microwave heating is the transfer of electromagnetic energy to thermal energy and is energy conversion rather than heat transfer.[8] Due to the ability of microwave radiation to penetrate into the material and supply energy, heat can be generated throughout the volume of the material, resulting in volumetric heating which allows rapid and uniform heating. Therefore, the thermal gradient in a microwave processed material is the reverse of that in a material processed by conventional heating.[9] The temperature profiles of microwave and conventional annealing for a reaction are shown in figure 1-1.

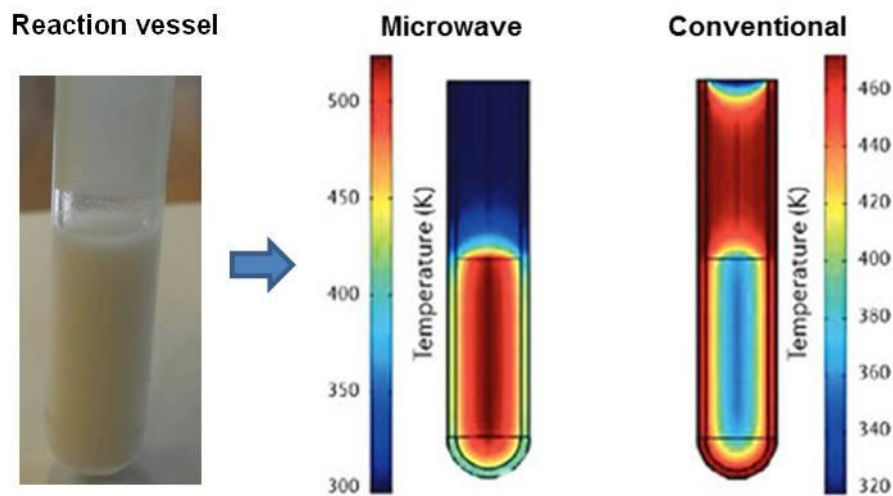


Figure 1-1. The temperature profiles of microwave and conventional annealing methods of the reaction mixture in the vessel.[10]

In conventional heating, slow heating rates are selected in order to reduce steep thermal gradients which lead to process-induced stresses. As a result, processing time and product quality has to be controlled closely.[8] However, due to the fact that microwaves transfer energy throughout the whole volume of the material there is a potential to reduce processing

time and enhance product quality by preserving the nanostructure. Furthermore, microwave characteristics such as penetrating radiation; controllable electric field distribution; rapid heating; selective heating of materials and self-limiting reactions lead to benefits and opportunities that are not available to conventional heating methods.[11] All in all, microwave heating is believed to be an advantageous alternative to conventional methods for the processing of materials.

The microwave absorbing characteristics of materials are related to the dielectric and magnetic properties such as, electric permittivity (ϵ) and magnetic permeability (μ) and the extent of heat generation by absorbed energy is determined by the loss tangent ($\tan \delta$) of the material. Therefore, when microwaves are in contact with materials of different dielectric properties, they will selectively couple with the higher loss tangent material and generate heat. The application of microwave energy to the processing of various materials such as ceramics, metals and composites offers several advantages over conventional heating methods.[12] These advantages include unique microstructure and properties, improved product yield, energy savings, reduction in manufacturing cost and synthesis of new materials. Due to the fact that materials are heated volumetrically, materials with a uniform microstructure can be produced using microwave heating, if energy losses from the surface are minimized. The nature of microwave heating is also much more efficient compared to resistance heating.[13] Due to these characteristics of microwave heating, microwave irradiation has great potential for the processing of different inorganic solids and semiconductor metal oxides (such as TiO_2 , ZnO , NiO and iron oxides) which are used heavily in making many electronic and optoelectronic devices.[14-17] Also due to the lower processing temperature requirements, the microwave process can open up the possibility of fabricating thin films of photoactive semiconductors on conducting plastic substrates which are highly important in making flexible devices.[18]

Main objectives of the project

The main objectives of this project include, monitoring the structural and functional changes of metal oxides on post-treatment under microwave radiation, identify the morphological and structural changes of semiconductor materials against microwave and conventional radiant post-treatment methods and find out the physical properties of mixed metal oxides against microwave irradiation and microwave processing of widely used semiconductor materials and glass ceramics to make a significant contribution to the improved power performance of optoelectronic and energy storage devices.

The studies were conducted under the following themes in order to achieve the project objectives,

- (a) Monitor the changes of the physical, chemical and photoelectrochemical properties of metal oxide thin films with different doses of microwave radiation.
- (b) Identify the structural and morphological changes of the materials during the post treatment step under microwave radiation and conventional heating methods.
- (c) Compare the different effects of microwave and conventional annealing techniques on a range of properties (i.e. structural, morphological, and functional) of different materials.
- (d) Microwave processing of semiconductor materials and glass ceramics to make a significant contribution to the improved power performance of electronic and optoelectronic devices such as lithium-ion batteries and solar energy devices.

The thesis contains ten chapters including four results and discussion chapters. The first chapter is the introduction and is followed by the second chapter which consists of a literature review explaining the fundamentals of microwave radiation, physical aspects of sintering, microwave processing of materials, including the interaction of microwave and materials, and

the mechanism of microwave heating, the microwave effect and recent developments in the field of microwave processing and organic/inorganic material synthesis. Chapter three contains a description of the experimental methods used for thin film preparation and material characterisation of thin films and inorganic materials. Chapter 4 is the first result and discussion chapter which compares the effect of microwave annealing on the photoelectrochemical (PEC) properties of TiO₂ photoelectrodes. Chapter 5 focuses on the effect of post annealing on the structure and PEC properties of ZnO nanorods by conventional thermal and microwave heat treatments. Chapter 6 compares the efficiency of oxidation of electrodeposited metallic Zn to ZnO using conventional thermal and microwave annealing methods in terms of their PEC performance. The work conducted for Johnson Matthey Plc is reported in chapter 7 which contains two sub sections. The first section reports the structural and morphological changes of Pd²⁺ incorporated TiO₂ (Ti_{0.97}Pd_{0.03}O_{1.97}) synthesised using microwave-assisted and conventional synthesis methods and the second section reports the effect on the electrical conductivity and structural properties of microwave and conventionally treated lithium aluminium titanium phosphate pellets. Each results and discussion chapter contains an overview, introduction, experimental, results and discussion and conclusion. Chapter 8 discuss the conclusions of the thesis along with the future work. Chapter nine and ten comprise the references and appendix respectively.

Chapter 2

Literature review

2.1 Theory and Background

2.1.1 Microwave fundamentals and microwave heating

Electromagnetic radiation is a form of energy that exhibits wave-like behaviour as it travels through space. It has both electric and magnetic field components, which oscillate in phase perpendicular to each other and perpendicular to the direction of energy propagation as in figure 2-1.[19] The electromagnetic theory was first presented by James Clerk Maxwell in 1864.[20]

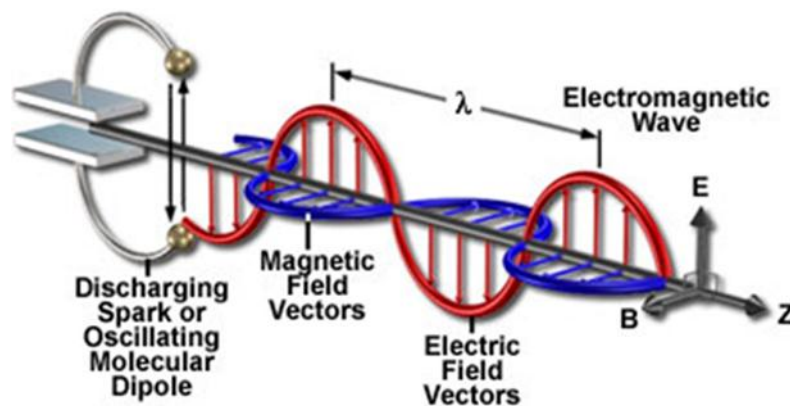


Figure 2-1. Electric and magnetic field components of electromagnetic radiation.[19]

Electromagnetic radiation is classified by the wavelength into radio waves, microwaves, infrared radiation, visible light, ultraviolet radiation, X-rays and gamma rays as shown in Figure 2-2.

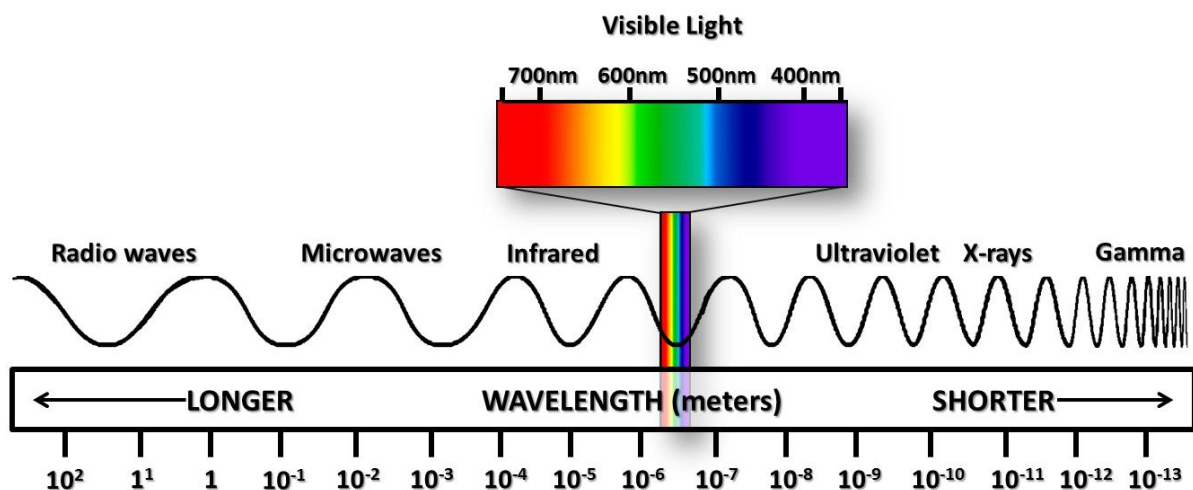


Figure 2-2. The electromagnetic spectrum.[21]

In the electromagnetic spectrum, microwaves are found in a transitional region between infrared and radio frequency radiation. The wavelengths are between 1 cm and 1 m and frequencies between 300 GHz and 300 MHz.[22] Microwaves can be further classified into three bands: the ultra-high frequency (UHF) band with frequencies ranging from 300 MHz to 3 GHz, the super-high frequency (SHF) band with frequencies ranging from 3 to 30 GHz and the extremely-high frequency (EHF) band with frequencies ranging from 30 to 300 GHz.[23] Although microwave frequencies range from 300 MHz to 300 GHz, most of the frequencies are restricted to government usage, leaving only a limited range of frequencies available for commercial and domestic usage.[24] The international telecommunication union (ITU) operating within the United Nations system provides the basic framework that is relevant for the international radio-regulatory arrangement. Regulatory authorities for different countries utilize the international table of frequency allocations of the ITU as a guideline to release certain bands termed as industrial, scientific and medical (ISM) bands for unregulated usage.[25] To avoid interference with telecommunications and cellular phone frequencies, heating applications must use unregulated ISM bands of 915 MHz, 2.45 GHz and 5.8 GHz.[26] Domestic ovens and laboratory microwave furnaces usually work at 2.45 GHz (i.e. wavelengths of 12.24 cm).[27]

Microwaves travel in the same way as light waves; they also change direction when travelling from one dielectric material into another; they are reflected by metallic objects, absorbed by some dielectric materials, and transmitted without significant absorption through other dielectric materials as shown in figure 2-3.[28]

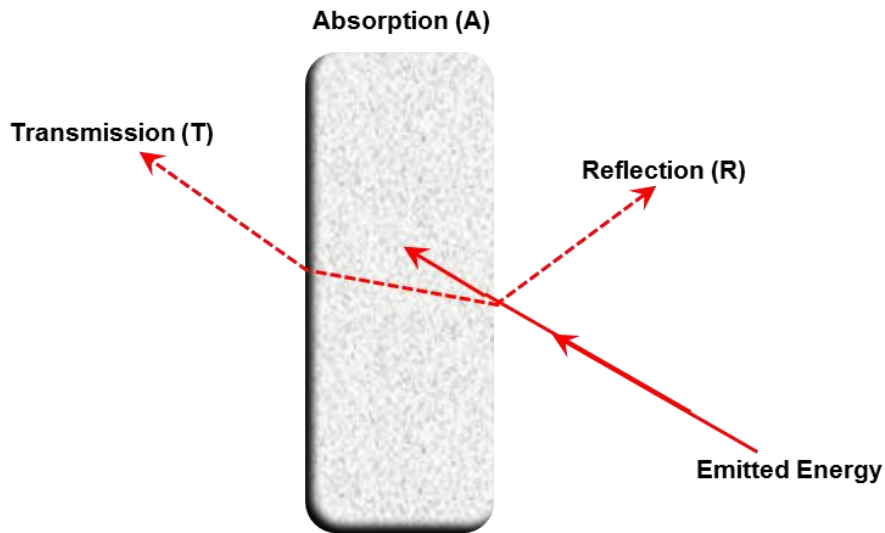


Figure 2-3. Transmission, Absorption, and Reflection of microwave radiation.

The fundamental relationship between electromagnetic radiation energy (E_i), frequency(ν), wavelength (λ) and angular frequency (ω) is given by equation 1,[29]

$$E_i = \hbar\omega = h\nu = \frac{hc}{\lambda} \quad (1)$$

where, h is the Planck's constant and c is the speed of light in vacuum.

Photonic energies corresponding to γ or X-ray radiation is responsible for inner or core electron excitation of materials, whereas ultraviolet and visible radiation initiates chemical reactions.[30] Energy corresponding to infrared radiation only enough to excites bond vibrations, while microwaves to excite molecular rotation. The microwave photon energy corresponding to the frequency used in microwave heating systems (2.45 GHz, 12.24 cm) is close to 0.00001 eV. According to the reported bond strength values in the table 1, this

microwave photon energy is not sufficiently energetic to break hydrogen bonds; it is also much smaller than that of Brownian motion. Therefore, there is no possibility to break chemical bonds of materials by absorbing microwave energy.

Table 1. Brownian motion and bond energies.[31]

	Brownian motion	Hydrogen bonds	Covalent bonds	Ionic bonds
Energy (eV)	~0.017 (200 K)	~ 0.04 to 0.44	~ 4.51 (C-H); ~ 3.82 (C-C)	~ 7.6
Energy (kJ mol ⁻¹)	1.64	~ 3.8 to 42	~ 435 (C-H); ~ 368 (C-C)	~ 730

2.1.2 Polarization mechanisms of materials

It has long been known that dielectric materials may be heated with the interaction of high frequency electromagnetic radiation. The heating effect arises from the interaction of the electric field component of the electromagnetic radiation with the dipoles in the material. When the dipoles of materials are subjected to an external electric field, it undergoes internal charge separation by aligning the positive end with the lower potential and the negative end with the higher potential.[32] This conversion of electromagnetic energy into molecular motion and through that into heat can be described by different mechanisms. The two main heating mechanisms, polarization and conduction are responsible for the heating of materials.[22] The interaction of electromagnetic radiation with dielectric materials can cause net polarization in materials. There are several mechanisms which are responsible for the polarization, including: electronic, ionic, molecular (dipolar) and interfacial (space-charge) polarization. Therefore, for a dielectric material the net polarization, P , is determined by the sum of the contributions from each mechanism, this can be seen in equation 2.

$$P = P_e + P_i + P_m + P_s \quad (2)$$

where, P_e is electronic polarization, P_i is ionic polarization, P_m is molecular (dipole) polarization and P_s is interfacial (space-charge) polarization.

2.1.2.1 Electronic polarization

This is caused by the displacement of the electron cloud of the material relative to its nucleus. Heating by electronic polarization originates by shifting of electrons from equilibrium, with respect to the positive nuclei, in the direction of the electric field (E) (Figure 2-4).

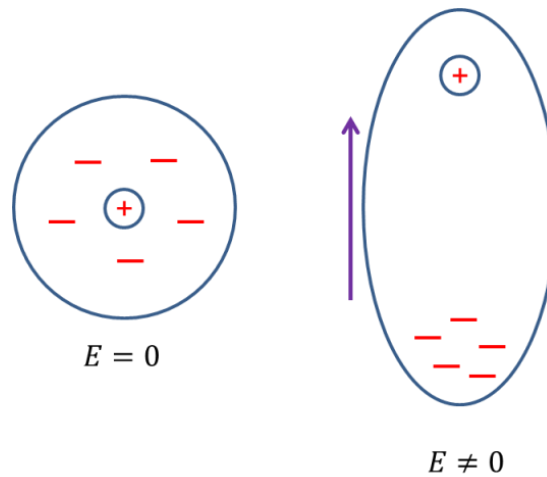


Figure 2-4. The electronic polarization in dielectric materials.

2.1.2.2 Ionic (atomic) polarization

Ionic polarization takes place due to the displacement of positive and negative ions toward the negative and positive electrodes, under an applied field (E), the resulting separation of charge yields a displacement of the cations and anions relative to their equilibrium positions (figure 2-5).

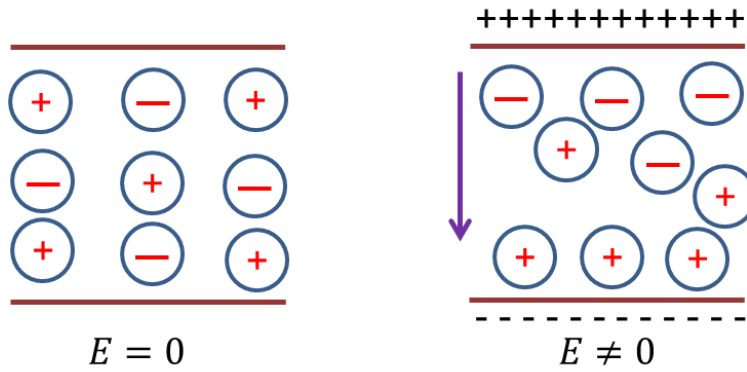


Figure 2-5. The ionic polarization in dielectric materials.

2.1.2.3 Molecular (dipolar) polarization

In their normal state, molecules are randomly oriented in the material in a way that there is no net charge present. In molecular or dipolar polarization permanent dipoles align parallel to the external field (E) (figure 2-6). Dipolar polarization is the phenomenon responsible for the majority of microwave heating effects specially observed in solvent systems.

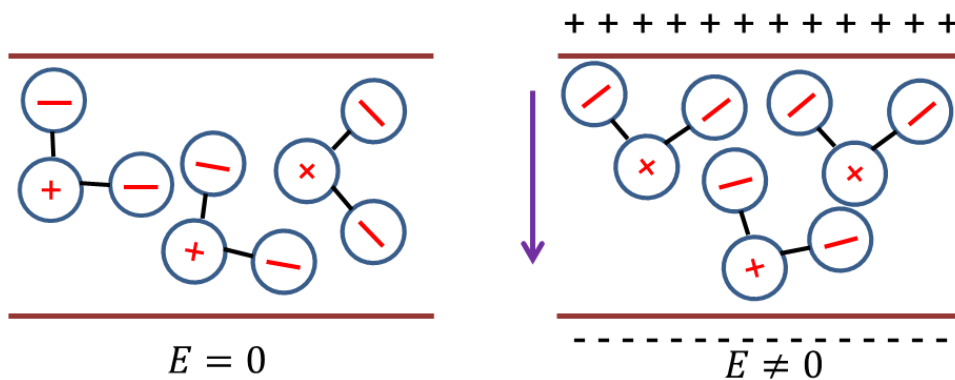


Figure 2-6. The molecular (dipolar) polarization in dielectric materials.

2.1.2.4 Interfacial (Space-charge) polarization

In interfacial or space-charge polarization mobile charge carriers in a heterogeneous material migrate an appreciable distance through the dielectric until they are trapped or impeded by

physical barriers. This build-up of charge dictates the polarization of the material. Grain/phase boundaries and free surface are common barriers (figure 2-7).

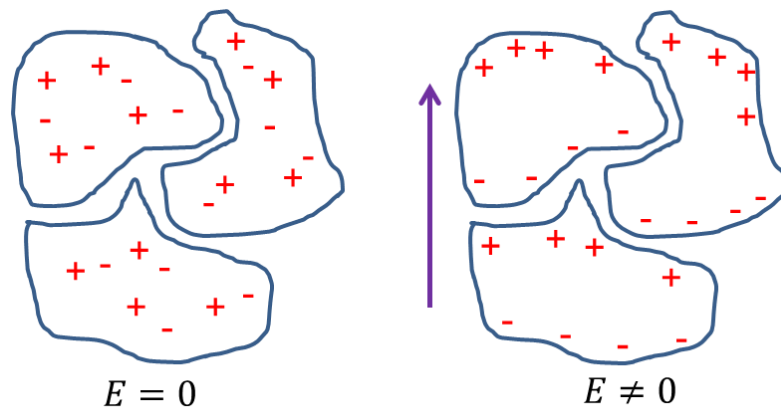


Figure 2-7. The interfacial (Space-charge) polarization in dielectric materials.

2.1.3 Microwave heat generation

Under low frequency irradiation (10^3 - 10^6 Hz), dipoles of the material align themselves in phase with the electric field of the radiation. However, the overall heating effect is trivial. Conversely under very higher frequency radiation (10^{15} - 10^{18} Hz) the dipoles do not have sufficient time to respond to the changing electric field so generally no motion is induced in the dipoles. This means no energy transfer takes place and so no heating takes place either. In between these two extremes, at frequencies ranging from 10^9 - 10^{12} Hz (i.e. microwave region), is the ideal frequency to induce molecular rotations. The microwave frequency is low enough that the dipoles have time to respond to the alternating field, and therefore to rotate, but high enough that the rotations does not precisely follow the direction of the electric field. Due to this the dipoles of the material, lagging behind the changing electric fields, causes molecular friction, which in turn is converted into heat. Dipolar and ionic polarization mechanisms are the dominant mechanisms that cause heating of dielectric materials at microwaves frequencies.[33] In dipolar polarization, dipoles of the material tend to align in

the direction of an external electric field and hence are polarized. The degree of polarization (P) is related to the dielectric properties of the material through the relation in equation 3,

$$P = \varepsilon_0(\varepsilon_r' - 1)E \quad (3)$$

where ε_0 is the permittivity of free space ($\varepsilon_0 = 8.86 \times 10^{-12} \text{ F m}^{-1}$), ε_r' is the relative permittivity of the material and E the applied electric field strength.

When an oscillating electric field is applied to a material by microwave radiation, the dipoles are constantly trying to align with the changing electric field (Figure 2-8a). The frequency of the field determines the way in which the orientation of the dipole affects the material. The mechanism of ionic polarization is similar to that of dipolar polarization (Figure 2-8b). When charge carriers in a material are subjected to an electric field, they are subjected to a force. The alternation of the electric field causes the direction of the force to alternate equally. This alternation leads to molecular motion, and collision, and thus generates heat.

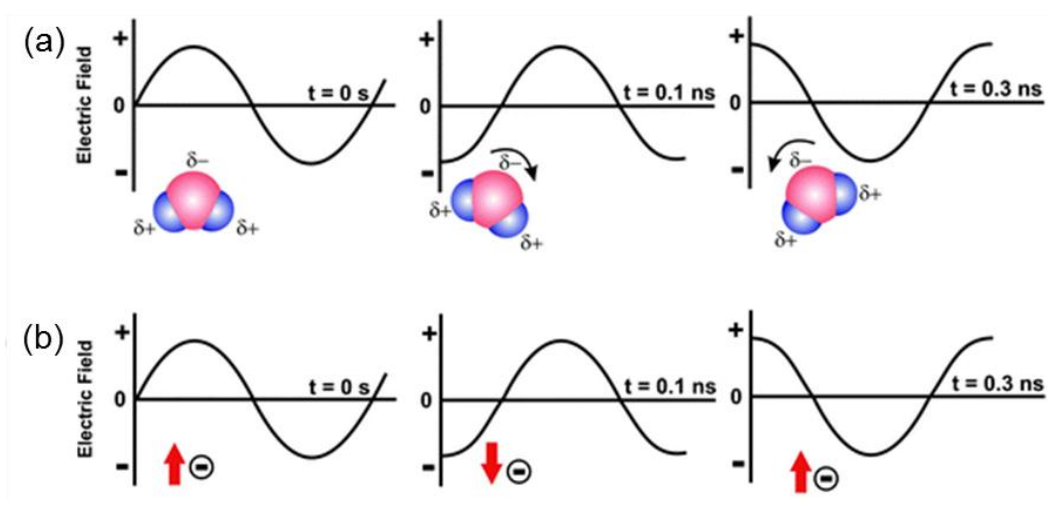


Figure 2-8. Two main heating mechanisms under microwave irradiation: (a) dipolar polarization; (b) ionic polarization.[34]

2.1.4 Microwave-material interactions

The electric field component of the electromagnetic wave may be reflected, transmitted or absorbed by materials. Also certain materials such as magnetic materials interact with the magnetic field component of the electromagnetic wave. Generally materials can be categorized in to four types with respect to their interaction with the microwave field.

1. Transparent or low dielectric loss materials: low loss tangent materials or insulating materials, which reflect and absorb electromagnetic waves to a negligible extent and allow microwaves to pass through them easily with little attenuation (i.e. glass, ceramic, and air).
2. Opaque or conducting materials: typically conducting materials with free electrons, such as metals, that reflect and do not allow electromagnetic waves to pass through (i.e. most of metals including steel, Al, and Cu).
3. Absorbing or high dielectric loss materials: materials whose properties range from conductors to insulators. They are usually referred to as lossy dielectrics or high dielectric loss materials and absorb electromagnetic energy and convert it to heat (i.e. SiC, CuO, TiO₂, ZnO, and iron oxide).
4. Magnetic materials: materials such as ferrites which interact with the magnetic component of the electromagnetic wave and get heated (i.e. Fe₂O₃, Fe, Ni, and Co).

Microwaves pass through transparent or low dielectric loss materials with little attenuation, opaque or conducting materials reflect the radiation without penetration and absorbing or high dielectric loss materials absorb microwave radiation in different levels based on their dielectric properties. The exact nature of microwave-material interaction and hence heat generation depends upon the mobility of charges in dielectric materials. When the charges are bound as dipoles in the material, the changing electric field of the microwaves induces

motion until it is balanced by the electrostatic interaction which leads to polarization.[35] Similarly, in ionic conduction, ions in the material are forced to move with the changing electric field until the net charge is balanced. If the charge carriers are mobile, the altering microwave field gives rise to a current flow which could cause resistive heating in the material. However, heat generation of composites or multi-phase materials upon microwave irradiation may involve both heating mechanisms and resistive heating.[36]

The interaction of microwaves with matter is quantified by the two complex physical quantities; dielectric permittivity, ϵ , and permeability (magnetic susceptibility), μ . [31] In reality, the permittivity and permeability are complex quantities which are defined as ϵ^* and μ^* respectively as below equations 4 and 5, [37]

$$\epsilon^* = \epsilon' - i\epsilon'' = \epsilon_0(\epsilon'_r - i\epsilon''_{eff}) \quad (4)$$

$$\mu^* = \mu' - i\mu'' = \mu_0(\mu'_r - i\mu''_{eff}) \quad (5)$$

where ϵ' is the dielectric constant which represents the time-independent polarizability of a material in the presence of an external electric field, that is to say it measures the resistance encountered when forming an electric field in a medium. ϵ'' is the dielectric loss or loss factor of the material, this indicates the time-dependent component of the permittivity which quantifies the ability of the material to convert absorbed energy into heat. ϵ_0 is the permittivity of free space ($\epsilon_0 = 8.86 \times 10^{-12} \text{ F m}^{-1}$) and ϵ'_r is the relative permittivity of the material which is the ratio of the permittivity of a substance to that of free space or vacuum. ϵ''_{eff} is the effective relative loss factor. μ' is the magnetic permeability, μ'' magnetic loss factor, μ_0 the permeability of free space ($\mu_0 = 4\pi \times 10^{-7} \text{ H m}^{-1}$), μ'_r is the relative permeability of the material and μ''_{eff} is the effective relative magnetic loss factor.

The dielectric properties of materials vary with the frequency due to the effect of the changing electric field on the movement of the charged species. The figure 2-9 shows the

frequency response of dielectric constant and dielectric loss for a typical dielectric material showing various phenomena caused by different polarization mechanisms across the electromagnetic spectrum.[38] The decrease of the complex permittivity, ϵ^* shows itself as a decrease in dielectric constant and rise of dielectric loss.

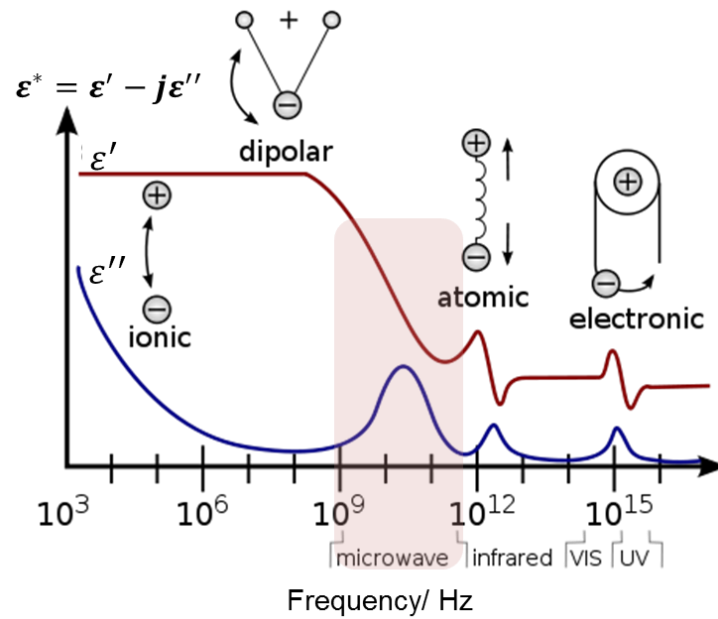


Figure 2-9. Frequency response of the complex permittivity for a typical dielectric material due to different polarization mechanisms.[39]

As discussed, the heating effect usually arises from the interaction of the electric field component of the microwaves with charged species in the materials. The dielectric constant signifies the ability of the material to absorb microwaves and store energy. Dielectric loss represents the ability of the material to convert absorbed energy into heat. The ratio of the dielectric loss to the dielectric constant is known as the loss tangent ($\tan\delta$) which is given in equation 6,[40]

$$\tan\delta = \frac{\epsilon''}{\epsilon'} \quad (6)$$

The angle δ represents the phase lag between the polarization of the material and the applied electric field. In order for microwaves to interact with the material, a balanced combination of

moderate dielectric constant (to permit adequate penetration) and high loss tangent (for higher energy to heat conversion) are required.[41]

The microwave power absorbed per unit volume of a material, P (W m^{-3}) is expressed as,[37]

$$P = \sigma |E|^2 = 2\pi f \varepsilon_0 \varepsilon_r' \tan \delta |E|^2 \quad (7)$$

where, E (V m^{-1}) is the magnitude of the internal field, σ the total effective conductivity (Sm^{-1}) and f the frequency (GHz). The above equation demonstrates that the power absorbed by the material varies linearly with the frequency, the relative dielectric constant, loss tangent and the square of the electric field.[23]

The penetration depth (D) of microwaves is a measure of how deep microwave radiation can penetrate into a material. The penetration depth of a material can be calculated using equation (8), which shows how it depends on the dielectric properties of the material. The penetration depth of microwaves at which the incident power is reduced by one half is expressed in equation 8,[26]

$$D = \frac{3\lambda_0}{8.686 \pi \tan \delta \sqrt{\varepsilon_r'}} \quad (8)$$

At a frequency of 2.45 GHz, the free space wavelength λ_0 is 122.4 mm. The calculated penetration depths for TiO_2 and ZnO are $0.5 \mu\text{m}$ and $0.4 \mu\text{m}$ respectively.

In general, if the penetration depth exceeds sample thickness, the material behaves as transparent to microwaves. The volumetric heating only results when the penetration depth is comparable with the sample thickness. If the sample is too thick, absorption is limited to the surface.[42]

The relative dielectric constant and the loss tangent are the parameters that describe the behaviour of a dielectric material under the influence of a microwave field. During heating,

the relative dielectric constant and the loss tangent change with temperature. It is clear that the power density will decrease exponentially from the surface to the core region. In order for microwaves to interact with the material and heat generation, a balanced combination of moderate dielectric constant (to permit adequate penetration) and high loss tangent (for higher energy to heat conversion) are required. Therefore it is clear that microwave heat generation in materials depends on many factors. These include power level, electric field distribution and material properties including dielectric constant, penetration depth, loss tangent, thermal and electrical conductivity, microstructure, size, shape of the grains, the amount of porosity, pore size, the distribution of the pores in the structure etc. The post heat treatment of semiconductor materials using microwaves or conventional methods helps to improve particle inter-connections and produces structural and morphological changes. These changes are very important in determining the electronic and photoelectrochemical performance of a material.

2.1.5 Semiconductor photonic materials

The generation of current through exposure to light is of foremost importance in semiconductor electrodes due to the photochemical properties of the semiconductor/electrolyte interface which is vital in solar energy conversion. The electronic structure of materials determines the properties of semiconductor and metallic electrodes. The electronic structure of these materials is typically discussed in terms of energy bands, which are made up of the atomic orbitals of the individual atoms.[43] Due to the large number of atomic orbitals of such materials, the difference in the energy between adjacent orbitals within a given energy band is quite small such that the band can effectively be considered a continuum of energy levels. The highest and lowest energy levels of a band are referred to as the band edges. The highest occupied energy band is called the valence band (E_{vb}) whereas

the lowest unoccupied energy band is called the conduction band (E_{cb}). The difference in energy between the upper edge of the valence band and the lower edge of the conduction band is the band gap (E_g), this determines the properties of the material. Conductivity of a solid state material requires that the electrons occupy partially filled orbitals which can be achieved by occupancy of the conduction band. For metals, the conduction and valence bands overlap, so the conduction band can be readily occupied.[44] For insulators, the band gap is sufficiently large that electrons cannot be promoted from the valence band to the conduction band. For semiconductors the band gap is not as large and electrons can be moved into the conduction band with relative ease. Figure 2-10 illustrates the electronic energies of metals, semiconductors and insulators.

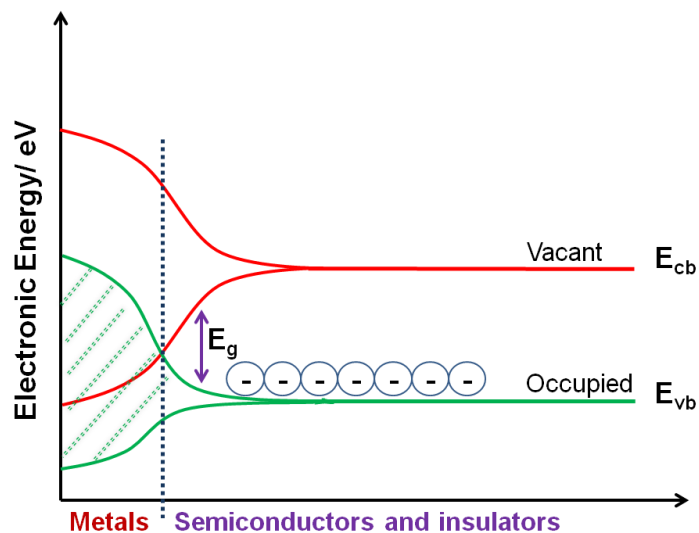


Figure 2-10. The electronic energies of metals, semiconductors and insulators.

Electrons can be excited either thermally or photochemically into a material's conduction band, leaving behind positively charged vacancies in the valence band. Doping is another method for generating charge carriers (i.e., electrons or holes) within a semiconductor. Doping involves the addition of another element, which has different levels of charge, into the semiconductor. The introduction of a group V element (e.g., P, As, Sb) or a group III

element (e.g., Al, Ga, In) into a group IV element (e.g., Si, Ge) is a simple example of doping. Doped semiconductors can be categorized into two types depending on their dominant charge carriers. The addition of group V element into group IV elements introduces occupied energy levels into the band gap close to the lower edge of the conduction band (E_D), thus allowing facile promotion of electrons into the conduction band, as shown in figure 2-11. In this case the majority charge carriers are electrons and these semiconductors are referred to as n-type semiconductors.

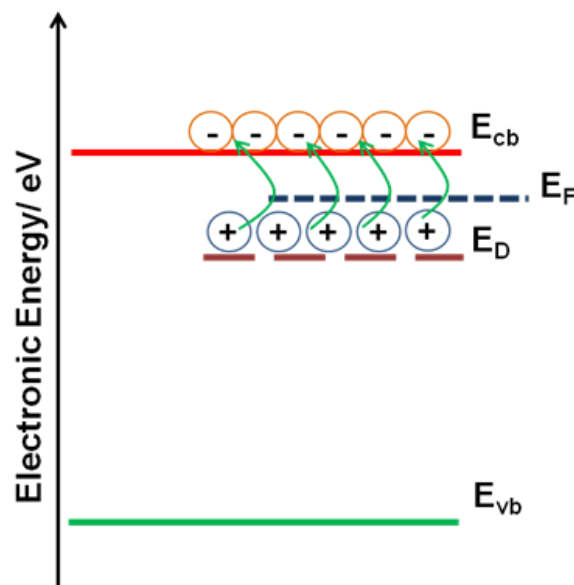


Figure 2-11. Schematic energy diagram of an n-type semiconductor.

The addition of group III elements introduces vacant energy levels into the band gap close to the upper edge of the valence band (E_A), this allows facile promotion of electrons from the valence band. This leads to the formation of holes in the valence band. The figure 2-12 illustrates the schematic energy diagram of a p-type semiconductor.

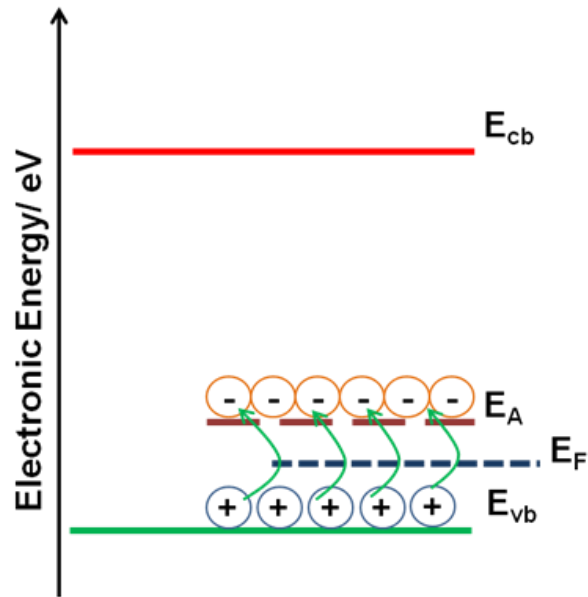


Figure 2-12. Schematic energy diagram of a p-type semiconductor.

Undoped semiconductors are referred to as intrinsic semiconductors and the schematic energy diagram is shown in figure 2-13.

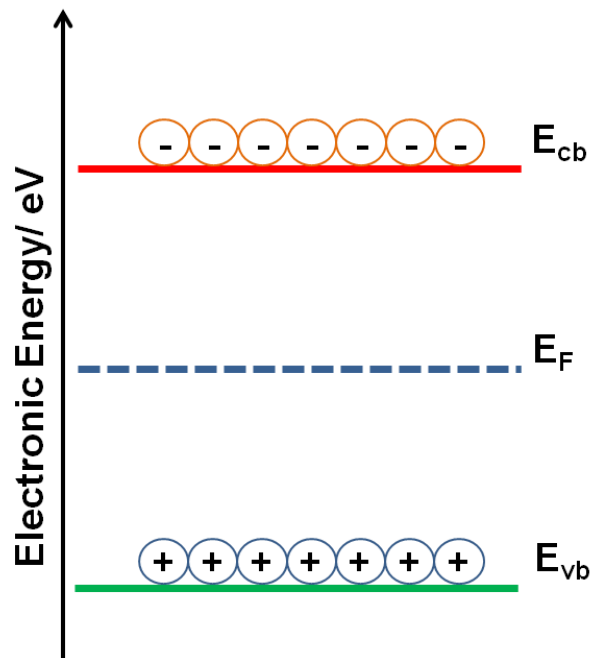


Figure 2-13. Schematic energy diagram of an intrinsic semiconductor.

The Fermi level is another important concept in solid state materials. The energy of the least tightly held electrons within a solid is specified by the Fermi level (E_F), which was first proposed by Enrico Fermi. The Fermi energy is the value of the Fermi level at absolute zero ($-273.15\text{ }^\circ\text{C}$) and each solid has a unique Fermi energy value. However, the position of the Fermi level changes with the electron density of the energy levels of the solid. To define it the Fermi level is any energy level having the probability that it is exactly half filled with electrons. Levels with lower energy than the Fermi level tend to be entirely filled with electrons, whereas energy levels higher than the Fermi tend to be empty. For an intrinsic semiconductor the Fermi level lies at the mid-point of the band gap (Figure 2-13) whereas Fermi levels of n-type and p-type semiconductors reside just below the conduction band (Figure 2-11) and just above the valence band (Figure 2-12) respectively. The position of the Fermi level changes with addition or removal of electrons from a solid. When solids with different individual Fermi levels are placed in contact, electrons flow from the solid with the higher Fermi level into the solid with the lower Fermi level. This transfer of electrons raises the lower Fermi level and lowers the higher Fermi level until the Fermi levels of the two solids are equal. The photoelectrochemical performance of semiconductor electrodes is usually determined in three electrode systems using an aqueous electrolyte. The band theory of solid/liquid interfaces is discussed in the next paragraph in order to understand the band energetic of such systems.

The Fermi level of a semiconductor or metallic electrode varies with the applied potential, i.e. moving to more negative potentials will raise the Fermi level and vice versa. In order for the semiconductor and electrolyte phases to be in equilibrium in the idealized semiconductor interface, their electrochemical potential must be equal. The electrochemical potential of the solution is determined by the redox potential of the electrolyte solution and the potential of the semiconductor is determined by the Fermi level. The redox potential of the solution and

the Fermi level of the semiconductor should lie at the same energy in order to equilibrate the two phases which can be achieved by a movement of charge between the semiconductor and the electrolyte. Unlike metallic electrodes, the excess charge located on the semiconductor at equilibrium does not lie at the electrode surface, but extends into the electrode for a significant distance ranging 100-10,000Å. Generally, this region is referred to as the space charge region, and has an associated electrical field generated by the associated charge separation. Therefore due to this, there are two double layers to be considered in the electrode/electrolyte system namely the interfacial (electrode/electrolyte) double layer and the space charge double layer. These layers act much like a capacitor. The capacitance associated with the space charge double layer is much smaller than the electrode/electrolyte double layer. Typical values for interfacial double layer capacitance (C_{id}) range from 10-100 $\mu\text{F cm}^{-2}$ whereas, space charge double layer capacitance (C_{sc}) range from 0.001 – 1 $\mu\text{F cm}^{-2}$. Since these capacitors are in series, the smallest capacitor will govern the response of the system as confirmed from equations 9 and 10.[45]

$$\frac{1}{C_T} = \frac{1}{C_{id}} + \frac{1}{C_{sc}} \quad (9)$$

Therefore,

$$C_T = \frac{C_{id}C_{sc}}{C_{id} + C_{sc}} = C_{sc} \text{ if } C_{id} \gg C_{sc} \quad (10)$$

The bands in the bulk of the semiconductor will move with changes in applied potential and the potential drop will appear in a region near the surface of the semiconductor (i.e. space charge region). Thus, for an ideal semiconductor/electrolyte interface, the major portion of the potential drop occurs in the semiconductor with very little in the solution side.

2.1.6 Energetics at semiconductor-electrolyte interface

For an n-type semiconductor electrode at open circuit, the Fermi level is typically higher than the redox potential of the electrolyte, and hence electrons will be transferred from the electrode into the solution. Therefore there is a positive charge associated with the space charge region and this is reflected in an upward bending of the band edges (figure 2-14). Since the majority charge carrier of the semiconductor has been removed from this region, this region is also referred to as a depletion layer.

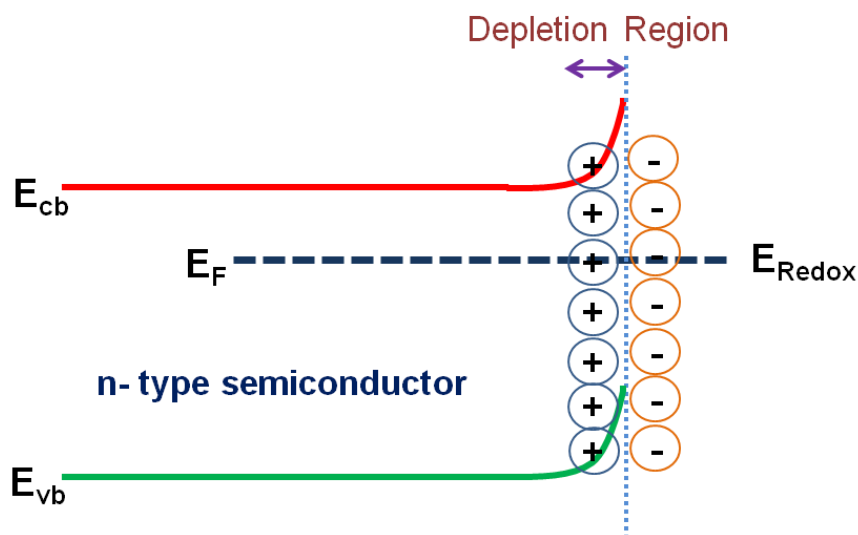


Figure 2-14. Band bending of an n-type semiconductor.

For a p-type semiconductor, the Fermi level is generally lower than the redox potential, hence electrons must transfer from the solution to the electrode to attain equilibrium. This generates a negative charge in the space charge region which causes a downward bending in the band edges (Figure 2-15). Since the holes in the space charge region are removed by this process, this region is again a depletion layer.

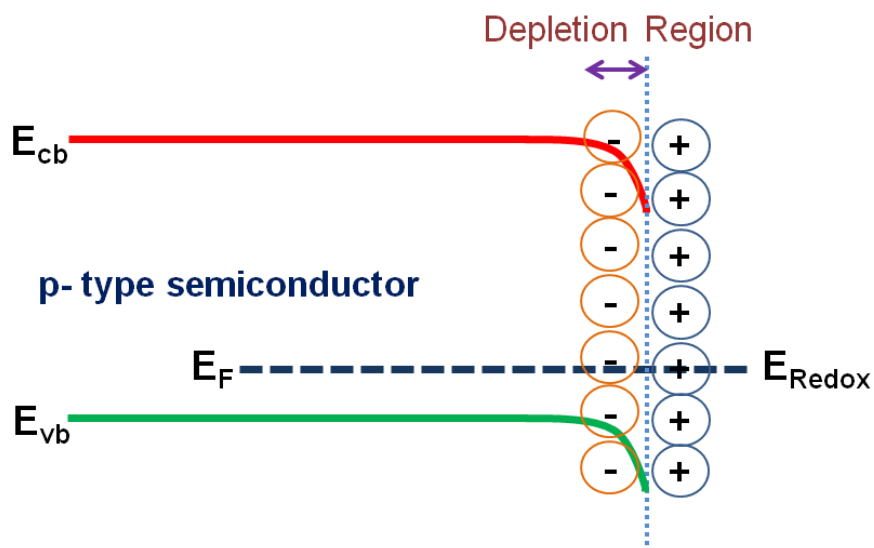


Figure 2-15. Band bending of a p-type semiconductor.

The Fermi level of a metallic electrode varies with the applied potential as the electron population of the electrode changes. The band edges in the interior of the semiconductor also vary with the applied potential in the same way as the Fermi level. However, the energies of the band edges at the interface are not affected by changes in the applied potential. Therefore there is a change in the energy of the band edges between the interior of the semiconductor and the interface, hence the magnitude and direction of band bending varies with the applied potential. At a certain potential the Fermi energy lies at the same energy as the solution redox potential. There is no net transfer of charge and hence there is no band bending. This potential is therefore referred to as the flatband potential (E_{fb}). The energy band diagrams of n-type and p-type semiconductors at flat band conditions are shown in figures 2-16 and 2-17 respectively.

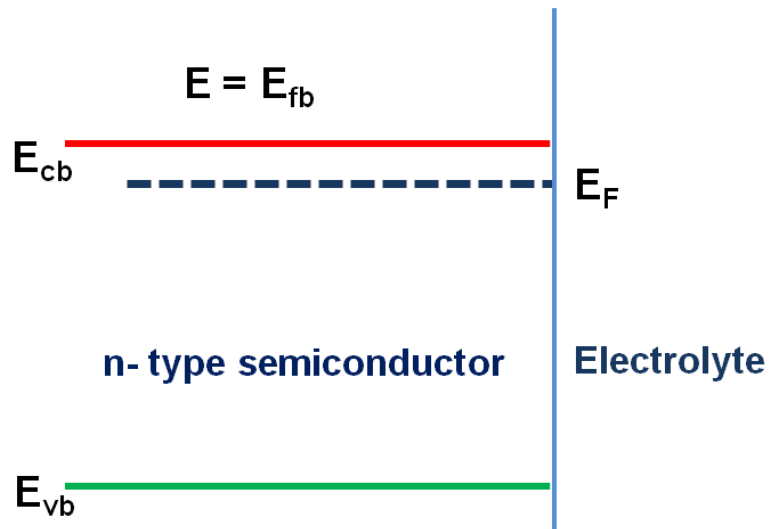


Figure 2-16. The energy band diagrams of an n-type semiconductor at flat band conditions.

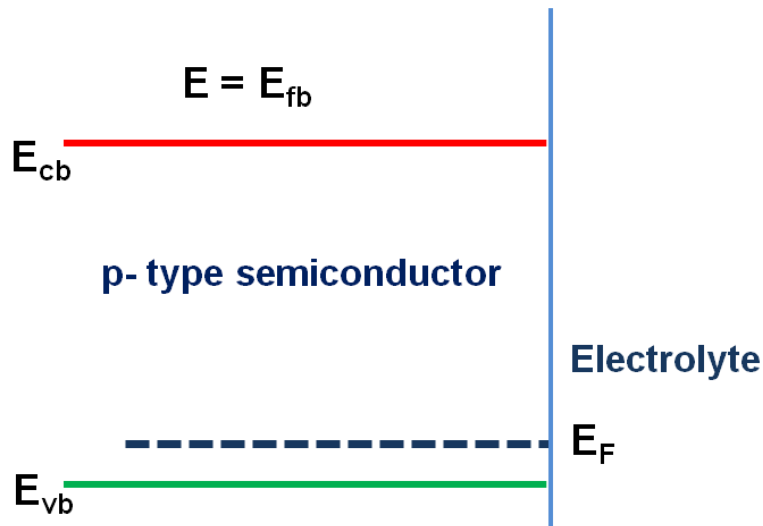


Figure 2-17. The energy band diagrams of a p-type semiconductor at flat band conditions.

Depletion regions arise at potentials positive of the E_{fb} for an n-type semiconductor and at potentials negative of E_{fb} for a p-type semiconductor. Figures 2-18 and 2-19 show the energy band diagrams of n-type and p-type semiconductors under depletion conditions at various applied potentials respectively.

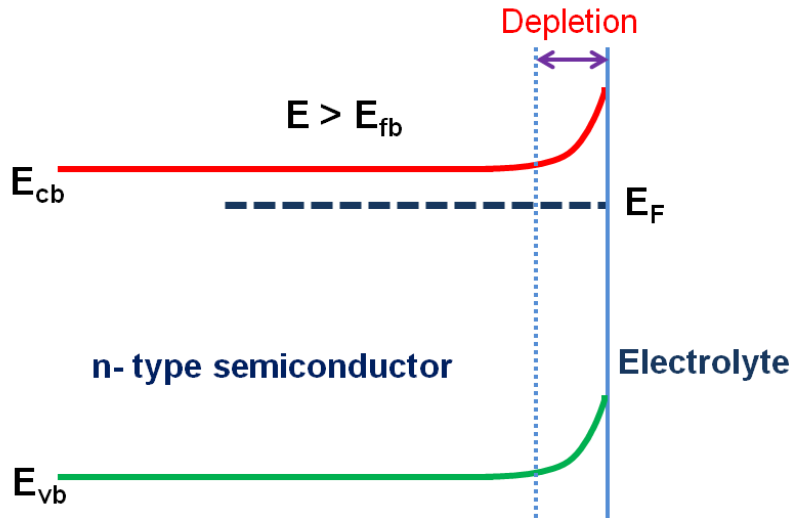


Figure 2-18. The energy band diagrams of an n-type semiconductor when applied potential is higher than the E_{fb} .

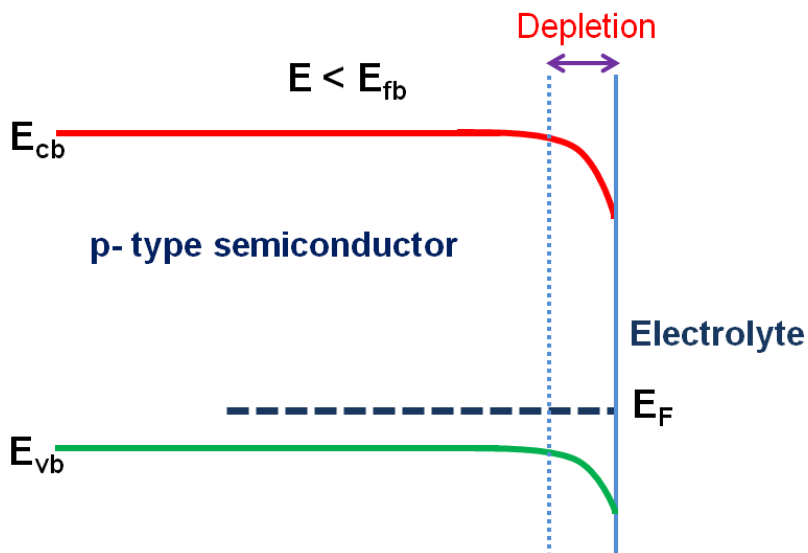


Figure 2-19. The energy band diagrams of a p-type semiconductor when applied potential is lower than the E_{fb} .

At potentials negative of the E_{fb} for an n-type semiconductor there is now an excess of the majority charge carrier (electrons) in this space charge region, this is referred to as an accumulation region. An accumulation region arises in a p-type semiconductor at potentials more positive than the E_{fb} . Figures 2-20 and 2-21 show the energy band diagrams of n-type

and p-type semiconductors under accumulation conditions at various applied potentials respectively.

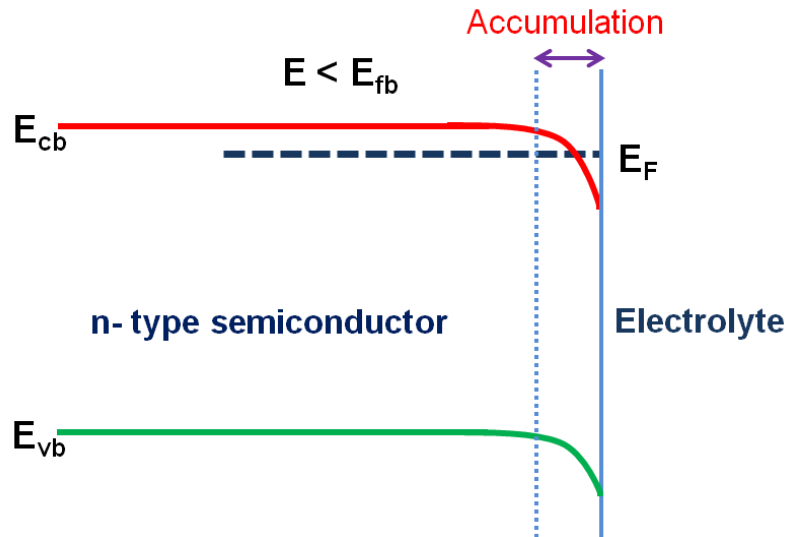


Figure 2-20. The energy band diagrams of an n-type semiconductor when applied potential is lower than the E_{fb} .

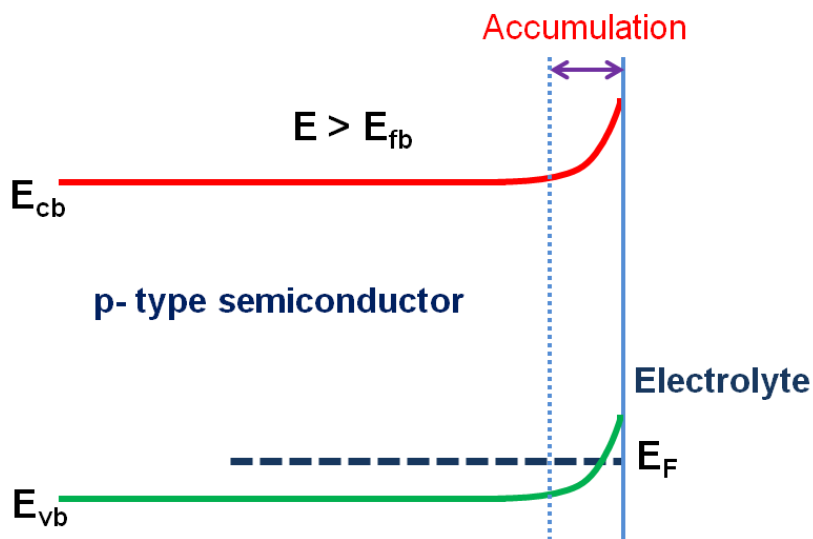
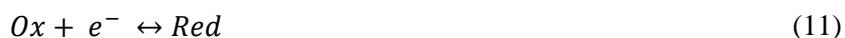


Figure 2-21. The energy band diagrams of a p-type semiconductor when applied potential is higher than the E_{fb}

The charge transfer abilities of a semiconductor electrode depend on whether there is an accumulation layer or a depletion layer. If there is an accumulation layer, the behaviour of a

semiconductor electrode is similar to that of a metallic electrode, since there is an excess of the majority of charge carrier available for charge transfer.

In contrast, if there is a depletion layer, then there are few charge carriers available for charge transfer and electron transfer reactions occur slowly. If the electrode is exposed to radiation of sufficient energy electrons will be promoted to the conduction band. If this process occurs in the interior of the semiconductor, recombination of the promoted electron and the resulting hole typically occurs together with the production of heat. However if it occurs in the space charge region, the electric field in this region will cause the separation of the charge. Metallic contacts are used to collect the separated electrons and holes in solid-state devices whereas redox species are used as carriers to collect electrons and holes in photoelectrochemical devices. In photoelectrochemical devices, band edges of n-type semiconductors at positive potentials ($E > E_{fb}$) curve upwards and hence the hole moves towards the semiconductor/electrolyte interface whilst the electron moves to the interior of the semiconductor. The hole is a high energy species that can extract an electron from a redox species in the electrolyte. The suitability of the redox species is determined by the type of semiconductor and its energetic positions. The energy levels for redox species arise by virtue of the donors (*Red*) and acceptors (*Ox*) in electrolyte.[46]



Redox species in the electrolyte are oxidized at the surface of illuminated n-type semiconductors whereas reduction occurs at illuminated p-type semiconductors. A simplified picture of the charge separation at the semiconductor/electrolyte interface of n- type and p- type semiconductors under illumination conditions is given in figures 2-22 and 2-23 respectively.

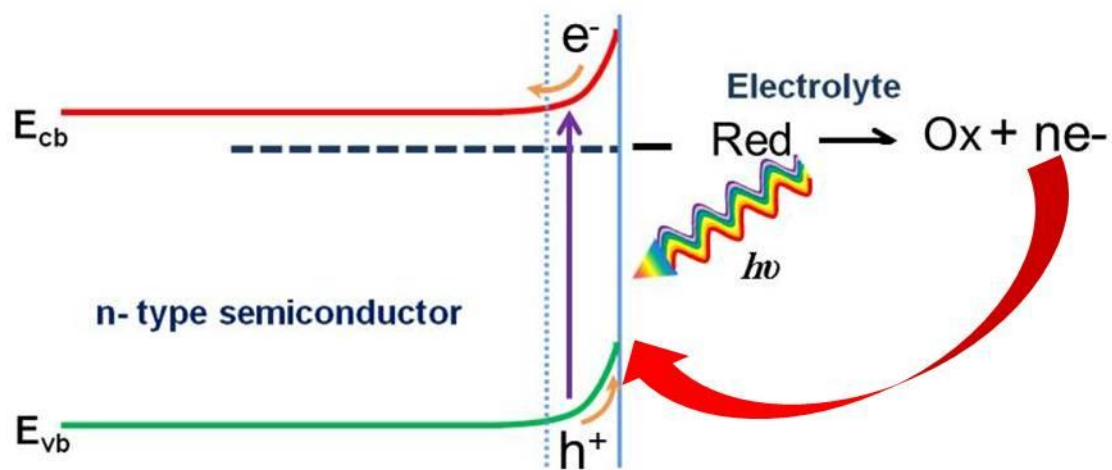


Figure 2-22. A simplified picture of the charge separation at the semiconductor/electrolyte interface for an n- type semiconductor under illumination conditions.

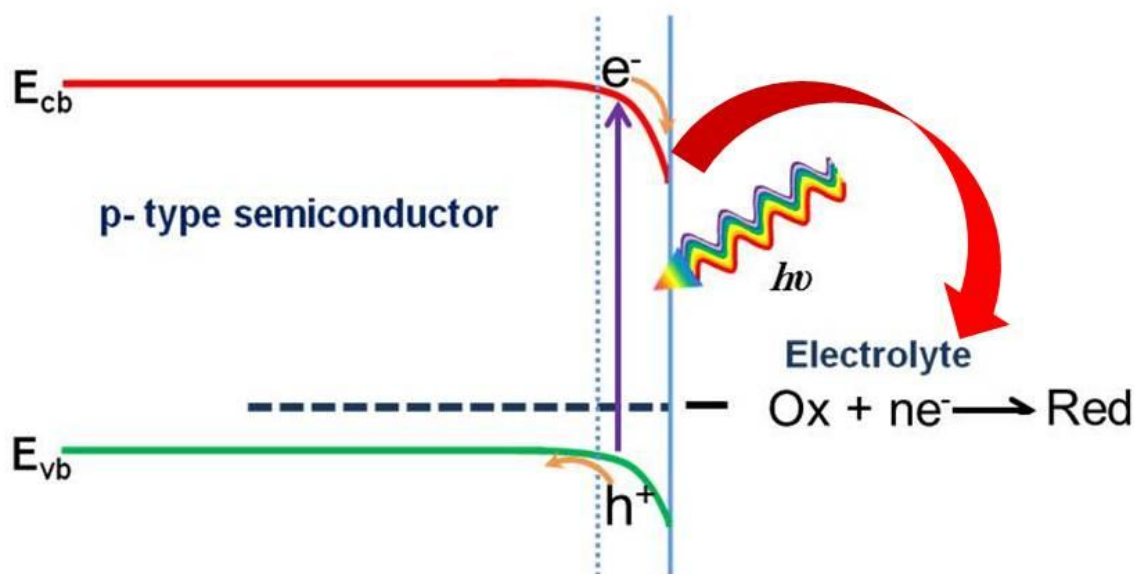


Figure 2-23. A simplified picture of the charge separation at the semiconductor/electrolyte interface for a p- type semiconductor under illumination conditions.

2.1.7 Ideal behaviour of an n-type semiconductor under dark and light

The Ideal behaviour for an n-type semiconductor electrode in the dark and under light is shown in figure 2-24.

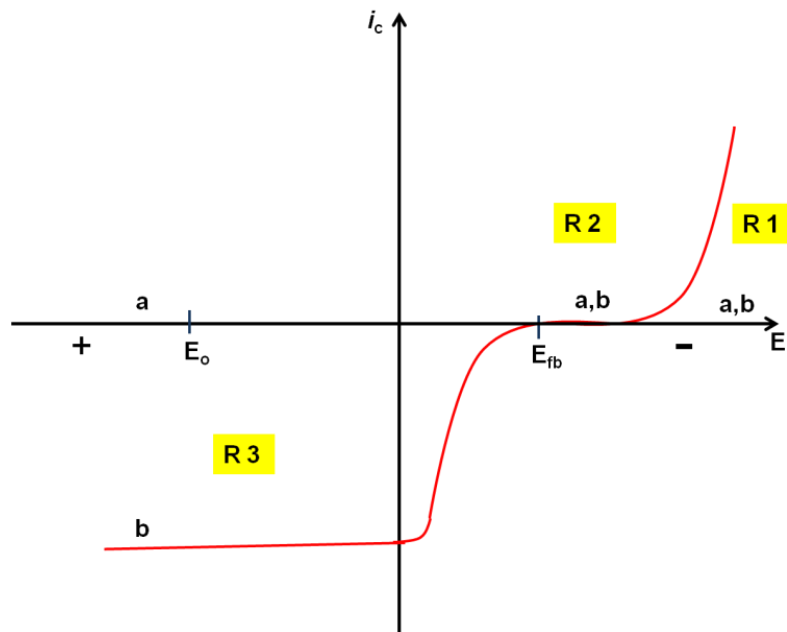


Figure 2-24. Ideal behaviour for an n-type semiconductor in (a) dark and (b) under light in an electrolyte.

As there is no electric field to separate any generated charge carriers at the E_{fb} no current is generated either in the dark or under the light (R2). An accumulation layer exists when the potential is negative to the E_{fb} . Under these conditions the electrode can act as a cathode under both light and dark (R1). Under these conditions the electrode is referred to as a dark cathode. At potentials positive to the E_{fb} a depletion layer exists, so there is no oxidative current in the dark (R3). Under the light conditions however, a photocurrent can be observed at potentials negative of the redox potential of the electrolyte (which lies at E_o). Some of the energy required for the oxidation reaction is provided by the radiation (via the high energy hole). Using similar reasoning, it can be shown that p-type semiconductor electrodes are dark anodes and photocathodes.

2.2 Microwave synthesis and processing of materials

In organic and inorganic material synthesis, some or all the reactants involved in the reaction should have a high coupling efficiency with microwaves. This provides adequate energy to overcome the activation energy barrier, allowing the reaction to proceed. The microwave absorbing properties of the reactants facilitate the rapid heating and lead to successful synthesis of the target material within a very short period of time. In the microwave-assisted synthesis, one often selects alternative reactants with favourable dielectric properties in order to achieve maximum product yield. If there are no alternative microwave absorbing reactants available for material synthesis, it is usually possible to find a secondary material that can act as a heat source; this is commonly referred to as a microwave susceptor. Microwave susceptors are substances that have the ability to absorb microwave energy and convert it to heat. In other words, a susceptor is a material that has a high dielectric loss tangent. Graphitic or amorphous carbon,[47-49] silicon carbide[49-51] and copper (II) oxide[52,53] are some of the examples of commonly used susceptors. These susceptor materials can be kept either in direct contact with the sample (by mixing with the other reagents) or placed outside (surrounding the sample). In some cases adding a susceptor into a reaction mixture can cause problems with the final product purity, yield and reaction rate.[35] Microwave susceptors can also be used in material post heat treatments to ramp up the temperature of poorly microwave absorbing materials. In such cases, the penetration depth plays a vital role in the heat generation. If the penetration depth exceeds susceptor thickness, the susceptor behaves as if it is transparent to microwaves.[54] The volumetric heating only occurs when the penetration depth is comparable to the sample thickness. If the sample is too thick, absorption is limited to the surface. The physical nature of materials, such as particle size, density and the medium

the material is present in, also determines the microwave penetration depth.[55] The variation of the penetration depth of SiC with the above physical properties is shown in figure 2-25.

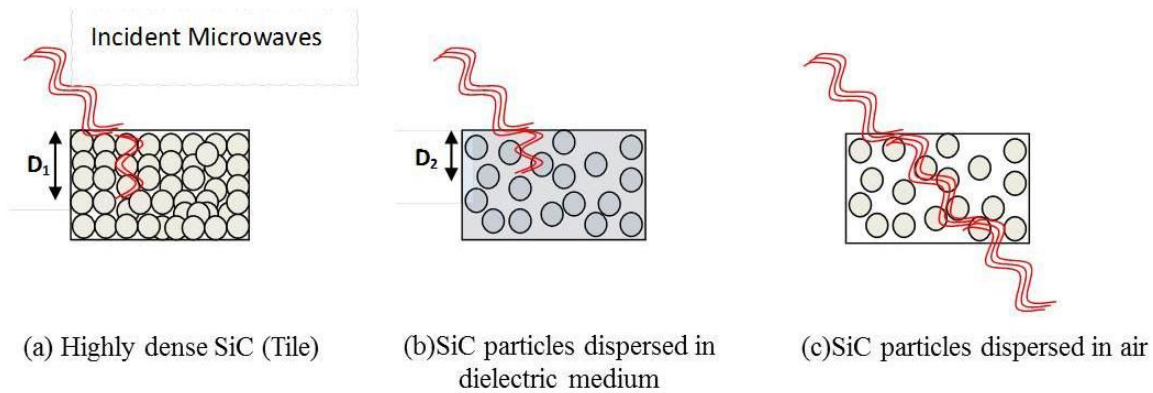


Figure 2-25. The variation in the penetration depth of microwaves with the density and the dispersion medium of SiC.

As indicated in the figure 2-25 the penetration depth of SiC varies with the density and the nature of the particle dispersion in the medium. This affects the microwave coupling and heat generation. Generally SiC is an abrasive material with a high density. The microwaves couple with SiC as a whole and penetrate well into the material to generate heat effectively because of its high density (figure 2-25a). When the SiC particles are dispersed in a dielectric medium, (such as water, ethanol etc.) microwaves interact with SiC particles as well as the dielectric medium to generate heat. Since both media couple well with microwaves, the penetration depth of such system (which determines by the sum of the contributions from each material's dielectric properties) are reasonably high, this leads to heat generation (figure 2-25b). In the case of SiC powders the voids between the particles are filled with air which is transparent to microwaves. Thus heat generation is only influenced by the particle size of SiC (figure 2-25c). In order to generate volumetric heating in SiC powders the penetration depth of microwaves needs to be comparable with the particle size of SiC (diameter of the particles). Therefore, it is not possible to heat SiC nanoparticles (< 100 nm) by microwaves unless they are mixed with another dielectric matrix.

2.2.1 Semiconductor metal oxides

Over the past decade many oxide compounds have been synthesised using microwave radiation. In most of the literature it is claimed that use of microwaves in microwave-assisted synthesis shortens the reaction times and reaction temperatures significantly compared to conventional synthetic techniques.[56] It is also noted that lattice distortions, electronic structure variations, nanostructure size and shape for metal oxides are affected when synthesised using microwave radiation.[56,57] Table 2 shows some of the metal oxides that have been synthesised using microwave radiation. They are listed by main experimental conditions, size and morphological features of the resulting nanostructures, mechanistic pathways involved, and growth-governing factors.

Table 2. The list of microwave-assisted synthesised metal oxides.[58]

Metal oxide	Precursors	Formation mechanism	Crystalline features	Reaction condition	Ref.
MgO	Mg(OAc) ₂	polymer-assisted growth	amorphous powders; 3.2 nm particles after annealing	30 min	[58]
Bi ₂ O ₃	Bi(NO ₃) ₃	polymer-assisted growth	rods (2×30 μm)	6 min reflux	[59]
CeO ₂	Ce(NO ₃) ₂	ligand-assisted growth self-aggregation	14 nm spheres assembled in hollow spheres (range 260 nm)	>30 min 170 °C	[60]
CeO ₂	(NH ₄) ₂ Ce(NO ₃) ₆ CeCl ₃	ion-assisted growth	spheres, 1.5–20 nm rods 7.5×30 nm	>60 min 160 °C	[61]
CeO ₂	(NH ₄) ₂ Ce(NO ₃) ₆	polyol-assisted growth	spheres average 2 nm	10 min 30 s MW cycles (9 s on/21 s off)	[62]

CeO ₂	(NH ₄) ₂ Ce(NO ₃) ₆	polyol-assisted growth	spheres 2–3 nm	10 min 30 s MW cycles (9 s on/21 s off) 100 °C 1 atm	[63]
CeO ₂	(NH ₄) ₂ Ce(NO ₃) ₆	co-precipitation	spheres 5.1±0.1 nm	5–240 min 194 °C 3– 14 atm	[64]
Cd(OH) ₂	Cd(NO ₃) ₂	oriented aggregation	nanowires 5–30 nm×0.3 μm	5 min	[65]
Co ₃ O ₄	Co(NO ₃) ₂	ligand-assisted growth	nanocrystals no singular shapes	15 min	[66]
Co ₃ O ₄	CoCl ₂	ligand-assisted growth (crystallization requires annealing at 300 °C required)	nanowires 80 nm×2 μm	6 h 110 °C	[67]
Co ₃ O ₄	Co(NO ₃) ₂	ligand-assisted growth	flakes arranged in Flower-like shapes 2–3 μm	15–90 min 85 °C	[68]
CuO	Cu(OAc) ₂	ligand-assisted growth	spheres average 4 nm	10 min 30 s MW cycles (6 s on/24 s off) reflux	[69]
CuO	CuCl ₂	ion-assisted growth	flower-like or leaf-like nanocrystals	10 min 80 °C	[70]
CuO	CuCl ₂	oriented attachment	urchin-like structures	15 min 100 °C	[71]
CuO.Cu ₂ O. Cu	Cu(OAc) ₂	ligand-assisted growth	wiskers: 80 nm×10 nm Cubes: 50 nm; Spheres: 100–120 nm	15 min 100–197 °C	[72]
Cu ₂ O	Cu(OAc) ₂	Ostwald ripening	ellipsoids ca. 300 nm	30 min 70 °C	[73]
α-Fe ₂ O ₃	FeCl ₃	ion-assisted oriented attachment	nanorings outer diameter 100 nm cubes, spindles	25 min 220±1 °C	[74,75]
α-Fe ₂ O ₃	FeCl ₃	solvent-assisted growth	spheres 14.7–40 nm polydisperse and agglomerated	1–150 min 150 °C >1 atm	[75]

α -Fe ₃ O ₄	Fe(OAc) ₂ , Fe(acac) ₃	solvent-assisted growth	spherical 4–9 nm polydisperse and agglomerated	30 s–3 min 200 °C >1 atm	[76][77]
α -Fe ₂ O ₃	FeCl ₃	solvent-assisted growth	spheres 31–66 nm	2–8 h 100– 160 °C	[78]
α -Fe ₂ O ₃	FeCl ₃	ligand-assisted growth	spheres 400–800 nm	20 min reflux	[79]
α -Fe ₂ O ₃	FeCl ₃	polymer-assisted oriented attachment	ellipsoids 100×200 nm	10 min 100 °C	[80]
α -Fe ₂ O ₃	FeCl ₃	polyol-assisted growth	amorphous 3–5 nm particles	10 min 30 s MW cycles (15 s on/15 s off)	[81]
α -Fe ₂ O ₃	Fe(NO ₃) ₃	polymer-assisted growth	octahedral 300 nm	24 h 200 °C	[82]
α -Fe ₂ O ₃	FeCl ₃	solvent-assisted growth	<20 nm	15 min 150 °C	[83]
α -Fe ₂ O ₃	Fe(NO ₃) ₃	solvent-assisted growth	rhombic-shaped 18–38 nm	0.5–48 h 100–120 °C	[84]
α -Fe ₂ O ₃	K ₄ [Fe(CN) ₆]	solvent-assisted growth	snowflake-like, pinetree-like assemblies 2–4.5 µm polydisperse	0.5–3 h 120– 220 °C >1 atm	[85,86]
Cr ₂ O ₃ MoO ₂	K ₃ [Cr(CN) ₆] K ₃ [Mo(CN) ₈]	solvent-assisted growth	snowflake-like assemblies 1–5 µm polydisperse	3 h 180 °C >1 atm	[87]
MeFe ₂ O ₄ (Me=Ni, Co, Mn)	Fe(NO ₃) ₃ Ni(NO ₃) ₂ Co(NO ₃) ₂ Mn(NO ₃) ₂	solvent-/surfactant- assisted growth surfactant-driven phase transfer	spherical 4–9 nm σ =10–30 %	1 h 160 °C >1 atm	[88]
Fe ₃ O ₄	FeSO ₄	Solvent-assisted growth	aggregates of ca. 35 nm particles	8 min 80 °C	[89]
Fe ₃ O ₄	FeSO ₄	polyol-assisted anisotropic growth	wires 30–50 nm >> 1µm	15 min 180 °C >1 atm	[90,91]
Fe ₃ O ₄	FeCl ₃	polyol-assisted or surfactant-assisted growth by oriented attachment	clusters made of <20 nm NCs 100 nm–5 µm σ =20– 30 %	15–60 min 160– 210 °C >1 atm	[92,93]
Fe ₃ O ₄	Fe(acac) ₃	surfactant-assisted growth	spheres 6 nm σ =30 %	5–10 min 250 °C	[94]

In ₂ O ₃	InCl ₃	NH ₄ OH-assisted (In(OH) ₃ converted into In ₂ O ₃ after calcination at 700 °C)	hexagons 22 nm $\sigma=10\%$	60 min (MW cycles: 12 s on/7 s off) reflux	[95]
Mn ₃ O ₄	Mn(OAc) ₂	Ostwald ripening	cubes rhombohedra 15–40 nm	10–60 min 80 °C	[96]
MnO ₂	KMnO ₄	growth confined in oil-in-water microemulsions Ostwald ripening	nanowires/belts polydisperse	8 min reflux	[97]
MnO	Mn(OAc) ₂ , Mn(acac) ₂	solvent-assisted ester elimination	cube-like 30–50 nm	0.5–3 min 200 °C	[98]
PdO	H ₂ [PdCl ₄]	polymer-assisted growth	spheres 1.8–3.2 nm $\sigma=25\%$	8 min reflux	[99]
PtO ₂	H ₂ [PtCl ₆]	polymer-assisted growth	spheres average 1.68 nm	10 min reflux	[100]
SnO	SnCl ₂	solvent-assisted growth	crystalline powders	10–15 min reflux	[101]
SnO ₂	SnCl ₄	solvent-assisted growth	spheres 3 nm polydisperse	15 min reflux	[102]
SnO ₂	SnCl ₄	solvent-assisted growth	average 5 nm	1–2 min 180 °C ca. 0.9 atm	[103]
SnO ₂	SnCl ₄	solvent-assisted growth	average 3 nm	0.5–4 h 100–200 °C	[104]
TiO ₂	Ti(OBu) ₄ TiCl ₄	growth confined in polymer micelles	spheres 5 nm $\sigma=5\%$ rods 30–50 nm × 0.5–1 μ m	5 min–8 h 25–80 °C 1 atm	[105,106]
TiO ₂	Ti(OBu) ₄ Ti(OiPr) ₄	solvent-assisted growth	spherical aggregates ca. 200 nm	2–30 min 240–285 °C	[107,108]
TiO ₂	Ti(OiPr) ₄	MW-induced recrystallization of TiO ₂ colloidal solutions	3–5 nm	5–10 min 121–145 °C 2–4 atm	[109]
TiO ₂	TiCl ₄	solvent-assisted growth	aggregates 150 nm polydisperse	5–15 min 100 °C	[110]
TiO ₂	TiCl ₄	solvent-assisted growth	aggregates 70 nm polydisperse	30 s ca. 0.4 atm	[111]

TiO ₂	TiCl ₄	solvent-assisted growth	<100 nm	5–120 min 100–160 °C	[112]
TiO ₂	TiCl ₄	solvent-assisted growth	aggregates 800 nm polydisperse	30–120 min 120–180 °C	[113]
TiO ₂	TiCl ₃	ion-assisted growth	cubes: 25 nm rods: 4×17 nm spheres: 8 nm	20–60 min	[114]
TiO ₂	TiOCl ₂	solvent-assisted growth	spheres (10 nm), rods (10×100 nm)	5–60 min 195 °C	[115]
TiO ₂	(NH ₄) ₂ TiF ₆	solvent-assisted growth	spheres 20–200 nm	10–60 min 70 °C	[116]
TiO ₂	Ti(OiPr) ₄	MW-driven crystallization of amorphous hydroxide particle precursor-s	truncated cubes 8–10 nm	40 min 1 atm	[117]
TiO ₂	TiF ₄	solvent-assisted growth MW-driven crystallization	sheets 2 μm×2 μm	90 min 210 °C >1 atm	[118]
WO ₃	WCl ₆	solvent-assisted growth	aggregates of 5–30 nm particles	5–15 min 210 °C	[119]
WO ₃	Na ₂ WO ₄	ion-assisted anisotropic growth	nanowires 20–30 nm× >1 μm	20 min–3 h 150 °C >1 atm	[120]
ZnO	Zn(OAc) ₂	polymer-assisted oriented attachment sequential seeding	clusters of 8 nm NCs 50–275 nm	1–5 min steps 120–180 °C 1 atm	[121]
ZnO	zinc oximate Zn(acac) ₂	solvent-assisted oriented attachment	clusters of 10–30 nm NCs 50–180 nm	4 min >1 atm	[122]
ZnO	Zn(OAc) ₂ Zn(acac) ₂	solvent-assisted growth	aggregates of 20–30 nm particles rods:100 nm×1 μm	0.5–3 min 200 °C	[123]
ZnO	Zn(NO ₃) ₂	oriented attachment	bipods, tripods, multipods	2–30 min 90 °C	[124]
ZnO	Zn(NO ₃) ₂ Zn(OAc) ₂	ligand-assisted growth	rods or needles or stars or disks or balls range 0.4–5 μm	15 min 90 °C	[125]
ZnO	Zn(NO ₃) ₂	solvent-assisted growth	rods range 1 μm	120 min 192 °C	[126]
ZnO	Zn(NO ₃) ₂ , Zn(OAc) ₂ ZnSO ₄ ZnCl ₂	ion-assisted growth	needles 11 μmσ=20–30 %	>15 min	[127,128]

ZnO	Zn(OAc) ₂	solvent-assisted growth	rods diam. 25–7 nm len. 0.5–1.5 μm	10 min	[129]
ZnO	Zn(OAc) ₂	solvent-assisted growth	dumbbells 2×5 μm	5–10 min	[130]
ZnO	Zn(OAc) ₂	polymer-assisted seeded growth	rods packed in micromer-sized bundles, spheres or flowers	different MW cycling modes 60–90 min	[131]
ZnO	Zn(OAc) ₂	polymer-assisted growth	rods 50–250 nm diameter×70–300 nm length	30 min 140 °C	[132]
ZrO ₂	Zr(NO ₃) ₄	polymer-assisted growth	aggregates of 2 nm particles	6 min (MW cycles: 10 s on/20 s off) 320 °C	[133]
ZrO ₂	ZrOCl	Solvent-assisted growth	spheres 10–20 nm	120 min 194 °C 14 atm	[134]
ZrO ₂	Zr(OiPr) ₄	ligand-assisted growth	spheres 100 nm	50–100 mL min ⁻¹ 60 °C 15 atm	[135]

2.2.2 Non-oxide semiconductors

Materials other than metal oxides have been produced using microwave-assisted synthesis. The reported literature on this illustrates the remarkable synthetic flexibility given by microwave assisted synthetic routes over the traditional methods. Table 3 summarizes reaction conditions, product characteristics, and main formation mechanisms of metal chalcogenides synthesised under microwave radiation which has been reported in a latest review article.[136]

Table 3. A summary of some metal chalcogenides synthesised by microwave irradiation.

Material	Precursors	Formation mechanism	Crystalline features	Reaction condition	Ref.
CdS	CdCl ₂	solvent-assisted growth	aggregated spheres 9 nm polydisperse	20 min reflux	[137]
CdS	Cd(OAc) ₂ thiourea	solvent-assisted growth	spheres <5 nm polydisperse	18 s 1 atm 80 °C	[138]
CdSe	CdSO ₄ , Na ₂ SeSO ₃	surfactant-assisted growth	agglomerated spheres ca. 5 nm polydisperse	0.5 min 1 atm reflux	[139]
CdSe	Cd(OAc) ₂ , Se	polyol-assisted growth	spherical aggregates of tiny clusters 6–7 nm	60 min reflux	[140]
CdTe	CdCl ₂ Na ₂ TeO ₃ , NaBH ₄	ligand-assisted growth	irregular spheres ≈3 nm	10–40 min >1 atm 80–140 °C	[141]
CdTe	CdO TeTBP	surfactant-assisted growth	Spheres ca. 4.4 nm $\sigma=5-10\%$	1–90 min 1 atm 180–280 °C	[142]
CdZnSe	Cd(OAc) ₂ , Zn(OAc) ₂ , Se	polyol-assisted growth	aggregated spheres ca. 6 nm polydisperse	60 min MW cycles (21 s on/9 s off) reflux	[143]
CuS	Cu(OAc) ₂ , thioacetamide	ligand-assisted growth	irregular spheres 5–10 nm	20 min reflux	[144]
CuInS ₂	CuCl ₂ , InCl ₃ , Na ₂ S	ligand-assisted growth	spheres 3 nm	30 min 90 °C	[145]
CuInS ₂	CuI, InCl ₃ , S	surfactant-assisted growth	irregular spheres 3–10 nm polydisperse	20–30 min >1 atm 120–220 °C	[146]
CuInTe ₂	CuCl, In, Te	ligand-assisted growth	irregular spheres ca. 94 nm	60 min 1 atm reflux	[147]
PbS	Pb(OAc) ₂ , S	ligand-assisted growth	irregular spheres 20–30 nm polydisperse	20 min 1 atm reflux	[148]
PbSe	Pb(OAc) ₂ selenourea	surfactant-assisted growth	polyhedrons, cubes 5–15 nm $\sigma=5-10\%$	1 min 3 bar 160 °C	[149]

ZnS	Zn(OAc) ₂	solvent-assisted growth	clustered spheres <100–300 nm polydisperse	15 min reflux	[150]
ZnS	Zn(OAc) ₂ , thiourea	polymer-assisted growth	spheres ca. 7 nm polydisperse	1–12 min MW 30 s cycles (9 s on/21 s off) 1 atm	[151]
ZnSe	Zn(OAc) ₂ , Se	surfactant-assisted growth	aggregated spheres/ellipsoids 20–500 nm polydisperse	20 min >1 atm 180 °C	[152]
ZnSeS	ZnCl ₂ NaHSe	ligand-assisted growth	spheres ca. 5 nm	55 min >1 atm 140 °C	[153]
ZnSe	Zn(OAc) ₂ selenourea	surfactant-assisted growth	nano-rods/wires 1–1.5 nm×5–450 nm σ =6–12 %	0.5–3 min (400 W) >1 atm	[154]

2.2.3 Metal oxide thin films

It is clear that microwave assisted material synthesis is widely acceptable for inorganic/organic material production as it gives more advantages than the conventional synthesis methods. However use of microwave radiation for materials post annealing treatment is a novel technological advancement alternative to conventional sintering. Recently a particularly interest has been made to improve the chemical, physical and hence photoelectrochemical performance of semiconductors by post-synthesis microwave treatment. The improved performance is attributed to improvements in the crystallinity and the particle-necking properties and the densification by microwave irradiation of thin film electrodes. Recent examples demonstrate that microwave processing is a promising alternative to conventional sintering for thin film post treatments for better photoelectrochemical performance. It is reported that the photoelectrochemical performance of microwave annealed α -Fe₂O₃ and TiO₂ thin films can be improved compared to those heated conventionally.[155][156] Also our recent study concluded that the microwave irradiation

caused sintering of individual ZnO nanorods resulting in the growth of rod diameter whilst the conventional thermal annealing deformed the hierarchical ZnO structure of thin films. However, to the best of my knowledge, there is very little literature available on the microwave post treatment of metal oxide semiconductor thin films which can be used in advanced electronic and optoelectronic devices.

2.3 Industrial use of microwaves for material processing

Microwave heating of materials offers many significant advantages over conventional heating methods. This technique has a huge number of applications for technology in industry. Microwave treated materials can be used as a high performance, nanostructured host for the preparation of advanced materials that exhibit specific optic, optoelectronic, and electrochemical properties suitable for supercapacitors, display devices, molecular wires, quantum electronics and non-linear optical devices.[157,158] As summarized in the previous section, a number of preparations of nano-scale materials on nanostructured template have been demonstrated using microwave technology. Iron oxide based magnetic materials have been extensively used as recording materials because of their good magnetic properties. The emergence of nano-magnetic technology has imposed new demands upon magnetic materials to fabricate ultrahigh density and ultrahigh speed data storage devices.[159]

Microwaves represent an alternative way of adding energy to chemical reactions and material processes. Although microwave radiation has been used in many industries as a heating method to improve the quality of final products, this method is yet to apply for the materials involving in energy storage devices such as supercapacitors and fuel cells. Supercapacitors are an energy storage device based on simple charge-separation at an electrochemical surface between an electrode and electrolyte. They have attracted more attention recently due to their

higher power density and longer life cycle compared to batteries.[160] Inter-particle connections and surface area of such supercapacitor materials can be improved by post synthesis treatment of the electrodes with microwave radiation. This is useful in getting better charge-separation properties. Fuel cells are also promising power sources for various applications, because of their low operating temperatures, relatively quick start-up, and high power density. Iron, iron oxides and ferrous alloys are used in an extensive range of applications in these kinds of energy storage devices. Microwave treatment of such metal oxides can improve the better inter-particle connections and surface area which is vital in better fuel cell operation characteristics. Walkiewicz *et al*[161] reported successful microwave heating of metallic powders for the first time. In the 1990s microwaves were used in the synthesis of intermetallic alloys, carbides and nitrides.[162,163] Later, Cheng *et al*[164] carried out a comprehensive study on microwave sintering of metals including ferrous alloys and concluded that microwave sintering not only provided a faster process at lower processing temperatures but the properties of final products were also improved significantly. Therefore, the microwave annealing method offers improved materials properties with energy savings, which would make it highly desirable for industrial scale up.

2.4 Unique performance characteristics to microwaves

Microwaves possess several characteristics that provide unique features that are not available in the conventional processing of materials. Some of the key characteristics of microwaves' interactions with materials are,

1. Penetrating radiation

The depth of penetration depends on several factors, including the wavelength of the radiation and the dielectric (and magnetic) properties of the material.

2. Controllable electric field distributions

In microwave applicators such as microwave furnaces, the electric field distributions can be focused and controlled to provide very high field strengths which provide a proper tuning to heat low-loss materials at low temperatures and heat selected regions between two materials to promote welding, brazing, or bonding or to generate plasmas for microwave-assisted sintering or chemical vapour deposition.

3. Rapid heating

For many materials, dielectric losses above a critical temperature accelerate with increasing temperature, allowing very rapid (bulk) heating that can result in very significant reductions in processing time. This rapid increase in dielectric loss can lead to uneven heating and thermal runaway. However this can be controlled by using hybrid heating or insulation.

4. Selective heating of materials

The range of dielectric responses of different materials and their ability to couple with microwaves is one of the most widely used features of microwave processing.

5. Self-limiting absorbance

Self-limiting absorbance can be occurred within the material when irradiated with microwaves when it contains two or more materials with different dielectric properties. These characteristics, either singly or in combination, represent opportunities and benefits not available from conventional heating or processing methods.

2.5. Microwave generators

Microwave generators include the magnetron, power grid tubes, traveling wave tubes (TWTs), Crossed field amplifiers (CFAs), klystron and gyrotron.[165] The selection of the types of microwave generators for use depends on various factors including power, frequency, efficiency, gain, bandwidth, phase, size, weight and cost. The magnetron is the most commonly used microwave generator because of its high efficiency, compact size and low cost.[166] Figure 2-26 shows a 2kW power magnetron which is used in domestic and industrial microwave ovens. A cross-section of a typical magnetron is shown in figure 2-27. It is used widely in microwave ovens and radar systems. A magnetron converts electrical energy to microwave radiation and typically operates at a frequency of 2.45 GHz.



Figure 2-26. Magnetron of 2kW power.[167]

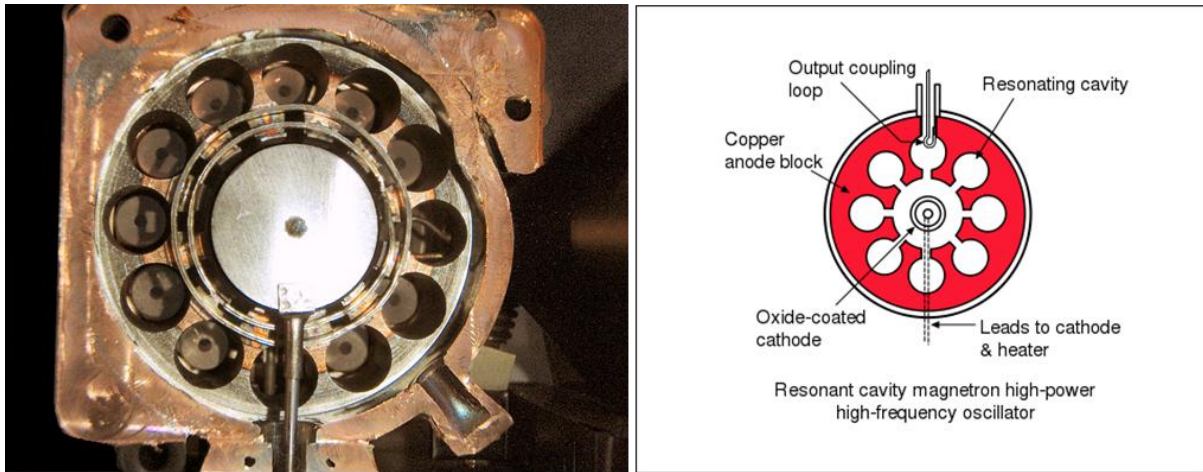


Figure 2-27. A cross-section of a typical magnetron.[168]

The magnetron is essentially a thermionic diode that converts electrical energy to microwave radiation. In the magnetron, heated cathodes act as a source of electrons. The cathode is surrounded by a circular anode having an array of radial slots acting as resonators tuned to the desired operating frequency. The electric field created by the applied DC voltage draws the electron from the cathode to anode region. In the presence of a magnetic field, the electrons cannot travel radially outward to the anode but they are forced to rotate circularly in the coaxial space between the cathode and the anode. Consequently, the bunching of the electron cloud occurs. The electron cloud would appear as a rotating spoke wheel. In the presence of an electromagnetic field, the electrons entering the positive microwave electric field gradient will accelerate and those entering the negative gradient will decelerate. The changes in the kinetic energy of the electrons leaving the cathode and arriving at the anode will result in the generation of the microwaves. The transfer of power from the DC power input to the microwave power is extremely efficient. The microwaves are then directed towards a target with the use of microwave guides which are usually made of sheet metals. The output microwave power can be generated in two ways; pulsed or continuous. Pulsed magnetrons produce output power of kilowatts to several megawatts for short durations while continuous magnetrons produce output power of a few watts to kilowatts continuously.

Chapter 3

Experimental Methods and Materials Characterization

3.1 Experimental Methods

3.1.1 Aerosol-assisted chemical vapour deposition

The aerosol-assisted chemical vapour deposition (AACVD) technique has been used to fabricate TiO_2 and ZnO thin films on fluorine-doped SnO_2 (FTO) glass substrates.[169] In the AACVD deposition method, an aerosol precursor solution is used which is transported into the reaction chamber by use of a carrier gas, whereby the solvent is evaporated and precursor molecules decompose onto the substrate.[170] The figure 3-1 shows a schematic diagram of the aerosol-assisted chemical vapour deposition apparatus.

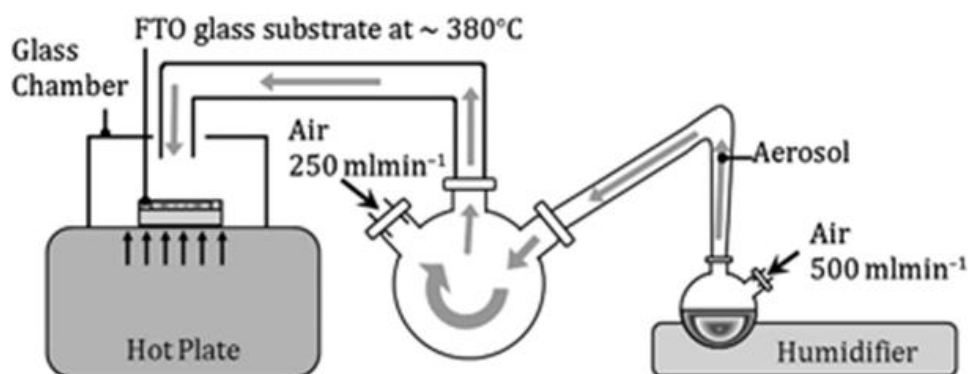


Figure 3-1. Schematic of the aerosol-assisted chemical vapor deposition apparatus.[171]

The precursor solution can be a pure liquid, single source precursor or a mixture of several liquid chemicals, or can be prepared by dissolving solid or liquid starting materials in an solvent. Usually, a criterion for the selection of solvents for AACVD is high solubility of the precursor, low vapour pressure, and low viscosity. Depending on the nature of the decomposition, the deposition can be take place by homogenous and heterogenous

mechanisms. At higher substrate temperatures, the major decomposition may occur much earlier in the vapour phase, leading to homogenous nucleation and the formation of fine particles on substrate. In the heterogeneous mechanism, preliminary decomposition of vaporized precursor may occur in the gas phase.[172] Either one or both these mechanisms can involve in growing TiO₂ and ZnO thin films on FTO glass substrates.

3.1.2 Chemical bath deposition

The chemical bath deposition (CBD) method for the preparation of thin films has recently been shown to be an attractive technique because of its simplicity, convenience, low cost and low temperature, and it has been successfully used for depositing metal oxide nanorods. This is a solution phase technique which allows fabricating semiconductor thin films from aqueous solutions. The CBD technique is widely used for the deposition of various metal oxides and chalcogenide thin films. This allows the control of growth factors such as film thickness, deposition rate and quality of crystallites by varying the solution pH, temperature and bath concentration.[173] The deposition of a film can be due to two types of nucleation in solution: homogeneous nucleation and heterogeneous nucleation. Homogeneous nucleation leads to rapid formation of large particles throughout the solution, as a precipitate. Conversely, heterogeneous nucleation occurs at the substrate surface and particles grow slowly to form a film.[174] The pre-treatment of the substrate with a seed layer avoids the disruption to heterogeneous nucleation which is the key to obtain hierarchical structures of materials. Growing of ZnO nanorods on FTO/ITO glass substrates from an alkaline solution requires a seed layer. A schematic of the CBD set-up is shown in figure 3-2.

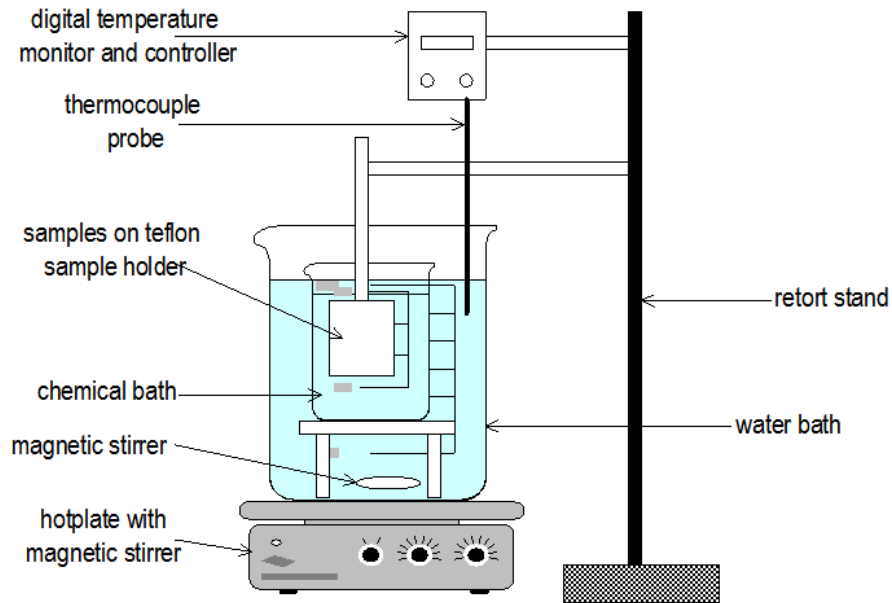


Figure 3-2. Chemical Bath deposition set-up.[175]

3.1.3 Annealing procedures

3.1.3.1 Conventional annealing

Conventional thermal annealing was carried out in a tube furnace (MTF-10-25-130, Carbolite, Hope Valley, UK) with a ramp rate of 15 °C/min to the desired temperature. Both ends of the tube were kept open to allow for the flow of air. After annealing the furnace was turned off and the samples were left in the furnace to cool down. The temperature of the samples was measured using a K-type thermocouple. An image of MTF-10-25-130 tube furnace is shown in figure 3-3.



Figure 3-3. Conventional thermal MTF-10-25-130 tube furnace.

3.1.3.2 Microwave-assisted annealing

Microwave-assisted annealing was performed using an industrial microwave furnace (MRF 16/22, Carbolite Ltd, UK) capable of producing a tuneable continuous power output up to a maximum of 2 kW operating at 2.45 GHz frequency (figure 3-4) and a modern microwave oven (Microwave research Applications Inc. BP-211/50, USA) operating at 2.45 GHz frequency with a maximum power of 3000 W (figure 3-5). The samples were placed inside a high purity insulator blocks to minimise the heat loss during the microwave processing. The thermal imaging cameras (Micro-Epsilon/ TIM 400 and M67/M67S IR temperature transmitter) are placed on top of the furnaces and temperature was recorded during the microwave treatment of samples (Figure 3-6) using itools software.



Figure 3-4. The images of (a) industrial MRF 16/22 microwave furnace with Micro-Epsilon/TIM 400 thermal imaging camera. (b) Microwave furnace chamber and the insulator blocks.

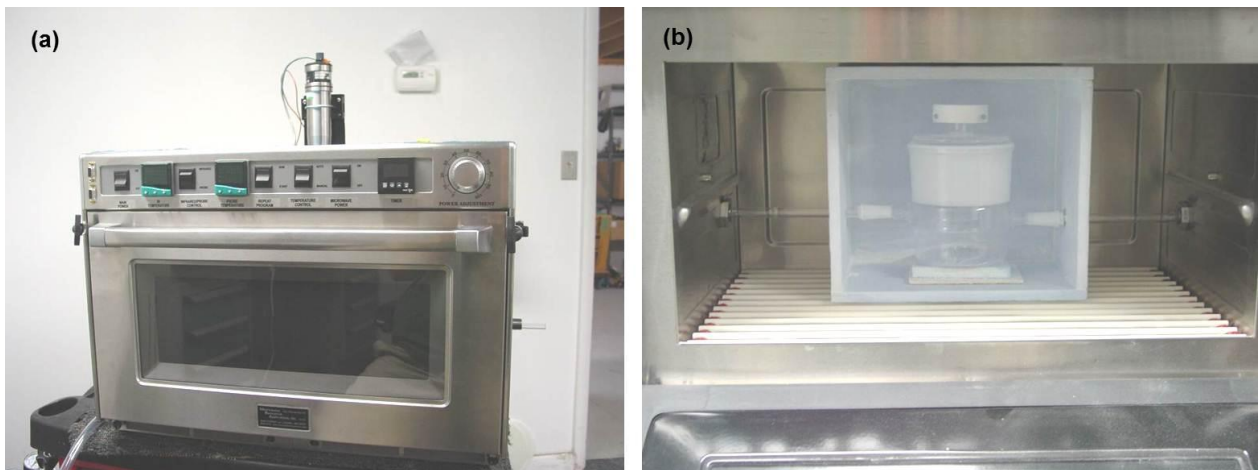


Figure 3-5. The images of (a) custom processing BP-211/50 microwave furnace with M67S IR temperature transmitter. (b) Microwave furnace chamber and the insulation.

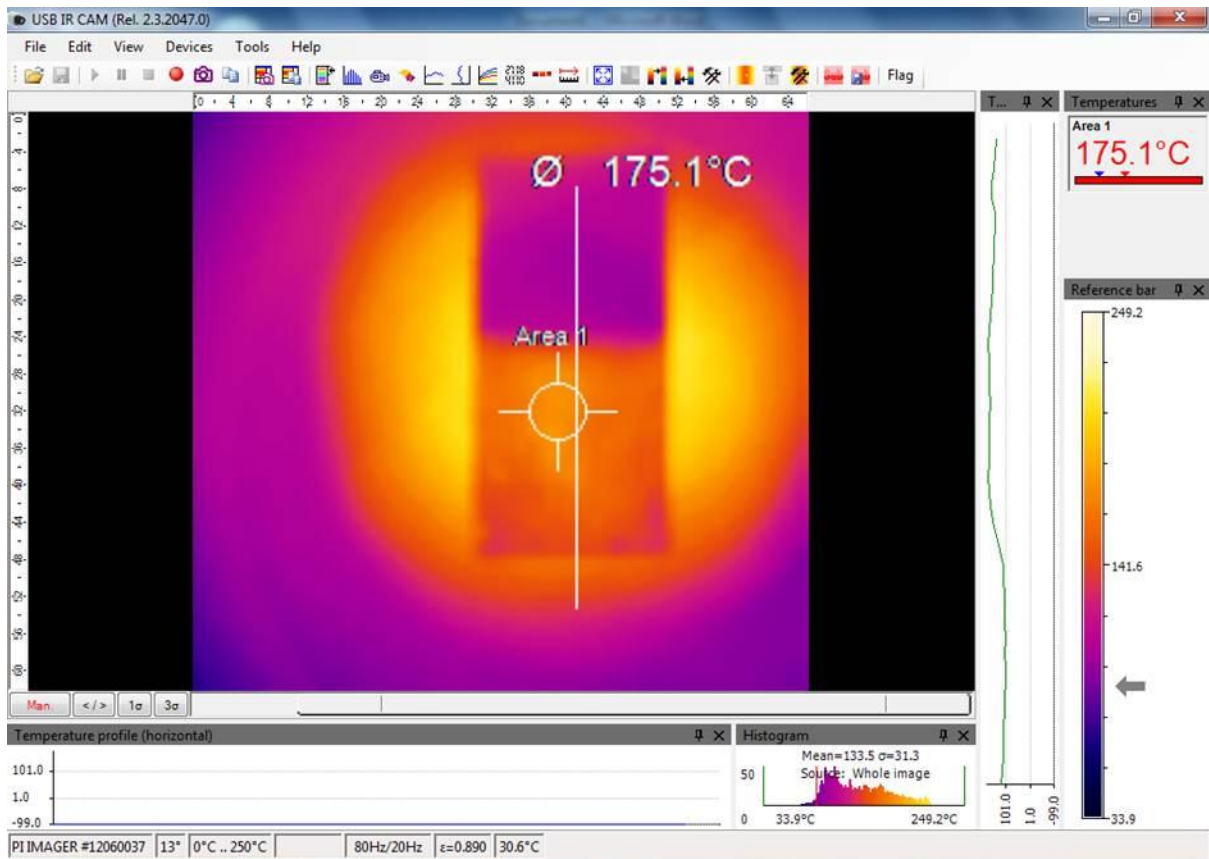


Figure 3-6. A screen shot of a thermal image of the itools software analysing the reading taken from the thermal imaging camera.

Power measurements in a microwave system are derived from elementary thermal concepts based on the heat capacity of a mass at constant pressure. Specific heat capacity, C_p ($\text{JK}^{-1}\text{kg}^{-1}$) is that quantity of heating experienced by a given mass per degree of temperature from energy absorbed to provide a rise in temperature, ΔT . If a quantity of energy is delivered for a unit of time, then P_w , the power absorbed by a substance (power density) in the microwave cavity may be expressed in the following relationship,

$$P_w = \frac{K C_p m \Delta T}{t} \quad (12)$$

where, K is the conversion factor, m is the mass of the sample and t is the time. The power calibration of the microwave furnaces was performed by using water test method as described elsewhere.[176]

3.1.3.3 Microwave-assisted synthesis

Microwave-assisted synthesis was performed in a Biotage Initiator EXP 8 reactor in 10-20 mL crimped vials. Figure 3-7 demonstrates a Biotage Initiator EXP 8 reactor which was used to the synthesis the materials.



Figure 3-7. Biotage Initiator EXP 8 reactor.

3.2 Materials Characterization

3.2.1 X-ray diffraction

X-ray diffraction (XRD) is one of the primary techniques that can be used to determine the crystalline structure of solid materials. When the X-rays interact with atoms in the crystal lattices of a solid, a diffraction pattern is generated. Since, each crystalline solid has a unique atomic architecture, the generated XRD pattern is characteristic of the material from which is obtained and can be used as a fingerprint to identify the crystalline phases and its structure (i.e. packing density of the atoms, crystalline state, shape, stresses in the crystal lattice and size of the unit cell etc.).

English physicists Sir W.H. Bragg and his son Sir W.L. Bragg developed a relationship in 1913 to explain why the incident X-ray beams reflect at certain angles when they are interact with atoms of the crystalline phases of solids. When X-rays interact with atoms in two lattice planes, and the path length difference between rays equals a whole multiple of the wavelength of the radiation, constructive interference occurs (Figure 3-8). Bragg's law describes the conditions for constructive interference in certain directions and the production of diffracted scattered X-rays:

$$n\lambda = 2d\sin\theta \quad (13)$$

where n = an integer, λ = the wavelength of the X-rays, d = the lattice spacing of a (h,k,l) plane, θ = the angle between the incoming X-ray and the atomic layer.

X-rays are scattered by atoms in the different crystalline planes (hkl) and are picked up by the detector, which then converts them in to intensity against 2θ spectrum. The XRD analysis enables to identify the material without destroying the sample.

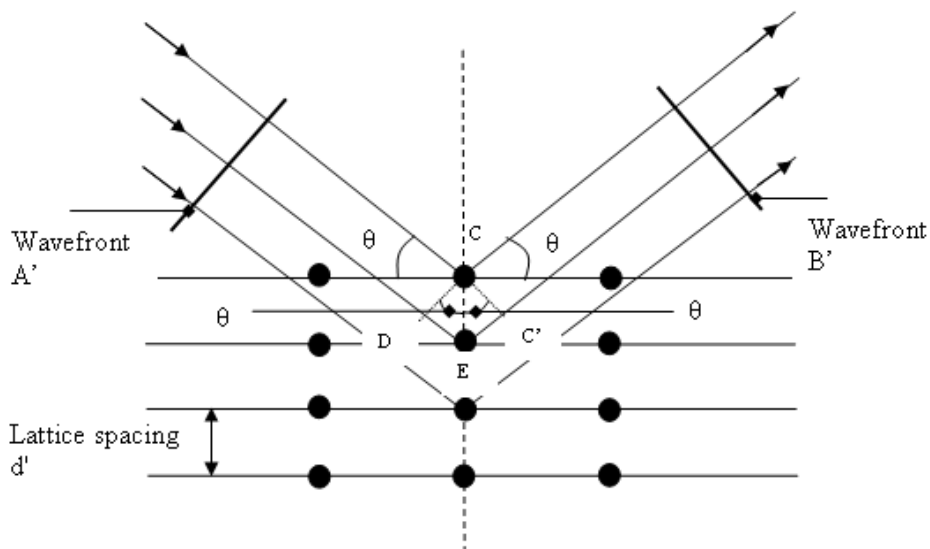


Figure 3-8. An X-ray diffraction beam schematic [177], showing the incident and scattered X-rays, from a pair of atoms in different lattice planes.

Figure 3-9 shows a photograph of the Bruker D8 X-ray diffractometer (XRD) operating with monochromatic high-intensity Cu K α ($\lambda = 0.154$ nm) radiation and a PSD detector which was used to characterise the thin films and the powder samples.



Figure 3-9. Photograph of the Bruker D8 X-ray diffractometer used in this study, the X-ray source is on the left, the sample is in the middle and the detector is on the right.

3.2.2 Raman spectroscopy

Raman spectroscopy is a technique used to collect a unique chemical fingerprint of molecules by observing inelastic (Raman) scattering from the sample. Here, the incident laser photons interact with the molecules and the scattered photons are shifted in frequency. Since each molecule has a unique set of vibrational energy levels, the emitted scattered photons show characteristic wavelength shifts. In Raman spectroscopy, the intensity of the emitted photons is recorded against the wavenumber to identify the corresponding molecules in a sample. The different peaks in the spectrum correspond to different Raman excitations which are important in materials characterization.

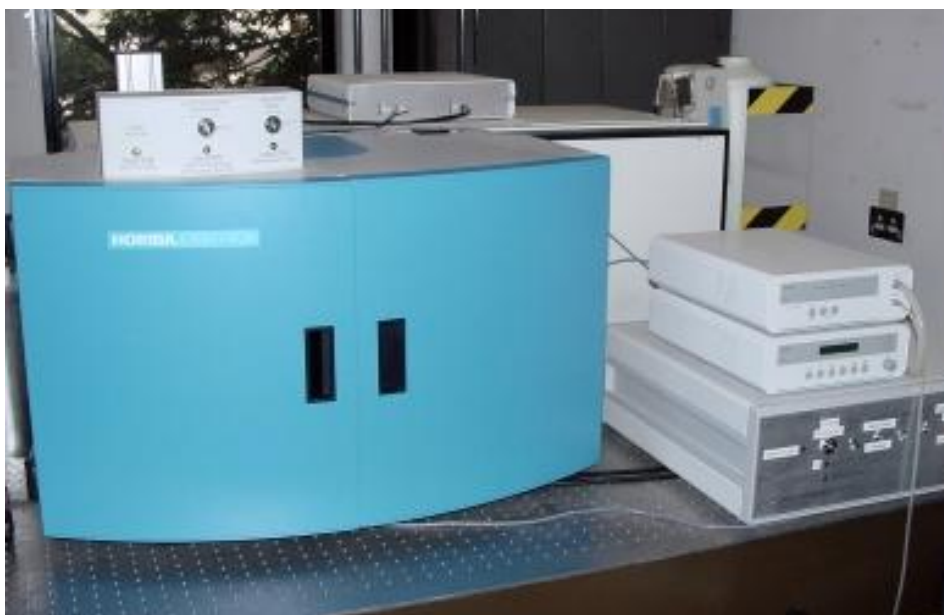


Figure 3-10. HORIBA Jobin Yvon LabRAM HR (with 632.8 nm He-Ne laser) Raman Spectrophotometer.

Raman spectroscopy was performed using a HORIBA Jobin Yvon LabRAM HR (with 632.8 nm He-Ne laser) Raman spectrophotometer (Figure 3-10) (HORIBA Jobin Yvon Ltd., Middlesex, UK). The spectra were obtained in the range of 100 to 1200 cm^{-1} .

3.2.3 Field emission gun scanning electron microscopy

A field emission gun scanning electron microscopy (FEG-SEM) is a type of electron microscope that produces images of a sample by scanning it with a focused beam of high-energy electrons (figure 3-11). The high-energy electrons interact with atoms in the sample, producing various signals which contain information about the sample's surface topography, orientation and composition.

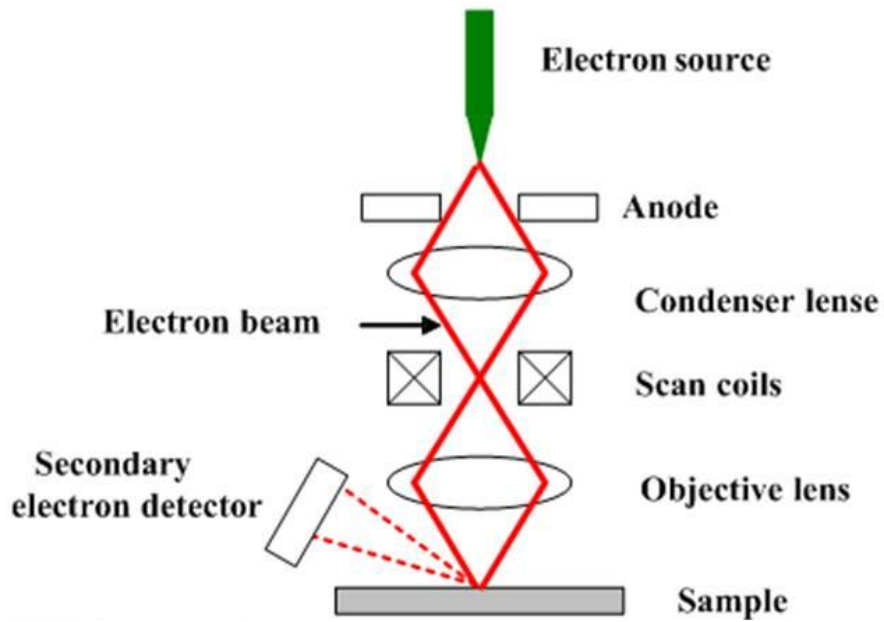


Figure 3-11. A schematic diagram of scanning electron microscope.[178]

The incident electron beam is scattered in the sample, both elastically and inelastically and gives rise to various signals such as secondary electrons, backscattered electrons, auger electrons, X-rays and cathode luminescence (figure 3-12).

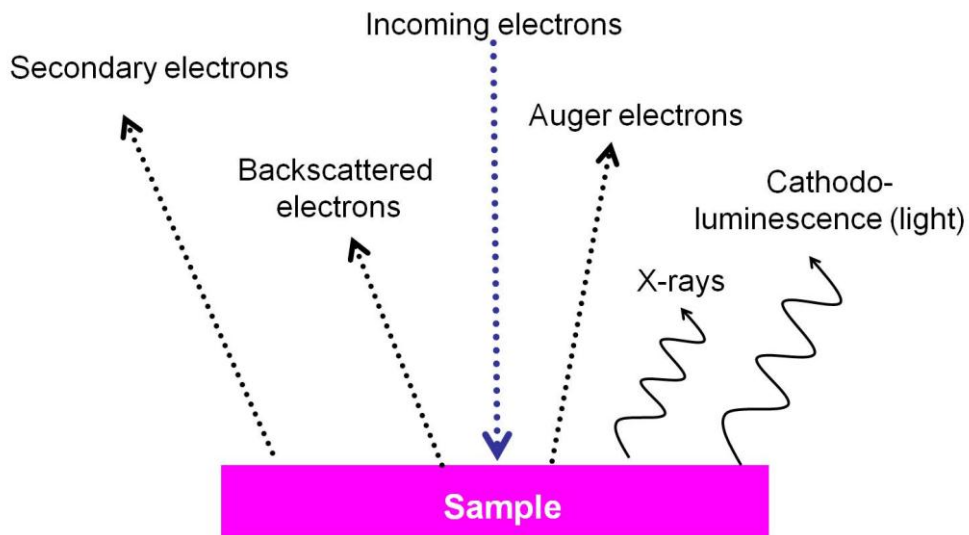


Figure 3-12. The elastically and inelastically scattering of incident electron beam.

FEG-SEM equipment mainly detects secondary electrons that result from interactions of the electron beam with atoms at or near the surface of the sample. In the standard secondary electron imaging mode, the FEG-SEM can produce very high-resolution images of a sample surface, revealing details less than 1 nm in size. Due to the very narrow electron beam, FEG-SEM surface topographic images have a large depth of field yielding a characteristic three-dimensional appearance useful for understanding the surface structure of a sample.



Figure 3-13. Leo 1530 VP FEG-SEM set-up.

The surface topographical images of samples and cross-sectional images of thin films were taken by a Leo 1530 VP FEG-SEM, Jeol Hertfordshire, UK (figure 3-13), with an accelerating voltage of 5 kV, and a working distance of 5 mm (this is the distance between the operating lens and the sample). The sample is required to be clean, vacuum compatible and electrically conductive. A thin layer of Pd-Au is sputter coated on to the surface of the

electrode to enhance the electrical conductivity of the samples. The system works by scanning the surface of the sample with a focused beam of electrons, which frees electrons from the atoms at the surface (from a depth of a few nm), as well as being reflected back from the sample. The secondary electrons are considered to be electrons with energies less than 50 eV. Secondary electrons are collected by an Everhard-Thornley detector and are converted in to a signal which is processed in to an image of the surface. Reflected electrons have energies greater than 50 eV and can be collected by a second detector. These electrons are commonly referred to as backscattered electrons and provide elemental analysis as elements with large atomic numbers generate a higher number of back scattered electrons than those with lower atomic numbers. When secondary electrons are knocked out of an inner energy orbital, the atom is left in an excited state, however as the atom relaxes an electron from a higher energy level may drop in to this orbital. In doing so, the electron releases energy which can be in the form of X-rays. As these X-rays are unique for each element, elemental analysis of the sample can be conducted.

3.2.4 UV-Vis optical absorbance

Optical absorbance measurements were conducted using a dual beam Perkin-Elmer Lambda 35 UV-Vis spectrometer (figure 3-14). Use of a dual beam allowed the absorbance to be automatically corrected, as a reference (in this case a plain FTO glass slide) was measured alongside the sample. The light source was provided by a tungsten and deuterium lamp with wavelengths ranging from 900 nm to 300 nm, so that infrared, visible and ultra violet regions of light were transmitted. The light passes through a series of slits and gratings before it is split in two equal beams (i.e. the dual beams). Consequently the light that passes to the samples travels in one direction and little scattering occurs. As the light travels through the sample, some of the light is absorbed by the various layers in the electrode. Light that is

transmitted is detected by the photodiode, which generates an electrical current proportional to the amount of light absorbed at different wavelengths, resulting in absorbance vs. wavelength spectrum.



Figure 3-14. Lambda 35 Perkin-Elmer UV-Vis spectrophotometer.

3.2.5 Incident photon to electron conversion efficiency

The incident photon to current conversion efficiency (IPCE) is determined by the light-harvesting efficiency, the quantum yield for electron injection to the conduction band of the semiconductor, and the collection efficiency of the electron at the back-contact.[179] IPCE is represented by the following equation,

$$IPCE = LHE \times \phi_{inj} \times \eta_c \quad (14)$$

where, LHE is the light harvesting efficiency, ϕ_{inj} is the electron injection efficiency and η_c is the electron collecting efficiency at back contact.

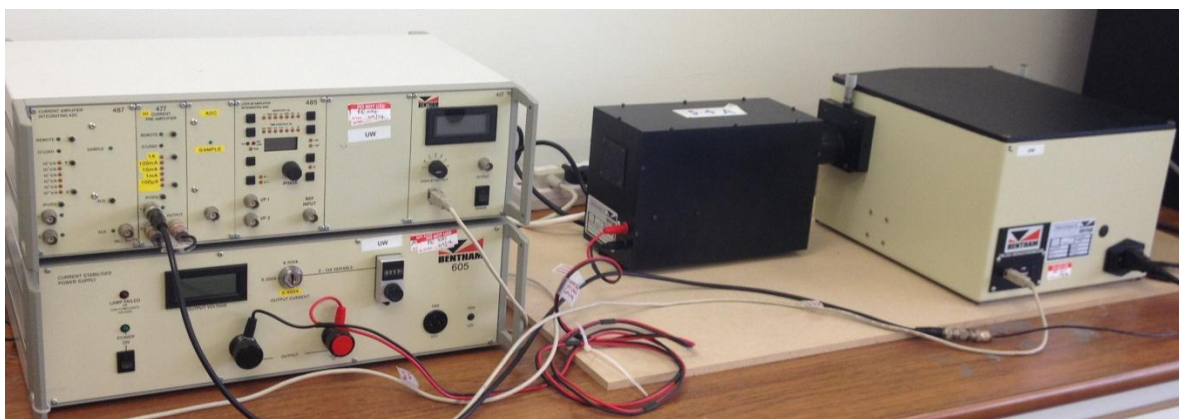


Figure 3-15. Xenon lamp, monochromator and lock-in amplifier of the IPCE set-up.

The IPCE was obtained by measuring the incident photon flux using a 75 W Xenon lamp connected to a monochromator (TMc300, Bentham Instruments Ltd., Berkshire, UK). The light was calibrated using a silicon photodiode. Photocurrent spectra were measured at a constant potential vs. Ag/AgCl using a combination of a lock-in amplifier (Bentham 485, Bentham Instruments Ltd., Berkshire, UK) and an in-house built potentiostat. Readings were collected at 5 nm intervals. The figure 3-15 shows the Xenon lamp, monochromator and lock-in amplifier used for the IPCE measurements.

3.2.6 Surface area measurements – dye adsorption-desorption studies

In order to find out the internal surface area of the deposited films, dye adsorption-desorption studies were performed. The surface area of thin films plays a significant role in determining the photoelectrochemical performance. Therefore, it is vital to estimate the internal surface area of electrodes after film fabrication and post treatment. Dye adsorption-desorption studies of TiO₂ and ZnO films were carried out by soaking the films in an ethanol solution of 1mM N719 dye for overnight.[180,181] Then the adsorbed acidic dye on the films was desorbed using NaOH solution. The concentration of the desorbed dye in a 0.1 M NaOH solution was recorded by measuring the absorbance (Lambda 35 Perkin-Elmer UV-Vis spectrometer).

Prior to recording the absorbance spectra, the solution was acidified by adding an appropriate amount of 0.1 M aqueous HCl solution. On the basis of the optical absorbance data of desorbed dye solution, the desorbed dye concentration was evaluated with the aid of the Beer-Lambert law (the extinction coefficient of the N719 dye at 525 nm, $\epsilon_{525} = 11,400 \text{ M}^{-1} \text{ cm}^{-1}$).^[182] Then, the total number of adsorbed dye molecules was calculated by taking into account the optical absorbance of desorbed dye solution at 525 nm. The surface area occupied by dye on a given film was determined by considering the area occupied by each dye molecule, 1.46 nm^2 .^[182] The internal surface area of the film was then estimated by taking into account the projected surface area of the electrode.

Chapter 4

Enhancement of Photoelectrochemical Performance of AACVD-produced TiO₂ Electrodes by Microwave Irradiation while Preserving the Nanostructure

4.1 Overview

TiO₂ electrodes are deposited on FTO-glass substrates at 350 and 400 °C by aerosol-assisted chemical vapour deposition (AACVD) and the deposited TiO₂ electrodes are irradiated with different microwave (2.45 GHz) power levels of 80, 200, 400, 800 W. These different power levels are equivalent to 10, 25, 50 and 100% microwave irradiation percentages of the furnace. The X-ray diffraction (XRD) reflections show that the deposited electrodes have the anatase phase TiO₂ oriented in the (101) direction, and the crystallinity of these electrodes increases after microwave treatment. Field emission gun scanning electron microscopy (FEG-SEM) surface topography analysis proves the preservation of the nanostructure after exposure to various percentages of microwave radiation. The photoelectrochemical (PEC) studies prove a threefold enhancement of photocurrent density of AACVD-produced TiO₂ electrodes after 100% microwave irradiation. This improved performance of PEC properties is attributed to improvements in the crystallinity and the particle-necking properties. The results presented demonstrate that microwave processing is a promising alternative method to conventional sintering for TiO₂ photoanodes.

4.2 Introduction

Titanium dioxide (TiO_2) is one of the most interesting semiconductor materials because of its excellent optical[183], electrical[184], photocatalytic[185], and thermal properties.[186] Interest in TiO_2 is mainly due to its non-toxicity and good stability in various environments.[187,188] TiO_2 is a wide band gap semiconductor that is transparent to visible light and has excellent optical transmittance which makes it a promising candidate for optoelectronic devices.[189,190] Conversion efficiencies of TiO_2 photoelectrodes have remained relatively low, mainly due to the slow charge transfer kinetics and low light absorption properties resulting from poor adherence between individual particles and particle-substrate.[191] Sintering may be considered to be the main process which improves the particle connections. TiO_2 can be deposited at high temperatures using methods such as atmospheric pressure chemical vapour deposition (APCVD)[192,193], aerosol assisted chemical vapour deposition (AACVD)[194], and spray pyrolysis[195]. However the major drawback of these deposition techniques is the particle growth and consequent collapse of the nanostructure as a result of the conventional annealing treatment.[196] This decreases the porosity and effective surface area which in turn affect the photoelectrochemical (PEC) performance.

It is very important to obtain particle-to-particle connections on the nanometer scale in order to fabricate efficient optoelectronic devices.[197] Particle interconnection (or necking) improves the electrical contact and conductivity of nanoparticle-based thin films which enhance the charge transfer properties and performance of the resulting electrodes.[198] The use of conventional sintering for materials processing, however, causes changes to the nanostructure and physical nature, which may lead to poor PEC performance.

Microwave processing is a relatively novel technique that offers new approaches to improving the physical properties of materials, as well as having economic advantages such as energy savings and accelerated product development.[199] There has been considerable interest in microwave processing on advanced semiconducting materials.[200,201] Meek and Blake [202] showed a significant difference between conventional and microwave processing of oxide ceramics. The microwave heat treatment of TiO₂ has been studied by Xie et al.[203] and they found that the microwave-sintered samples were densified more rapidly and at a much shorter time and lower temperature than that of the conventionally sintered samples. Similarly, Yarahmadi et al.[196] claimed that the improved PEC performance is attributable to the lower processing temperatures and rapidity of the microwave method that help to retain the nanostructure of the thin films whilst improving the degree of crystallinity of microwave-treated iron oxide films. However, to the best of our knowledge, there is very little literature available on the microwave processing of nanocrystalline TiO₂ thin films for the improvement of PEC performance. This chapter shows that microwave treatment of AACVD-produced TiO₂ electrodes appears to be an effective method of improving the electrode crystallinity without affecting its nanostructure, resulting in a significant improvement in the TiO₂ PEC characteristics.

The objective of this study is to compare the effect of microwave annealing on the PEC properties of TiO₂ photoelectrodes prepared at 350 and 400 °C by AACVD. The results obtained in this study show an enhanced PEC performance of TiO₂ electrodes on exposure to various percentages of microwave radiation (2.45 GHz). This improved performance in photocurrent density is attributed to improvements in the crystallinity and the particle-necking properties. The results demonstrate that microwave processing is a promising alternative to conventional sintering for TiO₂ photoanodes, providing the electrodes with increased photocurrent densities for various electronic and optoelectronic applications.

4.3 Experimental

Nanocrystalline TiO₂ films were prepared on FTO-glass substrates (1 cm × 2 cm) (TEC 8 Pilkington, 8 Ω/sq.) at temperatures of 350 and 400 °C by the AACVD technique.[204] Titanium(IV) isopropoxide (Sigma-Aldrich) (2.85 g) precursor was added to a mixture of toluene (80 mL) and ethanol (20 mL) in order to obtain a 0.1 M solution of the precursor in 100 mL volumetric flask. The AACVD-produced films were treated with various microwave power levels (80, 200, 400, 800 W) [which is equivalent to 10, 25, 50, 100% of microwave radiation percentages] for 20 min, using a microwave furnace (MRF 16/22, Carbolite Ltd, UK) operating at a frequency of 2.45 GHz. The photoelectrochemical properties of the TiO₂ electrodes were measured using a standard, three-electrode electrochemical cell fitted with a quartz window. The reference and counter electrodes were Ag/AgCl and Pt, respectively. All the measurements were carried out in 0.1 M Na₂SO₄ aqueous electrolyte at 298 K. Current-voltage measurements of the cells were carried out using a potentiostat (Eco Chemie micro-Autolab type III) under illumination from a halogen lamp at 100 mW cm⁻² light intensity, calibrated by a solar pyranometer (Solar Light Co., PMA2144 Class II). Surface morphology of the TiO₂ films was studied using a Leo 1530 VP FEG-SEM at an accelerating voltage of 5 kV and a working distance of 5 mm. Phase and crystallinity of the electrodes were characterized using a Bruker D8 XRD operating with monochromatic intensity Cu K_α ($\lambda = 1.54 \text{ \AA}$) radiation using a PSD detector. All the measurements were repeated at least three times to check the consistency and repeatability of the results.

4.4 Results and Discussion

TiO₂ electrodes with two different morphologies were deposited by AACVD at 350 and 400 °C to study the effect of microwave annealing on the structure, texture, morphology and

PEC performance. The electrodes deposited at 350 °C showed a morphology with rod-like features randomly oriented throughout the film, while the electrodes deposited at 400 °C demonstrated a granular morphology with nanoparticles sintered together to form clear, cauliflower-like features. It is well established that changing the temperature in AACVD experiments is very effective at changing the morphology and structure of the deposited thin films.[205,206] Unlike conventional sintering, microwave sintering preserves the nanostructure while improving the electrode performance.

4.4.1 XRD characteristics

The phase and crystallinity of the deposited films before and after microwave treatment has been studied by XRD. Figures 4-1 and 4-2 show XRD diffractograms of the TiO₂ thin films deposited at 350 and 400°C before (0%) and after microwave annealing at 10%, 25%, 50%, and 100% irradiations.

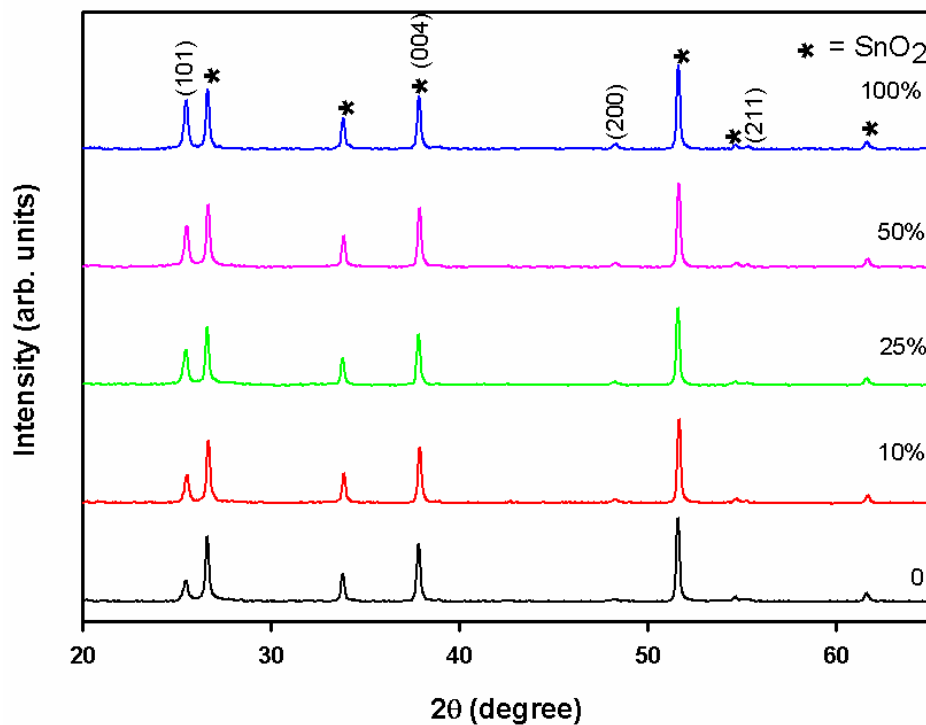


Figure 4-1. XRD diffractograms of TiO₂ electrodes deposited by AACVD at 350 °C and treated with different % of microwave radiation.

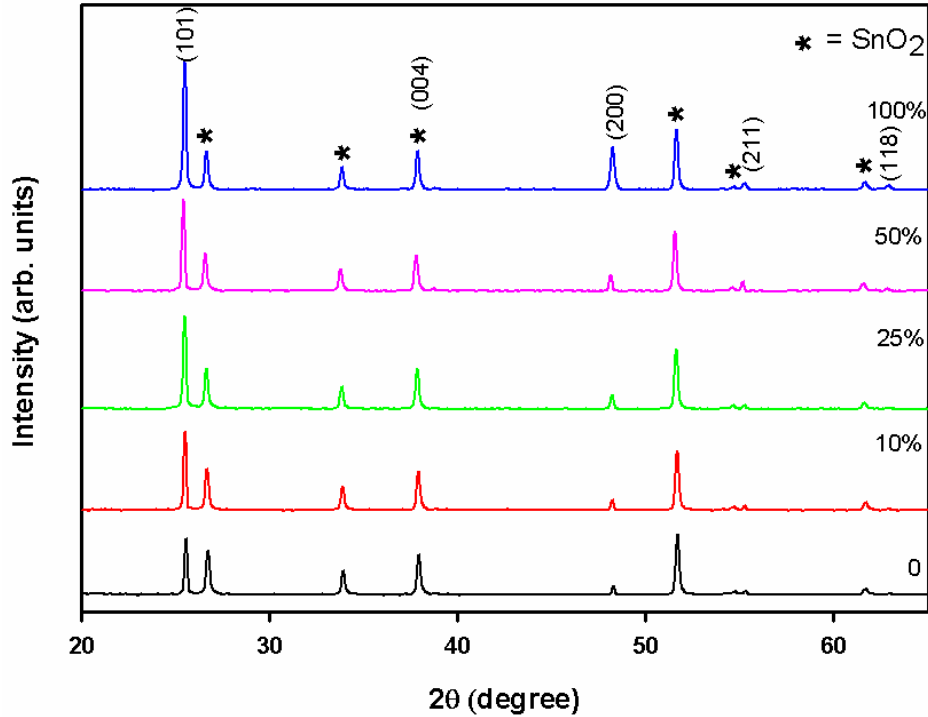


Figure 4-2. XRD diffractograms of TiO_2 electrodes deposited by AACVD at 400°C and treated with different % of microwave radiation.

The XRD diffractograms show reflections from the dense SnO_2 coating of the FTO substrate along with strong reflections of TiO_2 . The reflections indexed by (*) correspond to the SnO_2 layer of the FTO substrate. XRD analysis shows that the deposited films have a crystalline structure of the anatase phase oriented in the (101) direction. The diffraction reflections at 2θ values of 37.75° correspond to both TiO_2 (anatase) and SnO_2 . The XRD diffractograms also show that the films are oriented in the (101) direction. The higher intensity of reflections at 2θ values of 37.75° is due to the overlapping of SnO_2 reflections.

The overall XRD reflection of anatase remains unchanged after microwave treatment, but a slight increase in the reflection intensities has been observed, which we believe is due to the partial conversion of the amorphous TiO_2 phase to anatase crystallites. Anatase to rutile phase conversion is very common in TiO_2 . [207] Many researchers have found that anatase to rutile phase transition begins above 400°C . [208] In the current study, it was found that the anatase phase remains unchanged after annealing under microwave radiation, however it improves

the PEC performance of the deposited films. The XRD results proved that the microwave treatment is a promising alternative to traditional sintering for TiO₂ photoanodes in order to enhance the optoelectronic properties by increasing the crystallinity and particle connections while keeping the phase and orientation unaltered.

4.4.2 Morphological properties

The FEG-SEM images show the surface morphology of two sets of AACVD-produced TiO₂ electrodes treated with different microwave percentages. Figures 4-3 to 4-6 show the randomly oriented, rod-like structure and Figures 4-7-4.10 indicate the granular morphology of TiO₂ crystallites deposited at 350 °C and 400 °C, respectively, and treated with 25%-100% microwave radiation (i.e. 200 to 800 W). At higher microwave percentages, these TiO₂ crystallites grow and sinter to form well interconnected crystalline structures. In Figures 4-6 and 4-10 images show the change of rod-like orientation to ordered TiO₂ crystallite orientation, and granular morphology to sintered cauliflower-like structures, respectively. The cross-sectional image of AACVD-produced TiO₂ electrodes deposited at 400 °C is shown in figure 4-11. The image shows that the deposited TiO₂ film thickness is around 1 μm which is higher than the penetration depth of TiO₂ (i.e. 0.5 μm). It is clear that microwave radiation improves the crystal growth and crystallite necking properties to form highly porous crystallites which contribute to increase electrode-electrolyte interfaces throughout the electrode surface. Therefore, the resulting structural orientations with the microwave irradiation will favour electrolyte to be in contact with the electrode, which may be directly involved in improving the charge transfer kinetics of the electrode. SEM images clearly show that microwave irradiation enhanced the particle connections and porosity with a slight change in the nanostructure, which cannot be achieved with conventional sintering techniques. Therefore, microwave treatment of TiO₂ electrodes shows a good degree of crystallinity and

porosity while retaining the nanostructure, which promotes the photocurrent density of the electrodes.

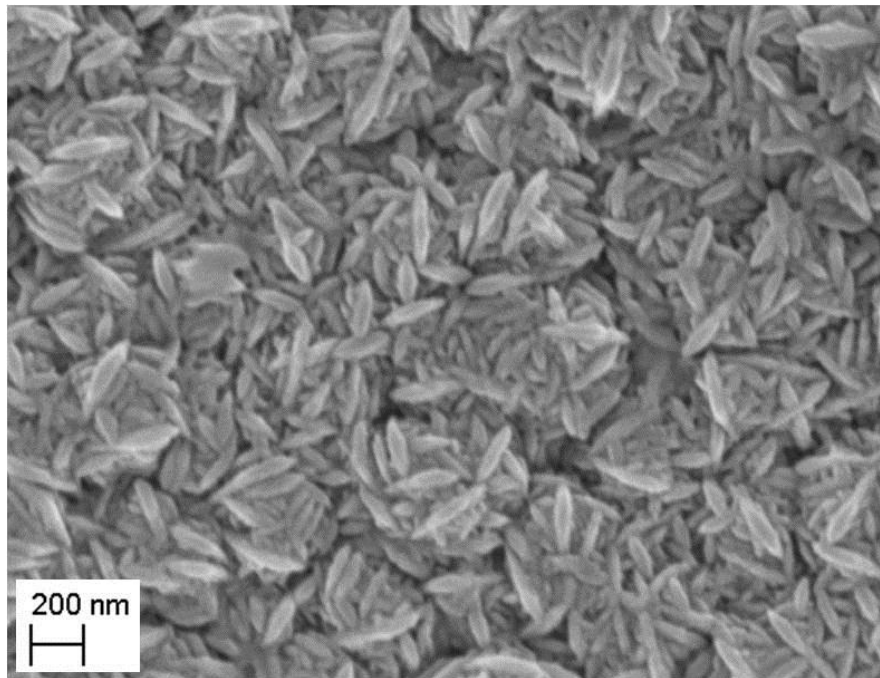


Figure 4-3. SEM image of AACVD-produced TiO₂ electrodes deposited at 350 °C and treated under 0 % microwave radiation.

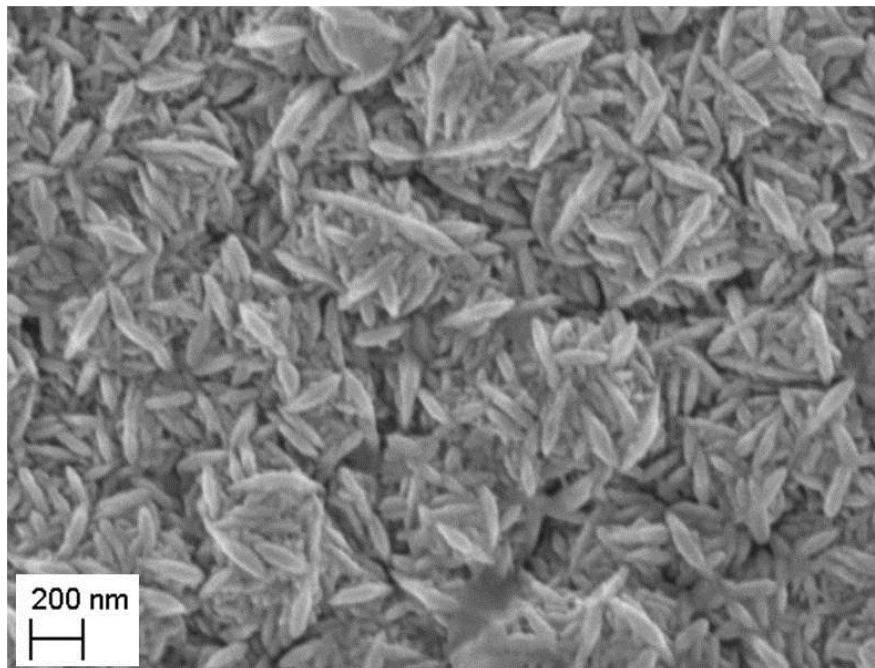


Figure 4-4. SEM image of AACVD-produced TiO₂ electrodes deposited at 350 °C and treated under 25 % microwave radiation.

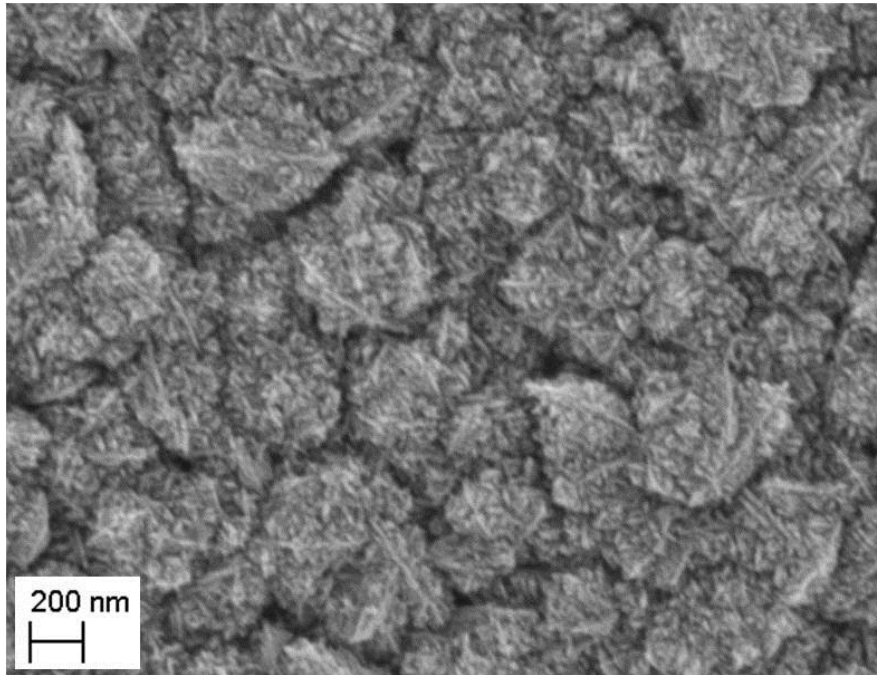


Figure 4-5. SEM image of AACVD-produced TiO₂ electrodes deposited at 350 °C and treated under 50 % microwave radiation.

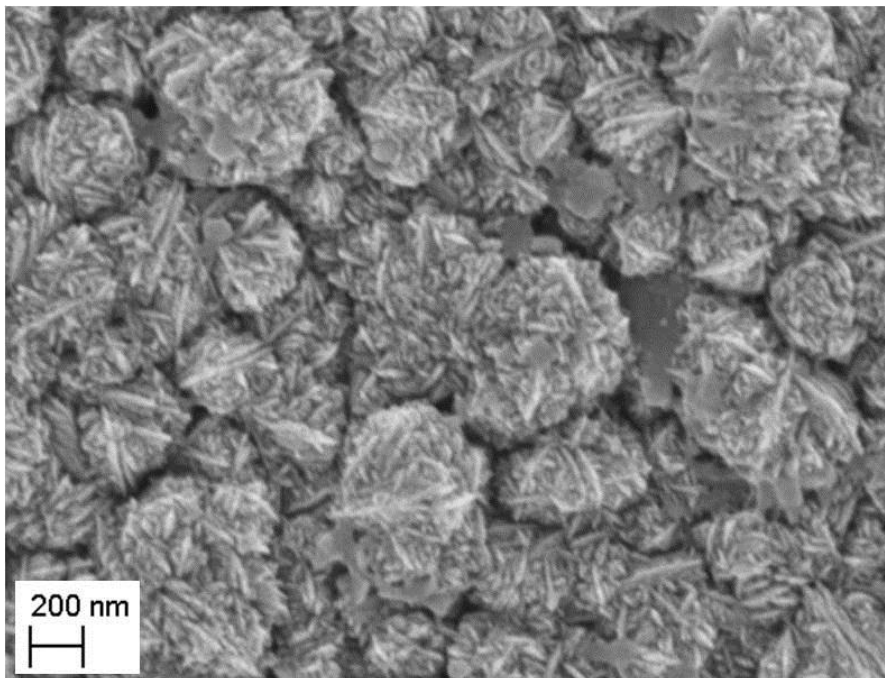


Figure 4-6. SEM image of AACVD-produced TiO₂ electrodes deposited at 350 °C and treated under 100 % microwave radiation.

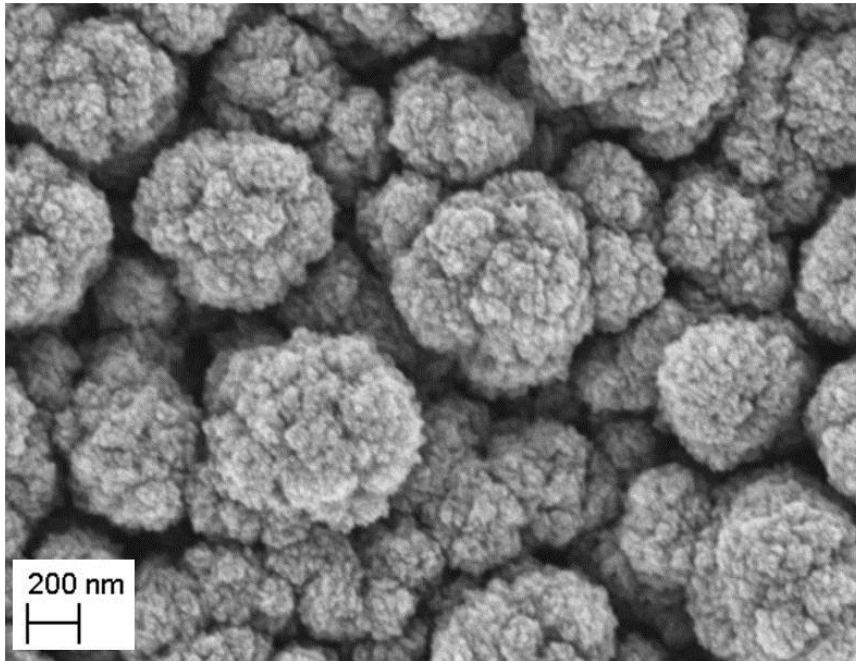


Figure 4-7. SEM image of AACVD-produced TiO_2 electrodes deposited at $400\text{ }^\circ\text{C}$ and treated under 0 % microwave radiation.

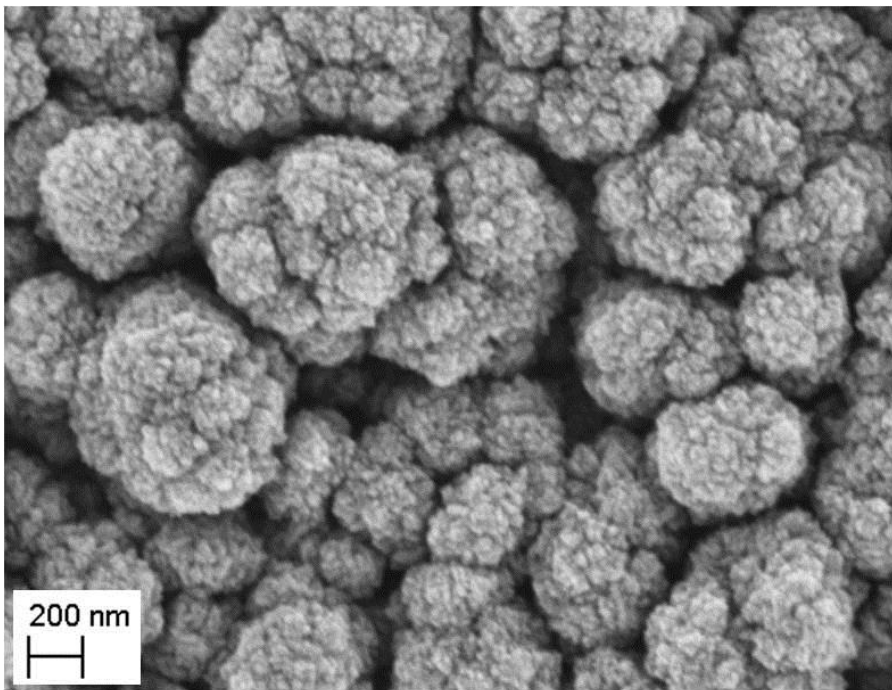


Figure 4-8. SEM image of AACVD-produced TiO_2 electrodes deposited at $400\text{ }^\circ\text{C}$ and treated under 25 % microwave radiation.

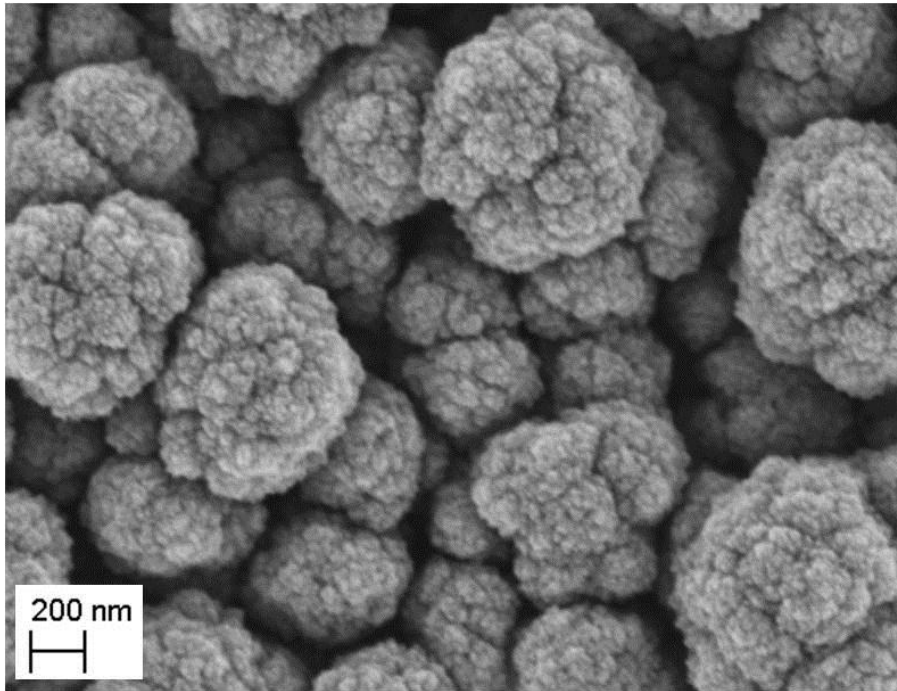


Figure 4-9. SEM image of AACVD-produced TiO_2 electrodes deposited at $400\text{ }^\circ\text{C}$ and treated under 50 % microwave radiation.

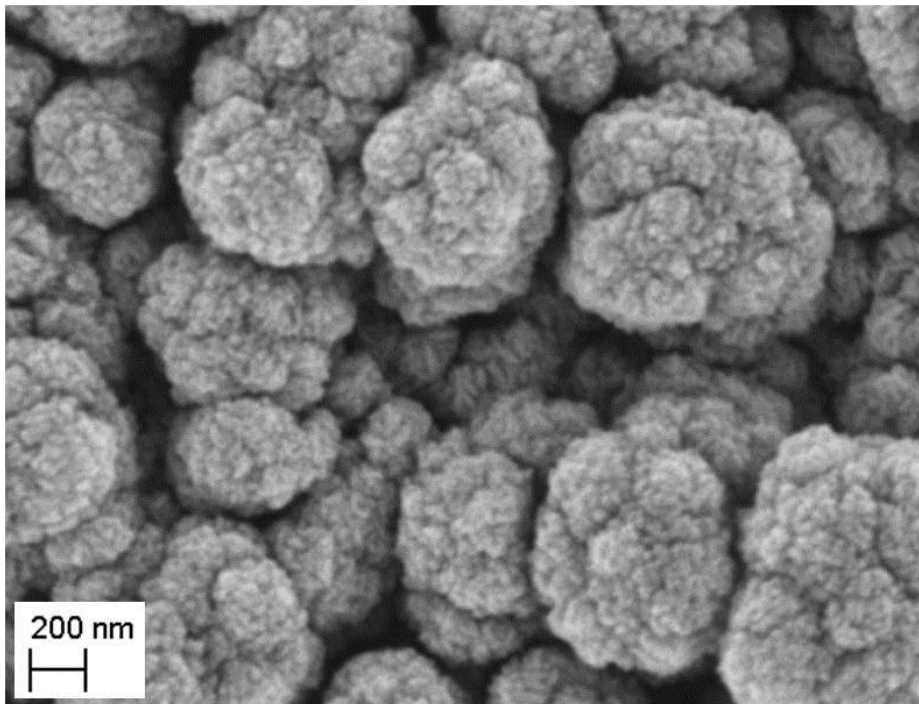


Figure 4-10. SEM image of AACVD-produced TiO_2 electrodes deposited at $400\text{ }^\circ\text{C}$ and treated under 100 % microwave radiation.

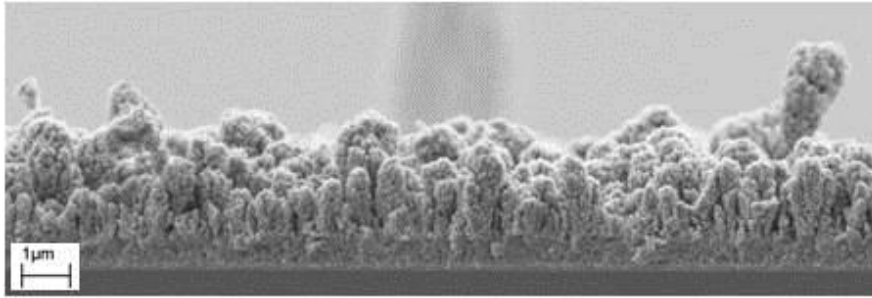


Figure 4-11. Cross-sectional image of AACVD-produced TiO₂ electrodes deposited at 400 °C and treated under 100 % microwave radiation.

4.4.3 Photoelectrochemical properties of electrodes

It is well known that Photoelectrochemical (PEC) performance of many semiconductor electrodes suffers from poor minority carrier collection and slow interfacial charge transfer reactions under illumination (often referred to as ‘the kinetic bottleneck’). The hole collection can generally be improved by having electrodes, fabricated with nanostructured fine texture, in which the feature size is comparable to the hole-diffusion length.[209] Modifying the electrode texture in such a way to improve the inter-particle connections is essential for better PEC performance of the electrode. The better inter-particle connections in the electrode may lead to a reduction in the recombination (in grain boundaries) and improve the charge collection efficiency. It has been proven in the literature that semiconducting electrodes deposited by AACVD have a better performance than those deposited using other techniques as this method allows one to control the nanostructure of electrodes.[210,211] In this study, we found that the PEC performance of TiO₂ electrodes can be enhanced by microwave irradiation. Electrodes deposited by AACVD showed two different morphologies; a compact film (deposited at 350 °C), and a relatively porous film with cauliflower-like features deposited at 400 °C. These were then exposed to different percentages of microwave irradiation. Figures 4-12 and 4-13 show the current-voltage (J-V) characteristics in 0.1 M Na₂SO₄ electrolyte for the TiO₂ electrodes deposited by AACVD at 350 and 400 °C before

(0%) and after microwave irradiation at 10, 25, 50% and 100% power levels respectively. The illumination was chopped manually to reveal the light and dark current. The photocurrent shows anodic behaviour, and the dark current is negligible up to 0.7 V vs. Ag/AgCl, beyond which it is dominated by the oxygen evolution. No photocurrent saturation is observed indicating strong recombination under depletion. The sharp anodic and subsequent cathodic spikes in the photocurrent transients indicate that the recombination is relatively high in the region where the space charge layer width is narrow. It is believed that, during AACVD in the low substrate temperature regime, the decomposition was incomplete and, as a result, the nanocrystals became rich in defects, leaving dislocations and kink sites. These dislocations and kink sites may act as the recombination centres for the photogenerated electron-hole pairs and consequently show poor photocurrent density. The exposure of electrodes to microwaves reduced these defects and improved the inter-particle connections while preserving the nanostructure. The improved PEC performance after microwave treatment can also be attributed to the increased orientation of crystallites in the (101) direction. Batzill [212] has proved that, on anatase (101) the water-oxygen bonds to a five-fold Ti surface atom, and the surface geometry allows both hydrogen atoms of the water molecule to form hydrogen bonds with two-fold surface oxygen atoms at the same time, and this orientation is quite active for water splitting. The XRD analysis also shows an improvement in the (101) direction after microwave treatment, which also contributes to the enhanced PEC performance of the deposited electrodes.

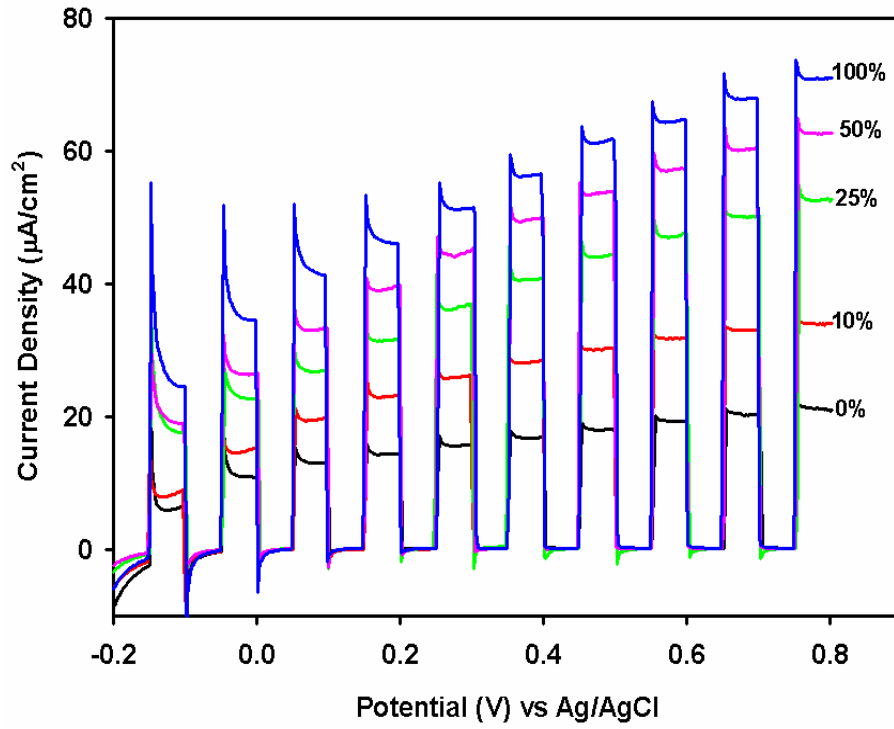


Figure 4-12. J-V Characteristics of TiO₂ photoelectrodes fabricated at 350 °C and irradiated under various % microwaves.

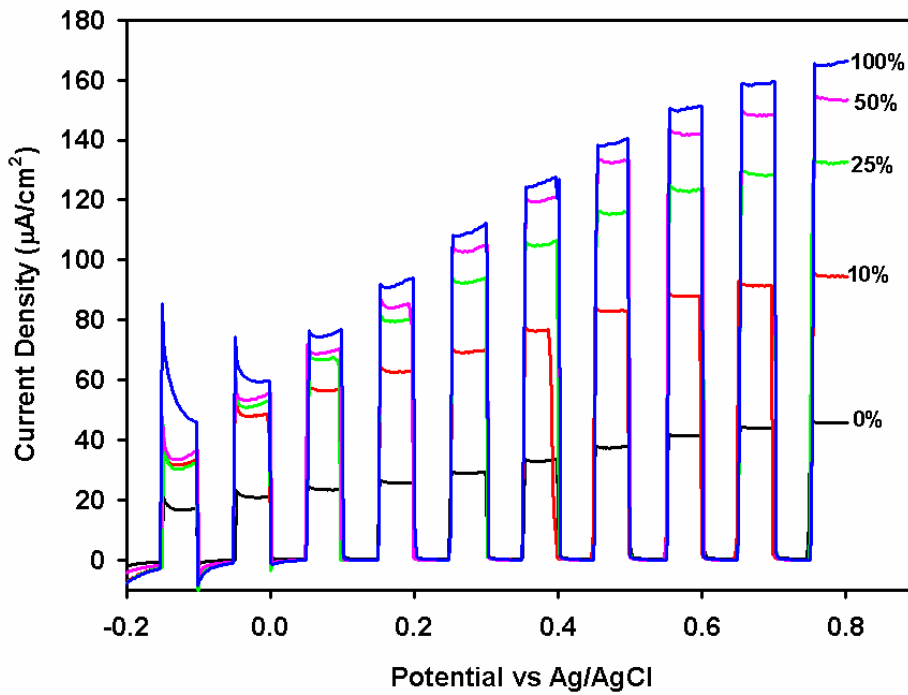


Figure 4-13. J-V Characteristics of TiO₂ photoelectrodes fabricated at 400 °C and irradiated under various % microwaves.

Figures 4-14 and 4-15 show the current-voltage characteristics in 0.1 M Na₂SO₄ electrolyte for the TiO₂ electrodes before (0%) and after microwave irradiation at 100% (800 W) for the electrodes deposited by AACVD at 350 and 400 °C respectively. It is clear that the photocurrent density trebled when the electrodes were irradiated with 100% microwave radiation. The corresponding incident photon to current conversion efficiency (IPCE) plots are shown in figure 4-16 and agree well with the observed photocurrent densities. The enhancement in the photocurrent density with the different microwave power levels is summarized in figure 4-17.

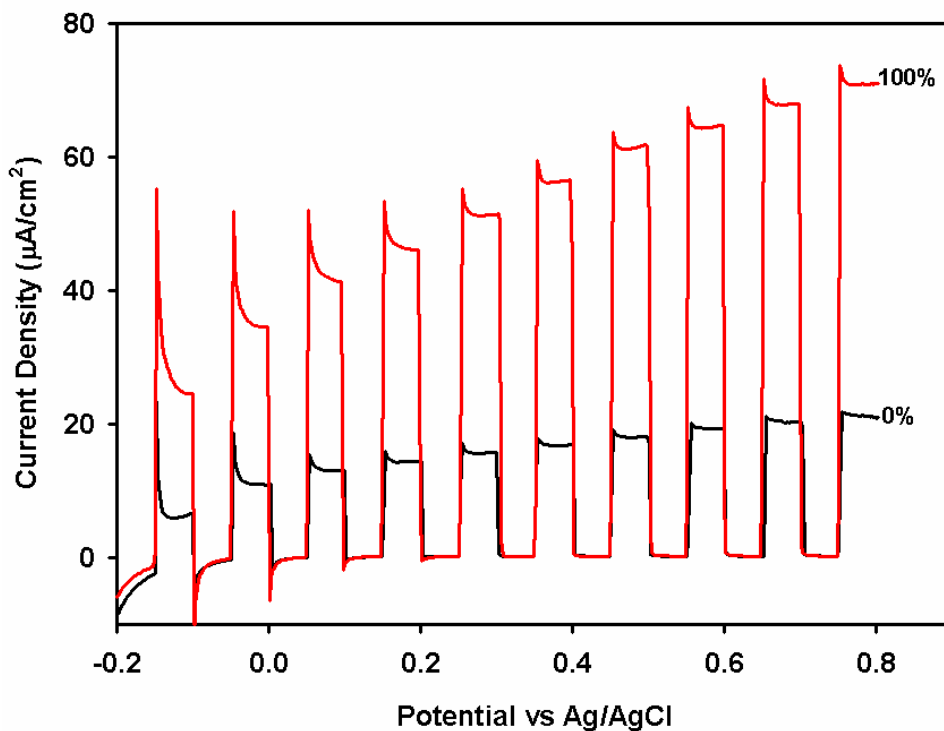


Figure 4-14. J-V characteristics of TiO₂ photoelectrodes fabricated at 350 °C under various percentages of microwave irradiation (2.45 GHz) [The data has been taken from figure 4.11].

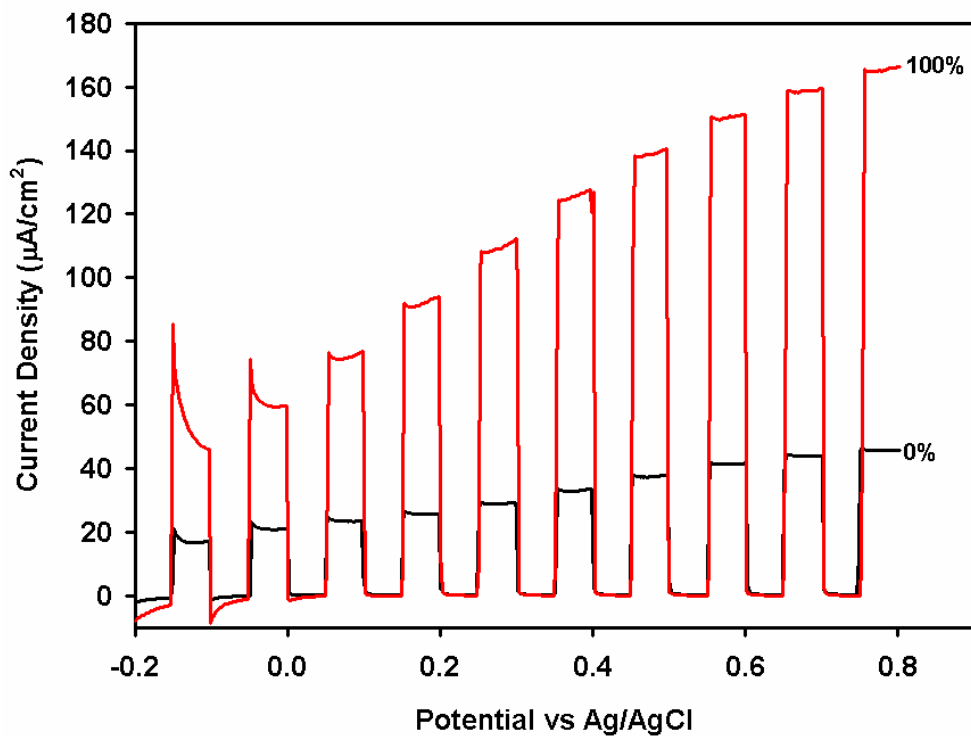


Figure 4-15. J-V characteristics of TiO₂ photoelectrodes fabricated at 400 °C under various percentages of microwave irradiation (2.45 GHz) [The data has been taken from figure 4.12].

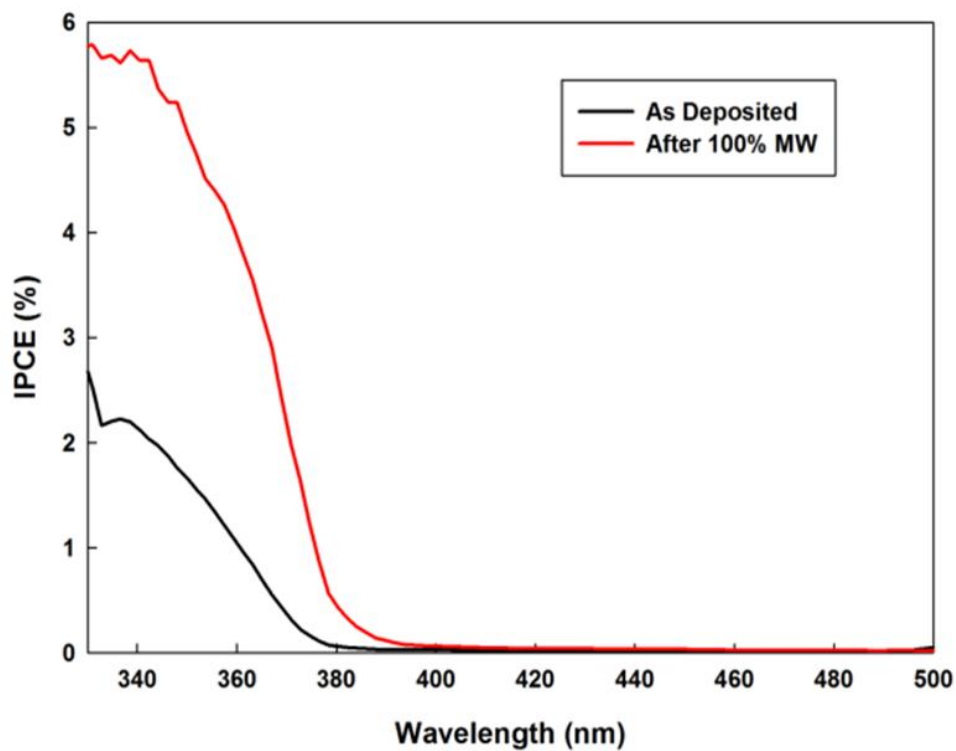


Figure 4-16. IPCE plots for as deposited film at 400 °C and after 100 % microwave treatment.

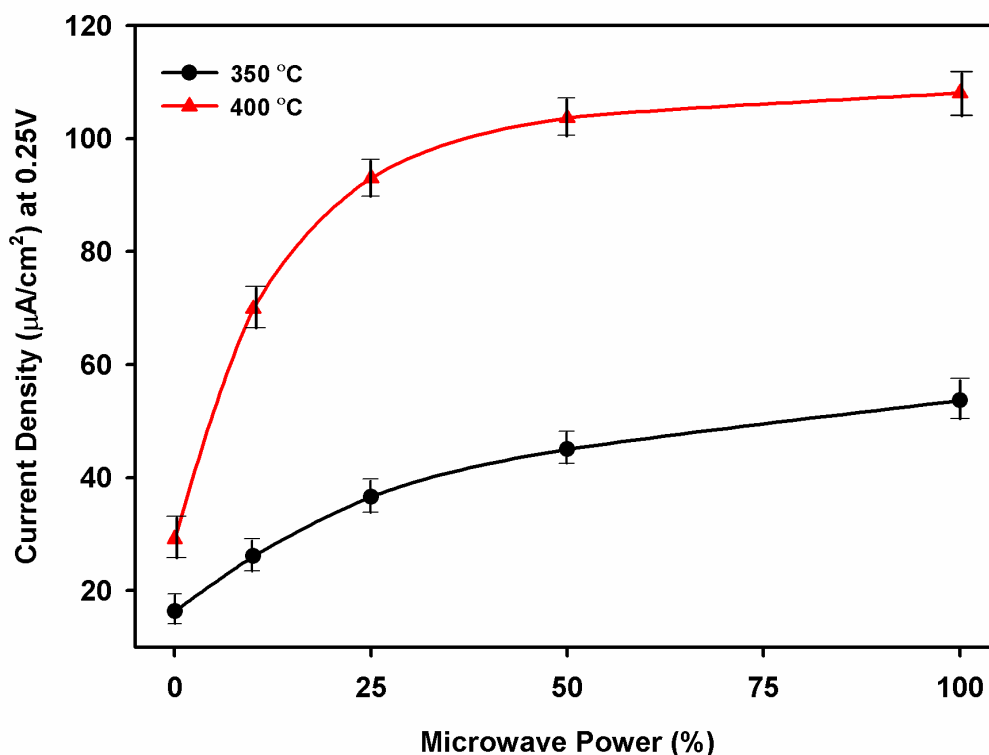


Figure 4-17. The variation of the photocurrent density of AACVD deposited TiO₂ electrodes at 350 °C and 400 °C against microwave power level.

The effect on the photocurrent density under conventional thermal annealing and microwave annealing is compared based on the corresponding J-V plots at same power level (Figure 4-18). The temperature-time profiles for each of the heat treatment methods are also constructed in order to find out the energy efficiencies of each process. The temperature-time profile of each electrode for the same power conditions is shown in figure 4-19. Under the same power levels, the area under the temperature-time plot gives an idea about the energy consumption by the furnace. The temperature-time profile clearly indicates reduction of post annealing temperature when using microwave radiations compared to conventional heating method. Microwave irradiation is a faster processing method which can be applied on an industrial scale. Furthermore, eco-friendly microwave annealing saves more than 70% of the total energy (figure 4-19).

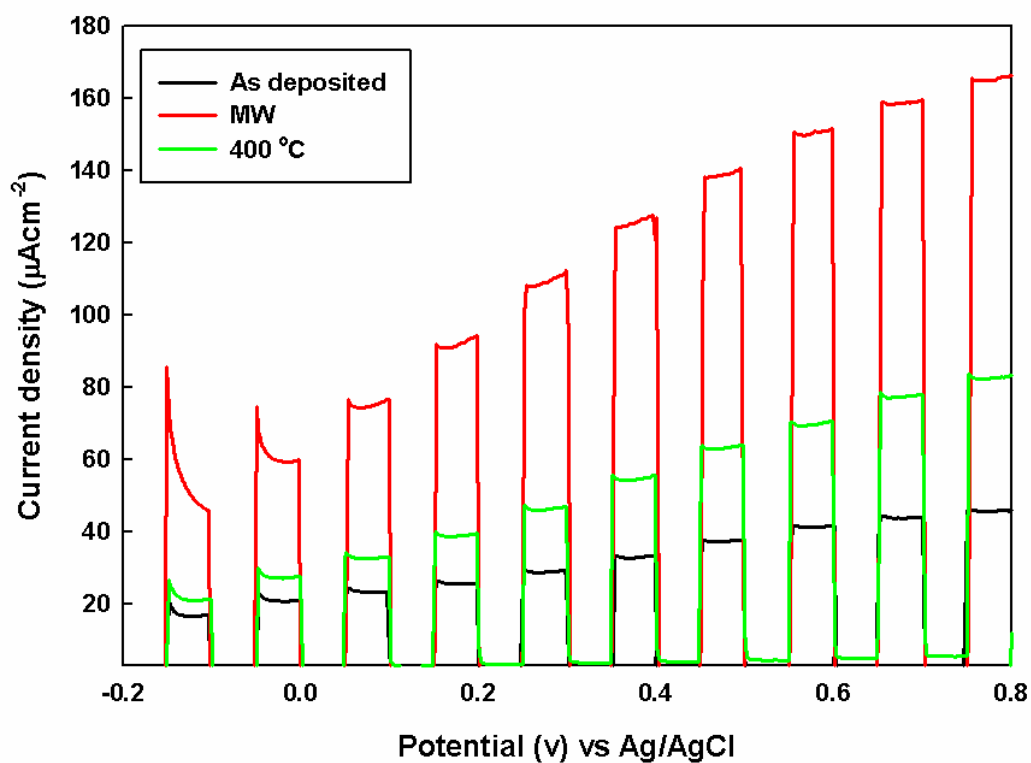


Figure 4-18. Variation of the photocurrent density against microwave and conventional annealing.

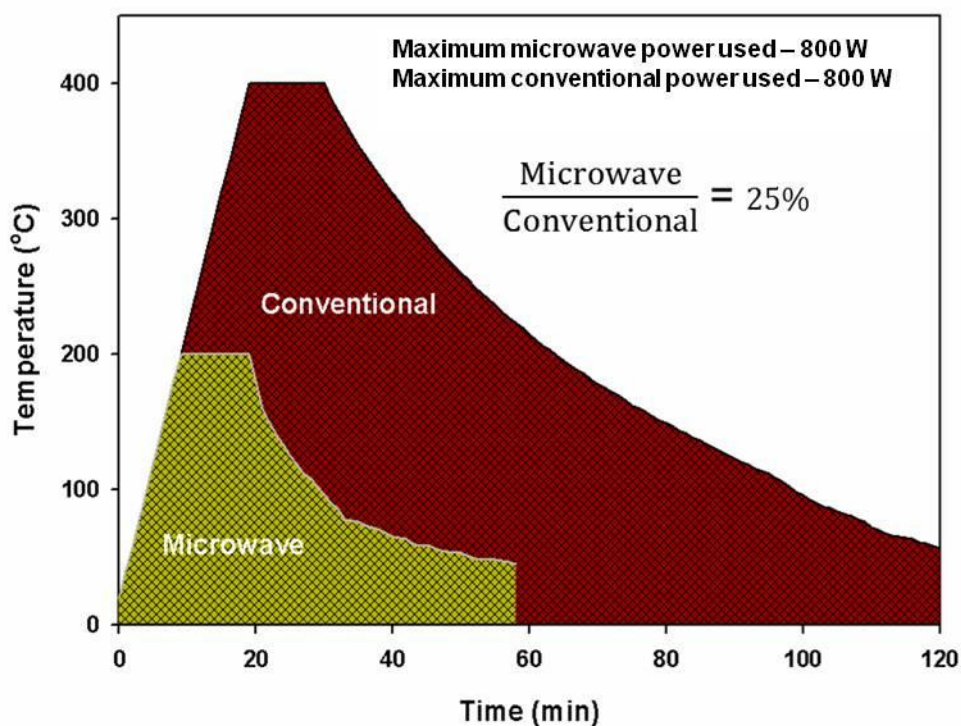


Figure 4-19. Temperature- time profile of microwave and conventionally deposited samples at 400 °C at the same power conditions

4.5 Conclusions

AACVD was used to deposit TiO₂ electrodes on FTO-glass substrates at 350 and 400 °C. The deposited electrodes were irradiated with various percentages of microwave radiation (10, 25, 50, and 100%) and the electrodes showed improved PEC performance when subjected to increased microwave radiation. XRD analysis confirmed that the deposited films show the anatase phase of TiO₂ oriented in the (101) direction. XRD analysis also shows an improvement in the crystallinity of the electrodes after microwave treatment. The surface topographical analysis shows that the nanostructure and texture of the films are less affected after microwave treatment. The *J-V* characteristics showed a three-fold increase in the photocurrent density after microwave treatment. The results demonstrate that microwave treatment is a promising alternative to conventional sintering for TiO₂ electrodes to enhance the optoelectronic performance while keeping the texture and nanostructure unaltered, and we believe that this method can open up a new research strategy for the engineering of the properties of semiconductor materials.

Chapter 5

Hierarchical ZnO nanorod electrodes: Effect of post annealing on structural and photoelectrochemical performance

5.1 Overview

Zinc oxide (ZnO) nanorods were deposited on ZnO seeded fluorine doped tin oxide (FTO) glass substrates by chemical bath deposition and the deposited films were treated under microwave irradiation and conventional thermal annealing. XRD diffractograms revealed that there is no significant difference in the film crystallinity. FEG-SEM images of microwave irradiated ZnO nanorods indicate that microwave radiation caused sintering between individual rods and bundling them up thereby creating new rods with large diameter, without significantly affecting the hierarchical rod structures. It shows that the internal surface area of treated films decreased compared to that of as-deposited film. The photoelectrochemical characteristics showed a decrease in the current density of the treated films compared to that of as-deposited film. The reduction of the photocurrent corresponding to conventional thermal annealed ZnO electrodes is more pronounced presumably due to deformation of rod structure and poor charge transport.

5.2 Introduction

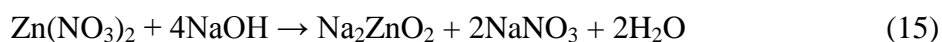
Synthesis of numerous ZnO nanostructures has recently attracted a significant interest due to their promising applications in solar cells,[181] transparent conducting film,[213] ultraviolet-protection films,[214] catalysis,[215] and gas sensors.[216] In particular, ZnO nanorods have received extensive attention in photonic, electronic, optoelectronic and electrochemical devices due to ease of fabrication at ambient conditions.[217]

Post-deposition heat treatment is one of the well-known processes that can be used to enhance electronic communication between substrate and electrode material by improving the adherence.[218] Conventional annealing using a furnace or hot plate is a common technique for the post-annealing of nano-materials containing electrodes.[219] A great deal of interest has been received in recent years for irradiation with microwaves as an alternative advanced material processing technique.[220,221] This technique is capable of improving particle necking and crystallinity with a minimum effect on the electrode texture which is due to the fact that microwave irradiation generates a completely different heating profile compared to that of conventional thermal heating. Microwave radiation interacts with lossy materials that result in rapid and uniform heating throughout the material which cannot be achieved by conventional thermal heating methods.[222] This in turns minimizes the thermal gradient, particle diffusion and the processing time.[223] It has also been reported that the materials fabricated using low temperature techniques contain certain amorphous regions that can be converted to crystalline phases by microwave irradiation without affecting the film texture (i.e. micro and nanostructure).[155] Processing materials under microwave irradiation is a relatively novel area of research and hence there is a scarcity of information in the literature. Therefore, further research is essential to understand the effect of microwave irradiation on processing of various materials.

This chapter focuses on the post annealing effect of ZnO nanorods by conventional thermal and microwave heat treatments on the structural and photoelectrochemical (PEC) properties. The results demonstrate that although the hierarchical texture of ZnO is retained to some extent during the microwave treatment, it reduces the internal surface area. Further, it appears that there is no significant advantage of the microwave treatment (i.e. improvements in contacts between rods and substrate by selective heating). As anticipated the conventional thermal heat treatment completely deforms the electrode texture thereby deteriorating the PEC performance.

5.3 Experimental

Fluorine doped tin oxide (FTO) glass substrates (TEC 8 Pilkington, 8 Ω /sq.) were cleaned and sonicated sequentially in acetone, ethanol and deionised water and stored in absolute ethanol. The effective area of the film was maintained at 1 cm². Aerosol assisted chemical vapour deposition (AACVD) was used to deposit a thin ZnO seed layer on FTO glass substrates at 400 °C using a precursor solution of 0.1 M zinc acetate (BDH Chemicals Ltd) in methanol. The deposition was carried out for 4 min and the thickness of the seed layer was in the order of 50-100 nm.[224] After deposition of the seed layer, electrodes were placed in a tube furnace and further annealed at 400 °C for 1 hour. The ZnO nanorods were grown on ZnO seeded FTO by chemical bath deposition (CBD) method using a mixture of 0.8 M sodium hydroxide (Fisher Scientific) and 0.02 M zinc nitrate (Sigma Aldrich) solution maintained at 80°C for 50 minutes. Reactions occurring during chemical bath deposition in the formation of ZnO nanorods on the surface of FTO-glass substrate at 80°C are as follows,[225]



Dried ZnO nanorod films were subjected to 100% microwave irradiation or conventional thermal annealing for 30 min using a microwave furnace (MRF 16/22, Carbolite Ltd, UK) operating at a frequency of 2.45 GHz and 2 kW power (during the heat treatments the temperature was maintained at 300 °C). The phase and crystallinity of as deposited and annealed ZnO nanorod films were studied using Bruker D8 XRD, operating with monochromatic Cu K α ($\lambda = 1.54 \text{ \AA}$) radiation and PSD detector. Topographic images for the as-deposited, microwave treated and conventionally annealed ZnO nanorods were taken using Leo 1530 VP field emission gun scanning electron microscopy at an accelerating voltage of 5 kV and a working distance of 6 mm. Surface areas of the films were investigated by conducting dye adsorption/desorption measurements.[226] The current-voltage characteristics of heat treated and untreated electrodes were studied by potentiostat (Eco Chemi micro-Autolab type III) by chopping the illumination from halogen lamp at 100 Mw cm $^{-2}$ light intensity. All the measurements were repeated at least three times to check the consistency and repeatability of the results.

5.4 Results and Discussion

5.4.1 XRD characterization

X-ray diffraction (XRD) diffractograms of ZnO nanorods grown on FTO glass substrates show the wurtzite crystallites of ZnO of (100), (002), (101), (102), (103), (200) and (110) orientations. [224] The figures 5-1, 5-2 and 5-3 show the diffractograms of as deposited, microwave treated and conventional thermal annealed ZnO nanorod electrodes respectively.

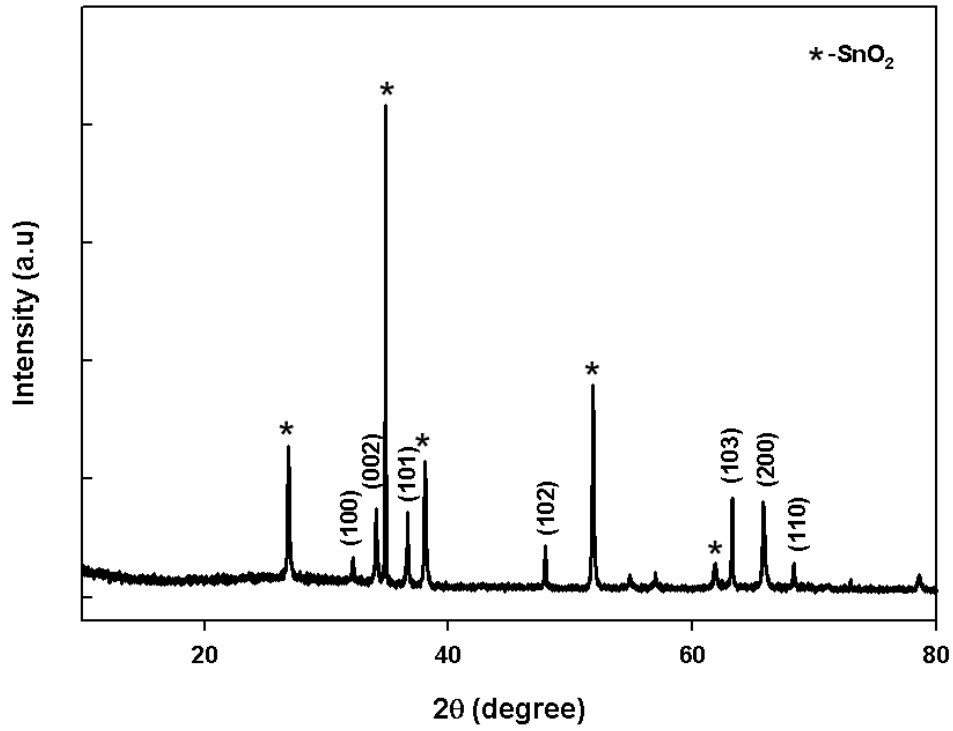


Figure 5-1. XRD diffractogram of as-deposited ZnO electrode.

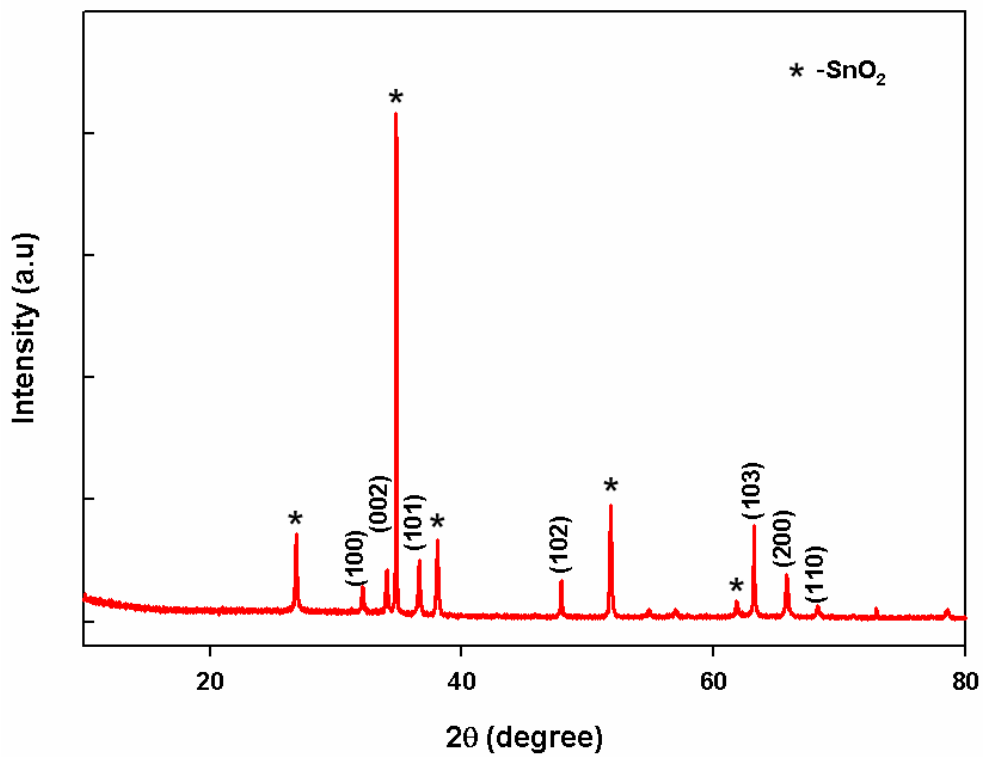


Figure 5-2. XRD diffractogram of microwave treated ZnO electrode.

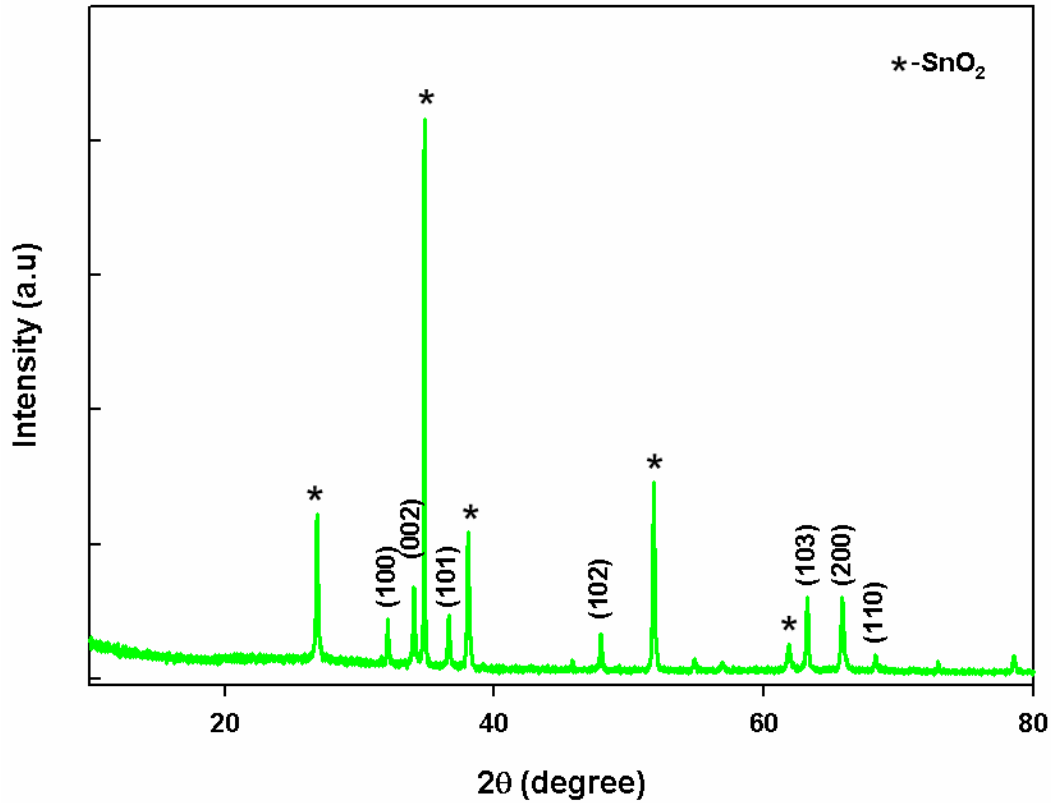


Figure 5-3. XRD diffractogram of conventionally annealed ZnO electrode.

The diffractograms reveal that there is no significant difference in the thin film crystallinity of as deposited, microwave irradiated and conventional thermal annealed ZnO nanorods. The XRD reflections indexed by asterisk (*) represent the SnO₂ coating on FTO glass substrate. The results indicate that the ZnO nanorods are in highly crystalline form; therefore microwave and conventional annealing do not have any further effect on its crystallinity (Figure 5-4). As discussed in chapter 4, microwave treatment of AACVD-TiO₂ films slightly improved the crystallinity due to the partial conversion of amorphous to crystalline TiO₂.^[221] The grain size along the (103) peak can be evaluated by using the Debye Scherrer equation 17.^[227,228]

$$D = \frac{0.9\lambda}{\beta \cos\theta} \quad (17)$$

where, D is the grain size of the crystallite, λ (0.154 nm) is the wavelength of the X-ray used, β is the broadening of diffraction line measured at half of its maximum intensity in radians and θ is the angle of diffraction.

The results indicate that as-deposited ZnO nanorods are highly crystalline in nature; therefore microwave and conventional annealing do not enhance the crystallinity any further. The grain size (along the (103) reflection) is evaluated by using the Debye-Scherer equation. The calculated values for the grain size of as-deposited and microwave irradiated ZnO nanorods are 34.4 and 67.9 nm respectively which closely agreed with the estimated grain size using FEG-SEM images (Figures 5-7 and 5-8).

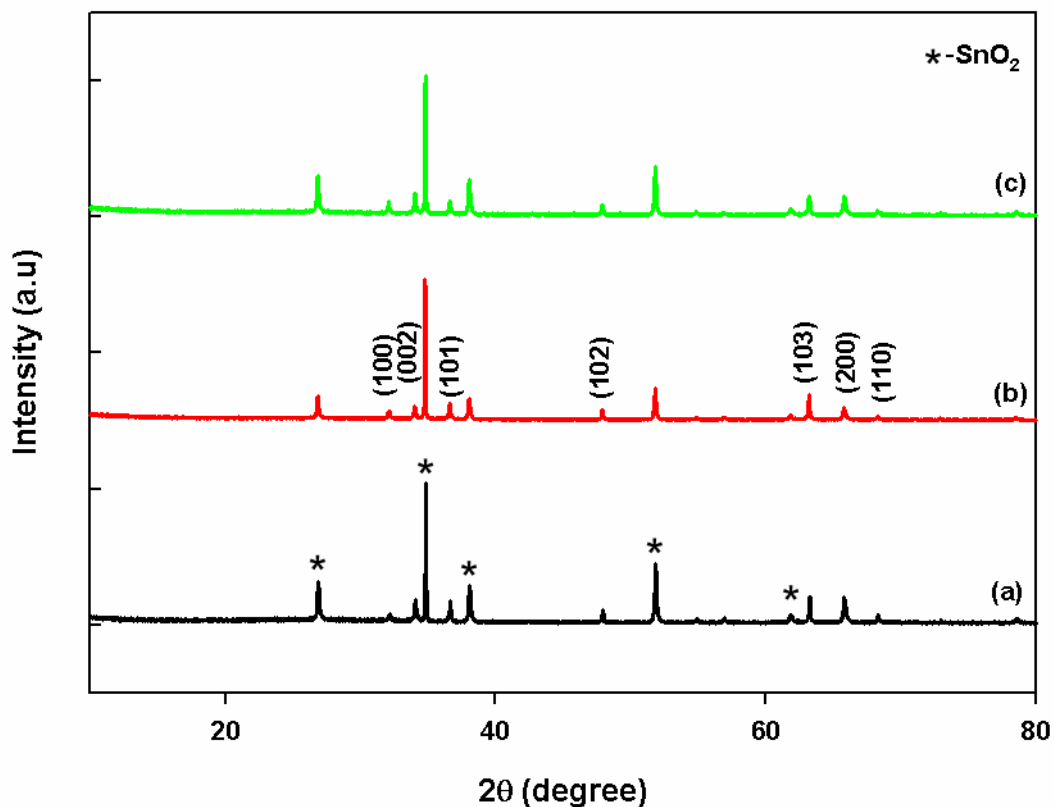


Figure 5-4. XRD diffractograms of (a) as-deposited, (b) microwave irradiated and (c) conventional thermal annealed ZnO electrodes. [The data has been taken from figures 5-1, 5-2 and 5.3]

5.4.2 Optical characterization

ZnO films were also characterized based on their optical properties. The absorbance spectrum of ZnO film was recorded in the wavelength range between 320-600 nm and contour indicates the significant absorption in the UV region as shown in Figure 5-5. The corresponding optical band gap (E_g) value was obtained from equation 18.[229]

$$(\alpha hv) = A(hv - E_g)^n \quad (18)$$

where A is a constant, hv the photon energy and n an exponent which is equal to 2 or 1/2 for direct or indirect transition respectively. The band gap values of the film were determined from $(\alpha hv)^2$ versus hv plot (Figure 5-6) by extrapolating the linear part of the absorption spectrum and found to be 3.2 eV which agrees well with literature value reported for ZnO nanorods.[230]

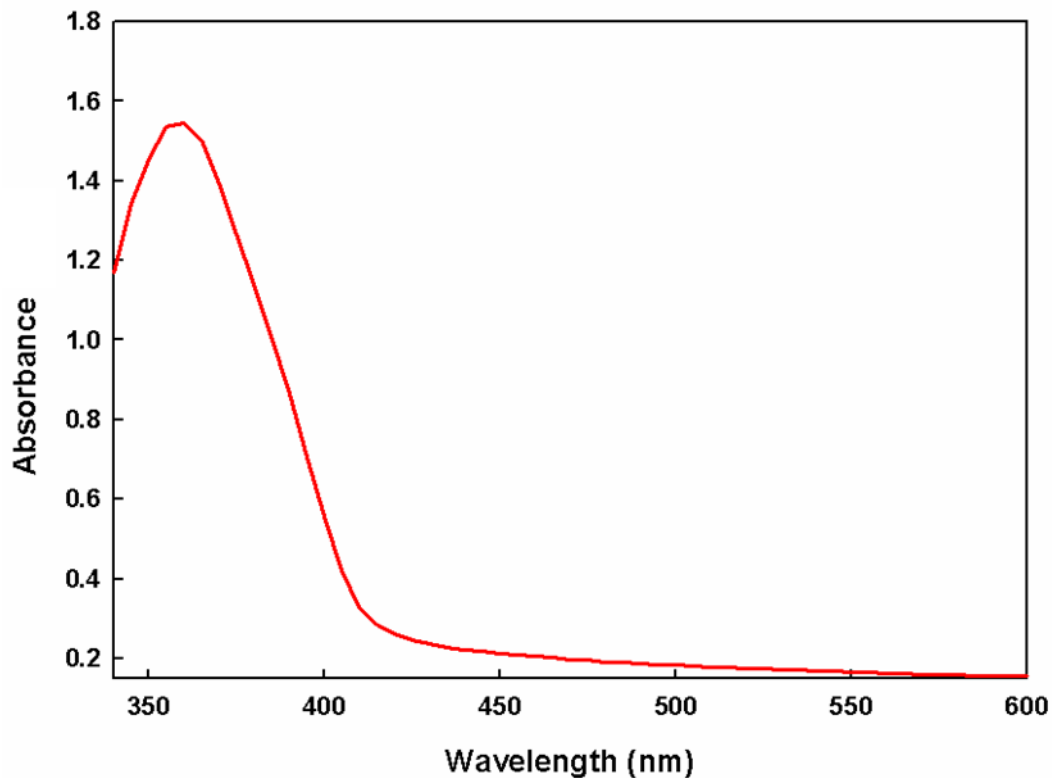


Figure 5-5. UV-Vis spectrum of ZnO nanorods on the FTO glass substrate.

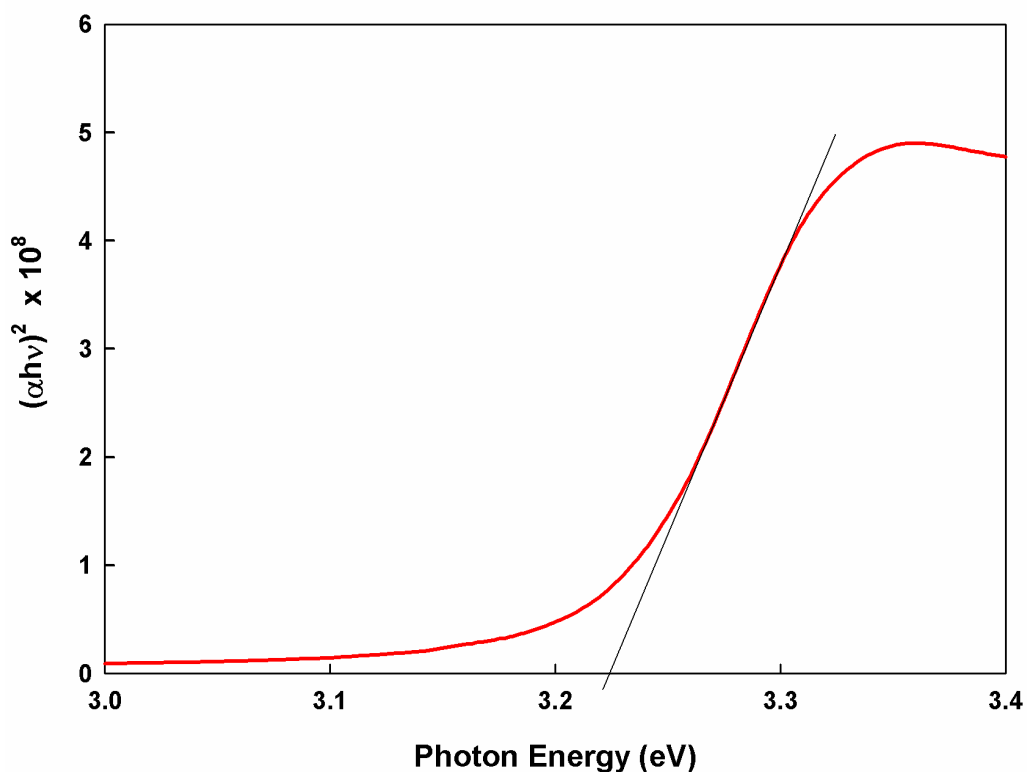


Figure 5-6. The plot for direct band gap determination of ZnO films.

5.4.3 Morphological properties

FEG-SEM has been used for the topographic study of as-deposited, microwave and conventional thermal annealed ZnO nanorod electrodes and the respective images are given in figures 5-7, 5-9 and 5-10. Figure 5-7 illustrates that as deposited ZnO nanorods are oriented almost perpendicular to the substrate. The figure 5-8 shows the cross-sectional image of as-deposited ZnO nanorod film. The thickness of the nanorods is estimated to be 0.6 μm which is higher than the calculated microwave penetration depth for ZnO (0.4 μm).

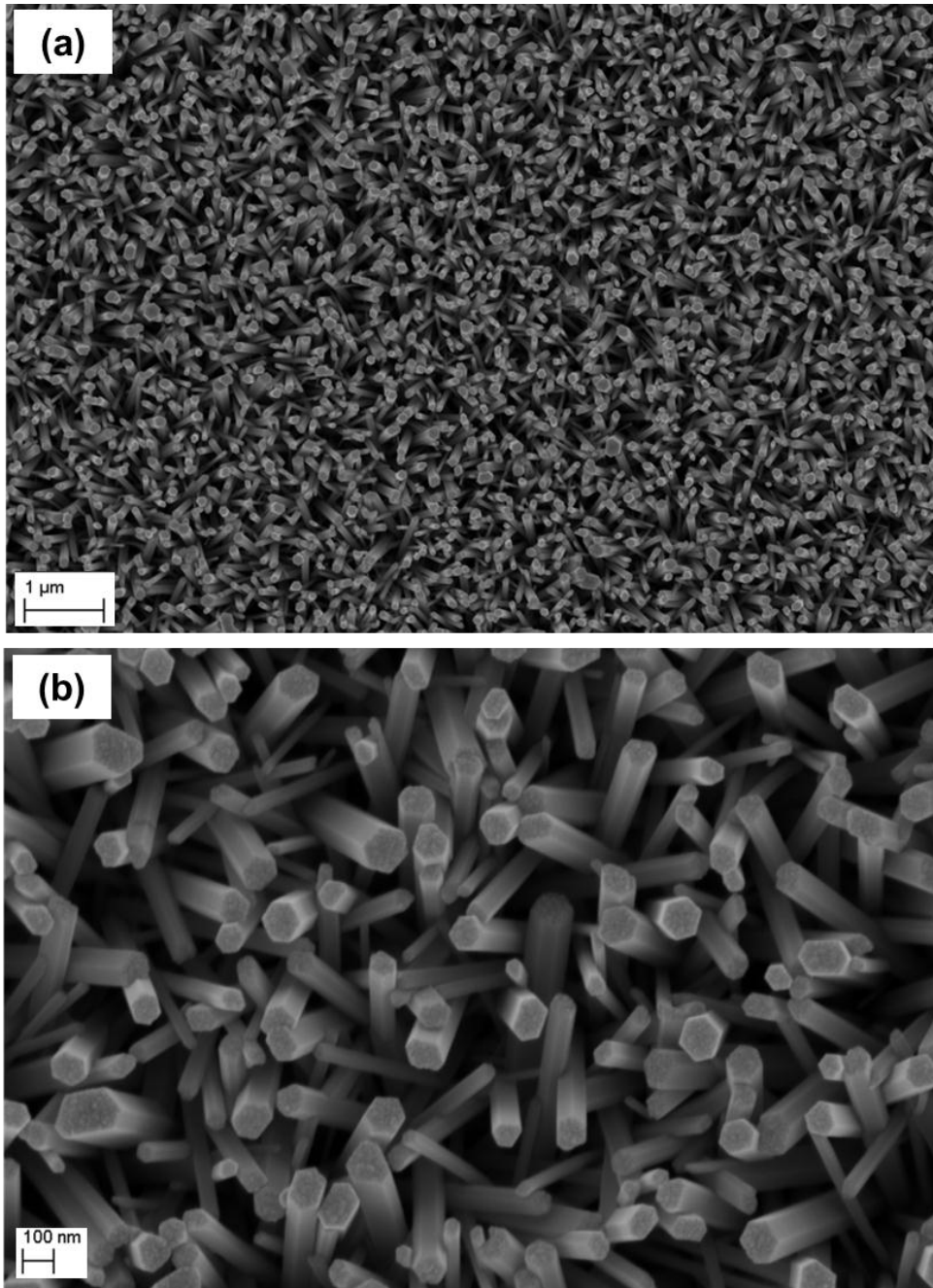


Figure 5-7. The FEG-SEM images of as deposited ZnO nanorods (a) low magnification (b) higher magnification.

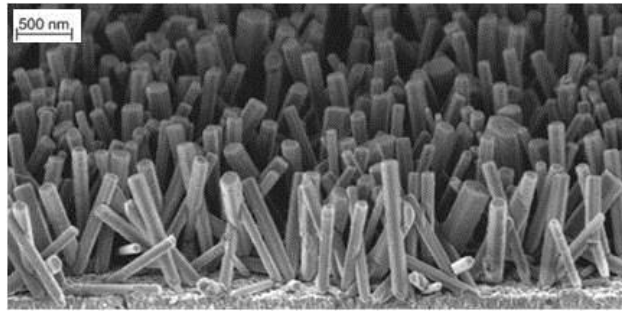


Figure 5-8. Cross-sectional image of ZnO nanorods grown on ZnO seed layer.

The topographical image of microwave irradiated ZnO nanorods indicates that microwave treatment of the films has caused sintering especially at the locations where the individual rods are close to each other, without significantly affecting the hierarchical structures (Figure 5-9). This is due to the fact that microwave heat generation takes place within the material by energy conversion rather than heat transfer, and hence there is less room for coagulation of individual rods.

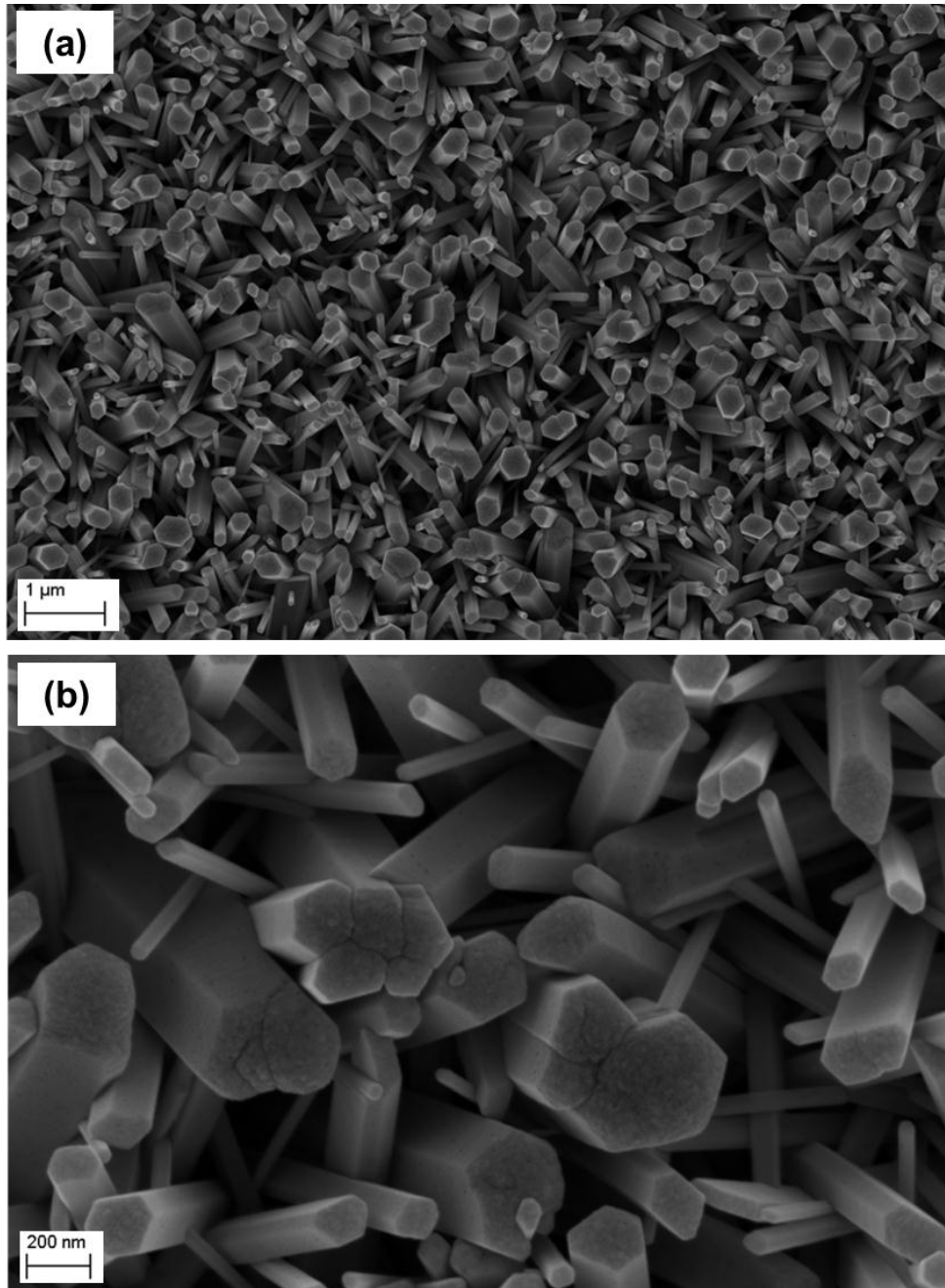


Figure 5-9. The FEG-SEM images of microwave treated ZnO nanorods (a) low magnification (b) higher magnification.

The effect of conventional thermal annealing (at 300 °C) on the surface morphology of ZnO nanorods were clearly identifiable in figure 5-10. It appears that ZnO nanorods have sintered together and deformed the hierarchical structure. There is also evidence to show that necking has occurred and boundaries (between remaining rod-like features) have formed during the thermal annealing step.

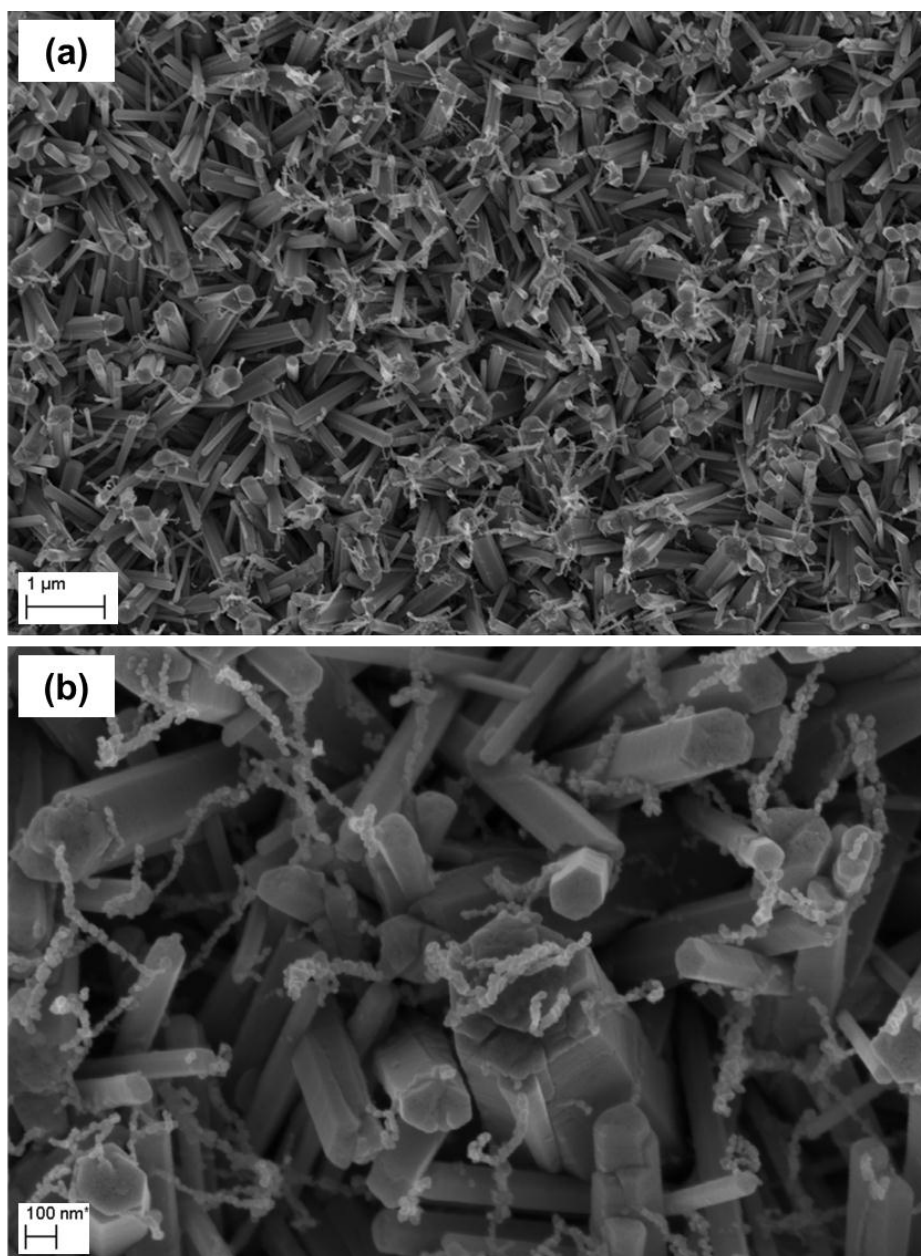


Figure 5-10. The FEG-SEM images of conventional thermal annealed ZnO nanorods (a) low magnification (b) higher magnification.

5.4.4 Internal surface area determination

The internal surface area of each electrode was determined by dye adsorption/desorption studies.[231] The projected surface area of ZnO electrodes of as deposited, microwave irradiated and conventionally thermal annealed are $1.47 \times 10^2 \pm 10$, $1.3 \times 10^2 \pm 10$ and $0.96 \times 10^2 \pm 20$ cm² (over 1 cm² of projected area) respectively. This indicates that the internal

surface area of microwave irradiated and conventional thermal annealed ZnO nanorods electrodes have decreased compared to that of the as-deposited counterpart. This is due to the secondary growth and agglomeration of individual rods as evident from the SEM images. This effect is more pronounced in conventional thermal annealing than microwave treatment causing the destruction of the hierarchical structure. It has been reported elsewhere [232] that the average grain size of the film increased with annealing. Grain boundaries are developed between different crystallographic phases which are responsible for specific properties of the materials.

5.4.5 Photoelectrochemical characterization

The photoelectrochemical (PEC) performance of ZnO electrodes was studied by evaluating the current density-voltage (J - V) characteristics for as-deposited, microwave irradiated and conventional thermal annealed samples. The chopped J - V plots uncorrected for internal surface area differences of as deposited, microwave treated and conventional thermal annealed electrodes are shown in figure 5-11.

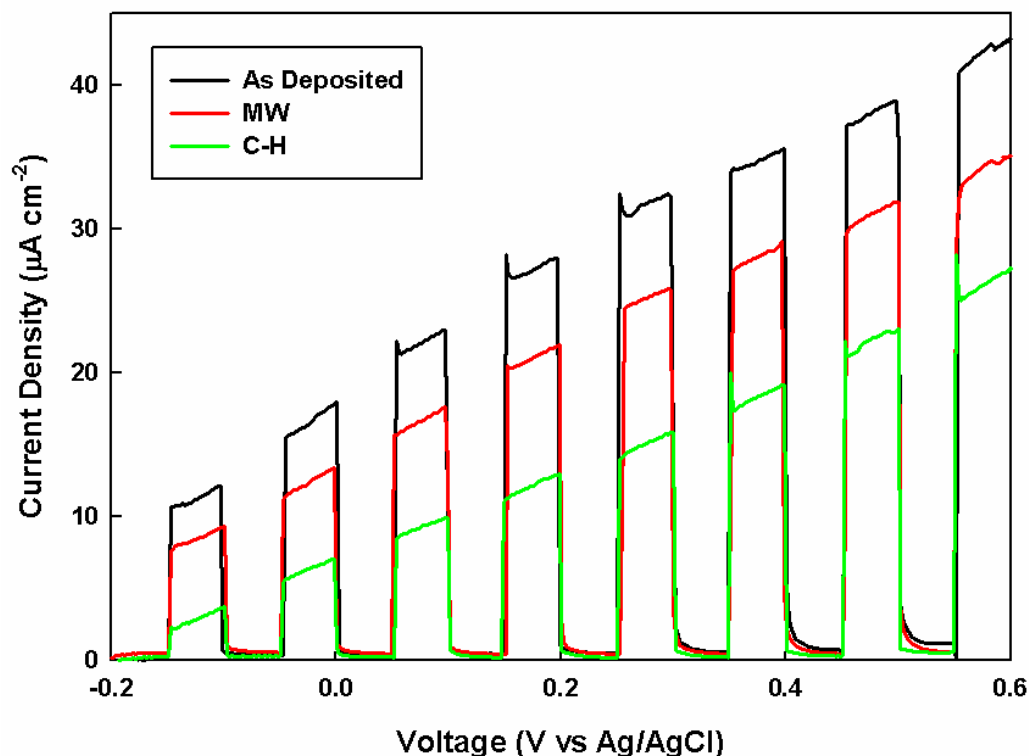


Figure 5-11. Current density versus voltage (J - V) characteristics of (a) as-deposited, (b) microwave irradiated and (c) conventional thermal annealed ZnO electrodes. The current density of each electrode is uncorrected for the internal surface area.

The plots illustrate that all the electrodes are resistive in nature. The current density of microwave irradiated electrodes decreases compared to that of the as-deposited electrodes. The reduction of the photocurrent corresponding to conventional thermal annealed ZnO electrodes is more pronounced, presumably due to deformation of the rod structure. This appeared to be due to the poor charge transport within the electrode containing deformed features in nanoscale. It is well known that the charge transport within ZnO nanorods is more efficient compared to randomly oriented nanostructured electrodes.[233] The J - V plots indicate the same trend with the calculated projected surface areas of the electrodes. The variation of the estimated surface area against the corrected photocurrent density for internal surface area of as-deposited and treated ZnO electrodes is plotted in figure 5-12.

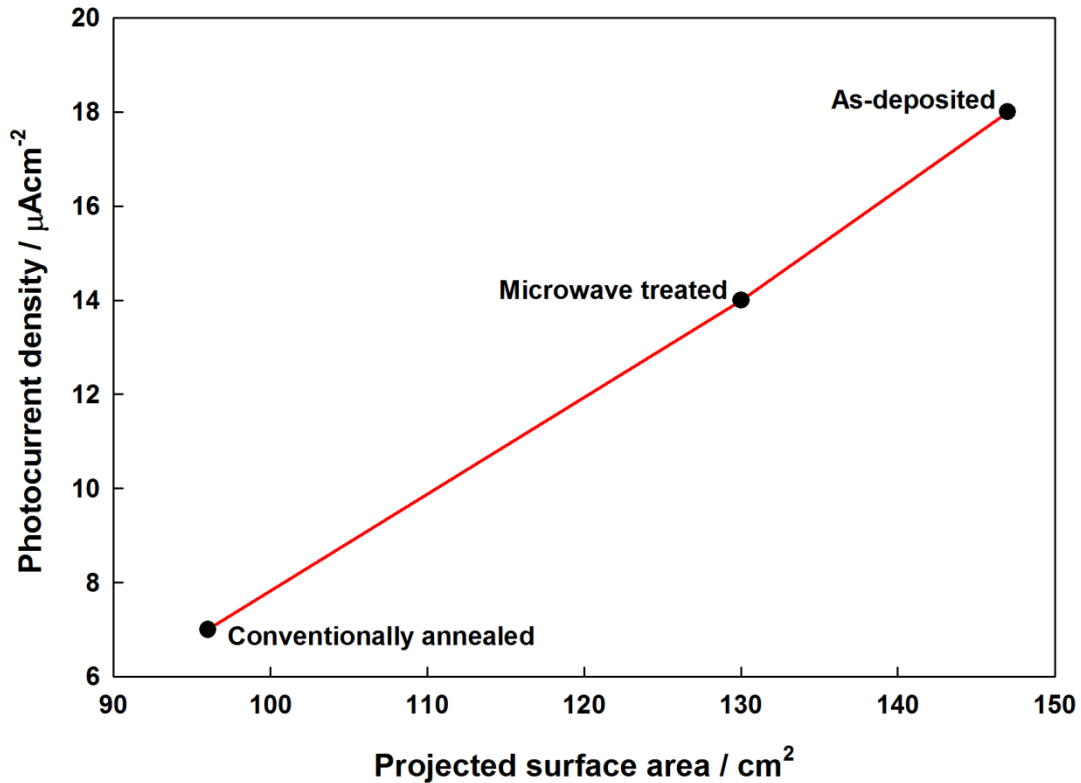


Figure 5-12. The comparison of estimated internal surface area versus corrected photocurrent density for internal surface area of as-deposited and treated ZnO electrodes.

It is evident in the present work that the microwave treatment preserves the structure of nanorods better than in the case of conventional thermal annealing. TiO₂ electrodes showed that microwave processing facilitates the growth of crystallites and inter-particles connections while preserving the electrode texture and improving the PEC properties appeared to be due to the enhanced charge collection.[221] It is clear from the present work that post annealing of ZnO nanorod has less effect on improving PEC performance as it leads to reduced internal surface area of the electrodes. Furthermore, the conventional thermal heat treatment completely deforms the electrode texture thereby deteriorating the PEC performance. The reduction of surface areas of the films mainly affects the PEC performance of the films which is confirmed by normalized *J-V* plot (Figure 5-13). The normalized *J-V* plots show the light current is almost same for as deposited, microwave and conventionally annealed electrodes

which proves the PEC behaviour corresponds to the changes occurred in the electrode surface areas due to the microwave irradiation and conventional annealing.

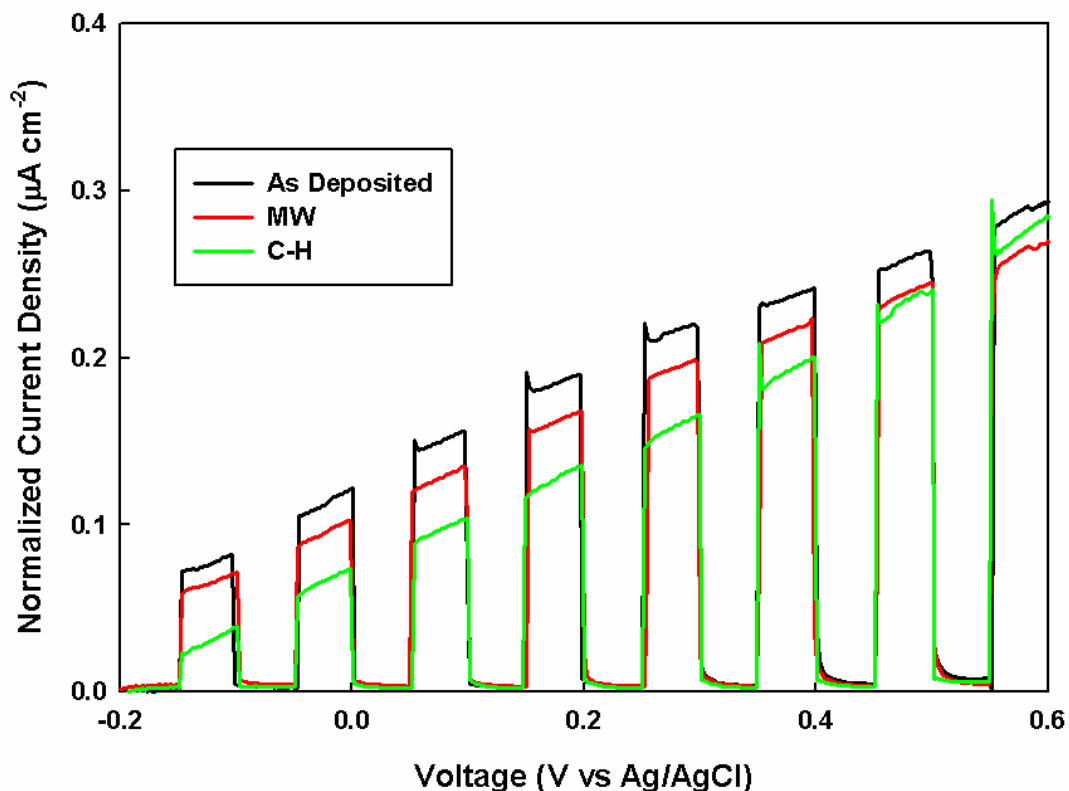


Figure 5-13. The normalised J-V plots of as-deposited, microwave irradiated and conventionally annealed ZnO electrodes.

5.5 Conclusions

Zinc oxide nanorods were grown on FTO-glass substrate by CBD method after depositing a seed layer by AACVD. The structural properties of as-deposited, microwave irradiated and conventional thermal annealed ZnO nanorods were studied by XRD. X-ray diffraction measurements show that ZnO nanorods grown in wurtzite crystal phase. There is no apparent change of the crystallinity of as-deposited, microwave irradiated and the conventionally annealed electrodes. The SEM images show that the microwave irradiation caused sintering of individual rods resulting in the growth of rod diameter whilst the conventional thermal

annealing deformed the hierarchical ZnO structure. The PEC studies indicate that all electrodes are resistive in nature. The current density of microwave irradiated electrode decreases compared to that of as-deposited electrode. The reduction of the photocurrent corresponding to conventional thermal annealed ZnO electrodes is more intense presumably due to deformation of rod structure. This appeared to be due to the poor charge transport in deformed electrodes.

Chapter 6

Microwave-assisted low temperature fabrication of nanostructured ZnO thin film electrodes for solar energy conversion

6.1 Overview

Metallic zinc (Zn) thin films were electrodeposited on to fluorine-doped tin oxide (FTO) substrates by electrodeposition and the deposited Zn was oxidised to zinc oxide (ZnO) using conventional radiant and microwave annealing methods. The oxidation temperatures of both methods were varied and the respective photoelectrochemical (PEC) performance was evaluated for each electrode. The best PEC performance of a photocurrent of $93 \mu\text{A cm}^{-2}$ at 1.23 V vs. NHE (0.74 V vs. Ag/AgCl) and an incident photon-to-electron conversion efficiency (IPCE) of 4.5% was achieved after oxidation of Zn at 425 °C for 15 min under conventional radiant annealing. X-ray diffractograms showed that the oxidation of Zn to ZnO was not 100% efficient during the annealing period as evidence for metallic Zn was still seen. Further increases in temperature resulted in lower photocurrents. For the microwave oxidation of Zn to ZnO, the best photocurrent of $130 \mu\text{A cm}^{-2}$ at 1.23 V vs. NHE and an IPCE of 6% were observed after annealing for 3 min, during which time the temperature reached 250 °C. The photocurrent was 40% higher for the microwave annealed sample compared to conventional radiant annealing at the same applied potential; this increase was attributed to higher surface area, confirmed by SEM surface topographical analysis, and better yields of conversion to crystalline ZnO. SEM analysis confirmed that the higher temperature used in the thermal annealing process leads to sintering of the nanostructure

which reduces the effective surface area. The oxidation of Zn to ZnO using microwave annealing was achieved at much lower temperatures and therefore the high surface area of the films was maintained while preserving the nanostructure. Overall, it was demonstrated that oxidation of Zn to ZnO can be accomplished by microwave annealing five times faster than conventional annealing and with much lower temperature, and this resulted in a ~75% power saving. This highly efficient microwave processing offers significant economic advantages for industrial scale up.

6.2 Introduction

The global increase in the demand for energy and the rapid depletion of non-renewable energy sources, such as natural gas coal and oil, has led researchers to search for new means of generating and storing energy. Hydrogen gas, as a mean of storing chemical energy has long been thought of as a possible alternative to fossil fuels, providing that it could be generated in a cheap and environmentally friendly way. Hydrogen gas can be generated in-situ using photoelectrochemical (PEC) water splitting at a semiconductor/electrolyte interface, or alternatively photovoltaic thin film technology can be used to supply the potential required to drive the water splitting reaction.[234] For all such solar harvesting devices, metal oxide semiconductors, for example Fe_2O_3 , [235] TiO_2 , [236,237] ZnO [238] and WO_3 , [239] have been extensively studied because they are inexpensive, inert and scalable for industrial production purposes, and are thus of great interest. ZnO in particular, has found applications in wide variety of devices ranging from photovoltaic devices (PEC cells, [240] dye-sensitized solar cells, [241] solid state solar cells [242]) to electronic devices (sensors, [243] field effect transistors, [244] Schottky diodes, [245] light emitting device arrays [246]) due to its unique and diverse properties; thus it is appropriate to develop low-cost and industrially scalable methods for its fabrication.

In the case of metal oxide thin films, photovoltaic device fabrication at an industrial scale usually involves a post deposition thermal annealing process. [247] This annealing process is essential as it controls the bulk properties of the material. For example annealing can improve the thin film's adhesion to the substrate, change the materials phase and crystallinity and hence conductivity, and change the surface morphology and therefore surface area of the material. [156] Such properties greatly influence the semiconductor performance in its respective device. As the typical annealing process makes use of extreme temperatures, it is

vastly energy intensive and time consuming, which has negative economic consequences.[247] Other drawbacks for thermal annealing are that the high temperatures can cause collapse of the nanostructure which greatly reduces the porosity and consequently the surface area, which in turn affects the PEC performance.[248] A promising alternative to conventional thermal annealing is microwave processing.[249-251] Microwave processing has been shown to offer significant cost savings through reduced processing times, reduced floor space and selective heating.[252,253]

The heating mechanism of thermal and microwave annealing is fundamentally different. In the conventional thermal annealing process, heat is transferred from the surroundings (i.e. from the furnace or hotplate) to the sample, whereas in microwave annealing, heat is generated within the sample itself (volumetric heating), which is a distinct advantage as it can minimize energy losses associated with energy transfer.[252] In thermal annealing, there is huge potential for energy losses in the process of heat transfer from the heating element to the sample. In general, there are two possible mechanisms in which energy conversion from microwave radiation to heat can occur – polarization or conduction. Polarization involves displacement of charge through the formation and rotation of electric dipoles, whereas conduction involves long range transport of charge.[252] The rotation of the electric dipole causes molecular friction which generates heat, and ionic conduction causes molecular motion and collision, which also results in heat generation. The ability to absorb microwave radiation and hence heat generation is determined by the dielectric loss (ϵ'') and loss tangent ($\tan \delta$) of the materials. In order for microwaves to interact with the material, a balanced combination of moderate dielectric constant (to permit adequate penetration) and high loss tangent (for higher energy to heat conversion) are required. However, use of microwave radiation to process post deposited semiconductor materials and material synthesis has shown promising results over conventional heating methods.

Microwave annealing has already shown great potential for low-cost processing of TiO₂[156], ZnO[248] and α -Fe₂O₃[247] thin films. Not only has microwave annealing proven to be a match for conventional thermal annealing, the thin films processed by microwave annealing have shown enhanced properties in terms of their PEC performance.[156] This has been attributed to an increase in the crystallinity of the material without significantly affecting its nanostructure. It has also been shown that processing times are greatly reduced compared with thermal annealing.[247] This chapter compares the efficiency of oxidation of electrodeposited metallic Zn to ZnO using conventional radiant and microwave annealing methods in terms of their PEC performance. A 40% increase in the photocurrent is seen when ZnO is produced using microwave annealing rather than conventional. Also better conversion yields and faster processing times at lower temperatures were achieved with microwave annealing; features that are highly desirable for large-scale industrial production of ZnO based electronic and optoelectronic devices.

6.3 Experimental

Fluorine-doped tin oxide (FTO) glass substrates (FTO, TEC8, Pilkington Glass, Ltd, St Helens UK) were cut to 1 x 2 cm² slides and were cleansed via a series of 15 min sonication treatments in 2-propanol, acetone, ethanol and deionized water (resistivity = 18.2 M Ω) and finally stored in absolute ethanol. The electrochemical solution of aqueous Zn(NO₃)₂ was prepared by dissolving 1 mM Zn(NO₃)₂·6H₂O (reagent grade, Sigma Aldrich, Dorset, UK) in 100 mL deionized water. The electrochemical deposition of Zn films was performed in a three-electrode configuration where the FTO was used as the working electrode, Pt wire as the counter electrode and Ag/AgCl as the reference electrode. When Zn was electrochemically deposited on FTO coated glass substrates, the area of the film was maintained at 1 cm². A potential of -1.25 V for 1800 s (total number of charges~ 1 x 10³ C)

was applied which resulted in a grey metallic Zn on the FTO conducting surface. The films were then washed with deionized water and left in air to dry. The calculated film thickness was ~600 nm. The oxidation of Zn to ZnO was studied using both conventional thermal and microwave annealing. Conventional thermal annealing was carried out in a tube furnace (MTF-10-25-130, Carbolite, Hope Valley, UK) with a ramp rate of 15 °C/min to its desired temperature which were within the range of 400 to 600 °C. Both ends of the tube were left open to allow air to flow in. After annealing, the furnace was turned off and the samples were allowed to cool in the tube furnace until the temperature reached to room temperature. Microwave assisted annealing was performed using a modern microwave oven (Microwave research Applications Inc. BP-211/50, USA) operating at 2.45 GHz frequency with a maximum power of 3000 W. A microwave monitor (CELTEK, S/N: 771459) was used to observe any radiation leakage and as the monitor read 0 mW cm⁻² thus no leakage was observed. The Zn films were oxidised using the microwave furnace from 3 min to 10 min durations and they were covered with an insulator, in order to minimise the heat loss. The temperature of the annealed substrates was monitored using an infrared temperature probe (Mikron infrared Inc. M67/M67S series, USA) with an error of ± 5 °C. The PEC performance of the annealed ZnO films was measured using a three-electrode configuration in 1 M Na₂SO₄ aqueous electrolyte, Ag/AgCl as the reference electrode and Pt wire as the counter electrode. The potential of the photoelectrode was controlled using computer-controlled software and a potentiostat (microAutoLab, type III, Windsor Scientific Limited, Berkshire, UK). The electrodes were illuminated through the electrolyte side and the illumination area was 1 cm². The illumination source was AM 1.5 class A solar simulator (16S – 300 solar simulator, Solar Light Co., Inc., PA, USA) equipped with a 300 W xenon lamp. The intensity of the light was calibrated at 100 mW cm⁻² using a class II pyranometer (PMA2144, Solar

Light Co., Inc., PA, USA) equipped with a digital photometer (PMA2100, Solar Light Co., Inc., PA, USA).

The microstructure and surface morphology of the thin films were investigated using field emission gun scanning electron microscopy (FEG-SEM, Leo 1530 VP) at an accelerating voltage of 5 keV and a working distance of 5 mm. The phase and crystallinity of the as deposited and annealed ZnO nanorod films were studied using Bruker D8 XRD, operating with monochromatic Cu K α ($\lambda = 1.54 \text{ \AA}$) radiation and PSD detector. The incident photon to electron conversion efficiency (IPCE) was obtained by measuring the incident photon flux using a 75 W xenon lamp connected to a monochromator (TMc300, Bentham Instruments Ltd. Berkshire, UK). The light was calibrated using a silicon diode. Photocurrent spectra were measured at 0.65 V vs. Ag/AgCl (1.23 V vs. NHE) using a combination of a lock-in amplifier (Bentham 485, Bentham Instruments Ltd., Berkshire, UK) and a custom built potentiostat.

6.4 Results and Discussion

6.4.1 Electrodeposition of Zn

Electrodeposition of Zn films on conductive substrates by cathodic reduction of Zn²⁺ ions is a well known process which is reported elsewhere.[254]

6.4.2 XRD characterisation

Metallic Zn thin films were deposited by electrodeposition and its oxidation to ZnO was conducted using conventional radiant annealing or microwave annealing. The phase and crystallinity of the films as a function of annealing temperature were studied using XRD.

Figure 6-1 shows the XRD reflections of as-deposited, conventionally annealed and microwave annealed samples. The XRD reflections of electrodeposited Zn (Figure 6-1a) confirmed that the sample consists only of Zn with an hcc crystal structure and a preferred orientation in the (101) direction. When the electrodes are conventionally annealed at 425 °C for 15 min in air, the deposited Zn is oxidised to ZnO with a wurtzite crystallites of (100), (002), (101), (102), (103), (200) and (110) orientations. However, during the 15 min annealing process not all of the Zn is oxidised as confirmed by the corresponding (101) reflection of Zn in the XRD diffractogram (Figure 6-1b). As shown in figure 6-1c, the XRD diffractogram of the microwave annealed sample at 250 °C for 3 min shows only ZnO reflections which indicate complete oxidation to ZnO. The corresponding ZnO wurtzite crystallites of (100), (002), (101), (102), (103), (200) and (110) reflections are more intense and well-defined compared to the films that are annealed under conventional heating, which indicates a higher degree of crystallinity of microwave annealing. This clearly indicates microwave treatment is an efficient way of oxidising Zn to ZnO compared with conventional heating. Another advantage is that microwave annealing resulted in the oxidation of Zn at a much lower temperature (i.e. 250 °C) with less processing time (i.e. 3 min) in contrast to conventional heating.

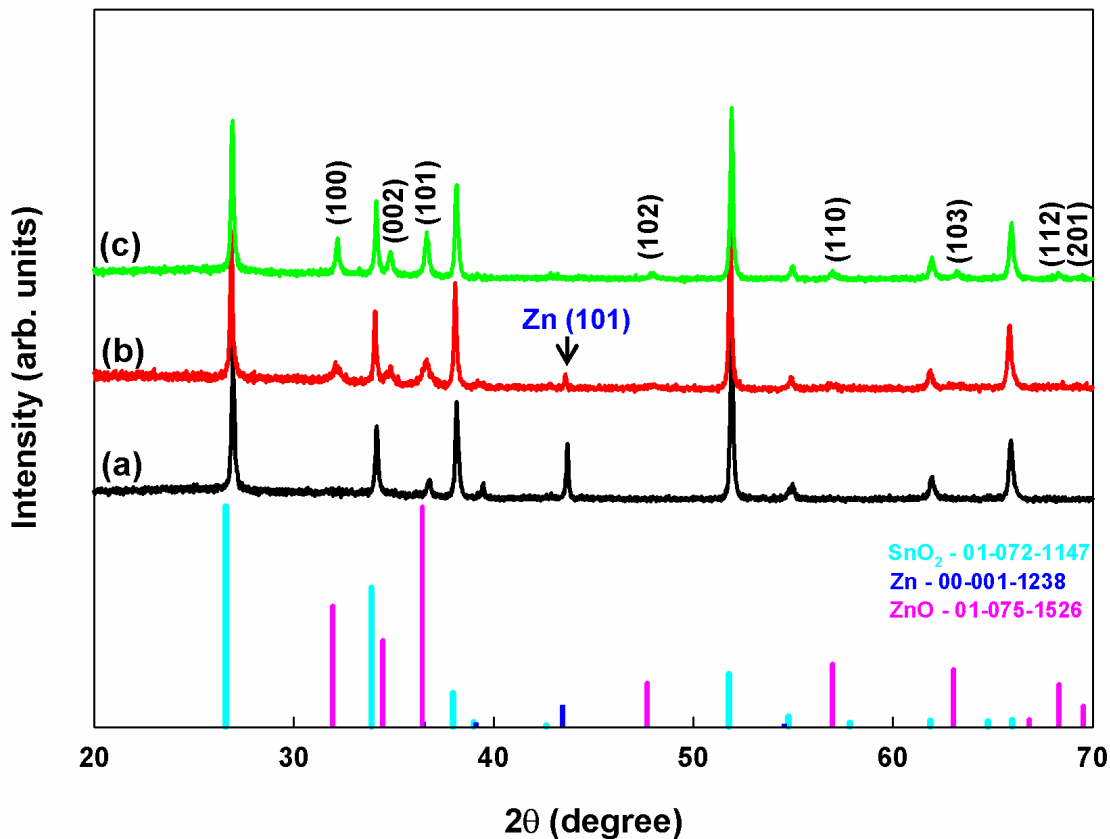


Figure 6-1. XRD diffractograms of (a) as electrodeposited Zn, (b) conventionally annealed at 425 °C for 15 min and (c) microwave annealed at 250 °C for 3 min. The (101) peak of Zn is shown with an arrow. The standard XRD reflections of SnO₂, Zn and ZnO are also shown.

6.4.3 Morphological properties and particle size

The impact of the annealing method on the morphology of the nanostructure was studied using FEG-SEM. Figures 6-2 shows the surface morphology of as deposited and annealed samples at different temperatures using thermal annealing. The respective magnified images are shown in figures 6-3. The surface of as-deposited Zn is shown in figure 6-3a which comprises nanostructures in the nanometre range having a broad size distribution. The particle shape is more or less spherical with some cluster/agglomeration between the particles. The large particles are spatially distributed on the surface which is surrounded by a blanket of clustered/agglomerated small Zn particles. The post annealing of Zn films resulted

in oxidation and sintering which lead to various morphological changes of the film depending on the annealing temperature, as shown in figures 6-3b-d. At 425 °C (figure 6-3c) the ZnO nanostructure adopts a cauliflower-like structure with high apparent surface area. Heating at a higher temperature of 600 °C resulted in agglomeration and sintering of the nanostructure (figure 6-3d), resulting in a lower apparent surface area.

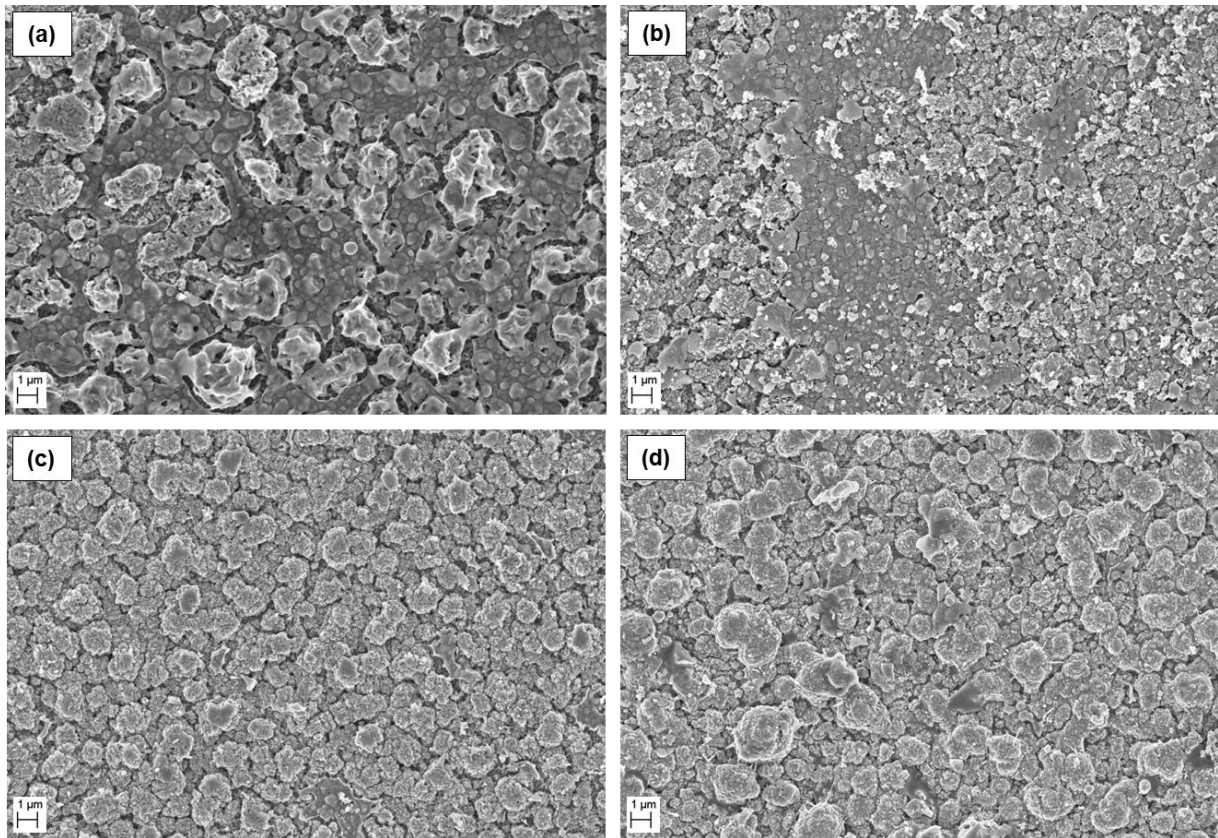


Figure 6-2. Surface topographical images of (a) as electrodeposited Zn, conventionally annealed Zn electrodes at (b) 400 °C (c) 425 °C and (d) 600 °C.

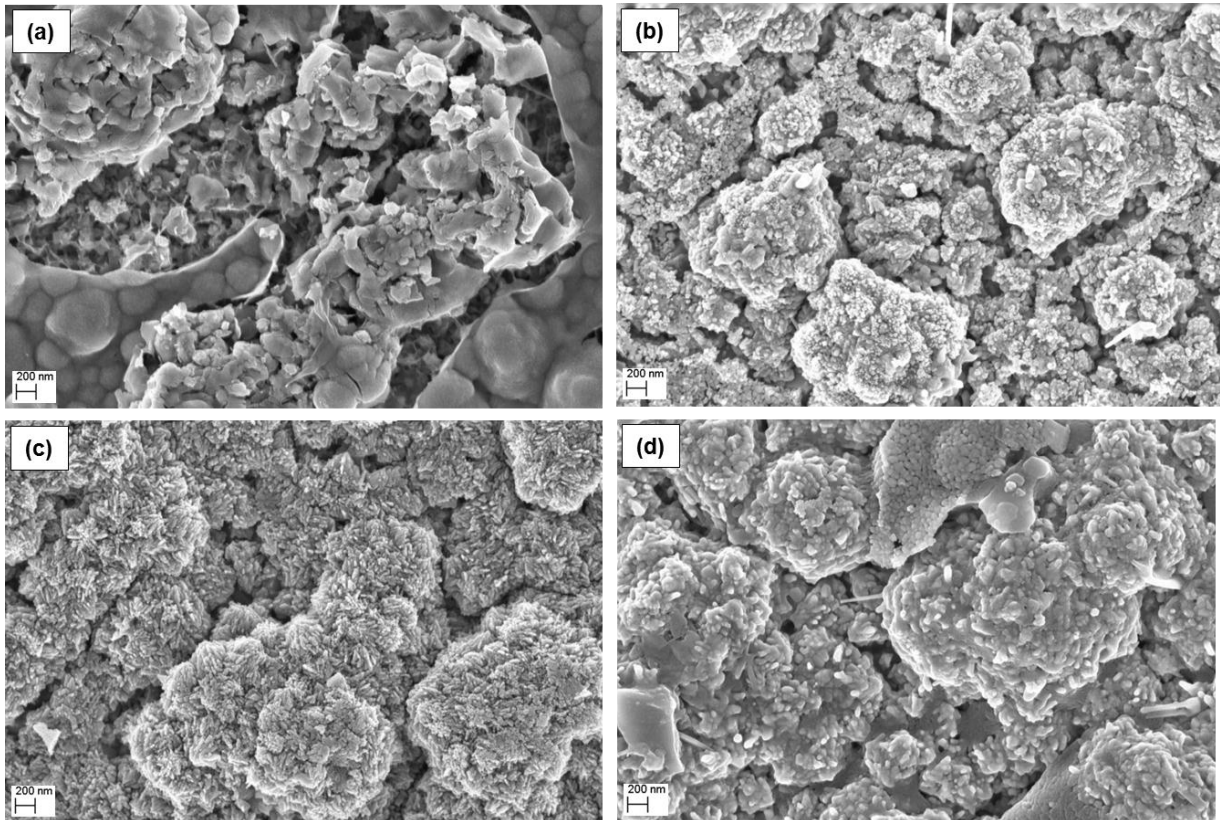


Figure 6-3. The magnified SEM images of (a) as electrodeposited Zn, conventionally annealed Zn electrodes at (b) 400 °C (c) 425 °C and (d) 600 °C [Respective magnified images of figure 6-2].

As found by XRD reflections, the microwave oxidation of electrodeposited Zn films to ZnO was shown to occur at lower temperatures and the rate of oxidation was higher compared to conventional thermal annealing. The surface morphology of the as-deposited and microwave oxidised films is shown in figure 6-4 for annealing temperatures of 180, 250 and 300 °C and the respective magnified images are shown in figures 6-5. For microwave annealing temperatures of 180 and 250 °C (figure 6-5b and 6-5c), there appears to be no significant change in the surface morphology compared with the as-deposited metallic Zn film. Evidence of particle agglomeration and sintering/melting begins to be observed at a higher microwave annealing temperature of 300 °C (figure 6-5d). However, it was shown from the XRD data that complete oxidation of Zn to ZnO occurs at 250 °C, hence the use of higher temperatures

is not required. As evident from the SEM images is it clear that microwave annealing preserves the nanostructure of the film compared to conventionally annealed samples due to its rapid and volumetric heating capabilities. This phenomenon agrees well with our previously reported articles and the literature.[156,247,253]

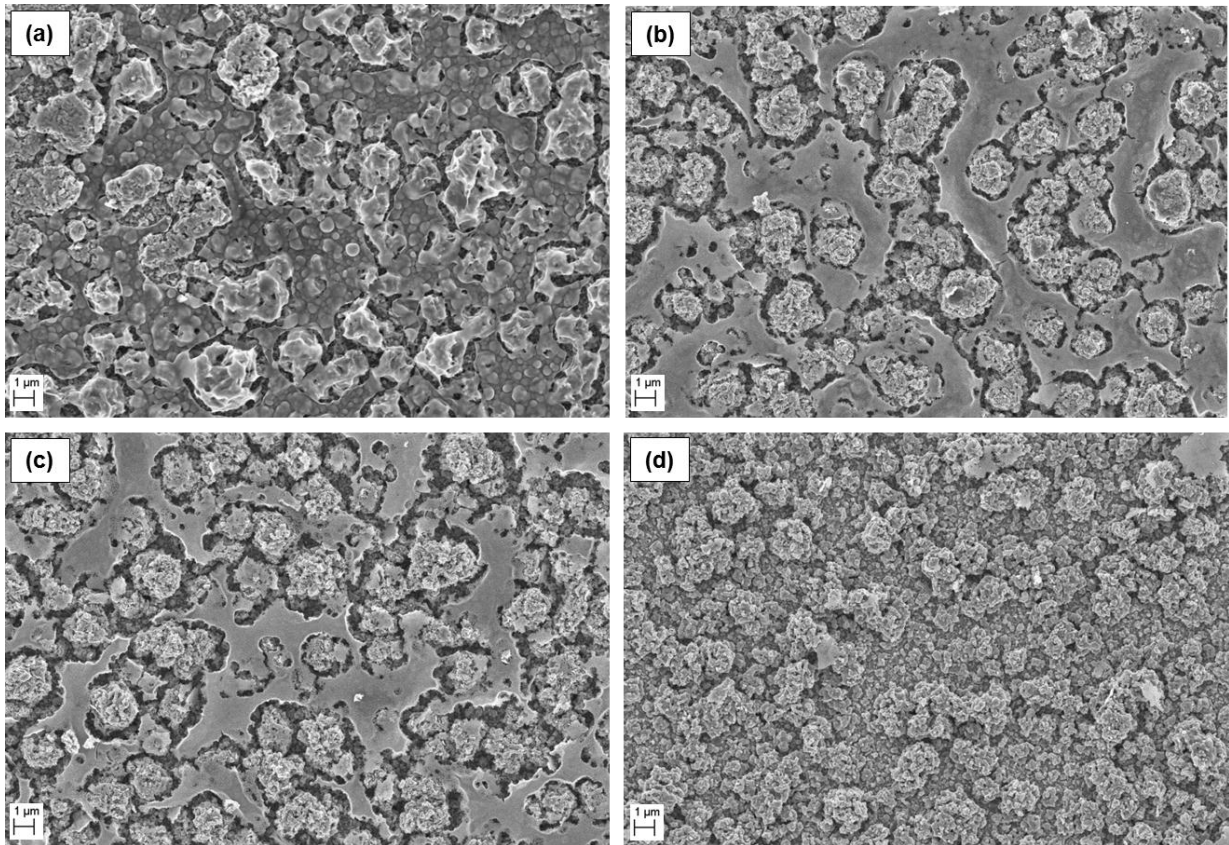


Figure 6-4. Surface topographical images of (a) as electrodeposited Zn, Microwave annealed Zn electrodes at (b) 180 °C (c) 250 °C and (d) 300 °C.

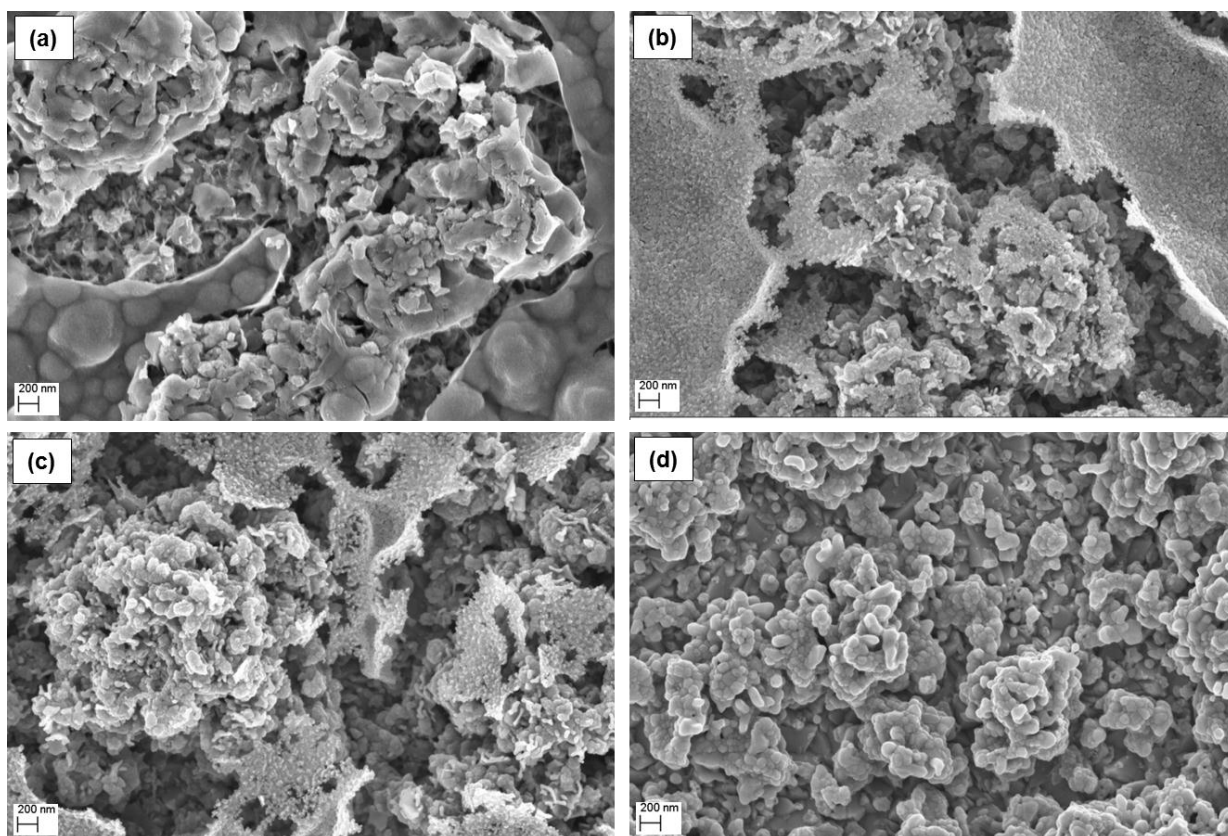


Figure 6-5. The magnified SEM images of (a) as electrodeposited Zn, microwave annealed Zn electrodes at (b) 180 °C (c) 250 °C and (d) 300 °C. [Respective magnified images of figure 6-4].

7.4.4 Photoelectrochemical properties of electrodes

Photoelectrochemical (PEC) studies were carried out for the annealed electrodes in order to find the effect on the performance for different annealing methods. The electrodes were scanned from -0.3 V to 1 V with reference to Ag/AgCl. The obtained current density-potential plots for electrodeposited Zn electrodes oxidised using both conventional and microwave heating are shown in figures 6-6 and 6-7 at various temperatures, respectively. The inset in the respective figures show the photocurrent densities obtained for microwave and conventionally annealed electrodes at 1.23 V vs. NHE (0.74 V vs. Ag/AgCl) as a function of annealing temperature. As shown in figure 6-6, the photocurrent density reached its maximum value, $93 \mu\text{A cm}^{-2}$ at 1.23 V vs. NHE, for the electrodeposited Zn films

conventionally annealed at 425 °C for 15 min. Further annealing at higher temperatures resulted in the reduction of the photocurrent density to 38 $\mu\text{A cm}^{-2}$ at 600 °C. This was most likely due to a reduction in the surface area caused by sintering of the nanostructure; this is confirmed by the differences seen in the surface morphology (figure 6-3d). The samples annealed at temperatures lower than 400 °C showed negligible photocurrent with a reasonable dark current due to the unconverted Zn in the film. Figure 6-7 shows the chopped photocurrent densities obtained for electrodeposited Zn electrodes oxidised by microwave radiation at various temperatures. The PEC performance of the microwave annealed electrodes showed an improvement until the sample temperature rose to 250 °C. Microwave annealing at temperatures higher than 250 °C resulted in lower photocurrents, most likely due to reduction in surface area caused by sintering and agglomeration of the nanostructure, as evidenced by the SEM images (figure 6-5d). The electrode annealed at 180 °C under microwave radiation showed a photocurrent density, about 73 $\mu\text{A cm}^{-2}$ at 1.23 V vs. NHE, whereas the electrode annealed at 250 °C showed a much higher photocurrent density of 130 $\mu\text{A cm}^{-2}$ at 1.23 V vs. NHE.

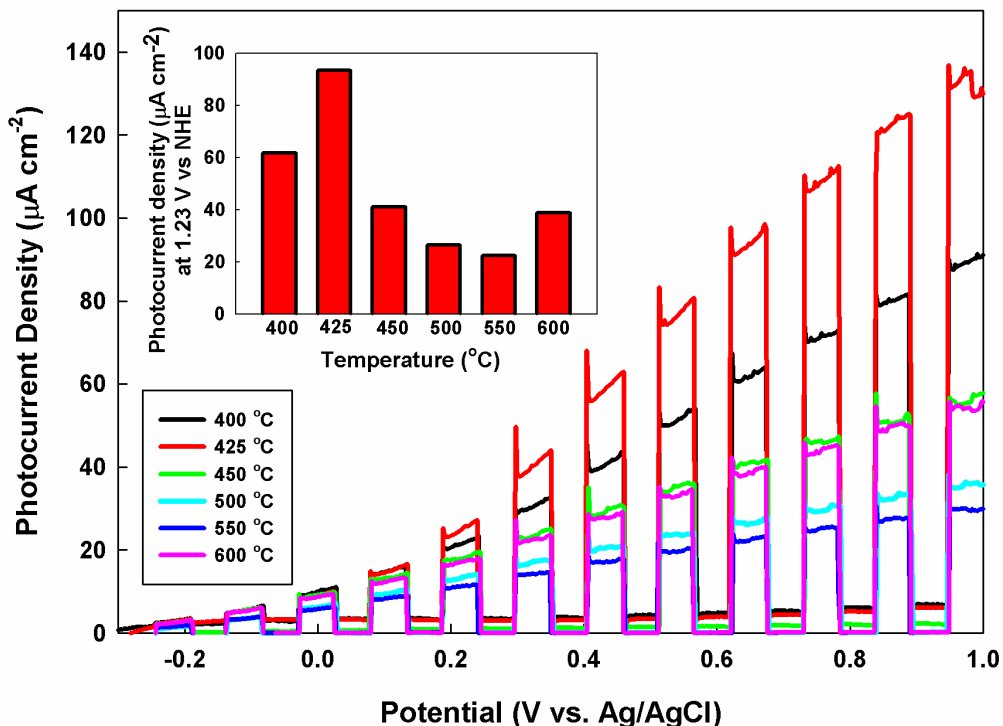


Figure 6-6. The chopped photocurrent density-applied potential plot of conventionally annealed electrodeposited Zn electrodes at various temperatures. Inset shows photocurrent densities obtained for the electrodes at 1.23 V vs. NHE annealed at corresponding temperatures using conventional heating.

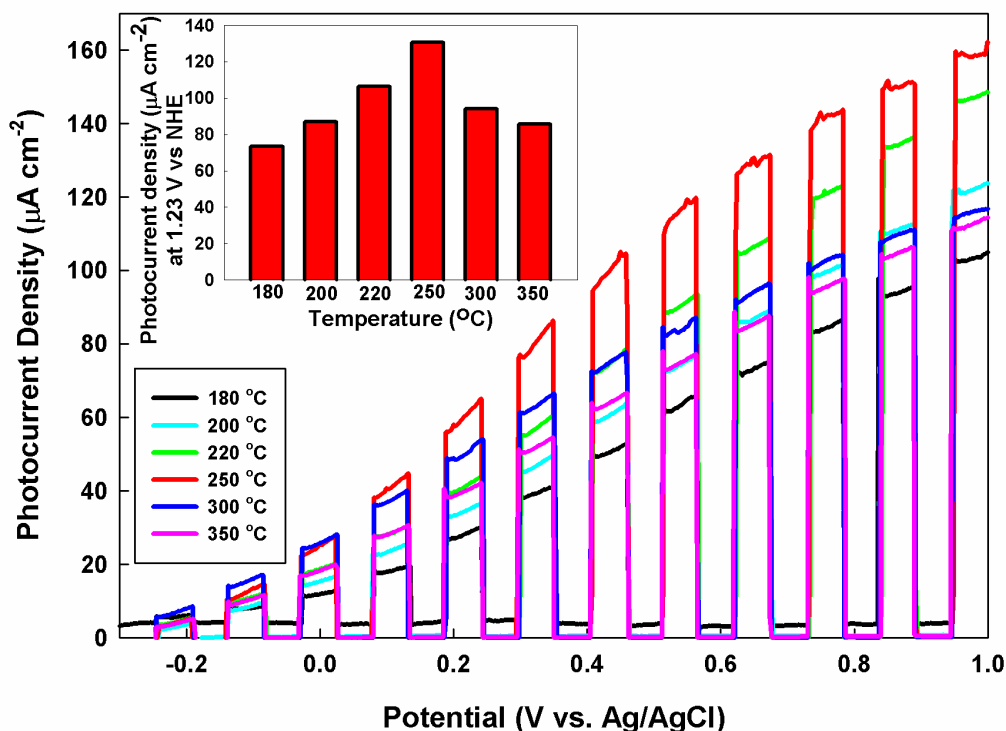


Figure 6-7. The chopped photocurrent density-applied potential plot of microwave annealed electrodeposited Zn electrodes at various temperatures. Inset shows photocurrent densities

obtained for the electrodes at 1.23 V vs. NHE annealed at corresponding temperatures using microwave heating.

Figure 6-8 compares the highest PEC performance obtained for conventional and microwave treated samples and the inset represents the highest photocurrent density obtained at 1.23 V vs. NHE. The maximum photocurrent (at 1.23 V vs. NHE) achieved by conventional thermal annealing was $93 \mu\text{A cm}^{-2}$, whereas the maximum photocurrent achieved for the microwave annealed sample was $130 \mu\text{A cm}^{-2}$, which was 40% higher.

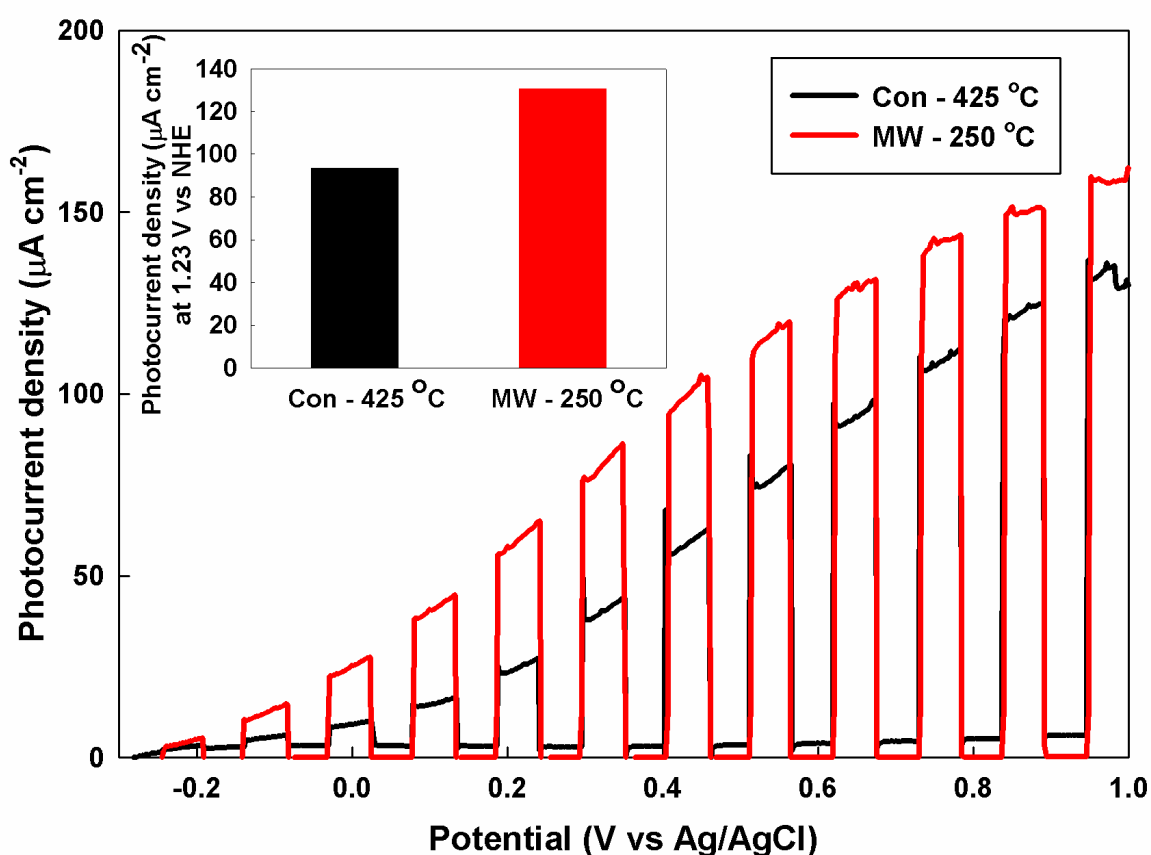


Figure 6-8. The plot of photocurrent density vs. applied potential for the electrodeposited Zn electrodes annealed at 425 °C for 15 min and 250 °C for 3 min using conventional and microwave heating respectively. Inset shows the photocurrent density obtained at 1.23 V vs NHE as a function of annealing temperature for the samples.

The 40% increase in the photocurrent achieved by microwave annealing compared with conventional thermal annealing could be attributed to three possible factors – an increase in crystallinity, more efficient oxidation of Zn to ZnO and higher surface area. Evidence for

these factors has already been seen in the XRD patterns and SEM images. For the best performing conventionally annealed sample (at 425 °C) the XRD pattern showed the presence of unconverted Zn. No such peak was seen for the microwave annealed sample, which therefore shows a complete oxidation to ZnO at low temperatures. Also, it can clearly be seen from the intensity of the ZnO reflections in the XRD patterns that the crystallinity of the microwave annealed sample is higher. The increase in the photocurrent also was confirmed by IPCE measurements conducted at 1.23 V vs. NHE, shown in figure 6-9. An IPCE of 4.5% and 6% was observed for the conventionally and microwave oxidised samples, respectively. This confirms the increase in charge generation most likely due to the increased surface area.

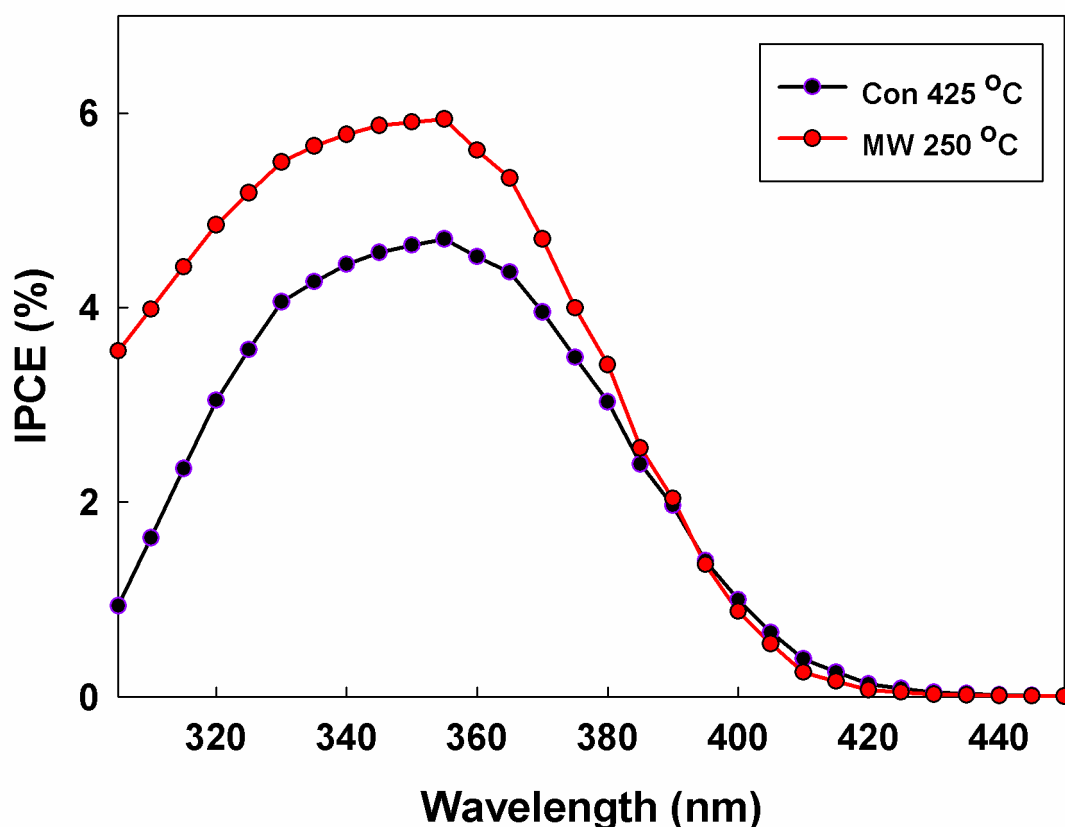


Figure 6-9. IPCE spectra as a function of wavelength at 1.23 V vs. NHE for electrodeposited Zn electrodes annealed under conventional and microwave radiation at 425 °C for 15 min and 250 °C for 3 min respectively.

6.4.5 Temperature-time profile

The benefit of using microwave radiation as an alternative to the conventional thermal annealing method is demonstrated by the temperature-time profiles. Figure 6-10 depicts the temperature-time profiles of both the annealing processes in a conventional furnace and in a microwave furnace for the samples with best PEC performance under each method. The area under the graph (not including the cooling process), roughly estimates the energy consumed during each annealing process, and shows that microwave annealing requires only 25% of the energy needed for conventional thermal annealing while operating at nearly one tenth of the maximum power level. Moreover, the microwave method also produced ZnO electrodes with 40% higher photocurrent than that of the conventionally annealed electrodes.

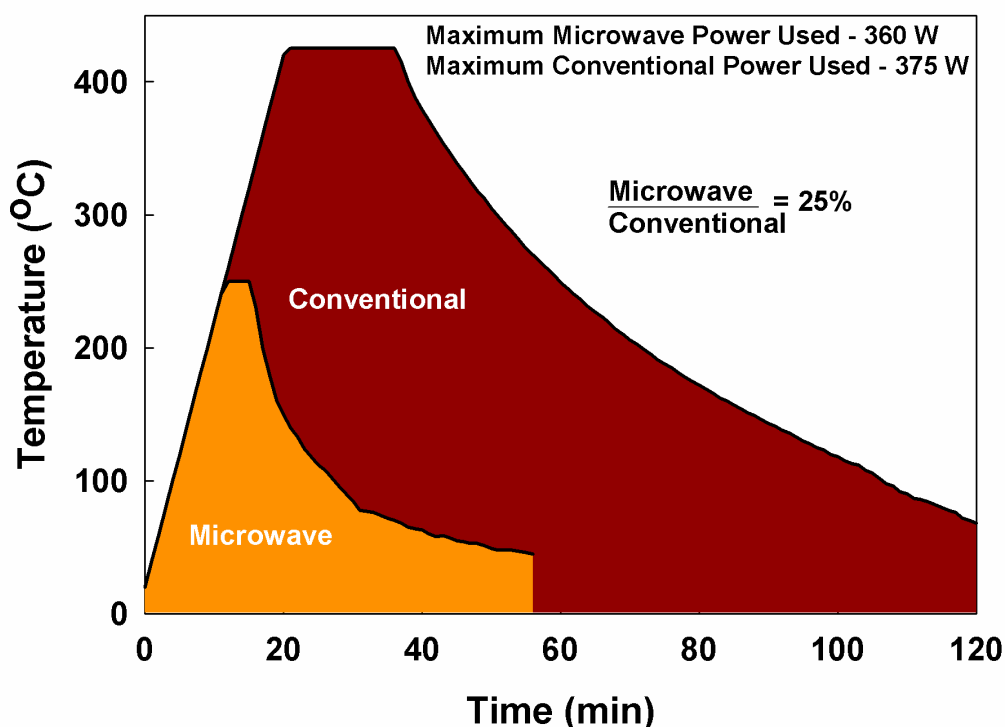


Figure 6-10. Temperature-time profile of the samples annealed at 425 and 250 °C for 15 and 3 min using conventional and microwave-assisted annealing respectively. The maximum power used at the soaking temperature corresponding to each annealing technique is also mentioned.

6.5 Conclusions

The oxidation of electrodeposited Zn films to ZnO was conducted using microwave and conventional thermal annealing methods at various temperatures and comparisons were drawn. A 40% higher photocurrent (at 1.23 V vs. NHE) was achieved for the microwave annealed films compared to their conventionally annealed counterparts. XRD patterns showed that the oxidation of Zn to ZnO was not 100% efficient as evidence for metallic Zn was seen. For the conventionally annealed film the highest performing film showed unconverted Zn whereas a microwave annealed film did not show any sign of Zn. The improvement in the PEC properties was attributed to higher surface area, confirmed by SEM surface topographical analysis, and better yields of Zn oxidation to ZnO, and higher crystallinity. It was found that the higher temperatures used in the thermal annealing result in sintering of the nanostructure which reduces the overall surface area. However, in contrast to conventional thermal annealing, microwave annealing preserves the nanostructure of the electrodes due to the difference in the heating mechanism (volumetric heating). Microwave annealing allowed complete oxidation to ZnO with excellent crystallinity. Also oxidation using microwave annealing was achieved five times faster. The techno-economic impact was considered by assessing the overall energy usage. This evaluation shows that the microwave annealing method offers energy savings of up to ~75%, which would make it highly desirable for industrial scale up. Also the lower oxidation temperatures could open up possibilities for ZnO processing for low temperature flexible substrates.

Chapter 7

Microwave-assisted synthesis and processing of inorganic materials for electronic and optoelectronic applications

7.1 Microwave assisted in-situ activation of lattice oxygen of TiO_2 by Pd^{2+} ion; Microwave-assisted synthesis of $\text{Ti}_{0.97}\text{Pd}_{0.03}\text{O}_{1.97}$ powders

7.1.1 Overview

Microwave-assisted chemistry is becoming very attractive in organic and inorganic synthesis due to its advantages over conventional heating methods. $\text{Ti}_{0.97}\text{Pd}_{0.03}\text{O}_{2-\delta}$ powder samples have been synthesised by conventional and microwave-assisted methods. The X-ray diffraction (XRD) shows that the observed reflections correspond to the anatase phase of TiO_2 for both conventional and microwave assisted methods. However, the absence of Pd metal or PdO diffraction lines in XRD diffractograms confirmed that the Pd ions are substituted in TiO_2 . The corresponding anatase reflections are more intense and notable for the $\text{Ti}_{0.97}\text{Pd}_{0.03}\text{O}_{1.97}$ sample synthesised using microwave-assisted method compared to the conventional synthesised method. The Raman spectra do not show any significant difference of the Raman peaks for the powders made by these two methods. The field emission gun scanning electron microscope (FEG-SEM) surface topography images showed a significant difference in the shape and the size of the $\text{Ti}_{0.97}\text{Pd}_{0.03}\text{O}_{1.97}$ powder synthesised by microwave-assisted and conventional methods. The average crystallite size of $\text{Ti}_{0.97}\text{Pd}_{0.03}\text{O}_{1.97}$ synthesised using microwave radiation is found to be in the range of 1-2 nm which is much smaller than the reported value for $\text{Ti}_{0.97}\text{Pd}_{0.03}\text{O}_{1.97}$ made by conventional method. The Brunauer–Emmett–

Teller (BET) measurements further confirm that the microwave synthesised $\text{Ti}_{0.97}\text{Pd}_{0.03}\text{O}_{1.97}$ powder has a slightly higher surface area ($244 \text{ m}^2/\text{g}$) than the conventionally synthesised powder which is $210 \text{ m}^2/\text{g}$.

7.1.2 Introduction

In recent years, microwaves are being explored as an efficient alternative energy source to traditional forms of heating (i.e. isomantles, oil baths, hot plates etc.) in material synthesis.[255] It has been shown that the use of microwave radiation for material synthesis has shown promising results over conventional heating methods in terms of the product yield and the reaction rate.[256] Over the past few decades, most of the microwave heating in chemistry has been limited to organic synthesis. More recently the use of microwave radiation for heating reactions in the laboratory has expanded to inorganic and materials chemistry.[257]

Titanium dioxide (TiO_2) has attracted extensive interest because of its wide applications in photocatalysis,[258] chemical sensors,[259] solar cells,[260] and hydrogen storage materials.[261] Due to the wide band gap of TiO_2 ($E_g - 3.2 \text{ eV}$) it has limitations for practical applications as it absorbs only from the UV region of the solar spectrum. Due to the poor charge generation and high recombination rates of photogenerated electron-hole pairs in TiO_2 electrodes results undesirable impact on such applications.[209] To overcome these difficulties, much effort has been made to modify TiO_2 nanoparticles by incorporating platinum group metals (i.e. Pd, Ru, Rh, Pt) into the structure.[262] The incorporation of these metal ions into the anatase phase of TiO_2 activates the lattice oxygen, which is of great interest due its ability to act as an active site for catalytic oxidation–reduction reactions.[263]

Among the other platinum group metals, palladium is the cheapest and most commonly used metal for such applications.

Microwave-assisted incorporation of Pt group metal ions into the structure of anatase TiO_2 is very attractive because it gives competitive advantages over other conventional synthesis methods. This section of the chapter reports the structural and morphological changes of Pd incorporated TiO_2 ($\text{Ti}_{0.97}\text{Pd}_{0.03}\text{O}_{1.97}$) synthesised using microwave-assisted and conventional synthesis methods.

7.1.3 Experimental

7.1.3.1 Synthesis of $\text{Ti}_{0.97}\text{Pd}_{0.03}\text{O}_{1.97}$ by traditional method

$\text{Ti}_{0.97}\text{Pd}_{0.03}\text{O}_{1.97}$ was prepared by solution combustion method.[264] In the synthesis 9.7 mmol of $\text{TiO}(\text{NO}_3)_2$ solution is taken, which is prepared by $\text{Ti}(\text{OC}_3\text{H}_7)_4$ (sigma Aldrich), 0.3 mmol of $\text{Pd}(\text{NO}_3)_2$ (Alfa Aesar), and 1.11 mmol of glycine (sigma Aldrich) as fuel in a 300 mL crystallizing dish. The components were fully dissolved in 15 mL of water. The solution was kept in a preheated conventional furnace at 350 °C for 2 hrs. The combustion takes place after the dehydration and the solid product is left behind.

7.1.3.2 Synthesis of $\text{Ti}_{0.97}\text{Pd}_{0.03}\text{O}_{1.97}$ by microwave assisted method

A solution mixture of 9.7 mmol of $\text{Ti}(\text{OC}_3\text{H}_7)_4$ (sigma Aldrich), 0.3 mmol of $\text{Pd}(\text{NO}_3)_2$ (Alfa Aesar), and 1.11 mmol of glycine (sigma Aldrich) as fuel (the self-sustained combustion process of glycine produces a high exothermic heat during the reaction which facilitates the facile intercalation of Pd^{2+} in to the TiO_2 structure) was added to the 20 mL microwave reaction vessel with a magnetic stirrer. The components were fully dissolved in 15 mL of

water. The components were fully dissolved and heated to 150 °C for 3 min. Microwave assisted synthesis was performed in a Biotage Initiator EXP 8 reactor in 10-20 mL crimped vials. After 3 min of microwave treatment, a black coloured fine solid dispersion was obtained. The solid was separated by centrifuge and kept in a desiccator overnight. The incorporation of Pd into the TiO₂ structure is qualitatively understood by the colour change of the reaction mixture after irradiated to microwaves (figure 7.1-1). The microwave reactor conditions during the microwave treatment are shown from the figure 7.1-2.

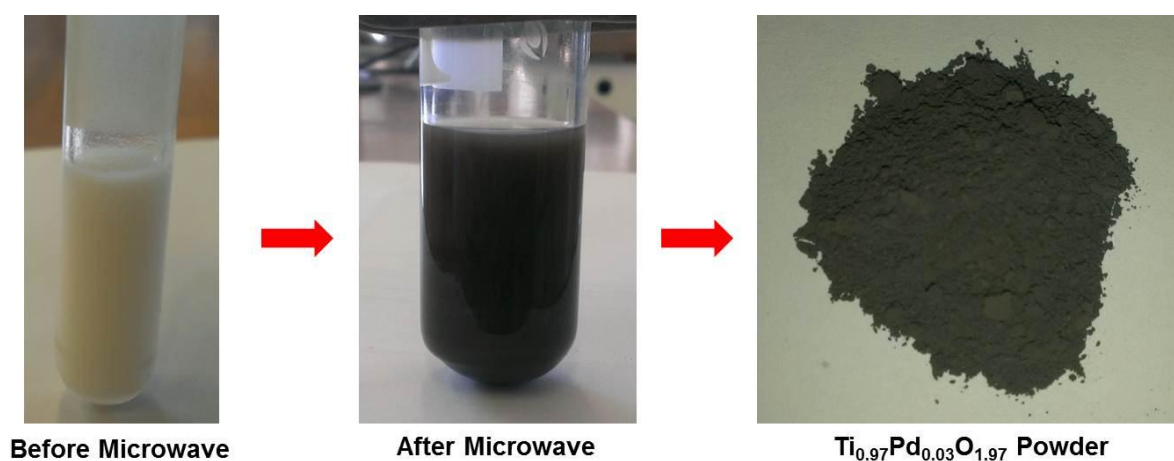


Figure 7.1-1. The images of reaction mixtures and the product at various preparation stages.

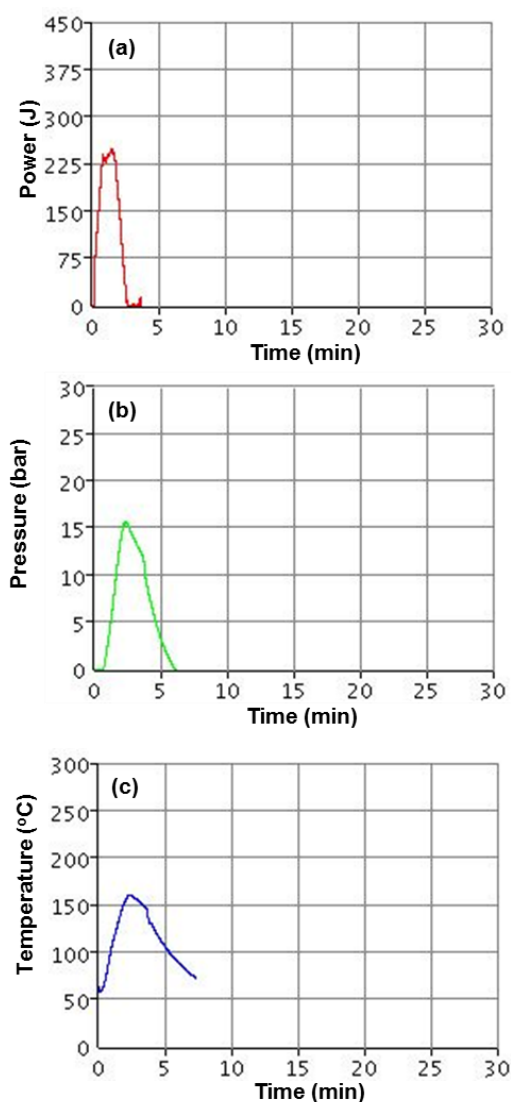


Figure 7.1-2. The microwave reactor conditions during the microwave treatment (a) power curve (b) Pressure curve (c) temperature curve.

7.1.3.3 Characterization

X-ray diffraction (XRD) analysis was employed to determine the crystalline structure of $\text{Ti}_{0.97}\text{Pd}_{0.03}\text{O}_{1.97}$ powder samples using Bruker D8 XRD, operating with monochromatic Cu K_α ($\lambda = 1.54 \text{ \AA}$) radiation and PSD detector. The Jobin -Yvon LabRam HR 800 (He-Ne laser (632.8 nm) / CCD detector) Raman spectroscope was used to obtain the Raman spectra. The surface morphology of the powders was obtained using a field emission gun scanning electron microscopy (FEG-SEM, Leo 1530 VP) at an accelerating voltage of 5 keV and

working distance of 5 mm. The Brunauer–Emmett–Teller (BET) measurements were conducted at Johnson Matthey Technology Centre, Sonning Common UK.

7.1.4 Results and Discussion

7.1.4.1 Structural characterization

The reported XRD diffractograms of Pd²⁺ ion substituted TiO₂ (i.e. Ti_{0.97}Pd_{0.03}O_{1.97}) is shown in Figure 7.1-3. The patterns are indexed to anatase TiO₂ polymorph of TiO₂ (Tetragonal, I4₁/amd, JCPDS no. 21-1272).[264]

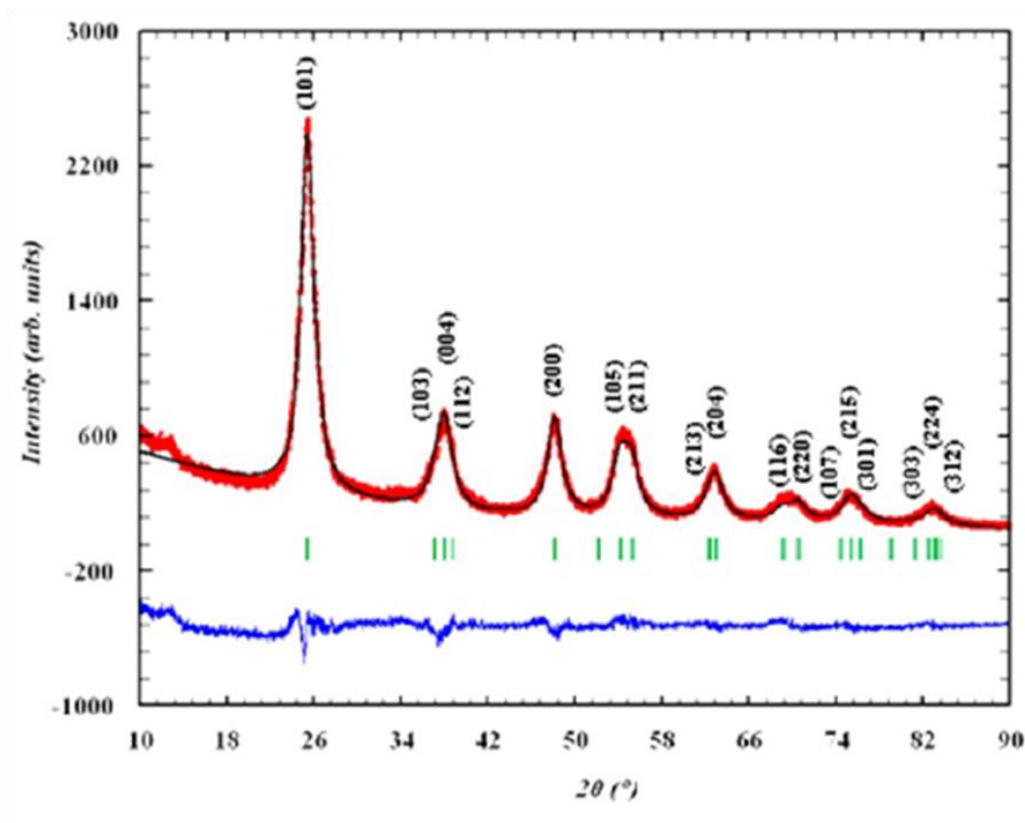


Figure 7.1-3. The rietveld refined XRD profile of Ti_{0.97}Pd_{0.03}O_{1.97}. [264]

Figure 7.1-4 indicates that the XRD reflections obtained for Ti_{0.97}Pd_{0.03}O_{1.97} which was synthesised using the reported method and microwave-assisted method. The reflections

correspond to anatase TiO₂ is observed in both conventional and microwave heating methods. The absence of Pd metal or PdO diffraction lines in Figure 7.1-3 and 7.1-4 indeed confirm that the Pd ions are substituted in TiO₂ structure. However, the corresponding anatase reflections are more intense and distinguished for the Ti_{0.97}Pd_{0.03}O_{1.97} sample synthesised using microwave irradiation which indicates that microwave-assisted synthesis enhances the anatase crystalline phase of TiO₂.

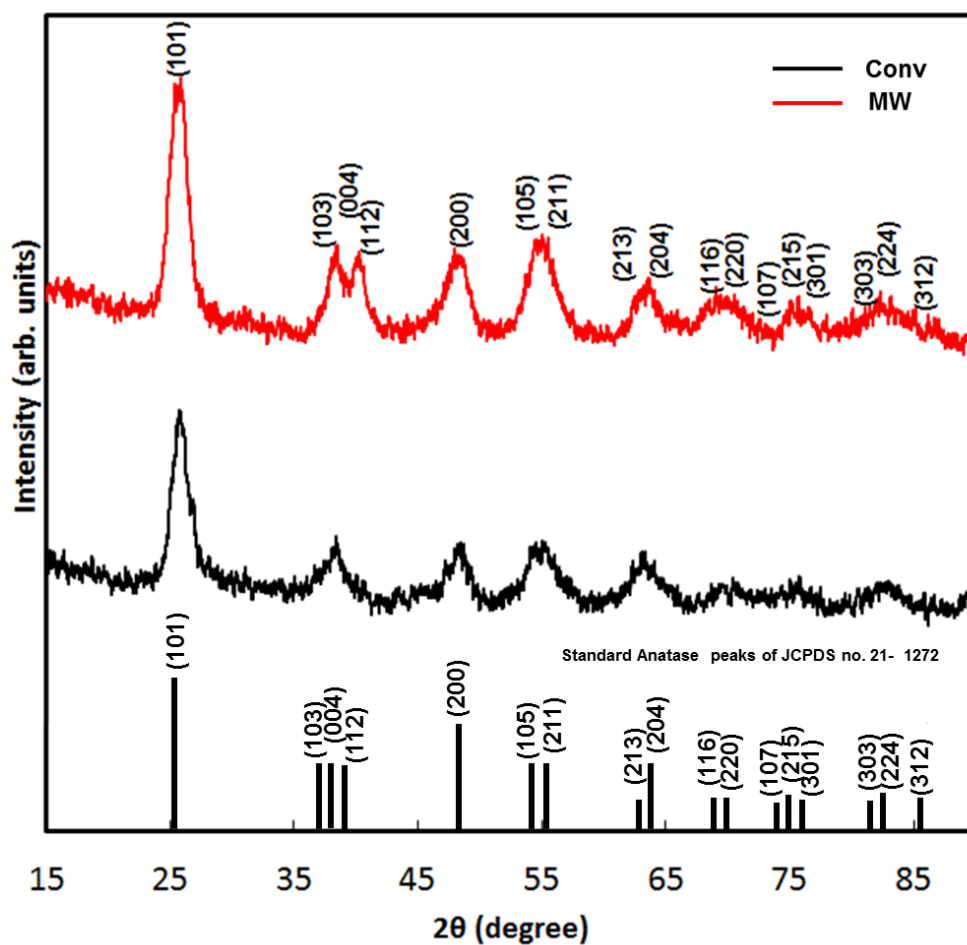


Figure 7.1-4. XRD reflections obtained for Ti_{0.97}Pd_{0.03}O_{1.97} powder samples made using conventional and microwave assisted methods.

Figure 7.1-5 illustrates the Raman peaks corresponding to Ti_{0.97}Pd_{0.03}O_{1.97} powder samples. The Raman spectra do not show any significant difference of the Raman peaks of corresponding anatase phase of TiO₂ at 153, 400, 503, 635 cm⁻¹ for the powders made by

these two methods. However, the peak height of the microwave-assisted $\text{Ti}_{0.97}\text{Pd}_{0.03}\text{O}_{1.97}$ sample is comparatively high compared to the conventionally made sample.

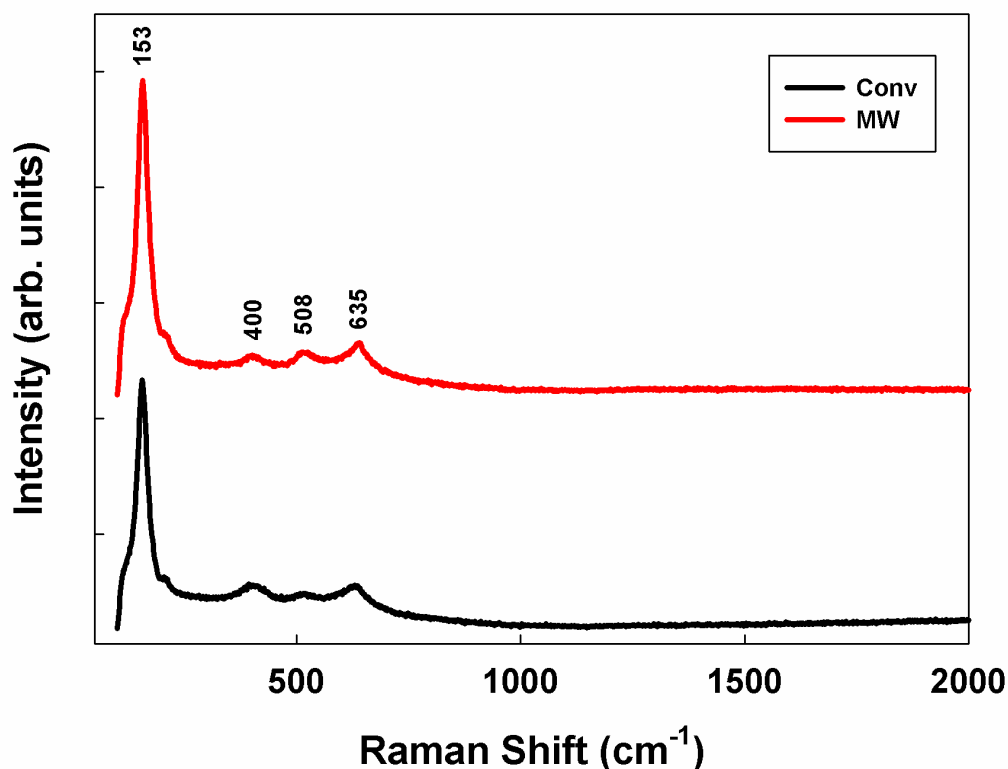


Figure 7.1-5. The Raman spectra obtained for $\text{Ti}_{0.97}\text{Pd}_{0.03}\text{O}_{1.97}$ under conventional and microwave assisted methods.

7.1.4.2 Surface morphology

The FEG-SEM surface topography images showed a significant difference in the shape and the size of $\text{Ti}_{0.97}\text{Pd}_{0.03}\text{O}_{1.97}$ synthesised by microwave-assisted and conventional methods. Figure 7.1-6 shows the SEM images of $\text{Ti}_{0.97}\text{Pd}_{0.03}\text{O}_{1.97}$ powder from the microwave-assisted synthesis and figure 7.1-7 indicates the morphology of the conventionally made powder. In microwave assisted synthesis the powder consisted of spherical nanoparticle clusters, whereas in the conventional method the particles look like disks (layer structure) with much larger particle size. It is clear that microwave radiation improves the crystal growth to form

highly porous spherical nanocrystallites which leads to a higher internal surface in the powder.

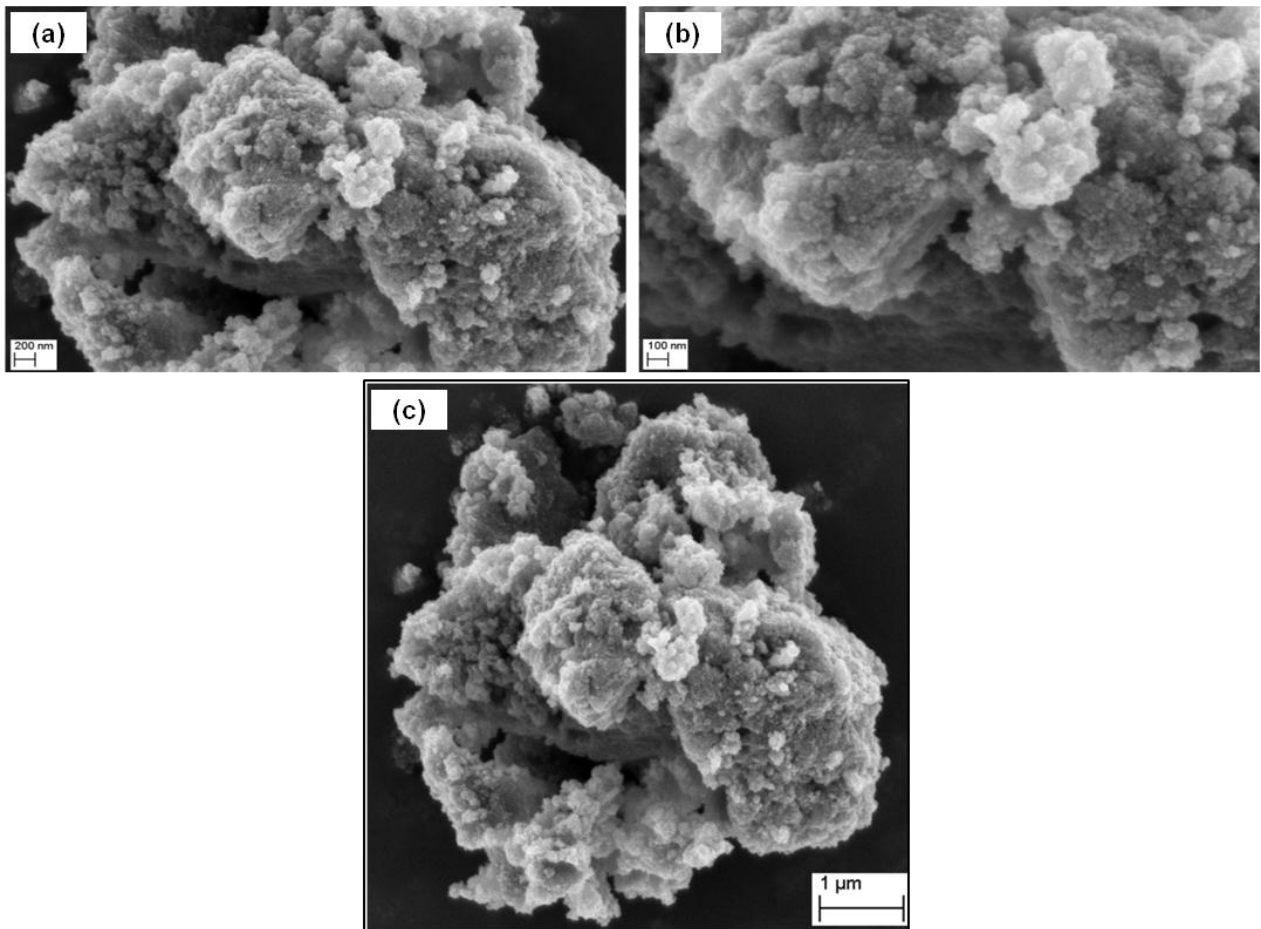


Figure 7.1-6. The SEM images of $\text{Ti}_{0.97}\text{Pd}_{0.03}\text{O}_{1.97}$ powder synthesised using microwave radiation.

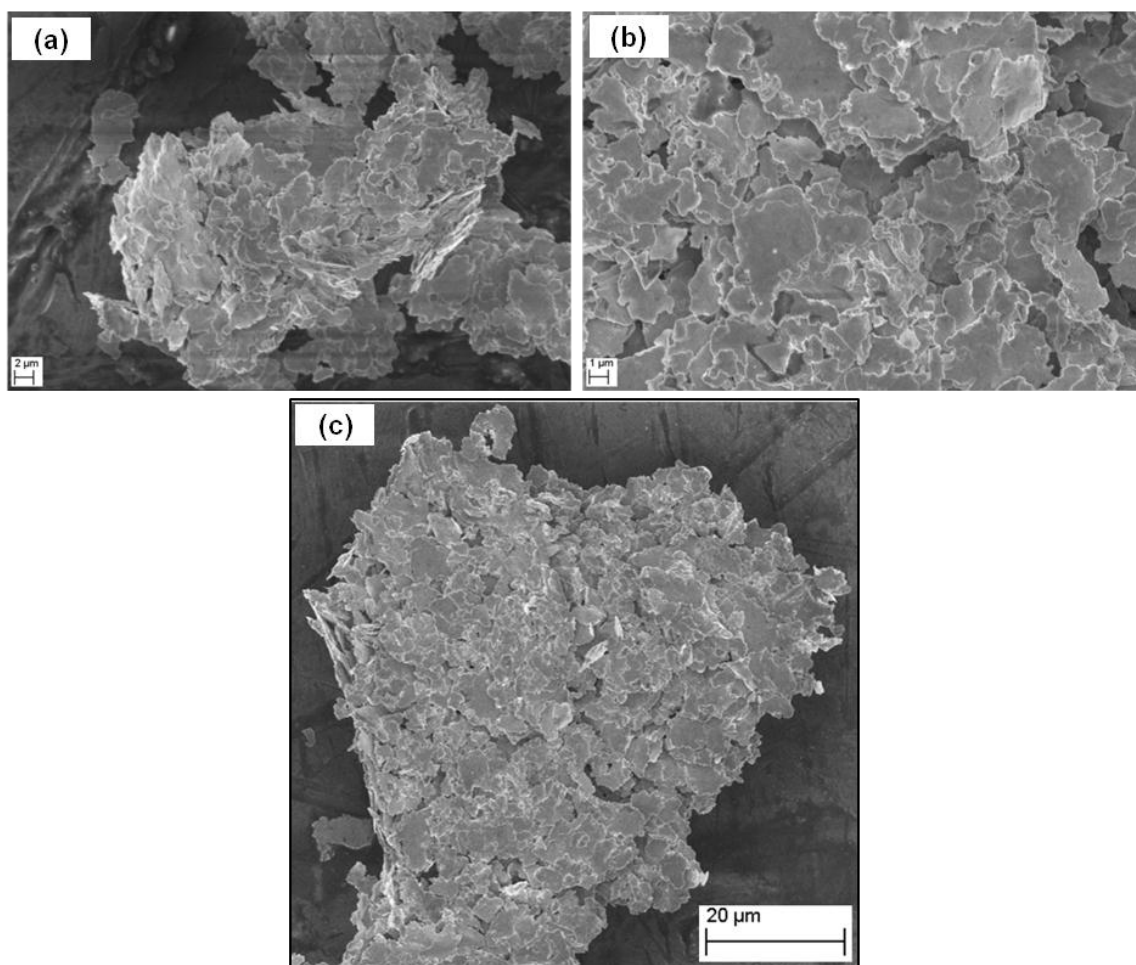


Figure 7.1-7. The SEM images of $\text{Ti}_{0.97}\text{Pd}_{0.03}\text{O}_{1.97}$ powder synthesised by conventional method.

The surface topographical images confirmed that the average crystallite size of $\text{Ti}_{0.97}\text{Pd}_{0.03}\text{O}_{1.97}$ synthesised using microwave radiation is found to be in the range of 1-2 nm. However, the size is much smaller than the reported value for $\text{Ti}_{0.97}\text{Pd}_{0.03}\text{O}_{1.97}$ made by conventional method which is in the range of 13 ± 2 nm. The particle size of the composite made by conventional method is higher than the reported value; it is in the range of 1-3 μm . The Brunauer–Emmett–Teller (BET) measurements indicated that the microwave synthesised $\text{Ti}_{0.97}\text{Pd}_{0.03}\text{O}_{1.97}$ powder has a slightly higher surface area ($244 \text{ m}^2/\text{g}$) than the conventionally synthesised powder which is $210 \text{ m}^2/\text{g}$.

7.1.5 Conclusions

$\text{Ti}_{0.97}\text{Pd}_{0.03}\text{O}_{1.97}$ was prepared by solution combustion method crystallizing in anatase TiO_2 structure. The compound was synthesised by using conventional sintering and microwave sintering methods and compared structural and morphological differences. The XRD patterns confirmed that the corresponding reflections of anatase phase has increased by microwave assisted synthesis than the conventional method. Raman spectroscopy indicated that the phases and the structure of the compound prepared by microwave and conventional methods were in good agreement. The SEM images confirmed a significant difference in the shape and the size of $\text{Ti}_{0.97}\text{Pd}_{0.03}\text{O}_{1.97}$ crystallites made under conventional and microwave methods. The average crystallite size of $\text{Ti}_{0.97}\text{Pd}_{0.03}\text{O}_{1.97}$ synthesised under microwave radiation is found to be in the range of 1-2 nm which is much smaller than the reported value for $\text{Ti}_{0.97}\text{Pd}_{0.03}\text{O}_{2-\delta}$ under conventional heating method. The BET measurements further confirmed that the microwave synthesised $\text{Ti}_{0.97}\text{Pd}_{0.03}\text{O}_{1.97}$ powder has slightly higher surface area than the conventionally synthesised powder which is well agreed with the surface topographical images.

7.2 The effect of post annealing on the electrical conductivity of lithium aluminium titanium phosphate pellets

7.2.1 Overview

Nowadays, lithium ion batteries are widely used in our daily life as they are the main power source for the most mobile devices. Electrolytes with high conductivity, good mechanical properties and good chemical stability are essential to be used in lithium ion batteries. Lithium aluminum titanium phosphate (LATP) is a potential inorganic solid electrolyte for lithium ion batteries with NASICON (Na-Super-Ionic-Conductor) type structure. Post-deposition heat treatment is one of the ways to improve ionic conductivity by enhancing the electronic communication between particles and crystallinity. In this section of the chapter, the effect of post heat treatment on the electrical conductivity of the LATP pellets by electrochemical impedance spectroscopy (EIS) is discussed. The differences in structural and morphological properties of the LATP pellets were studied using XRD, Raman spectroscopy and FEG-SEM. The XRD and Raman analysis showed that the post heat treatment increase the crystallinity of the pellets without any structural changes. The SEM images confirmed that crystallized grains of microwave treated LATP is more uniform and the crystallites are fairly small in size compared to the conventionally annealed pellets. The EIS results confirmed that the comparable conductivities to conventional annealing at 800°C for 1 hr can be obtained when the LATP pellets are irradiated with microwave for 3 min. This is attributed to formation of improved crystallinity, grain homogeneity and contacts by microwave post treatment of LATP pellets.

7.2.2 Introduction

Lithium aluminum titanium phosphate (LATP) has shown a great research interest as it is a very good candidate electrolyte material which has a comparable ionic conductivity in bulk form with the ionic conductivities currently found in the liquid-type electrolytes of Li-ion batteries.[265] Better electrochemical properties of these electrolyte materials can be obtained by varying the crystal sizes with different morphologies, homogeneity of the chemical composition with a higher phase purity and crystallinity. Post-deposition heat treatment is one of the well-known processes that can be used to enhance electronic communication between particles of these materials by improving the crystallinity and the nanostructure. In recent years, a great deal of interest has been focused on irradiation with microwaves as an alternative advanced material processing technique. This technique is capable of improving particle necking and crystallinity with a minimal effect on the material's nanostructure. In order for microwaves to interact with the material and generate heat, a balanced combination of moderate dielectric constant (to permit adequate penetration) and high loss tangent (for higher energy to heat conversion) are required. Since the dielectric properties of the materials are temperature dependent, the microwave absorption properties can be enhanced by elevating the temperature of materials using hybrid heating or microwave susceptors. This section of the chapter discusses the effect on the electrical conductivity and structural properties of microwave and conventionally treated LATP pellets.

7.2.3 Experimental

The Lithium Aluminium Titanium Phosphate (LATP) pellets (Johnson Matthey Technology Centre, Sonning Common UK) were sintered using microwaves and conventional sintering methods. The conductivity of the post treated pellets with microwave and conventional thermal methods were compared with the as prepared LATP sample. During the microwave treatment, temperature of the LATP samples was increased using a SiC tile as it generates heat rapidly when irradiated with microwaves. The monitored temperature of the microwave sample placed on SiC tile after 180 S is ~ 600 °C. Microwave treatment was performed using a furnace operating at a frequency of 2.45 GHz and 2 kW radiation power (MRF 16/22, Carbolite Ltd, UK). For comparison, temperatures of 600 °C and 800 °C were used to fire the pellets for 1 hr under conventional sintering method using a tube furnace (MTF-10-25-130, Carbolite, Hope Valley, UK) with a ramp rate of 15 °C/min to its desired temperature. Both ends of the tube were left open to allow air to flow in. After annealing, the furnace was turned off and the pellets were allowed to cool in the tube furnace to room temperature. X-ray diffraction (XRD) analysis was employed to determine the crystalline structure of LATP pellets using Bruker D8 XRD, operating with monochromatic Cu K_α ($\lambda = 1.54 \text{ \AA}$) radiation and PSD detector. The Jobin -Yvon LabRam HR 800 (He-Ne laser (632.8 nm) / CCD detector) Raman spectroscopy was used to obtain the Raman spectra. The surface morphology of the pellets was obtained using a field emission gun scanning electron microscopy (FEG-SEM, Leo 1530 VP) at an accelerating voltage of 5 keV and working distance of 5 mm. Electrochemical impedance spectroscopy measurements were carried out to determine ionic conductivity of the pellets using a potentiostat (Eco Chemie Autolab PGSTAT302N) and the measurements were performed in the frequency range from 0.01 Hz to 1 MHz. The results were analyzed using Zview Software (v3.2d, Scribner Associate, Inc.,

USA). Aluminium plates were placed either side of the pellet for the better electrical contacts for the electrical impedance measurements.

7.2.4 Results and Discussion

7.2.4.1 X-ray diffraction analysis

X-ray diffraction (XRD) analysis was employed to determine the crystalline structure of LATP pellets. Figure 7.2-1 shows the X-ray diffraction (XRD) pattern of LATP powder pellet obtained from Johnson Matthey (JM) Technology Centre UK. From the XRD reflections, it can be seen that the LATP pellets consist with two phases of $\text{LiAl}(\text{PO}_4)_3$ and $\text{LiTi}_2(\text{PO}_4)_3$ and the sharp reflections indicated that the phases are crystallized. The XRD suggested the LATP is obtained by doping Al into the major phase of $\text{LiTi}_2(\text{PO}_4)_3$ which can be indexed to a rhombohedral (R3-c) NASICON structure.[266]

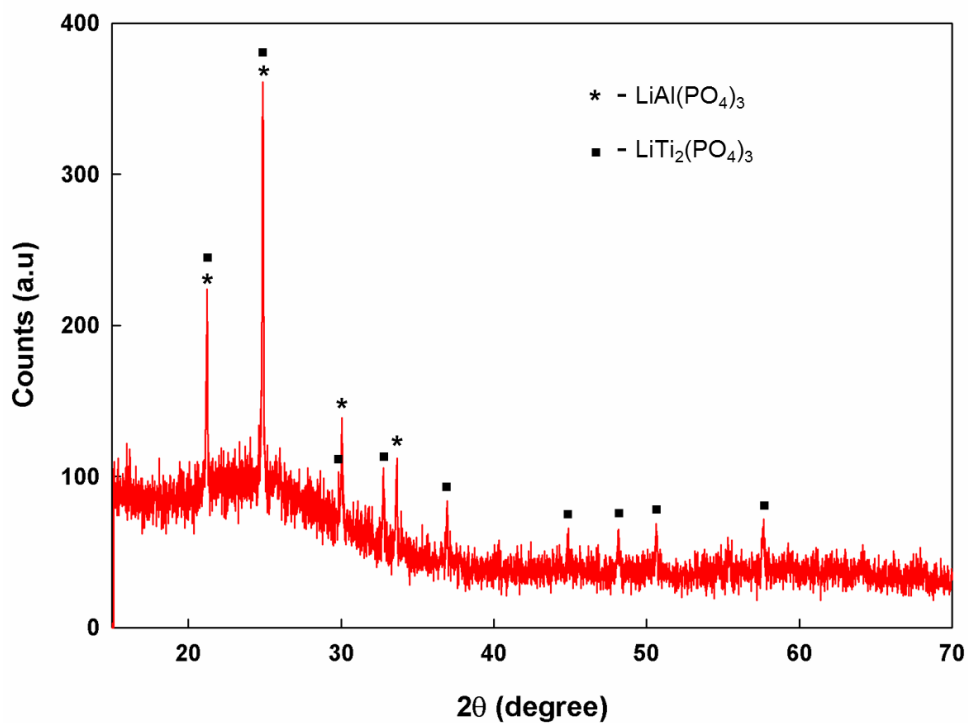


Figure 7.2-1. X-ray diffraction pattern of LATP powder pellet obtained from JM.

The figure 7.2-2 shows the XRD reflections of as prepared and post treated powder pellets. The peak intensity of post treated pellets confirmed that the crystallinity of LATP is improving with the conventional and microwave heating without any structural changes. The major 2 reflections correspond to mixed phases of LATP at 21° and 25° significantly increased with microwave treatment and conventional heating at 800°C . The crystallinity of conventionally annealed samples at 800°C for 1 hr is slightly higher than microwave treated and conventionally annealed samples 600°C . However, microwave treated pellet at 600°C for 3 min showed a better crystallinity than the conventionally annealed sample at 600°C for 1 hr.

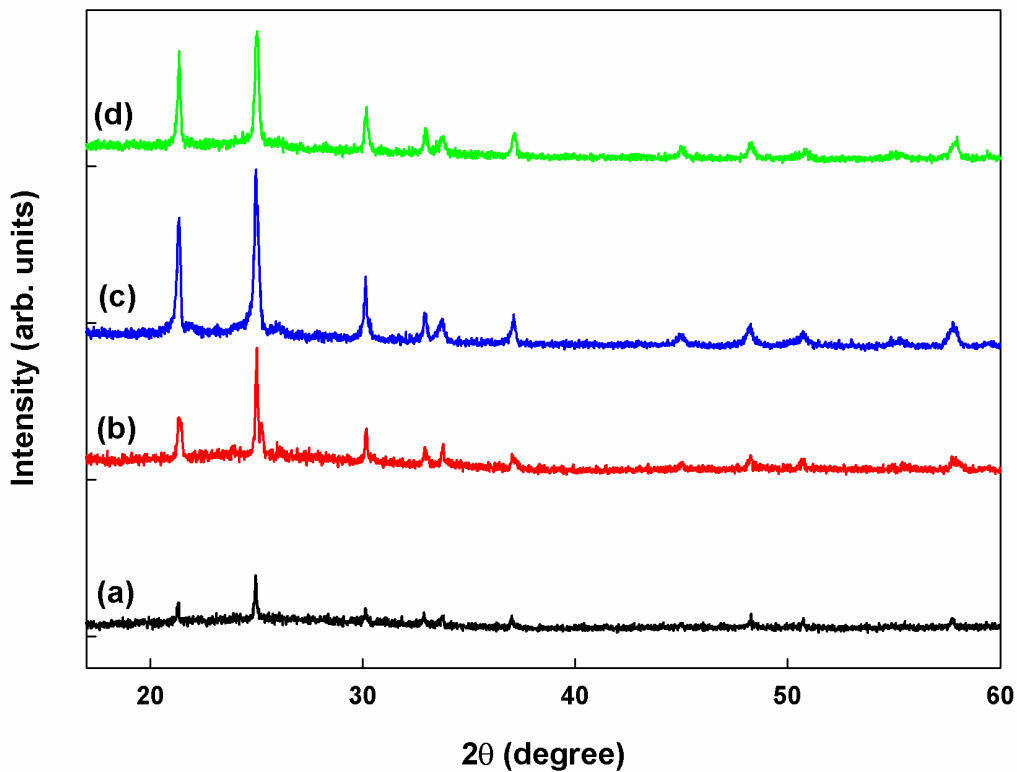


Figure 7.2-2. The XRD reflections of (a) as-prepared, (b) conventionally annealed at 600°C (c) conventionally annealed at 800°C and (d) microwave treated LATP pellets.

7.2.4.2 Raman analysis

The figure 7.2-3 shows the Raman spectra of as prepared, conventionally annealed and microwave treated LATP pellets. In the Raman spectra several strong broad Raman bands are appeared mainly in the ranges of 300–500 and 900–1300 cm^{-1} . The observed Raman peaks agree well with the published results for $\text{Li}_{1.3}\text{Al}_{0.3}\text{Ti}_{1.7}(\text{PO}_4)_3$. [267] The bands in the range of 300–500 cm^{-1} are assigned to symmetrical bending vibrations of PO_4 group, while those in 900–1100 and 1100–1300 cm^{-1} are ascribed to the stretching vibrations of PO_3 and PO_2 in LATP sample respectively. The intensity of the Raman bands increased after conventional and microwave post annealing. Microwave treated LATP showed very sharp peaks compared to the conventionally annealed samples. The Raman analysis confirmed that there is no structural change in the LATP pellets after microwave or conventional annealing as there are no peak shifts observed in the spectra.

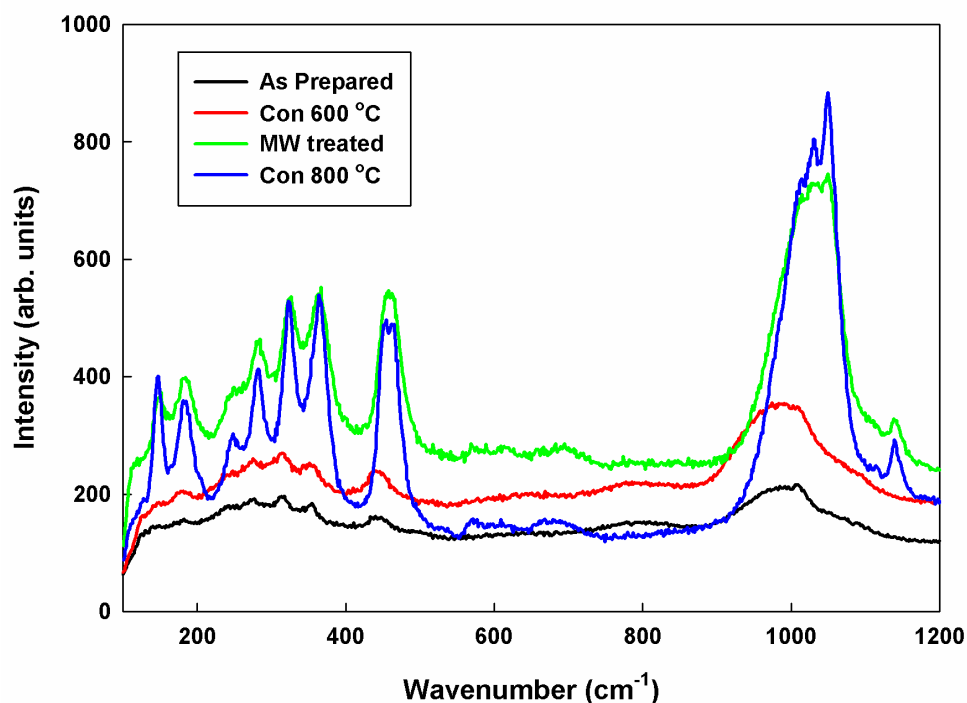


Figure 7.2-3. Raman spectra of as-prepared, conventionally annealed at 600 °C and 800 °C and microwave treated LATP pellets.

7.2.4.3 Morphology and microstructure

The scanning electron microscopy (SEM) images of as-prepared, microwave irradiated and conventionally annealed LATP pellets are shown in figure 7.2.4. It is interesting that the edges of the crystallites of microwave treated LATP pellets are smoother compared to conventionally annealed samples. The average crystallite size of as-prepared, microwave treated and conventionally annealed LATP pellets is about 1- 1.5 μm , 0.5 μm and 1 μm respectively. The crystallized grains of microwave treated LATP are more uniform than conventionally annealed pellets. Due to the difference in the heating profile of microwave and conventional annealing, it is highly likely that comparatively large crystallites will be obtained by melting the agglomerated small crystallites during the conventional sintering process. The difference in particle size and uniformity may be the factors affecting the electrochemical performance of the LATP crystallites.

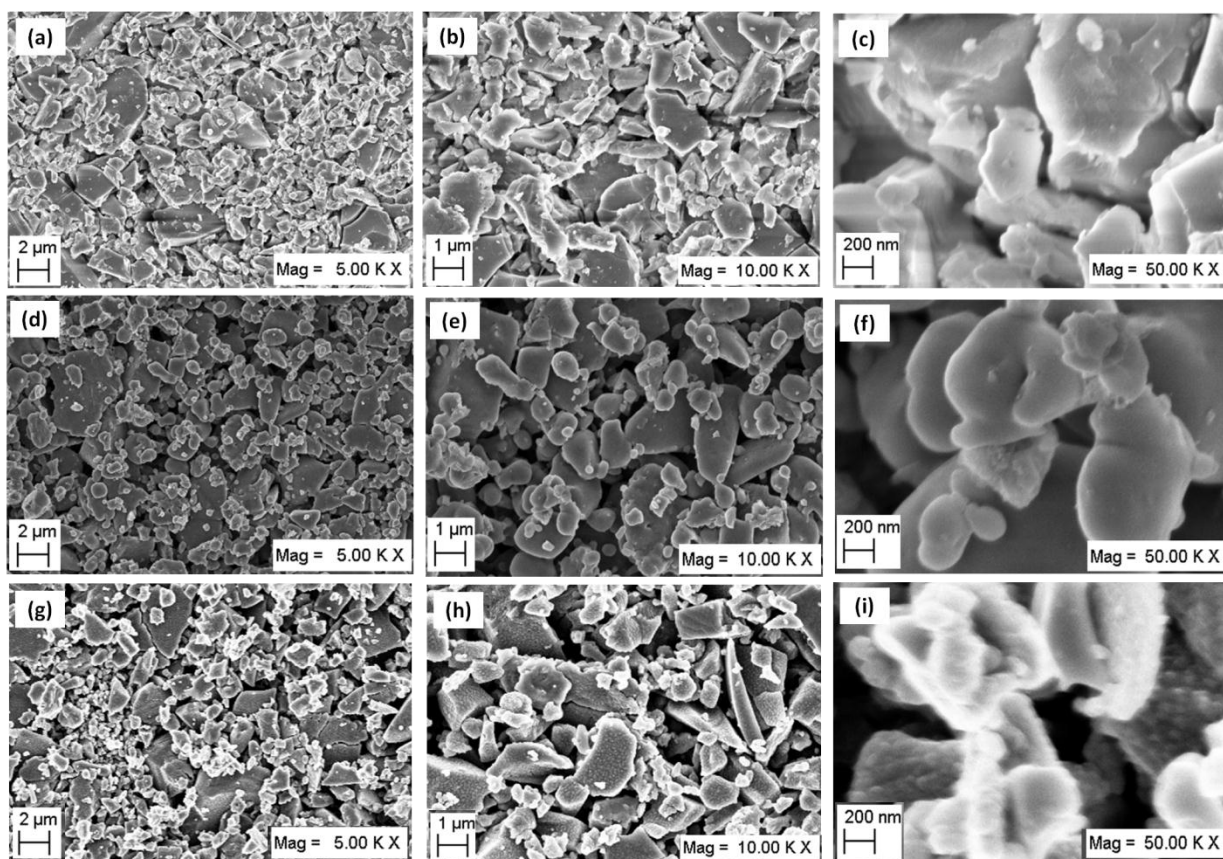


Figure 7.2-4. The SEM images of LATP pellets; (a-c) as-prepared, (d-f) microwave irradiated and (g-i) conventionally annealed at 800 °C.

7.2.4.3 Impedance analysis

The conductivity properties of LATP pellets are critical to its practical application in Li ion batteries. The ionic conductivity was studied by electrochemical impedance spectroscopy (EIS). In EIS measurements are presented in Nyquist plots as shown in figure 7.2.5.

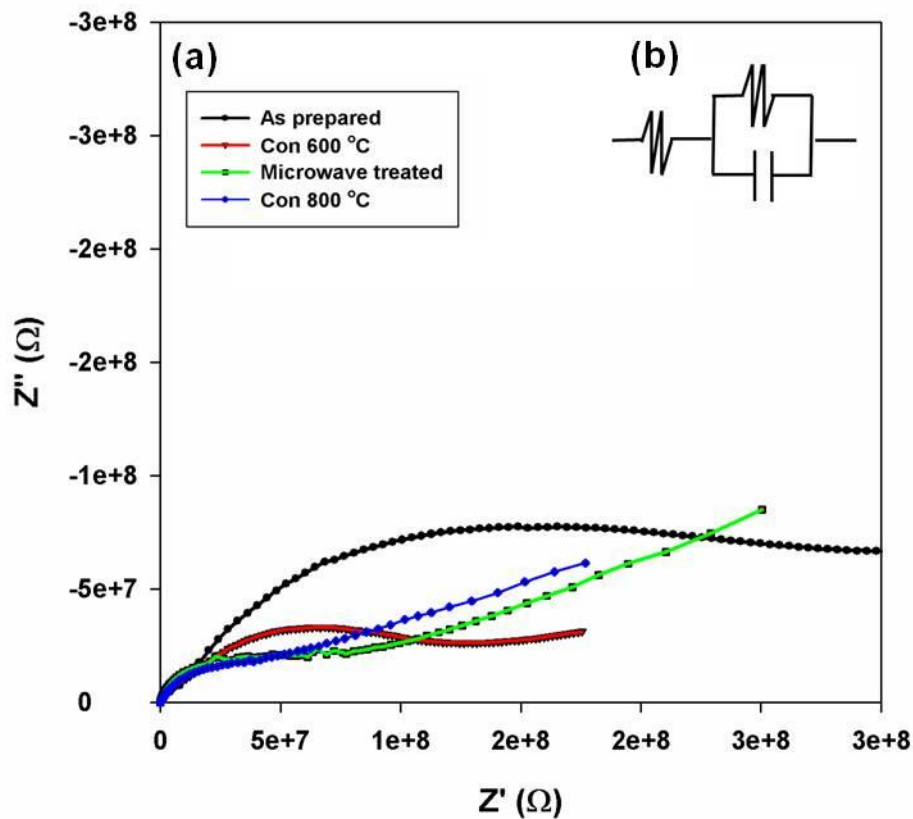


Figure 7.2-5. Nyquist plots of (a) as-prepared and post treated LATP pellets (b) the respective equivalent circuit model.

The total resistance of the LATP pellet can be determined from the Nyquist plots. The total ionic resistance of a LATP pellet is a combination of bulk (R_b) and grain boundary (R_{gb}) resistance of the pellet. The R_b can be obtained from the left intercept of the semicircle with the real axis (Z') whereas R_{gb} can be acquired from the right intercept of the semicircle with the Z' . The semi-circles in the complex plane indicate that the post treatment greatly reduces the total resistance of LATP pellets. With the conventional and microwave treatment the semicircles move to higher frequencies (to the left). It is clear that with the conventional and microwave treatment, the equivalent resistance decrease which means the conventional and microwave annealing decrease especially the R_b of LATP. However, the effect on R_b by

microwave annealing is much more pronounced than the conventionally annealed sample at 600 °C. The resistance of microwave treated sample for 3 min is almost same with the conventionally annealed sample at 800 °C for 1 hr. The values of R_b and R_{gb} are used to calculate the total conductivity by the following equation 19.

$$\sigma = \frac{d}{AR} \quad (19)$$

where d is the thickness of pellet, A is the area of the electrode and R is the total resistance ($R_b + R_{gb}$) obtained from the Nyquist plot. The calculated total conductivities of as-prepared and post treated LATP pellets are summarised in table 4. The table shows that the almost the same conductivity of sample conventionally annealed at 800 °C for 1hr can be obtained under microwave treatment for 3 min on SiC tile.

Table 4. The summary of the total conductivities of as-prepared and post treated LATP pellets.

Sample	Total Resistance (M Ω)	Conductivity x 10 ⁻⁸ (Sm ⁻¹)
As-prepared	312	2.83
Microwave treated	80	11.10
Conventional (600 °C)	131	6.77
Conventional (800 °C)	72	12.31

7.2.5 Conclusions

Lithium aluminium titanium phosphates (LATP) pellets were obtained from Johnson Matthey (JM) Technology Centre UK. The pellets were post annealed using microwave radiation and conventional thermal heating. As-prepared and treated pellets were compared in order to find the differences in the structural, morphological and electrical properties using XRD, Raman, SEM and EIS. The XRD and Raman analysis showed that the post heat treatment increased the crystallinity of the pellets without causing any structural changes. The SEM images confirmed that crystallized grains of microwave treated LATP were more uniform and the crystallites were fairly small compared to the conventionally annealed pellets. The EIS results confirmed that the comparable conductivities to conventional annealing at 800 °C for 1 hr could be obtained when the LATP pellets were irradiated with microwave for 3 min. The enhancement in the ionic conductivity in microwave treatment is due to the uniformity and the lower resistance of the LATP crystallites acquired from better sintering characteristic from the microwave post treatment. Therefore, microwave post treatment of LATP is more advantageous than conventional annealing in terms of energy saving and the production cost.

Chapter 8

8.1 Conclusions

Microwave processing of materials is a relatively novel technology advancement alternative to conventional sintering that offers new approaches to improve the physical properties of materials as well as economic advantages through energy savings and accelerated product development. Microwave irradiation has shown a great potential for processing of different inorganic solids and semiconductor materials. The main aim of this thesis was to understand the microwave effect on various materials and then investigate the viability of using them in various advance optoelectronic devices.

TiO₂ is one of the most widely used semiconductor materials for various optoelectronic devices; therefore the microwave effect on such materials has been studied. The AACVD method was used to deposit TiO₂ electrodes on FTO-glass substrates at 350 and 400 °C. The deposited electrodes were irradiated with different percentages of microwave radiation (10, 25, 50 and 100%) and the electrodes showed improved photoelectrochemical performance when irradiated with more power level percentages of microwave radiation. The XRD analysis confirmed that the deposited films has anatase phase of TiO₂ oriented in (101) direction. The XRD analysis also shows an improvement in the crystallinity of the electrodes after microwave treatment. The surface topographical analysis shows that the nanostructure and texture of the films remains unchanged after microwave treatment. The current-voltage characteristics showed a 3 fold increase in the photocurrent density after microwave treatment. Further work such as quantum efficiency calculations and charge transport

measurements are under progress to find out the reason for the enhancement of the photocurrent density after microwave treatment.

ZnO is a unique material that exhibits semiconducting and piezoelectric dual properties which use as optoelectronic material in fabrication of advance devices. In particular, ZnO nanorods have received extensive attention in photonic, electronic, optoelectronic and electrochemical devices due to ease of fabrication at ambient conditions. The effect of different post annealing methods on ZnO nanorods was studied. ZnO nanorods were grown on FTO-glass substrate by chemical bath deposition method after depositing a seed layer by AACVD technique. The structural properties of as-deposited, microwave irradiated and conventional radiant annealed ZnO nanorods were studied by XRD. X-ray diffraction measurements show that ZnO nanorods grow in a wurtzite crystal phase and no apparently change is observed in the crystallinity after microwave and conventional post annealing. The SEM images show that the microwave irradiation caused sintering of individual rods resulting in the growth of rod diameter whilst the conventional radiant annealing deformed the hierarchical ZnO structure. The current density of microwave irradiated electrode decreases compared to that of as-deposited electrode. The reduction of the photocurrent corresponding to conventional radiant annealed ZnO electrodes is more intense presumably due to deformation of rod structure. This appeared to be due to the poor charge transport in deformed electrodes.

The oxidation of electrodeposited Zn films to ZnO was conducted using microwave and conventional thermal annealing methods at various temperatures and comparisons were drawn. A 40% higher photocurrent was achieved for the microwave annealed films compared to their conventionally annealed electrodes. XRD patterns showed that the oxidation of Zn to

ZnO was not 100% efficient as evidence for metallic Zn was seen. For the conventionally annealed film the highest performing film showed unconverted Zn whereas a microwave annealed film did not show any sign of Zn. The improvement in the PEC properties was attributed to higher surface area, confirmed by SEM surface topographical analysis, and better yields of Zn oxidation to ZnO, and higher crystallinity. Microwave annealing preserves the nanostructure of films compared to conventional annealing due to the difference in the heating mechanism (volumetric heating). Microwave annealing allowed complete oxidation to ZnO with excellent crystallinity. Also oxidation using microwave annealing was achieved five times faster and offers energy savings of up to ~75%, which would make it highly desirable for industrial scale up.

The incorporation of Pd ions into the anatase phase of TiO₂ offers active site for catalytic oxidation–reduction reactions for energy devices. Ti_{0.97}Pd_{0.03}O_{1.97} was synthesised by using conventional sintering and microwave sintering methods and compared structural and morphological differences. The XRD patterns confirmed that the corresponding reflections of anatase phase has increased by microwave assisted synthesis than the conventional method. Raman spectroscopy indicated that the phases and the structure of the compound prepared by microwave and conventional methods were in good agreement. The SEM images confirmed a significant difference in the shape and the size of the crystallites by two different synthesis methods. The average crystallite size of Ti_{0.97}Pd_{0.03}O_{1.97} synthesised under microwave radiation is found to be in the range of 1-2 nm which is much smaller than the reported value under conventional method. The BET measurements further confirmed that the microwave synthesised Ti_{0.97}Pd_{0.03}O_{1.97} powder has slightly higher surface area than the conventionally synthesised powder.

Lithium aluminum titanium phosphate (LATP) is a potential inorganic solid electrolyte for lithium ion batteries. The LATP pellets were post treated using microwaves and conventional annealing methods and the differences in the structural, morphological and electrical properties of the post treated pellets were studied using XRD, Raman, SEM and EIS. The XRD and Raman analysis showed that the post heat treatment increased the crystallinity of the pellets without causing any structural changes. The SEM images confirmed that crystallized grains of microwave treated LATP were more uniform and the crystallites were fairly small compared to the conventionally annealed pellets. The electrochemical impedance results confirmed that the conductivities of the LATP pellets can be improved by microwave treatment at relatively low temperature and time. This improvement in the ionic conductivity is due to the uniformity and the lower resistance of the LATP crystallites acquired from better sintering characteristic from the microwave post treatment. Therefore, microwave post treatment of LATP is more advantageous than conventional annealing in terms of energy saving and the production cost.

Overall, the results of the thesis demonstrate that microwave treatment is a promising alternative method to the conventional sintering and it opens up a new research strategy for the engineering of semiconductor materials properties while keeping the texture and nanostructure unaltered for use in advanced electronic and optoelectronic devices.

8.2 Further Work

Microwaves have been explored as an efficient alternative energy source in thin film processing and materials synthesis for advance electronic and optoelectronic devices. Although the use of microwaves has shown promising results over conventional heating methods, further work is essential to develop a comprehensive understanding of how microwaves interact with mixed oxide materials and non-oxides materials under different processing environments and conditions. One approach that could be used in the future is to change the gas environment whilst microwave processing semiconductor electrodes. This allows one to understand the impact on structural, morphological and photoelectrochemical properties when using an alternative environment to atmospheric microwave processing conditions. Further work on the effect of microwave heating on thin films with the ferrite structure such as ZnFe_2O_4 , CuFe_2O_4 and CoFe_2O_4 ; pervoskite structure such as CaTiO_3 and MnZnO_3 ; metal chalcogenides and metal nitrides will be carried out using a hybrid microwave methodology. This is where both radiant and microwave heat is present. In this study the effects of microwave heating can be understood by varying the microwave power level whilst the conventional radiant heat is kept at a constant. This will lead to enhanced properties of functional nano-materials through unusual nanostructures and unique phases. These will be useful in the development of advanced energy harvesting and storage devices.

Also due to its lower processing temperature requirements, the microwave process can also open up the possibility of fabricating thin films of photoactive semiconductors on conducting, flexible, plastic substrates which are highly important in making flexible solar cells and other renewable energy applications.

Chapter 9

References

[1] Noboru Yoshikawa. Recent Studies on Fundamentals and Application of Microwave Processing of Materials, Advances in Induction and Microwave Heating of Mineral and Organic Materials, Prof. Stanisław Grundas (Ed.), 2011. ISBN: 978-953-307-522-8.

[2]<http://www.ewp.rpi.edu/hartford/~ernesto/S2013/ET/MaterialsforStudents/Ott/Wave%20Energy%20SourcesOtt/Encyclopedia%20of%20Energy/Energy%20related%20tables.pdf> Last updated on 2003; Accessed on 13/03/2014.

[3] Clark DE, Sutton WH. Microwave processing of materials. Annu Rev Mater Sci 1996;26:299-331.

[4] Katz JD. Microwave sintering of ceramics. Annu Rev Mater Sci 1992;22:153-70.

[5] Oda SJ. Dielectric Processing of Hazardous Materials-Present and Future Opportunities. MRS Proceedings 1992;269.

[6] Balakrishnan E, Nelson MI, Chen XD. Microwave assisted ignition to achieve combustion synthesis. J Appl Math Decis Sci 2001;5:151-64.

[7] Galema SA. Microwave chemistry. Chem Soc Rev 1997;26:233-8.

[8] Das S, Mukhopadhyay A, Datta S, Basu D. Prospects of microwave processing: An overview. Bull Mater Sci 2009;32:1-13.

- [9] Jones D, Lelyveld T, Mavrofidis S, Kingman S, Miles N. Microwave heating applications in environmental engineering—a review. *Resour Conserv Recycling* 2002;34:75-90.
- [10] Kappe CO, Dallinger D. The impact of microwave synthesis on drug discovery. *Nat Rev Drug Discov* 2006;5:51-63.
- [11] Thostenson E, Chou T. Microwave processing: fundamentals and applications. *Compos Part A- Appl S* 1999;30:1055-71.
- [12] Oghbaei M, Mirzaee O. Microwave versus conventional sintering: A review of fundamentals, advantages and applications. *J Alloys Compounds* 2010;494:175-89.
- [13] Gupta M, Leong EWW. *Microwaves and metals*: John Wiley & Sons, 2008.
- [14] Hart JN, Menzies D, Cheng Y, Simon GP, Spiccia L. Microwave processing of TiO₂ blocking layers for dye-sensitized solar cells. *J Sol Gel Sci Technol* 2006;40:45-54.
- [15] Xu G, Lloyd IK, Carmel Y, Olorunyolemi T, Wilson OC. Microwave sintering of ZnO at ultra-high heating rates. *J Mater Res* 2001;16:2850-8.
- [16] Parada C, Morán E. Microwave-assisted synthesis and magnetic study of nanosized Ni/NiO materials. *Chem Mater* 2006;18:2719-25.
- [17] Katsuki H, Komarneni S. Microwave-Hydrothermal Synthesis of Monodispersed Nanophase α -Fe₂O₃. *J Am Ceram Soc* 2001;84:2313-7.
- [18] Yuan H, Ma Z. Microwave thin-film transistors using Si nanomembranes on flexible polymer substrate. *Appl Phys Lett* 2006;89:212105.

- [19] <http://micro.magnet.fsu.edu/primer/java/polarizedlight/emwave/index.html> Last updated on 2014; Accessed on 08/03/2014.
- [20] Maxwell JC. A dynamical theory of the electromagnetic field. Phil Trans R Soc 1865:459-512.
- [21] <http://www.ces.fau.edu/nasa/module-2/radiation-sun.php> Last updated on 2013; Accessed on 08/03/2014.
- [22] Thostenson E, Chou T. Microwave processing: fundamentals and applications. Compos Part A- Appl S 1999;30:1055-71.
- [23] Meredith RJ. Engineers' handbook of industrial microwave heating.: IET, 1998.
- [24] Gupta M, Leong W, Eugene W. Introduction to Microwaves. Microwaves and Metals: John Wiley & Son, 2007, 1-23.
- [25] Metaxas A, Meredith RJ. Industrial microwave heating. : IET, 1983.
- [26] Metaxas A. Foundations of Electroheat. A Unified Approach. Fuel and Energy Abstracts 1996;37.
- [27] Saltiel C, Datta AK. Heat and mass transfer in microwave processing. Adv heat transfer 1999;33:1-94.
- [28] Yarlagadda PK, Cheok E. Study on the microwave curing of adhesive joints using a temperature-controlled feedback system. J Mater Process Technol 1999;91:128-49.

[29] Banwell CN, McCash EM. Fundamentals of molecular spectroscopy.: McGraw-Hill London, 1983.

[30] van de Kruijs, Bastiaan Helena Peter. Microwave-matter effects in metal (oxide)-mediated chemistry and in drying. PhD thesis, Eindhoven University of Technology, 2010. ISBN: 978-90-386-2178-4.

[31] Stuerger D. Microwave-material interactions and dielectric properties, key ingredients for mastery of chemical microwave processes. Microwaves in Organic Synthesis (Loupy A, ed).2nd ed.Weinheim, Germany: Wiley-VCH Verlag GmbH & Co.KGAA 2006:1-61.

[32] Fröhlich H. Theory of dielectrics.: Clarendon Press Oxford, 1949.

[33] Lidström P, Tierney J, Wathey B, Westman J. Microwave assisted organic synthesis- a review. Tetrahedron 2001;57:9225-83.

[34] Bilecka I, Niederberger M. Microwave chemistry for inorganic nanomaterials synthesis. Nanoscale 2010;2:1358-74.

[35] Kitchen HJ, Vallance SR, Kennedy JL, Tapia-Ruiz N, Carassiti L, Harrison A et al. Modern Microwave Methods in Solid-State Inorganic Materials Chemistry: From Fundamentals to Manufacturing. Chem Rev 2014;114:1170–1206.

[36] Clark DE, Folz DC, West JK. Processing materials with microwave energy. Mat Sci Eng A 2000;287:153-8.

- [37] Bruce RW. New frontiers in the use of microwave energy: power and metrology. Mater Res Soc Symp 1988;124:3-15.
- [38] Cabanes-Sempere M, Cozzo C, Vaucher S, Catalá-Civera J, Pouchon M. Innovative production of nuclear fuel by microwave internal gelation: Heat transfer model of falling droplets. Prog Nuclear Energy 2012;57:111-6.
- [39] http://en.wikipedia.org/wiki/File:Dielectric_responses.svg Last updated on 2010; Accessed on 11/03/2014.
- [40] Chen M, Siochi E, Ward T, McGrath J. Basic ideas of microwave processing of polymers. Polym Eng Sci 1993;33:1092-109.
- [41] Thostenson E, Chou T. Microwave processing: fundamentals and applications. Compos Part A- Appl S 1999;30:1055-71.
- [42] Ramesh PD, Brandon D, Schächter L. Use of partially oxidized SiC particle bed for microwave sintering of low loss ceramics. Mat Sci Eng A 1999;266:211-20.
- [43] Bott AW. Electrochemistry of semiconductors. Curr Sep 1998;17:87-92.
- [44] Bard AJ, Faulkner LR. Electrochemical methods: fundamentals and applications.: Wiley New York, 1980.
- [45] Turner JA. Energetics of the semiconductor-electrolyte interface. J Chem Educ 1983;60:327.

- [46] Gelderman K, Lee L, Donne S. Flat-band potential of a semiconductor: using the Mott–Schottky equation. *J Chem Educ* 2007;84:685.
- [47] Bhat MH, Miura A, Vinatier P, Levasseur A, Rao KJ. Microwave synthesis of lithium lanthanum titanate. *Solid State Commun* 2003;125:557-62.
- [48] Yang G, Wang G, Hou W. Microwave solid-state synthesis of LiV_3O_8 as cathode material for lithium batteries. *J Phys Chem B* 2005;109:11186-96.
- [49] Panneerselvam M, Rao K. Microwave preparation and sintering of industrially important perovskite oxides: LaMO_3 (M= Cr, Co, Ni). *Mater Chem* 2003;13:596-601.
- [50] Agostino A, Benzi P, Castiglioni M, Rizzi N, Volpe P. Y $\text{Ba}_2\text{Cu}_3\text{O}_7$ synthesis using microwave heating. *Supercon Sci Tech* 2004;17:685.
- [51] Peelamedu RD, Roy R, Agrawal DK. Microwave-induced reaction sintering of NiAl_2O_4 . *Mater Lett* 2002;55:234-40.
- [52] Nakayama M, Watanabe K, Ikuta H, Uchimoto Y, Wakihara M. Grain size control of LiMn_2O_4 cathode material using microwave synthesis method. *Solid State Ionics* 2003;164:35-42.
- [53] Guo J, Dong C, Yang L, Fu G. A green route for microwave synthesis of sodium tungsten bronzes Na_xWO_3 ($0 < x < 1$). *J Solid State Chem* 2005;178:58-63.
- [54] Gelderman K, Lee L, Donne S. Flat-band potential of a semiconductor: using the Mott–Schottky equation. *J Chem Educ* 2007;84:685.

- [55] Shpil'ko A, Kirilenko E, Soltis M, Petrovskii VY. Microwave absorptivity of refractory powders depending on particle size. *Powder Metal Met Ceram* 2010;49:304-16.
- [56] Rao K, Vaidhyathan B, Ganguli M, Ramakrishnan P. Synthesis of inorganic solids using microwaves. *Chem Mater* 1999;11:882-95.
- [57] Kawashima S, Nishida M, Ueda I. Ba (Zn^{1/3}Ta^{2/3}) O₃ ceramics with low dielectric loss at microwave frequencies. *J Am Ceram Soc* 1983;66:421-3.
- [58] Rao K, Mahesh K, Kumar S. A strategic approach for preparation of oxide nanomaterials. *Bull Mater Sci* 2005;28:19-24.
- [59] Anandan S, Wu JJ. Microwave assisted rapid synthesis of Bi₂O₃ short nanorods. *Mater Lett* 2009;63:2387-9.
- [60] Cao C, Cui Z, Chen C, Song W, Cai W. Ceria hollow nanospheres produced by a template-free microwave-assisted hydrothermal method for heavy metal ion removal and catalysis. *J Phys Chem C* 2010;114:9865-70.
- [61] Gao F, Lu Q, Komarneni S. Fast synthesis of cerium oxide nanoparticles and nanorods. *J Nanosci Nanotechnol* 2006;6:3812-9.
- [62] Liao X, Zhu J, Zhu J, Xu J, Chen H. Preparation of monodispersed nanocrystalline CeO₂ powders by microwave irradiation. *Chem Comm* 2001:937-8.
- [63] Wang H, Zhu J, Zhu J, Liao X, Xu S, Ding T et al. Preparation of nanocrystalline ceria particles by sonochemical and microwave assisted heating methods. *PCCP* 2002;4:3794-9.

- [64] Corradi AB, Bondioli F, Ferrari A, Manfredini T. Synthesis and characterization of nanosized ceria powders by microwave-hydrothermal method. *Mater Res Bull* 2006;41:38-44.
- [65] Raj DS, Krishnakumar T, Jayaprakash R, Donato N, Latino M, Neri G. Synthesis and characterization of Cd(OH)₂ nanowires obtained by a microwave-assisted chemical route. *Sci Adv Mater* 2010;2:432-7.
- [66] Ai L, Jiang J. Rapid synthesis of nanocrystalline Co₃O₄ by a microwave-assisted combustion method. *Powder Technol* 2009;195:11-4.
- [67] Li W. Microwave-assisted hydrothermal synthesis and optical property of Co₃O₄ nanorods. *Mater Lett* 2008;62:4149-51.
- [68] Ding Y, Xu L, Chen C, Shen X, Suib SL. Syntheses of nanostructures of cobalt hydroxalate like compounds and Co₃O₄ via a microwave-assisted reflux method. *J Phys Chem C* 2008;112:8177-83.
- [69] Wang H, Xu J, Zhu J, Chen H. Preparation of CuO nanoparticles by microwave irradiation. *J Cryst Growth* 2002;244:88-94.
- [70] Volanti DP, Orlandi MO, Andrés J, Longo E. Efficient microwave-assisted hydrothermal synthesis of CuO sea urchin-like architectures via a mesoscale self-assembly. *Cryst Eng Comm* 2010;12:1696-9.
- [71] Zhao Y, Zhu J, Hong J, Bian N, Chen H. Microwave-Induced Polyol-Process Synthesis of Copper and Copper Oxide Nanocrystals with Controllable Morphology. *Eur J Inorg Chem* 2004;2004:4072-80.

- [72] Liu J, Wang S, Wang Q, Geng B. Microwave chemical route to self-assembled quasi-spherical Cu₂O microarchitectures and their gas-sensing properties. *Sensors Actuators B: Chem* 2009;143:253-60.
- [73] Hu X, Yu JC, Gong J, Li Q, Li G. α -Fe₂O₃ Nanorings Prepared by a Microwave-Assisted Hydrothermal Process and Their Sensing Properties. *Adv Mater* 2007;19:2324-9.
- [74] Hu X, Yu JC. Continuous Aspect-Ratio Tuning and Fine Shape Control of Monodisperse α -Fe₂O₃ Nanocrystals by a Programmed Microwave-Hydrothermal Method. *Advanced Functional Materials* 2008;18:880-7.
- [75] Li Y, Li H, Cao R. Facile Fabrication of Pure α -Fe₂O₃ Nanoparticles via Forced Hydrolysis Using Microwave-Assisted Esterification and their Sensing Property. *J Am Ceram Soc* 2009;92:2188-91.
- [76] Bilecka I, Djerdj I, Niederberger M. One-minute synthesis of crystalline binary and ternary metal oxide nanoparticles. *Chem Comm* 2008:886-8.
- [77] Bilecka I, Elser P, Niederberger M. Kinetic and thermodynamic aspects in the microwave-assisted synthesis of ZnO nanoparticles in benzyl alcohol. *ACS nano* 2009;3:467-77.
- [78] Katsuki H, Komarneni S. Microwave-Hydrothermal Synthesis of Monodispersed Nanophase α -Fe₂O₃. *J Am Ceram Soc* 2001;84:2313-7.

- [79] Xue B, Liu R, Xu Z, Zheng Y. Microwave Fabrication and Magnetic Property of Hierarchical Spherical α -Fe₂O₃ Nanostructures. *Chem Lett* 2008;37:1058-9.
- [80] Wang W, Zhu Y, Ruan M. Microwave-assisted synthesis and magnetic property of magnetite and hematite nanoparticles. *J Nanopart Res* 2007;9:419-26.
- [81] Liao X, Zhu J, Zhong W, Chen H. Synthesis of amorphous Fe₂O₃ nanoparticles by microwave irradiation. *Mater Lett* 2001;50:341-6.
- [82] Guo X, Deng Y, Gu D, Che R, Zhao D. Synthesis and microwave absorption of uniform hematite nanoparticles and their core-shell mesoporous silica nanocomposites. *J Mater Chem* 2009;19:6706-12.
- [83] Li Y, Li H, Cao R. Facile Fabrication of Pure α -Fe₂O₃ Nanoparticles via Forced Hydrolysis Using Microwave-Assisted Esterification and their Sensing Property. *J Am Ceram Soc* 2009;92:2188-91.
- [84] Katsuki H, Shiraishi A, Komarneni S, Moon WJ, Toh S, Kaneko K. Rapid synthesis of monodispersed α -Fe₂O₃ nanoparticles from Fe(NO₃)₃ solution by microwave irradiation. *Nippon seramikku kyokai gakujutsu ronbunshi* 2004;112:384-7.
- [85] Polshettiwar V, Nadagouda MN, Varma RS. The synthesis and applications of a micro-pine-structured nanocatalyst. *Chem Comm* 2008:6318-20.
- [86] Hu X, Yu JC, Gong J. Fast production of self-assembled hierarchical α -Fe₂O₃ nanoarchitectures. *J Phys Chem C* 2007;111:11180-5.

- [87] Polshettiwar V, Baruwati B, Varma RS. Self-assembly of metal oxides into three-dimensional nanostructures: synthesis and application in catalysis. *ACS nano* 2009;3:728-36.
- [88] Baruwati B, Nadagouda MN, Varma RS. Bulk synthesis of monodisperse ferrite nanoparticles at water-organic interfaces under conventional and microwave hydrothermal treatment and their surface functionalization. *J Phys Chem C* 2008;112:18399-404.
- [89] Du X, Wang C, Chen M, Jiao Y, Wang J. Electrochemical performances of nanoparticle Fe_3O_4 /activated carbon supercapacitor using KOH electrolyte solution. *J Phys Chem C* 2009;113:2643-6.
- [90] Muraliganth T, Murugan AV, Manthiram A. Facile synthesis of carbon-decorated single-crystalline Fe_3O_4 nanowires and their application as high performance anode in lithium ion batteries. *Chem Comm* 2009:7360-2.
- [91] Hu X, Yu JC. Microwave-Assisted Synthesis of a Superparamagnetic Surface-Functionalized Porous Fe_3O_4 /C Nanocomposite. *Asian J Chem* 2006;1:605-10.
- [92] Ai Z, Deng K, Wan Q, Zhang L, Lee S. Facile microwave-assisted synthesis and magnetic and gas sensing properties of Fe_3O_4 nanoroses. *J Phys Chem C* 2010;114:6237-42.
- [93] Zhang H, Zhong X, Xu J, Chen H. Fe_3O_4 /polypyrrole/Au nanocomposites with core/shell/shell structure: synthesis, characterization, and their electrochemical properties. *Langmuir* 2008;24:13748-52.

- [94] Hu H, Yang H, Huang P, Cui D, Peng Y, Zhang J et al. Unique role of ionic liquid in microwave-assisted synthesis of monodisperse magnetite nanoparticles. *Chem Comm* 2010;46:3866-8.
- [95] Patra CR, Gedanken A. Rapid synthesis of nanoparticles of hexagonal type In_2O_3 and spherical type Ti_2O_3 by microwave irradiation. *New J Chem* 2004;28:1060-5.
- [96] Yang L, Zhu Y, Tong H, Wang W, Cheng G. Low temperature synthesis of Mn_3O_4 polyhedral nanocrystals and magnetic study. *J Solid State Chem* 2006;179:1225-9.
- [97] Yu P, Zhang X, Chen Y, Ma Y, Qi Z. Preparation and pseudo-capacitance of birnessite-type MnO_2 nanostructures via microwave-assisted emulsion method. *Mater Chem Phys* 2009;118:303-7.
- [98] Bilecka I, Djerdj I, Niederberger M. One-minute synthesis of crystalline binary and ternary metal oxide nanoparticles. *Chem Comm* 2008:886-8.
- [99] Wang K, Huang T, Liu H, Zhao Y, Liu H, Sun C. Size control synthesis of palladium oxide nanoparticles by microwave irradiation. *Colloids Surf A Physicochem Eng Asp* 2008;325:21-5.
- [100] Pan R, Wu Y, Wang Q, Hong Y. Preparation and catalytic properties of platinum dioxide nanoparticles: A comparison between conventional heating and microwave-assisted method. *Chem Eng J* 2009;153:206-10.
- [101] Wu D, Han C, Wang S, Wu N, Rusakova I. Microwave-assisted solution synthesis of SnO nanocrystallites. *Mater Lett* 2002;53:155-9.

- [102] Zhu J, Zhu J, Liao X, Fang J, Zhou M, Chen H. Rapid synthesis of nanocrystalline SnO₂ powders by microwave heating method. *Mater Lett* 2002;53:12-9.
- [103] Jouhannaud J, Rossignol J, Stuerger D. Rapid synthesis of tin (IV) oxide nanoparticles by microwave induced thermohydrolysis. *J Solid State Chem* 2008;181:1439-44.
- [104] Krishna M, Komarneni S. Conventional-vs microwave-hydrothermal synthesis of tin oxide, SnO₂ nanoparticles. *Ceram Int* 2009;35:3375-9.
- [105] Jia X, He W, Zhang X, Zhao H, Li Z, Feng Y. Microwave-assisted synthesis of anatase TiO₂ nanorods with mesopores. *Nanotechnology* 2007;18:075602.
- [106] Spatz J, Mößmer S, Möller M, Kocher M, Neher D, Wegner G. Controlled Mineralization and Assembly of Hydrolysis-Based Nanoparticles in Organic Solvents Combining Polymer Micelles and Microwave Techniques. *Adv Mater* 1998;10:473-5.
- [107] Periyat P, Leyland N, McCormack DE, Colreavy J, Corr D, Pillai SC. Rapid microwave synthesis of mesoporous TiO₂ for electrochromic displays. *J Mater Chem* 2010;20:3650-5.
- [108] Pol VG, Langzam Y, Zaban A. Application of microwave superheating for the synthesis of TiO₂ rods. *Langmuir* 2007;23:11211-6.
- [109] Wilson GJ, Will GD, Frost RL, Montgomery SA. Efficient microwave hydrothermal preparation of nanocrystalline anatase TiO₂ colloids. *J Mater Chem* 2002;12:1787-91.

- [110] Inada M, Kamada K, Enomoto N, Hojo J. Microwave effect for synthesis of TiO₂ particles by self-hydrolysis of TiOCl₂. *Nippon seramikku kyokai gakujutsu ronbunshi* 2006;114:814-8.
- [111] Gressel-Michel E, Chaumont D, Stuerger D. From a microwave flash-synthesized TiO₂ colloidal suspension to TiO₂ thin films. *J Colloid Interface Sci* 2005;285:674-9.
- [112] Baldassari S, Komarneni S, Mariani E, Villa C. Microwave-hydrothermal process for the synthesis of rutile. *Mater Res Bull* 2005;40:2014-20.
- [113] Baldassari S, Komarneni S, Mariani E, Villa C. Rapid microwave-hydrothermal synthesis of anatase form of titanium dioxide. *J Am Ceram Soc* 2005;88:3238-40.
- [114] Suprabha T, Roy HG, Thomas J, Kumar KP, Mathew S. Microwave-assisted synthesis of titania nanocubes, nanospheres and nanorods for photocatalytic dye degradation. *Nanoscale Res Lett* 2009;4:144-52.
- [115] Corradi AB, Bondioli F, Focher B, Ferrari AM, Grippo C, Mariani E et al. Conventional and Microwave-Hydrothermal Synthesis of TiO₂ Nanopowders. *J Am Ceram Soc* 2005;88:2639-41.
- [116] Zhang L, Liu P, Su Z. Facile Microwave Assisted Liquid Phase Deposition Process to TiO₂ Nanocrystallines. *Chin J Chem* 2006;24:19-21.
- [117] Ding K, Miao Z, Liu Z, Zhang Z, Han B, An G et al. Facile synthesis of high quality TiO₂ nanocrystals in ionic liquid via a microwave-assisted process. *J Am Chem Soc* 2007;129:6362-3.

[118] Zhang D, Li G, Yang X, Jimmy CY. A micrometer-size TiO₂ single-crystal photocatalyst with remarkable 80% level of reactive facets. *Chem Comm* 2009:4381-3.

[119] Le Houx N, Pourroy G, Camerel F, Comet M, Spitzer D. WO₃ nanoparticles in the 5–30 nm range by solvothermal synthesis under microwave or resistive heating. *J Phys Chem C* 2009;114:155-61.

[120] Phuruangrat A, Ham DJ, Hong SJ, Thongtem S, Lee JS. Synthesis of hexagonal WO₃ nanowires by microwave-assisted hydrothermal method and their electrocatalytic activities for hydrogen evolution reaction. *J Mater Chem* 2010;20:1683-90.

[121] Hu X, Gong J, Zhang L, Yu JC. Continuous Size Tuning of Monodisperse ZnO Colloidal Nanocrystal Clusters by a Microwave-Polyol Process and Their Application for Humidity Sensing. *Adv Mater* 2008;20:4845-50.

[122] Schneider JJ, Hoffmann RC, Engstler J, Klyszcz A, Erdem E, Jakes P et al. Synthesis, characterization, defect chemistry, and FET properties of microwave-derived nanoscaled zinc oxide. *Chem Mater* 2010;22:2203-12.

[123] Bilecka I, Djerdj I, Niederberger M. One-minute synthesis of crystalline binary and ternary metal oxide nanoparticles. *Chem Comm* 2008:886-8.

[124] Hu X, Zhu Y, Wang S. Sonochemical and microwave-assisted synthesis of linked single-crystalline ZnO rods. *Mater Chem Phys* 2004;88:421-6.

[125] Cho S, Jung S, Lee K. Morphology-controlled growth of ZnO nanostructures using microwave irradiation: from basic to complex structures. *J Phys Chem C* 2008;112:12769-76.

[126] Komarneni S, Bruno M, Mariani E. Synthesis of ZnO with and without microwaves. *Mater Res Bull* 2000;35:1843-7.

[127] Komarneni S, Bruno M, Mariani E. Synthesis of ZnO with and without microwaves. *Mater Res Bull* 2000;35:1843-7.

[128] Ledwith D, Pillai SC, Watson GW, Kelly JM. Microwave induced preparation of a-axis oriented double-ended needle-shaped ZnO microparticles. *Chem Commun* 2004:2294-5.

[129] Bhat DK. Facile synthesis of ZnO nanorods by microwave irradiation of zinc-hydrazine hydrate complex. *Nanoscale Res Lett* 2008;3:31-5.

[130] Yang L, Dong S, Sun J, Feng J, Wu Q, Sun S. Microwave-assisted preparation, characterization and photocatalytic properties of a dumbbell-shaped ZnO photocatalyst. *J Hazard Mater* 2010;179:438-43.

[131] Zhu P, Zhang J, Wu Z, Zhang Z. Microwave-assisted synthesis of various ZnO hierarchical nanostructures: effects of heating parameters of microwave oven. *Cryst Growth Des* 2008;8:3148-53.

[132] Erten-Ela S, Cogal S, Icli S. Conventional and microwave-assisted synthesis of ZnO nanorods and effects of PEG400 as a surfactant on the morphology. *Inorg Chim Acta* 2009;362:1855-8.

[133] Liang J, Deng Z, Jiang X, Li F, Li Y. Photoluminescence of tetragonal ZrO₂ nanoparticles synthesized by microwave irradiation. *Inorg Chem* 2002;41:3602-4.

- [134] Bondioli F, Ferrari AM, Leonelli C, Siligardi C, Pellacani GC. Microwave-Hydrothermal Synthesis of Nanocrystalline Zirconia Powders. *J Am Ceram Soc* 2001;84:2728-30.
- [135] Bondioli F, Bonamartini Corradi A, Ferrari AM, Leonelli C. Synthesis of Zirconia Nanoparticles in a Continuous-Flow Microwave Reactor. *J Am Ceram Soc* 2008;91:3746-8.
- [136] Baghbanzadeh M, Carbone L, Cozzoli PD, Kappe CO. Microwave-Assisted Synthesis of Colloidal Inorganic Nanocrystals. *Angewandte Chemie International Edition* 2011;50:11312-59.
- [137] Zhu J, Zhou M, Xu J, Liao X. Preparation of CdS and ZnS nanoparticles using microwave irradiation. *Mater Lett* 2001;47:25-9.
- [138] Wada Y, Kuramoto H, Anand J, Kitamura T, Sakata T, Mori H et al. Microwave-assisted size control of CdS nanocrystallites. *J Mater Chem* 2001;11:1936-40.
- [139] Zhu J, Palchik O, Chen S, Gedanken A. Microwave assisted preparation of CdSe, PbSe, and Cu_{2-x}Se nanoparticles. *J Phys Chem B* 2000;104:7344-7.
- [140] Palchik O, Kerner R, Gedanken A, Weiss A, Slifkin M, Palchik V. Microwave-assisted polyol method for the preparation of CdSe “nanoballs”. *J Mater Chem*. 2001;11:874-8.
- [141] Duan J, Song L, Zhan J. One-pot synthesis of highly luminescent CdTe quantum dots by microwave irradiation reduction and their Hg^{2+} -sensitive properties. *Nano Res* 2009;2:61-8.

- [142] Song Q, Ai X, Topuria T, Rice PM, Alharbi FH, Bagabas A et al. Microwave-assisted synthesis of monodispersed CdTe nanocrystals. *Chem Comm* 2010;46:4971-3.
- [143] Grisar H, Palchik O, Gedanken A, Palchik V, Slifkin M, Weiss A. Preparation of the $\text{Cd}_{1-x}\text{Zn}_x\text{Se}$ alloys in the nanophase form using microwave irradiation. *J Mater Chem* 2002;12:339-44.
- [144] Liao X, Zhu J, Chen H. Microwave synthesis of nanocrystalline metal sulfides in formaldehyde solution. *Mater Sci Eng B* 2001;85:85-9.
- [145] Bensebaa F, Durand C, Aouadou A, Scoles L, Du X, Wang D et al. A new green synthesis method of CuInS_2 and CuInSe_2 nanoparticles and their integration into thin films. *J Nanopart Res* 2010;12:1897-903.
- [146] Pein A, Baghbanzadeh M, Rath T, Haas W, Maier E, Amenitsch H et al. Investigation of the formation of CuInS_2 nanoparticles by the oleylamine route: comparison of microwave-assisted and conventional syntheses. *Inorg Chem* 2010;50:193-200.
- [147] Grisar H, Palchik O, Gedanken A, Palchik V, Slifkin MA, Weiss AM. Microwave-assisted polyol synthesis of CuInTe_2 and CuInSe_2 nanoparticles. *Inorg Chem* 2003;42:7148-55.
- [148] Ding T, Zhang J, Long S, Zhu J. Synthesis of HgS and PbS nanocrystals in a polyol solvent by microwave heating. *Microelectron Eng* 2003;66:46-52.

- [149] Sliem MA, Chemseddine A, Bloeck U, Fischer RA. PbSe nanocrystal shape development: oriented attachment at mild conditions and microwave assisted growth of nanocubes. *Cryst Eng Comm* 2011;13:483-8.
- [150] Zhao Y, Hong J, Zhu J. Microwave-assisted self-assembled ZnS nanoballs. *J Cryst Growth* 2004;270:438-45.
- [151] He R, Qian X, Yin J, Xi H, Bian L, Zhu Z. Formation of monodispersed PVP-capped ZnS and CdS nanocrystals under microwave irradiation. *Colloids Surf Physicochem Eng Aspects* 2003;220:151-7.
- [152] Han D, Song C, Li X. Microwave-assisted synthesis of ZnSe of various morphologies using alkylamines as ligating solvent. *Mater Chem Phys* 2009;116:41-5.
- [153] Qian H, Qiu X, Li L, Ren J. Microwave-assisted aqueous synthesis: a rapid approach to prepare highly luminescent ZnSe (S) alloyed quantum dots. *J Phys Chem B* 2006;110:9034-40.
- [154] Panda AB, Glaspell G, El-Shall MS. Microwave synthesis of highly aligned ultra narrow semiconductor rods and wires. *J Am Chem Soc* 2006;128:2790-1.
- [155] Saremi-Yarahmadi S, Vaidhyanathan B, Wijayantha KGU. Microwave-assisted low temperature fabrication of nanostructured α -Fe₂O₃ electrodes for solar-driven hydrogen generation. *Int J Hydrogen Energy* 2010;35:10155-65.

- [156] Tahir AA, Peiris TAN, Wijayantha KGU. Enhancement of Photoelectrochemical Performance of AACVD-produced TiO₂ Electrodes by Microwave Irradiation while Preserving the Nanostructure. *Chem Vap Deposition* 2012;18:107-11.
- [157] Dag Ö, Kuperman A, Ozin GA. Nanostructures: New forms of luminescent silicon. *Adv Mater* 1995;7:72-8.
- [158] Rigneau P, Bellon K, Zahreddine I, Stueriga D. Microwave flash-synthesis of iron oxides nanoparticles. *Eur Phys J Appl Phys* 1999;7:41-3.
- [159] Moser A, Takano K, Margulies DT, Albrecht M, Sonobe Y, Ikeda Y, Sun S and Fullerton EE, Magnetic recording: advancing into the future, *J Phys D Appl Phys* 2002;35:R157–67.
- [160] Simon P, Gogotsi Y. Materials for electrochemical capacitors. *Nat Mater* 2008;7:845-54.
- [161] Walkiewicz JW, Raddatz AE, McGill SL. Microwave-assisted grinding. *IEEE* 1989:1528-32.
- [162] Vaidhyanathan B, Rao K. Synthesis of Ti, Ga, and V nitrides: microwave-assisted carbothermal reduction and nitridation. *Chem Mater* 1997;9:1196-200.
- [163] Roy R, Agrawal D, Cheng J, Gedevanishvili S. Full sintering of powdered-metal bodies in a microwave field. *Nature* 1999;399:668-70.

- [164] Cheng J, Roy R, Agrawal D. Radically different effects on materials by separated microwave electric and magnetic fields. *Mater Res Innov* 2002;5:170-7.
- [165] Gupta M, Leong W, Eugene W. Introduction to Microwaves. *Microwaves and Metals*.: John Wiley & Sons 2007:1-23.
- [166] Wheeler GJ, Kosow IL. Introduction to microwaves.: Prentice-Hall, 1963.
- [167] <http://www.hitachi-power-solutions.com/en/products/product07/p041.html> Last updated on 2013; Accessed on 11/03/2014.
- [168] http://en.wikipedia.org/wiki/Cavity_magnetron Last updated on 2014; Accessed on 11/03/2014.
- [169] Kavan L, Grätzel M. Highly efficient semiconducting TiO₂ photoelectrodes prepared by aerosol pyrolysis. *Electrochim Acta* 1995;40:643-52.
- [170] Marchand P, Hassan IA, Parkin IP, Carmalt CJ. Aerosol-assisted delivery of precursors for chemical vapour deposition: expanding the scope of CVD for materials fabrication. *Dalton Transactions* 2013;42:9406-22.
- [171] Dharmadasa R, Tahir AA, Wijayantha KGU. Single Step Growth and Characterization of Zinc Oxide, Tin Oxide, and Composite (Zn_xSn_{1-x}O_y) Nanoplate and Nanocolumn Electrodes. *J Am Ceram Soc* 2011;94:3540-6.

[172] Mgabi LP. Deposition of Co_xS_y , Ni_xS_y MnS and CdS thin films from their alkylthiourea precursors using the Aerosol Assisted Chemical Vapour Desposition (AACVD) technique, 2008. URI: <http://hdl.handle.net/10530/307>.

[173] Sankapal B, Sartale S, Lokhande C, Ennaoui A. Chemical synthesis of Cd-free wide band gap materials for solar cells. *Sol Energy Mater Sol Cells* 2004;83:447-58.

[174] Kathalingam A, Ambika N, Kim M, Elanchezhian J, Chae Y, Rhee J. Chemical bath deposition and characterization of nanocrystalline ZnO thin films. *Materials Science (0137-1339)* 2010;28.

[175] Musembi R, Aduda B, Mwabora J, Rusu M, Fostiropoulos K, Lux-Steiner M. Effect of Recombination on Series Resistance in eta Solar Cell Modified with $\text{In}(\text{OH})_x\text{S}_y$ Buffer Layer. *Int J Hydrogen Energy* 2013;3:183-9.

[176] Kingston H, Jassie L. Fundamental relationships in acid decomposition of samples for elemental analysis using microwave energy. *MRS Proceedings* 1988;124:121.

[177] Suryanarayana C, Norton MG. X-ray diffraction: a practical approach. *Microsc Microanal* 1998;4:513-14.

[178]http://www.substech.com/dokuwiki/lib/exe/detail.php?id=scanning_electron_microscope&cache=cache&media=electron_microscope.png Last updated on 2012; Accessed on 07/04/2014.

[179] Park N, Van de Lagemaat J, Frank A. Comparison of dye-sensitized rutile-and anatase-based TiO_2 solar cells. *J Phys Chem B* 2000;104:8989-94.

- [180] Peiris TAN, Senthilarasu S, Wijyantha KGU. Enhanced Performance of Flexible Dye-Sensitized Solar Cells: Electrodeposition of $Mg(OH)_2$ on a Nanocrystalline TiO_2 Electrode. *J Phys Chem C* 2011;116:1211-8.
- [181] Peiris TAN, Alessa H, Sagu JS, Bhatti IA, Isherwood P, Wijyantha KGU. Effect of ZnO seed layer thickness on hierarchical ZnO nanorod growth on flexible substrates for application in dye-sensitized solar cells. *J Nanopart Res* 2013;15:1-10.
- [182] Alexaki N, Stergiopoulos T, Kontos A, Tsoukleris D, Katsoulidis A, Pomonis P et al. Mesoporous titania nanocrystals prepared using hexadecylamine surfactant template: Crystallization progress monitoring, morphological characterization and application in dye-sensitized solar cells. *Micropor Mesopor Mat* 2009;124:52-8.
- [183] Tennakone K, Kumara G, Wijyantha KGU. The suppression of the recombination of photogenerated carriers in a dye-sensitized nano-porous solid-state photovoltaic cell. *Semicond Sci Technol* 1996;11:1737.
- [184] García-Cañadas J, Peter LM, Wijyantha KGU. Characterisation of electrochromic viologen-modified nanocrystalline TiO_2 films by frequency-resolved optical transmission spectroscopy. *Electrochem Commun* 2003;5:199-202.
- [185] Tennakone K, Kumara G, Wijyantha KGU, Kottegoda I, Perera V, Aponso G. A nanoporous solid-state photovoltaic cell sensitized with copper chlorophyllin. *J Photochem Photobiol A* 1997;108:175-7.

- [186] Corradi AB, Bondioli F, Focher B, Ferrari AM, Grippo C, Mariani E et al. Conventional and Microwave-Hydrothermal Synthesis of TiO₂ Nanopowders. *J Am Ceram Soc* 2005;88:2639-41.
- [187] Mathews N, Jacome M, Morales ER, Antonio J. Structural and spectroscopic study of the Fe doped TiO₂ thin films for applications in photocatalysis. *physica status solidi (c)* 2009;6:S219-23.
- [188] Evans P, Sheel D. Photoactive and antibacterial TiO₂ thin films on stainless steel. *Surf Coat Technol* 2007;201:9319-24.
- [189] Banerjee AN. The design, fabrication, and photocatalytic utility of nanostructured semiconductors: focus on TiO₂-based nanostructures. *Nanotechnol Sci Appl* 2011;4:35-65.
- [190] Hyett G, Darr JA, Mills A, Parkin IP. Substrate-Dependant Ability of Titanium (IV) Oxide Photocatalytic Thin Films Prepared by Thermal CVD to Generate Hydrogen Gas from a Sacrificial Reaction. *Chem Vap Deposition* 2010;16:301-4.
- [191] Peiris TAN, Senthilarasu S, Wijyantha KGU. Enhanced Performance of Flexible Dye-Sensitized Solar Cells: Electrodeposition of Mg(OH)₂ on a Nanocrystalline TiO₂ Electrode. *J Phys Chem C* 2011;116:1211-8.
- [192] Kay A, Cesar I, Grätzel M. New benchmark for water photooxidation by nanostructured α -Fe₂O₃ films. *J Am Chem Soc* 2006;128:15714-21.

- [193] Nolan M, Pemble M, Sheel D, Yates H. One step process for chemical vapour deposition of titanium dioxide thin films incorporating controlled structure nanoparticles. *Thin Solid Films* 2006;515:1956-62.
- [194] Tahir AA, Wijyantha KGU, Saremi-Yarahmadi S, Mazhar M, McKee V. Nanostructured α -Fe₂O₃ thin films for photoelectrochemical hydrogen generation. *Chem Mater* 2009;21:3763-72.
- [195] Ingler WB, Khan SU. Photoresponse of spray pyrolytically synthesized copper-doped p-Fe₂O₃ thin film electrodes in water splitting. *Int J Hydrogen Energy* 2005;30:821-7.
- [196] Saremi-Yarahmadi S, Vaidhyanathan B, Wijyantha KGU. Microwave-assisted low temperature fabrication of nanostructured α -Fe₂O₃ electrodes for solar-driven hydrogen generation. *Int J Hydrogen Energy* 2010;35:10155-65.
- [197] Meng Q, Takahashi K, Zhang X, Sutanto I, Rao T, Sato O et al. Fabrication of an efficient solid-state dye-sensitized solar cell. *Langmuir* 2003;19:3572-4.
- [198] Pan H, Ko SH, Grigoropoulos CP. The solid-state neck growth mechanisms in low energy laser sintering of gold nanoparticles: A molecular dynamics simulation study. *J Heat Transfer* 2008;130:092404.
- [199] Pan H, Ko SH, Grigoropoulos CP. The neck growth mechanisms in low energy laser sintering of gold nanoparticles: a molecular dynamics simulation study. *Photon Processing in Microelectronics and Photonics VI* 2007:64581J.

- [200] Fang Y, Agrawal DK, Roy DM, Roy R. Fabrication of porous hydroxyapatite ceramics by microwave processing. *J Mater Res* 1992;7:490-4.
- [201] Xie Z, Li J, Huang Y, Kong X. Microwave sintering behaviour of ZrO_2 - Y_2O_3 with agglomerate. *J Mater Sci Lett* 1996;15:1158-60.
- [202] Meek T, Blake R. Ceramic-ceramic seals by microwave heating. *J Mater Sci Lett* 1986;5:270-4.
- [203] Xie Z, Fan X, Huang Y. Accelerated sintering and phase transformation of TiO_2 in microwave radiation. *J Mater Res* 1998;13:3417-22.
- [204] Tahir AA, Wijyantha KGU, Mazhar M, McKee V. $ZnFe_2O_4$ thin films from a single source precursor by aerosol assisted chemical vapour deposition. *Thin Solid Films* 2010;518:3664-8.
- [205] Sultan M, Tahir AA, Mazhar M, Wijyantha KGU, Zeller M. Isostructural copper–zinc mixed metal complexes for single source deposition of Cu–ZnO composite thin films. *Dalton Trans* 2011;40:7889-97.
- [206] Edusi C, Hyett G, Sankar G, Parkin IP. Aerosol-Assisted CVD of Titanium Dioxide Thin Films from Methanolic Solutions of Titanium Tetraisopropoxide; Substrate and Aerosol-Selective Deposition of Rutile or Anatase. *Chem Vap Deposition* 2011;17:30-6.
- [207] Shi J, Wang X. Growth of rutile titanium dioxide nanowires by pulsed chemical vapor deposition. *Cryst Growth Des* 2011;11:949-54.

- [208] Byun C, Jang J, Kim I, Hong K, Lee B. Anatase-to-rutile transition of titania thin films prepared by MOCVD. *Mater Res Bull* 1997;32:431-40.
- [209] Zhang Q, Cao G. Nanostructured photoelectrodes for dye-sensitized solar cells. *Nano Today* 2011;6:91-109.
- [210] Tahir AA, Wijyantha KGU. Photoelectrochemical water splitting at nanostructured ZnFe₂O₄ electrodes. *J Photochem Photobiol A* 2010;216:119-25.
- [211] Tahir AA, Ehsan MA, Mazhar M, Wijyantha KGU, Zeller M, Hunter A. Photoelectrochemical and photoresponsive properties of Bi₂S₃ nanotube and nanoparticle thin films. *Chem Mater* 2010;22:5084-92.
- [212] Batzill M. Fundamental aspects of surface engineering of transition metal oxide photocatalysts. *Energy Environ Sci* 2011;4:3275-86.
- [213] Lee J, Ko K, Park B. Electrical and optical properties of ZnO transparent conducting films by the sol-gel method. *J Cryst Growth* 2003;247:119-25.
- [214] Chen Z, Ni A, Li F, Cong H, Cheng H, Lu GQ. Synthesis and photoluminescence of tetrapod ZnO nanostructures. *Chem Phys Lett* 2007;434:301-5.
- [215] Tian ZR, Voigt JA, Liu J, Mckenzie B, Mcdermott MJ, Rodriguez MA et al. Complex and oriented ZnO nanostructures. *Nat Mater* 2003;2:821-6.
- [216] Gupta S, Joshi A, Kaur M. Development of gas sensors using ZnO nanostructures. *J Chemical Sci* 2010;122:57-62.

- [217] Park JY, Choi S, Kim SS. Fabrication of a highly sensitive chemical sensor based on ZnO nanorod arrays. *Nanoscale Res Lett* 2010;5:353-9.
- [218] Mahmood K, Song D, Park SB. Effects of thermal treatment on the characteristics of boron and tantalum-doped ZnO thin films deposited by the electrospraying method at atmospheric pressure. *Surf Coat Tech* 2012;206:4730-40.
- [219] Roy R, Agrawal D, Cheng J, Gedevanishvili S. Full sintering of powdered-metal bodies in a microwave field. *Nature* 1999;399:668-70.
- [220] Clark DE, Folz DC, West JK. Processing materials with microwave energy. *Mater Sci Eng A* 2000;287:153-8.
- [221] Tahir AA, Peiris TAN, Wijayantha KGU. Enhancement of Photoelectrochemical Performance of AACVD-produced TiO₂ Electrodes by Microwave Irradiation while Preserving the Nanostructure. *Chem Vap Deposition* 2012;18:107-11.
- [222] Bilecka I, Niederberger M. Microwave chemistry for inorganic nanomaterials synthesis. *Nanoscale* 2010;2:1358-74.
- [223] Kalyani P, Kalaiselvi N, Renganathan N. Microwave-assisted synthesis of LiNiO₂ - A preliminary investigation. *J Power Sources* 2003;123:53-60.
- [224] Tahir AA, Smith TD, Wijayantha KGU. Effects of AACVD and Electrodeposited ZnO Seed Layer on the Growth and Alignment of ZnO Nanorods by Chemical Bath Deposition. *Nanosci Nanotechnol Lett* 2011;3:674-8.

- [225] Belaidi A, Dittrich T, Kieven D, Tornow J, Schwarzburg K, Kunst M et al. ZnO-nanorod arrays for solar cells with extremely thin sulfidic absorber. *Sol Energ Mat Sol C* 2009;93:1033-6.
- [226] Peiris TAN, Senthilarasu S, Wijyantha KGU. Enhanced Performance of Flexible Dye-Sensitized Solar Cells: Electrodeposition of Mg (OH)₂ on a Nanocrystalline TiO₂ Electrode. *J Phys Chem C* 2011;116:1211-8.
- [227] Wei Y, Ke L, Kong J, Liu H, Jiao Z, Lu X et al. Enhanced photoelectrochemical water-splitting effect with a bent ZnO nanorod photoanode decorated with Ag nanoparticles. *Nanotech* 2012;23:235401.
- [228] Ilican S, Caglar M, Caglar Y. Determination of the thickness and optical constants of transparent indium-doped ZnO thin films by the envelope method. *Materials Science-Poland* 2007;25.
- [229] Prepelita P, Medianu R, Sbarcea B, Garoi F, Filipescu M. The influence of using different substrates on the structural and optical characteristics of ZnO thin films. *Appl Surf Sci* 2010;256:1807-11.
- [230] Greene LE, Law M, Yuhas BD, Yang P. ZnO-TiO₂ core-shell nanorod/P3HT solar cells. *J Phys Chem C* 2007;111:18451-6.
- [231] Kaewprasit C, Hequet E, Abidi N, Gourlot JP. Quality measurements. *J.Cotton Sci* 1998;2:164-73.

- [232] Sengupta J, Sahoo R, Bardhan K, Mukherjee C. Influence of annealing temperature on the structural, topographical and optical properties of sol–gel derived ZnO thin films. *Mater Lett* 2011;65:2572-4.
- [233] Strandwitz NC, Turner-Evans DB, Tamboli AC, Chen CT, Atwater HA, Lewis NS. Photoelectrochemical Behavior of Planar and Microwire-Array Si| GaP Electrodes. *Adv Energy Mater* 2012;2:1109-16.
- [234] Walter MG, Warren EL, McKone JR, Boettcher SW, Mi Q, Santori EA et al. Solar water splitting cells. *Chem Rev* 2010;110:6446-73.
- [235] Tahir AA, Wijayantha KU, Saremi-Yarahmadi S, Mazhar M, McKee V. Nanostructured α -Fe₂O₃ thin films for photoelectrochemical hydrogen generation. *Chem Mater* 2009;21:3763-72.
- [236] Fujishima A, Honda K. Photolysis-decomposition of water at the surface of an irradiated semiconductor. *Nature* 1972;238:37-8.
- [237] O'Regan B, Grätzel M. Low cost and highly efficient solar cells based on the sensitization of colloidal titanium dioxide. *Nature* 1991;335:7377.
- [238] Ozgur U, Alivov YI, Liu C, Teke A, Reshchikov M, Dogan S et al. A comprehensive review of ZnO materials and devices. *J Appl Phys* 2005;98:041301,041301-103.
- [239] Su J, Feng X, Sloppy JD, Guo L, Grimes CA. Vertically aligned WO₃ nanowire arrays grown directly on transparent conducting oxide coated glass: synthesis and photoelectrochemical properties. *Nano letters* 2010;11:203-8.

- [240] Wolcott A, Smith WA, Kuykendall TR, Zhao Y, Zhang JZ. Photoelectrochemical study of nanostructured ZnO thin films for hydrogen generation from water splitting. *Adv Funct Mater* 2009;19:1849-56.
- [241] Keis K, Magnusson E, Lindström H, Lindquist S, Hagfeldt A. A 5% efficient photoelectrochemical solar cell based on nanostructured ZnO electrodes. *Sol Energ Mat Sol C* 2002;73:51-8.
- [242] Meng Q, Takahashi K, Zhang X, Sutanto I, Rao T, Sato O et al. Fabrication of an efficient solid-state dye-sensitized solar cell. *Langmuir* 2003;19:3572-4.
- [243] Wan Q, Li Q, Chen Y, Wang T, He X, Li J et al. Fabrication and ethanol sensing characteristics of ZnO nanowire gas sensors. *Appl Phys Lett* 2004;84:3654-6.
- [244] Fan Z, Wang D, Chang P, Tseng W, Lu JG. ZnO nanowire field-effect transistor and oxygen sensing property. *Appl Phys Lett* 2004;85:5923.
- [245] Park W, Yi G, Kim J, Park S. Schottky nanocontacts on ZnO nanorod arrays. *Appl Phys Lett* 2003;82:4358-60.
- [246] Liu C, Zapien JA, Yao Y, Meng X, Lee CS, Fan S et al. High Density, Ordered Ultraviolet Light Emitting ZnO Nanowire Arrays. *Adv Mater* 2003;15:838-41.
- [247] Saremi-Yarahmadi S, Vaidhyanathan B, Wijyantha KGU. Microwave-assisted low temperature fabrication of nanostructured α -Fe₂O₃ electrodes for solar-driven hydrogen generation. *Int J Hydrogen Energy* 2010;35:10155-65.

- [248] Ahmad BI, Peiris TAN, Smith TD, Wijayantha KGU. Hierarchical ZnO nanorod electrodes: Effect of post annealing on structural and photoelectrochemical performance. *Mater Lett* 2013;93:333–36.
- [249] Xie Z, Li J, Huang Y, Kong X. Microwave sintering behaviour of ZrO_2 - Y_2O_3 with agglomerate. *J Mater Sci Lett* 1996;15:1158-60.
- [250] Meek T, Blake R. Ceramic ceramic seals by microwave heating. *J Mater Sci Lett* 1986;5:270-4.
- [251] Fang Y, Agrawal DK, Roy DM, Roy R. Fabrication of porous hydroxyapatite ceramics by microwave processing. *J Mater Res* 1992;7:490-4.
- [252] Clark DE, Sutton WH. Microwave processing of materials. *Annu Rev Mat Sci* 1996;26:299-331.
- [253] Ku HS, Siores E, Taube A, Ball JA. Productivity improvement through the use of industrial microwave technologies. *Comput Ind Eng* 2002;42:281-90.
- [254] Heusler K.E. Die kinetik der zinkelektrode in wassrigen malonatlosungen. *Electrochim Acta* 1973;18:855-61.
- [255] Manseki K, Sugiura T, Yoshida T. Microwave synthesis of size-controllable SnO₂ nanocrystals for dye-sensitized solar cells. *New J Chem* 2014;38:598-603.
- [256] Lagashetty A, Havanoor V, Basavaraja S, Balaji S, Venkataraman A. Microwave-assisted route for synthesis of nanosized metal oxides. *Sci Technol Adv Mater* 2007;8:484-93.

- [257] Kitchen HJ, Vallance SR, Kennedy JL, Tapia-Ruiz N, Carassiti L, Harrison A et al. Modern Microwave Methods in Solid-State Inorganic Materials Chemistry: From Fundamentals to Manufacturing. *Chem Rev* 2014;114:1170–1206.
- [258] Wold A. Photocatalytic properties of titanium dioxide (TiO₂). *Chem Mater* 1993;5:280-3.
- [259] Kumazawa N, Rafiqul Islam M, Takeuchi M. Photoresponse of a titanium dioxide chemical sensor. *J Electroanal Chem* 1999;472:137-41.
- [260] Kavan L, Tétreault N, Moehl T, Grätzel M. Electrochemical Characterization of TiO₂ Blocking Layers for Dye Sensitized Solar Cells. *J Phys Chem C* 2014. DOI: 10.1021/jp4103614.
- [261] Liu B, Liu L, Lang X, Wang H, Lou XWD, Aydil E. Doping High-Surface-Area Mesoporous TiO₂ Microspheres with Carbonate for Visible Light Hydrogen Production. *Energy Environ Sci* 2014. DOI: 10.1039/C4EE00472H.
- [262] El-Rady AAA, El-Sadek MSA, Breky MME, Assaf FH. Characterization and Photocatalytic Efficiency of Palladium Doped-TiO₂ Nanoparticles. *ANP* 2013;2:372.
- [263] Lazzeri M, Vittadini A, Selloni A. Structure and energetics of stoichiometric TiO₂ anatase surfaces. *Phys Rev B* 2001;63:155409.
- [264] Mukri BD, Dutta G, Waghmare UV, Hegde M. Activation of Lattice Oxygen of TiO₂ by Pd²⁺ Ion: Correlation of Low-Temperature CO and Hydrocarbon Oxidation with Structure of Ti_{1-x}Pd_xO_{2-x} (x= 0.01–0.03). *Chem Mater* 2012;24:4491-502.

[265] Popovici D, Nagai H, Fujishima S, Akedo J. Preparation of lithium aluminum titanium phosphate electrolytes thick films by aerosol deposition method. *J Am Ceram Soc* 2011;94:3847-50.

[266] Aono H, Sugimoto E, Sadaoka Y, Imanaka N, Adachi G. Ionic conductivity and sinterability of lithium titanium phosphate system. *Solid State Ionics* 1990;40:38-42.

[267] Pang M, Suzuki R, Saito M, Machida K, Hanzawa H, Nojiri Y et al. Fabrication and crystal line patterning of $\text{Li}_{1.3}\text{Al}_{0.3}\text{Ti}_{1.7}(\text{PO}_4)_3$ ion conductive glass by Ni atom heat processing method. *Appl Phys Lett* 2008;92:041112-3.

Chapter 10

Appendix

10.1 Awards

1. Awarded the Loughborough University Graduate School Research Student Prize 2014.
2. Awarded a travel bursary from RSC to attend the Early Career Energy Sector Chemists Symposium 2013, UKERC, London.
3. Awarded a travel bursary from RSC to attend the Early Career Energy Sector Chemists Symposium 2012, Cranfield University.
4. Graduate School Conference Fund award 2012, Loughborough University, 14th February 2013.
5. Best Poster Award, Energy and Sustainability Expo 2013, Loughborough University.
6. Best Student Poster Award 2012, Chemistry Department Industrial Research Network Meeting, Loughborough University, 25th April 2012.
7. Best Poster Award 2011, Great Western Electrochemistry Group Meeting, University of Bath, 6th June 2011.
8. Second Best Poster Award 2011, Midlands Electrochemistry Group Meeting, University of Warwick, 5th May 2011.

10.2 Peer-reviewed and submitted articles in scientific journals

1. **T. A. Nirmal Peiris**, S. Senthilarasu, and K. G. Upul Wijayantha, Enhanced Performance of Flexible Dye-Sensitized Solar Cells: Electrodeposition of Mg(OH)₂ on a Nanocrystalline TiO₂ Electrode, *Journal of Physical Chemistry C*, **2012**, 116, 1211–1218.
2. Asif Ali Tahir, **T. A. Nirmal Peiris**, and K. G. Upul Wijayantha, Enhancement of Photoelectrochemical Performance of AACVD-produced TiO₂ Electrodes by Microwave Irradiation while Preserving the Nanostructure, *Chemical Vapour Deposition*, **2012**, 18, 107–111.
3. S. Senthilarasu, **T. A. Nirmal Peiris**, Jorge García-Cañadas, and K. G. Upul Wijayantha, Preparation of Nanocrystalline TiO₂ Electrodes for Flexible Dye- Sensitized Solar Cells: Influence of Mechanical Compression, *Journal of Physical Chemistry C*, **2012**, 116, 19053–19061.
4. Muhammad Ali Ehsan, **T. A. Nirmal Peiris**, K.G. Upul Wijayantha, Hamid Khaledi, Huang Nay Ming, Misni Misran, Zainudin Arifin, Muhammad Mazhar, Surface morphological and photoelectrochemical studies of ZnS thin films developed from single source precursors by aerosol assisted chemical vapour deposition, *Thin Solid Films*, **2013**, 540, 1–9.
5. Ijaz Ahmad Bhatti, **T. A. Nirmal Peiris**, Thomas D. Smith, K. G. Upul Wijayantha, Hierarchical ZnO nanorod electrodes: Effect of post annealing on structural and photoelectrochemical performance, *Materials Letters*, **2013**, 93, 333–336.

6. Muhammad Ali Ehsan, **T. A. Nirmal Peiris**, K. G. Upul Wijayantha, Marilyn M. Olmstead, Zainudin Arifin, Muhammad Mazhar, K. M. Lo and Vickie McKee, Development of molecular precursors for deposition of indium sulphide thin film electrodes for photoelectrochemical applications, *Dalton Transactions*, **2013**, 42, 10919–10928.
7. **T. A. Nirmal Peiris**, Hussain Alessa, Jagdeep S Sagu, Ijaz Ahmad Bhatti, Patrick Isherwood, K. G. Upul Wijayantha, Effect of ZnO seed layer thickness on hierarchical ZnO nanorod growth on flexible substrates for application in dye-sensitized solar cells, 2013, Journal of Nanoparticle Research, *Journal of Nanoparticle Research*, **2013**, 15:2115.
8. **T. A. Nirmal Peiris**, K. G. Upul Wijayantha and Jorge García-Cañadas, Insights into mechanical compression and the enhancement in performance by Mg(OH)₂ coating in flexible dye sensitized solar cells, *Physical Chemistry Chemical Physics*, **2014**, 16, 2912-2919.
9. K. G. Chathuranga Senarathna, M. M. M. G. P. G. Mantilaka, **T. A. Nirmal Peiris**, H. M. T. G. A. Pitawala, D.G.G.P. Karunaratne, R.M.G. Rajapakse, Nanocomposites of alkyd resin/polyaniline/vaterite with superior anticorrosive performance on stainless steel surfaces, *Electrochimica Acta*, **2014**, 117, 460– 469.
10. Jagdeep S. Sagu, **T. A. Nirmal Peiris**, K.G. Upul Wijayantha, Rapid and simple potentiostatic deposition of copper (II) oxide thin films, *Electrochemistry Communications*, **2014**, 42, 68–71.
11. Muhammad Mazhar, Muhammad Ali Ehsan, Huang Nay Ming, V McKee, **T. A. Nirmal Peiris**, Upul Wijayantha and Zainudin Arifin, Vysotskite structured photoactive

palladium sulphide thin films from dithiocarbamate derivatives, *New J Chem.* 2014, Accepted Manuscript, DOI: 10.1039/C4NJ00564C.

12. M. A. Mansoor, N. Huang, V. Mckee, **T. A. Nirmal Peiris**, K. G. U. Wijayantha, Z. Arifin and M. Mazhar, Ilmenite-structured and Photoelectrochemically Potent Single Phase MnZnO_3 Solid Solution Thin Films, **2014**, submitted to *Journal of Materials Chemistry A*.

13. **T. A. Nirmal Peiris**, Jagdeep S Sagu, K. G. Upul Wijayantha and Jorge García-Cañadas, Electrochemical Determination of the Density of States of Nanostructured NiO Films, **2014**, Submitted to *ACS Applied Materials & Interfaces*.

14. Sohail Ahmed, Rabia Naeem, Kong Mun Lo, Wan Jeffrey Basirun, Rosiyah Yahya, Zainudin Arifin, **T. A. Nirmal Peiris**, Jagdeep S. Sagu, Upul Wijayantha and Muhammad Mazhar, Realization of Fullerene-Like Structured Tin(IV) Oxide Mesoporous Nano-ball thin films, **2014**, submitted to *Angewandte communications*.

15. Paul Brack, Jagdeep S. Sagu, **T. A. Nirmal Peiris**, Mauro Senili, Andrew McInnes, K. G. U Wijayantha, Frank Marken and Elena Selli Aerosol assisted chemical vapour deposition of bismuth vanadate thin films with enhanced photoelectrochemical properties for solar water splitting, **2014**, submitted to *Chemical Vapour Deposition*.

16. Jagdeep S. Sagu, **T. A. Nirmal Peiris**, Asif A. Tahir and K. G Upul Wijayantha, A p- CuFe_2O_4 photocathode for photoelectrochemical water splitting, **2014**, submitted to *Journal of Physical Chemistry Letters*.

17. **T. A. Nirmal Peiris**, Jagdeep S Sagu and K. G. Upul Wijayantha, Microwave-assisted low temperature fabrication of nanostructured ZnO thin film electrodes for solar energy conversion, **2014**, submitted to *Journal of Materials Chemistry A*.

18. **T. A. Nirmal Peiris**, Jagdeep S. Sagu and K. G. Upul Wijayantha, Fabrication of CoFe₂O₄ thin films by AACVD and their supercapcitive properties, **2014**, submitted to *Electrochemistry Communications*.

19. Jagdeep S Sagu, **T. A. Nirmal Peiris** and K. G. U. Wijayantha, NiO electrodes for flexible electronics: Excellent stabilization effect of formic acid, 2014, submitted to *Langmuir*.

10.3 Conference participations and presentations

1. The IET Seminar on Microwave Heating and Processing of Materials, Nottingham University, 2 February 2011.
2. **T. A. Nirmal Peiris**, S. Senthilarasu and K.G.U. Wijayantha, Novel Routes for Flexible and Colourful Solar Cells, *Research Presentation Gala for PhD Researches*, Loughborough University, 5 May 2011.
3. **T. A. Nirmal Peiris**, S. Senthilarasu and K.G.U. Wijayantha, An Electrochemical Route to Enhance the Performance of Flexible Dye-Sensitized Solar Cells, *Midlands Electrochemistry Group Meeting (MEG 2011)*, University of Warwick, 5 May 2011.
4. **T. A. Nirmal Peiris**, S. Senthilarasu and K.G.U. Wijayantha, Improved Flexible Dye-Sensitized Solar Cells by Surface Passivation of TiO₂, *Great Western Electrochemistry Research Meeting (GWR 2011)*, University of Bath, 6 June 2011.
5. S. Senthilarasu, **T. A. Nirmal Peiris** and K. G. U. Wijayantha, An Electrochemical Route for Improved Flexible DSC, *Electrochem 2011*, University of Bath, September 5-6, 2011,
6. **T. A. Nirmal Peiris**, S. Senthilarasu and K.G.U. Wijayantha, Future Vision of Green Energy; Improved Flexible DSCs, *MEGS II Annual Conference 2011*, Park Inn Nottingham, 8 and 9 September 2011.
7. **T. A. Nirmal Peiris** and K.G.U. Wijayantha, Enhancement of Photoelectrochemical Performance of TiO₂ electrodes, *Research Conference - Research That Matters*, Loughborough University, 6 March 2012.

8. **T. A. Nirmal Peiris** and K.G.U. Wijayantha, Improved Flexible Dye-Sensitized Solar Cells, *Science Matters Research Conference 2012*, Loughborough University, 21 March 2012.
9. **T. A. Nirmal Peiris** and K.G.U. Wijayantha, Enhancement of Photoelectrochemical Performance of TiO₂ electrodes under Microwave Irradiation, *Johnson Matthey Academic Conference*, Loughborough University, 27 and 28 March 2012.
10. **T. A. Nirmal Peiris**, S. Senthilarasu and K.G.U. Wijayantha, Future Vision of Green Energy; Improved Flexible Dye-Sensitized Solar Cells, *International Conference on Low-cost, electricity generating heat engines for rural areas*, East Midlands Conference Centre, Nottingham, 2 and 3 April 2012.
11. **T. A. Nirmal Peiris**, S. Senthilarasu and K.G.U. Wijayantha, Future Vision of Green Energy; Improved Flexible Dye-Sensitized Solar Cells, *International Conference on UK Low Carbon Energy for Development Network (LCEDN)*, Loughborough University, 4 and 5 April 2012.
12. **T. A. Nirmal Peiris**, S. Senthilarasu and K.G.U. Wijayantha, Improved Flexible Dye-Sensitized Solar Cells for Future Energy Needs, *The Midlands Energy Consortium/Sustainability Research School conference "Smart Energy Cities: UK – Japanese Perspectives"*. Loughborough University, 17 and 18 April 2012.
13. **T. A. Nirmal Peiris**, S. Senthilarasu and K.G.U. Wijayantha, Improved Flexible Dye-Sensitized Solar for Future, *Chemistry Department Research Network Meeting 2012*, Loughborough University, 25 April 2012.

14. **T. A. Nirmal Peiris**, S. Senthilarasu and K.G.U. Wijayantha, Future vision for green chemistry, “*Smart Low Carbon Cities Conference 2012*”, National Exhibition Centre, Birmingham, 23 May 2012.
15. **T. A. Nirmal Peiris** and K.G.U. Wijayantha, Enhancement of Photoelectrochemical Performance of Semiconductor Electrodes: Processing by Microwave Irradiation, *Great Western Electrochemistry Conference*, University of Bath, 2012, 18 June 2012.
16. **T. A. Nirmal Peiris** and K.G.U. Wijayantha, Enhancement of Photoelectrochemical Performance of TiO₂ Electrodes under Microwave Irradiation, *Midlands Electrochemistry Group Meeting 2012*, University of Birmingham, 27 June 2012.
17. **T. A. Nirmal Peiris** and K.G.U. Wijayantha, Enhancement of Photoelectrochemical Performance of Semiconductor Electrodes: Processing by Microwave Irradiation, *International Conference on Advanced Materials, Science and Engineering (ICAMSE-12)*. Colombo, Sri Lanka. 1 - 4 July, 2012.
18. **T. A. Nirmal Peiris**, I.A. Bhatti and K.G.U. Wijayantha, Enhancement in Photoelectrochemical Properties of Microwave Treated Electrodes, *Electrochem 2012*, Trinity College, Dublin, Ireland. 2- 4 September, 2012.
19. I. A. Bhatti, **T. A. Nirmal Peiris**, T. Smith and K.G.U. Wijayantha, Fabrication and Photoelectrochemical Characterisation of Nanostructured ZnO Thin Films, *Electrochem 2012*, Trinity College, Dublin, Ireland. 2- 4 September, 2012.
20. **T. A. Nirmal Peiris**, S. Senthilarasu and K.G.U. Wijayantha, Transitions to Low Carbon Energy Systems; Improved Flexible Dye-sensitized Solar Cells, *International Conference*

on UK Low Carbon Energy for Development Network (LCEDN), University of Sussex, Brighton. 10- 11 September 2012.

21. **T. A. Nirmal Peiris**, S. Senthilarasu and K.G.U. Wijayantha, Transitions to Low Carbon Energy Systems; Improved Flexible Dye-sensitized Solar Cells, *MEGS III Annual Conference*, University of Birmingham. 18- 19 September, 2012.
22. **T. A. Nirmal Peiris**, I.A. Bhatti and K.G.U. Wijayantha, Microwave-assisted processing of semiconductor materials for sustainable energy applications, *ENERGY MATERIALS - Meeting the Challenge conference*, Loughborough University, 16-17 October 2012.
23. **T. A. Nirmal Peiris** and K.G.U. Wijayantha, Enhancement of Photoelectrochemical Performance of Semiconductor Electrodes: Processing by Microwave Irradiation, *The Association of professional Sri Lankan in the UK (APSL), APSL Research Symposium*, Sheffield, 17 November 2012.
24. **T. A. Nirmal Peiris** and K.G.U. Wijayantha, Enhancement in Photoelectrochemical Properties of Microwave Treated Electrodes, *The Association of professional Sri Lankan in the UK (APSL), APSL Research Symposium*, Sheffield 17 November 2012.
25. I. A. Bhatti, **T. A. Nirmal Peiris**, T. Smith and K.G.U. Wijayantha, Fabrication and Photoelectrochemical Characterisation of Nanostructured ZnO Thin Films, *The Association of professional Sri Lankan in the UK (APSL), APSL Research Symposium*, Sheffield, 17 November 2012.
26. **T. A. Nirmal Peiris**, S. Senthilarasu and K.G.U. Wijayantha, Transitions to Low Carbon Energy Systems; Improved Flexible Dye-sensitized Solar Cells, *RSC Energy Sector Early*

Career Energy Sector Chemists Symposium 2012, Cranfield University, Bedfordshire, 27 November 2012.

27. **T. A. Nirmal Peiris**, S. Senthilarasu and K.G.U. Wijayantha, Development of high efficiency dye sensitized solar cells: Electrodeposition of $\text{Mg}(\text{OH})_2$ on TiO_2 Electrodes, *MEGS III Christmas Conference*, National College, Triumph Road, Nottingham, 14 December 2012.
28. **T. A. Nirmal Peiris**, S. Senthilarasu and Upul Wijayantha, Recent Advances in Flexible Dye-Sensitized Solar Cells, *Energy and Sustainability Expo 2013*, Loughborough University, 14 February 2013.
29. **T. A. Nirmal Peiris**, Rob Potter and Upul Wijayantha, Microwave-assisted Processing of Solid Materials for Sustainable Energy Related Electronic and Optoelectronic Applications, *Johnson Matthey Academic Conference 2013*, Loughborough University, 16 and 17 April 2013.
30. H. Alessa, **T. A. Nirmal Peiris**, I. Bhatti and K. G. U Wijayantha, ZnO nanorods for energy related applications, *Midlands Electrochemistry Group Meeting 2013*, University of Nottingham, 17 April 2013.
31. **T. A. Nirmal Peiris**, S. Senthilarasu and Upul Wijayantha, Recent Advances in Flexible Solar Cells, *Science Matters 2013*, Loughborough University, 1 May 2013.
32. H. Alessa, **T. A. Nirmal Peiris**, I. Bhatti and K. G. U Wijayantha, ZnO nanorods for energy related applications, *Science Matters 2013*, Loughborough University, 1 May 2013.

33. **T. A. Nirmal Peiris** and Upul Wijayantha, Photoelectrochemical studies of microwave treated electrodes, *ISE Satellite Student Regional Symposium: Great Western Photoelectrochemistry Meeting 2013*, University of Bath, 10 June 2013.
34. Jagdeep S Sagu, K. G. Upul Wijayantha, Asif Tahir, **T. A. Nirmal Peiris**, Spinel Ferrites as an Emerging class of semiconductor for solar energy conversion, *Electrochem 2013*, University of Southampton, 01-03 September 2013.
35. **T. A. Nirmal Peiris**, K. G. Upul Wijayntha, Jorge García-Cañadas, Electrochemical Analysis of the effect of electrodeposited $Mg(OH)_2$ layer on the performance of mechanically compressed flexible dye sensitized solar cells, *Electrochem 2013*, University of Southampton, 01-03 September 2013.
36. Hussain Alessa, Jagdeep S Sagu, **T. A. Nirmal Peiris**, Ijaz Ahamad Bhatti, K. G. Upul Wijayantha, ZnO Nanorods on glass and plastic based substrates for various energy applications, *Electrochem 2013*, University of Southampton, 01-03 September 2013.
37. **T. A. Nirmal Peiris**, S. Saremi-Yarahmadi and K. G. Upul Wijayantha, Microwave Processing of Semiconductor Electrodes for various Electronic Applications, *14th International Conference on Microwave and High Frequency Heating (AMPERE 2013)*, University of Nottingham UK, 16-19 September 2013.
38. **T. A. Nirmal Peiris** and K. G. Upul Wijayantha, Transitions to Low Carbon Energy Systems; Improved Plastic based Solar Cells, *Early Career Energy Sector Chemists Symposium 2013*, RSC Energy Sector, London, 21 November 2013.

39. **T. A. Nirmal Peiris** and K. G. Upul Wijayantha, Low Carbon Energy; Flexible Colourful Solar Cells, *MEGS IV Christmas Conference*, Midlands Energy Graduate School, Birmingham, 12 December 2013.
40. H. Alessa, Jagdeep S Sagu, **T. A. Nirmal Peiris**, I. Bhatti and K. G. U Wijayantha, ZnO nanorods for energy related applications, *Midlands Electrochemistry Group Meeting 2014*, Loughborough University, 1 April 2014.
41. UK representative in *Researcher Links workshop between Egypt and the UK*, Nottingham University, 31 March- 3 April 2014.
42. **T. A. Nirmal Peiris**, Rob Potter and Upul Wijayantha, Microwave-assisted Processing of Solid Materials for Sustainable Energy Related Electronic and Optoelectronic Applications, *Johnson Matthey Academic Conference 2014*, Loughborough University, 15 and 16 April 2014.
43. Contestant of *Engineering YES - Heat 3* – Birmingham, Birmingham Holiday Inn, 18-21 May 2014.
44. **T. A. Nirmal Peiris**, Rob Potter and Upul Wijayantha, Microwave-assisted Processing of Solid Materials for Sustainable Energy Related Electronic and Optoelectronic Applications, *Chemistry Research Day 2014*, Loughborough University, 21 May 2014.
45. Hussain Alessa, Jagdeep S Sagu, **T. A. Nirmal Peiris**, Ijaz Ahamad Bhatti, K. G. Upul Wijayantha, ZnO Nanorods based flexible dye-sensitized solar cells, *Chemistry Research Day 2014*, Loughborough University, 21 May 2014.

46. **T. A. Nirmal Peiris**, Subhashi Jayathilake, Hussain Alessa and Upul Wijayantha, Transition to Renewable Energy Systems; Efficient Flexible Solar Cells, *Chemistry Research Day 2014*, Loughborough University, 21 May 2014.
47. **T. A. Nirmal Peiris**, Subhashi Jayathilake, Hussain Alessa and Upul Wijayantha, Transition to Renewable Energy Systems; Efficient Flexible Solar Cells, *Science Matters 2014*, Loughborough University, 22 May 2014.
48. Hussain Alessa, Jagdeep S Sagu, **T. A. Nirmal Peiris**, Ijaz Ahamad Bhatti, K. G. Upul Wijayantha, ZnO Nanorods based flexible dye-sensitized solar cells, *Science Matters 2014*, Loughborough University, 22 May 2014.
49. **T. A. Nirmal Peiris**, Subhashi Jayathilake, Hussain Alessa, Jorge García-Cañadas and Upul Wijayantha, Electrochemical Analysis of the Effect of Electrodeposited Mg(OH)₂; Efficient Flexible Solar Cells, *Great Western Electrochemistry Meeting*, University of Bath, 2 June 2014.
50. Hussain Alessa, Jagdeep S Sagu, **T. A. Nirmal Peiris**, Ijaz Ahamad Bhatti, K. G. Upul Wijayantha, ZnO Nanorods based flexible dye-sensitized solar cells, *Great Western Electrochemistry Meeting*, University of Bath, 2 June 2014.
51. Jagdeep S Sagu, **T. A. Nirmal Peiris**, K. G. Upul Wijayantha, Rapid Electrodeposition of light harvesting CuO Photocathodes, *Great Western Electrochemistry Meeting*, University of Bath, 2 June 2014.
52. Subhashi Jayathilake, **T. A. Nirmal Peiris**, Hussain Alessa, Jagdeep S Sagu, Jorge García-Cañadas and Upul Wijayantha, Flexible High Efficiency Dye-sensitized and Perovskite based Solar Cells, *Regional Postgraduate Symposium: Great Western Photoelectrochemistry Meeting*, University of Bath, 9 June 2014.

53. Jagdeep S Sagu, **T. A. Nirmal Peiris**, K. G. Upul Wijayantha, Rapid and simple potentiostatic deposition of CuO thin films, Regional Postgraduate Symposium: Great Western Photoelectrochemistry Meeting, University of Bath, 9 June 2014.
54. Hussain Alessa, Jagdeep S Sagu, **T. A. Nirmal Peiris**, Ijaz Ahamad Bhatti, K. G. Upul Wijayantha, ZnO Nanorods based flexible dye-sensitized solar cells, *Great Western Electrochemistry Meeting*, University of Bath, 9 June 2014.
55. **T. A. Nirmal Peiris**, Subhashi Jayathilake, Hussain Alessa and Upul Wijayantha, Transition to Renewable Energy Systems; Efficient Flexible Solar Cells, *Research That Matters: Research Challenges in Focus*, Loughborough University, 18 June 2014.
56. **T. A. Nirmal Peiris**, Extracurricular skills development during the PhD, *Research That Matters: Research Challenges in Focus*, Loughborough University, 18 June 2014.